Development of an Eulerian multiphase CFD model for simulating a liquid organic hydrogen carrier dehydrogenation reactor

Daniel Alejandro Yáñez Díaz

TUDelft

VOYEX

Development of an Eulerian multiphase CFD model for simulating a liquid organic hydrogen carrier dehydrogenation reactor

by

Daniel Alejandro Yáñez Díaz

Submitted to obtain the degree of Master of Science
in Mechanical Engineering at the Delft University of Technology.

An electronic version of this thesis is available at `http://repository.tudelft.nl/`.

Abstract

Hydrogen has emerged as a promising candidate for energy storage, offering an alternative to fossil fuels as a primary fuel source. It can be safely stored in a liquid organic hydrogen carrier (LOHC) and recovered upon demand through the reversible hydrogenation/dehydrogenation of the LOHC. Voyex, a technology-driven startup, is developing a novel LOHC that can be loaded onto ships and dehydrogenated onboard, providing hydrogen for ship propulsion as an alternative to fossil fuels. The successful implementation of this new technology requires a dehydrogenation reactor that may provide the conditions necessary for LOHC dehydrogenation to meet the ship's power demand.

This work develops a computational fluid dynamics (CFD) model to simulate the LOHC dehydrogenation reaction within a cocurrent upward-flow fixed-bed reactor. While lab-scale studies have examined the effect of operating conditions on the dehydrogenation of specific LOHCs, only a few works have studied LOHC dehydrogenation reactors and the inner flow details have yet to be understood. A CFD model will allow for a better understating of the flow, temperature, and species distribution within the reactor, and help gain more insight into the design and operating parameters on the reactor performance as measured by conversion and hydrogen yield.

This thesis delves into the distinct phenomena at play within an LOHC dehydrogenation reactor including hydrodynamics, heat transfer, species transport, and reaction kinetics, discussing ways to incorporate them into a numerical model. These effects are brought together in an Eulerian multiphase CFD model, as this approach is found to provide a good balance between modelling accuracy and computational demand.

The result of this research is a computationally inexpensive Eulerian multiphase CFD model capable of adapting to various LOHC systems and reactor configurations. Through multiple sensitivity analyses, the impact of design variables including reactor dimensions, temperature, flow rate, and catalyst pellet diameter on reactor performance is explored. These analyses yield valuable insights and design parameters to enhance reactor efficiency. Additionally, these analyses lead to several design improvement proposals such as raising the reactor inlet temperature, using a low inlet LOHC mass flux, incorporating gas-liquid separation methods, adding internal heating mechanisms, and employing internal baffles to disrupt flow and enhance heat transfer. The findings underscore potential for reactor design improvements, thereby proving the CFD model as a research and design tool for packed-bed multiphase reactors.

Contents

List of Figures

List of Tables

Nomenclature

Abbreviations

Abbreviation	Definition
0H-DBT	Dibenzyltoluene
18H-DBT	Perhydro-dibenzyltoluene
0H-NEC	N-ethylcarbazole
4H-NEC	Tetrahydro-N-ethylcarbazole
8H-NEC	Octahydro-N-ethylcarbazole
12H-NEC	Perhydro-N-ethylcarbazole
ANN	Artificial neural network
BET	Brunauer, Emmett and Teller
CFD	Computational fluid dynamics
CSTR	Continuous stirred-tank reactor
CT	Computer tomography
DEM	Discrete element method
DoH	Degree of hydrogenation
FBR	Flooded-bed reactor
LDA	Laser Doppler anemometry
LDV	Laser Doppler velocimetry
LHS	Left-hand side
LHV	Lower heating value
LOHC	Liquid organic hydrogen carrier
MCH	Methylcyclohexane
MRI	Magnetic resonance imaging
NLPM	Normal litre per minute
TBR	Trickle-bed reactor
PDE	Partial differential equation
PFR	Plug flow reactor
PIV	Particle image velocimetry
PTV	Particle tracking velocimetry
RBD	Rigid body dynamics
RHS	Right-hand side
rGO	Reduced graphene oxide
RKE	Realizable $k - \varepsilon$
RNG	Renormalization-group $k - \varepsilon$
SKE	Standard $k - \varepsilon$
STEPS	Stated policies scenario
UDF	User-defined function
UDM	User-defined memory
UDS	User-defined storage
VLE	Vapor-liquid equilibrium
VOF	Volume of fluid
WMS	Wire mesh sensors

Symbols

Symbol	Definition	Unit
A	Arrhenius reaction rate equation pre-exponential factor	[-]
A_p	Particle surface area	[m^2]
B	Deformation factor	[-]
Bi	Biot number	[-]
C	Concentration	[mol/l]
C_f	Shape factor	[-]
c_sat	Concentration of saturation	[mol/m^3]
c_p	Specific heat capacity	[J/(kg·K)]
$\mathcal{D}^{\circ}_{i,j}$	Binary diffusion coefficient of component i in component j at infinite dilution	[cm^2/s]
D	Reactor diameter	[m]
D_r	Radial dispersion coefficient	[m^2/s]
D_a	Axial dispersion coefficient	[m^2/s]
D_m	Mixture molecular diffusion coefficient	[m^2/s]
d_p	Particle diameter	[m]
d_pe	Equivalent sphere particle diameter	[m]
E	Ergun constants	[-]
E_a	Activation energy	[kJ/mol]
Eo	Eötvos number	[-]
f	Shape factor	[-]
F	Drag force per unit volume	[N/m^3]
Fr	Froude number	[-]
f_LG	Two-phase friction factor	[-]
G	Gas mass flux	[kg/m^{2}s]
Ga	Galileo number	[-]
$\boldsymbol{g}$	Acceleration due to gravity	[m/s^2]
h	Specific enthalpy	[J/kg]
h_fs	Fluid-solid heat transfer coefficient	[W/m^{2}K]
h_pq	Interphase enthalpy	[J/kg]
h_w	Wall heat transfer coefficient	[W/m^{2}K]
ΔH	Heat of reaction	[J/mol]
J	Mass flux	[kg/m^{2}s]
J_0, J_1	Bessel function of the first kind of order zero and one, respectively	[-]
$\boldsymbol{J}^i_q$	Hydrodynamic dispersive flux of species i in phase q	[kg/m^{2}s]
k	Reaction rate constant	[s^{-1}]
k	Turbulent kinetic energy	[J/kg]
k	Relative permeability	[-]
k_ls	Liquid-solid mass transfer coefficient	[m/s]
K_pq	Interface momentum exchange coefficient	[kg/m^{2}s]
L	Liquid mass flux	[kg/m^{2}s]
$\dot{m}_{i,q}$	Mass flow rate of qth phase through cell i in the axial direction	[kg/s]
$\dot{m}_\mathsf{pq}$	Mass transfer from the pth phase to the qth phase	[kg/s]
M	Molecular weight	[g/mol]
Nu	Nusselt number	[-]
p_c	Capillary pressure	[Pa]
P	Pressure	[Pa]
Pe	Péclet number	[-]
Pr	Prandtl number	[-]
$\boldsymbol{q}$	Heat flux	[W/m^2]
$\boldsymbol{Q}_\mathsf{pq}$	Intensity of heat exchange between p^th and q^th phases	[J/s]
r_p	Particle radius	[m]
$r_\mathsf{p,v}$	Reaction rate per unit particle volume	[mol/m^{3}s]

Symbol	Definition	Unit
r_v	Reaction rate per unit bed volume	[mol/m^{3}s]
R	Universal gas constant	[J/(K·mol)]
R_r	Reactor radius	[m]
Re	Reynolds number	[-]
S_{mass}	Mass source	[kg/s]
$\boldsymbol{S}_{momentum}$	Momentum source	[kg/m^{2}s^2]
S_{energy}	Energy source	[J/s]
$S_{species}$	Species source	[kg/m^{3}s]
Sh	Sherwood number	[-]
T	Temperature	[K]
$\boldsymbol{U}$	Interstitial velocity	[m/s]
$\boldsymbol{V}$	Superficial velocity	[m/s]
V_p	Particle volume	[m^3]
We	Weber number	[-]
X	Lockart-Martinelli factor	[-]
x_i	Mole fraction of species i	[-]
y_i	Mass fraction of species i	[-]
Greek symbols		
α_G	Gas saturation	[-]
β_L	Liquid saturation	[-]
δ_L	Reduced liquid saturation	[-]
ϵ	Porosity	[-]
ϵ_B	Mean bed porosity	[-]
ϵ_L	Emissivity of liquid	[-]
ε	Turbulent energy dissipation rate	[J/(kg·s)]
ε_q	Volume fraction of phase q	[-]
ε_q^0	Static liquid volume fraction of phase q	[-]
η_{WE}	External particle wetting efficiency	[-]
λ	Thermal conductivity	[W/(m·K)]
λ_{rad}	Radiative heat transfer equivalent thermal conductivity	[W/(m·K)]
Λ_e	Effective radial thermal conductivity	[W/(m·K)]
μ	Dynamic viscosity	[Pa·s]
ρ	Density	[kg/m^3]
σ	Surface tension	[N/m]
σ_{SB}	Stefan-Boltzmann constant	[W/m^{2}K^4]
τ	Tortuosity factor	[-]
$\bar{\bar{\tau}}$	Shear stress tensor	[Pa]
φ	Particle sphericity	[-]
ϕ	Flattening coefficient	[-]
Subscripts		
a	Axial	
G	Gas phase	
i	i^{th} specie	
j	j^{th} specie	
p	p^{th} phase	
q	q^{th} phase	
L	Liquid phase	
m	Mixture	
r	Radial	
S	Solid phase	
w	Wall	

<div align="right">

1

</div>

Introduction

1.1. Introduction

As the world strives towards an electrifying future, where global electricity demand is projected to grow by 24% between 2021 and 2030, and 77% by 2050 [51], the spotlight shines on renewable energy sources and the pressing need for large-scale energy storage solutions. These projections follow the "Stated Policies Scenario" (STEPS) of the International Energy Agency (IEA) [51] and the numbers are even higher with more optimistic scenarios. This is due to factors including population increase, electrification, development of new areas, and a shift from hydrocarbon fuels to electric powered applications in the transport, industry, and buildings sectors. Leading the electricity production growth are the renewable energy sources whose share of electricity production is expected to rise from 28% in 2021 to 43% in 2030 and 65% by 2050 in the STEPS scenario [51].

The substantial increase in electricity production from renewable sources, and the desire to shift to these energy sources within the transport sector, brings about a novel need for large-scale energy storage. A main challenge encountered in the seamless integration of large-scale renewable energy within the existing energy system is the inherent intermittency of its production. Renewable energy sources such as solar photovoltaic units and wind turbines are highly dependent on meteorological conditions that have strong daily and seasonal variations. This creates a need for energy storage as an imbalance develops between energy production and demand, both temporally and spatially as locations with high potential for renewable energy production are often far from electricity demand.

Electric energy must be either utilized immediately upon production or transformed into another form of energy for its storage. For example, it may be stored as mechanical energy (e.g. pumped hydro storage, compressed air, or flywheel energy storage), thermal energy (e.g. molten salt storage), electrochemical (e.g. batteries), or chemical energy (e.g. biofuels, hydrogen). Among these possibilities, hydrogen has been identified as a flexible energy storage medium that can be produced from any energy source. The main challenges for hydrogen implementation are related to its production and storage.

Hydrogen production relies heavily on methods such as hydrocarbon reforming and gasification (e.g. steam methane reforming or coal gasification). These approaches, known as "black and gray hydrogen," yield substantial carbon dioxide emissions. If the carbon emissions from these processes are captured, the resulting hydrogen is referred to as "blue hydrogen". Furthermore, hydrogen generated without any greenhouse gas emissions is dubbed "green hydrogen". Green hydrogen is produced by using surplus renewable energy to split water molecules in an electrolyzer into hydrogen and oxygen molecules. The hydrogen can then be stored and utilized when required as fuel for internal combustion engines, gas turbines, fuel cells, or as a base chemical for producing biofuels or other chemicals.

An advantage of hydrogen as an energy storage medium is its high gravimetric energy density (120 MJ/kg compared to gasoline's 46 MJ/kg). However, a major drawback is its exceedingly low volumetric energy density under ambient conditions (0.01 MJ/l compared to gasoline's 38 MJ/l for gasoline). Therefore, effective storage methods are needed to facilitate its widespread adoption. Generally, hydrogen can be stored using various methods including compression, liquefaction, physical adsorption by porous materials, and chemical binding to solid or liquid substances.

Compressed hydrogen involves storing hydrogen gas at high pressures (350-700 bar), providing a mature technology that allows for rapid refueling. Compressed hydrogen, however, requires robust and heavy storage tanks, and the compression process itself requires a significant energy input. Liquefied hydrogen offers a higher energy density than compressed gas, but around a third of the hydrogen's lower heating value is required to bring the gas to a liquid state (-253°C at atmospheric pressure)

[21]. Liquefied hydrogen is prone to boil-off losses over time and further requires special vessels and heavy insulation, increasing system complexity and cost. Additionally, hydrogen can be physically adsorbed through van der Waals interactions onto porous materials such as zeolites, metal organic frameworks, carbon structures, and metal hydrides. While this approach can offer lightweight and compact solutions, the adsorption and desorption processes tend to be slow and may require high pressure and temperatures.

One of the more flexible methods for hydrogen storage involves forming chemical bonds with liquid compounds known as liquid organic hydrogen carriers (LOHCs). These compounds can be reversibly hydrogenated and dehydrogenated in the presence of a catalyst. LOHCs are unsaturated organic compounds that can react with hydrogen under elevated temperatures and pressures to break double bonds within the LOHC molecule and saturate them with hydrogen atoms. The hydrogenated molecule can be easily stored at ambient conditions, making it suitable for long-term storage. When required, the stored hydrogen can be recovered by dehydrogenating the molecule at elevated temperatures, leaving the original molecule unchanged. The LOHC can then be reused in a subsequent hydrogenation-dehydrogenation cycle.

Selecting the most suitable hydrogen storage method depends on factors such as storage time, transport requirements, safety considerations, and the desired balance between energy density and system complexity.

Focusing on the transport industry, a way to shift towards renewable energies has been through the development of electric vehicles. These, however, have mostly been limited to light vehicles with batteries that can store relatively small amounts of energy as required by light vehicles. Heavy-duty vehicles such as trucks or ships, have large power and energy demands that are more difficult to cover with batteries. For such applications, LOHCs can become an alternate solution and be a pathway for the energy transition in the heavy-duty vehicle industry.

Voyex is a technology driven startup that has developed a new LOHC for powering heavy-duty maritime applications. Voyex envisions utilizing the LOHC for heavy-duty ships by hydrogenating the LOHC at a station near a port, loading the hydrogenated LOHC onto a ship, and subsequently utilizing an onboard reactor to dehydrogenate the LOHC. This process supplies the ship with gaseous hydrogen to be utilized by a fuel cell system, or it can be combusted in an internal combustion engine to generate power for propelling the ship. The dehydrogenated LOHC would then be stored in a second tank and interchanged for hydrogenated LOHC upon arrival at port.

Voyex has achieved significant progress with the LOHC on a laboratory scale and is now progressing towards a pilot-scale design for the hydrogenation and dehydrogenation processes. This thesis focuses on the dehydrogenation reactor, which must be installed onboard the ship to provide the correct conditions for LOHC dehydrogenation and produce the amount of hydrogen required. The reactor design and operating conditions have yet to be determined, and this work will dive into dehydrogenation reactor modeling to understand the effect of diverse design parameters. The initial reactor type proposed by Voyex is a fixed-bed reactor and its suitability compared to other reactor designs will be discussed further on.

The objective of this work is to understand the LOHC dehydrogenation reaction within a fixed-bed reactor by developing a numerical model to simulate the process within the reactor. The model will need to incorporate various aspects of the reactive flow including hydrodynamics, heat transfer, and the chemical reaction. Given that the dehydrogenation reaction produces a significant amount of gas, it is hypothesized that the gas bubbles may interfere with the ongoing reaction by blocking liquid LOHC from reaching catalyst particles. As such, a goal of this work is to understand the effect of hydrogen bubbles on the ongoing reactions and discuss possibilities to improve reactor performance.

Voyex has begun developing two LOHC dehydrogenation experimental setups with different capacities shown in Figure 1.1. While this work will focus on the numerical modeling of the reactor, experimental work using these setups may be done at a later stage to help validate and adjust the numerical model.

(a) 345 ml dehydrogenation reactor.

(b) 1500 ml dehydrogenation reactor.
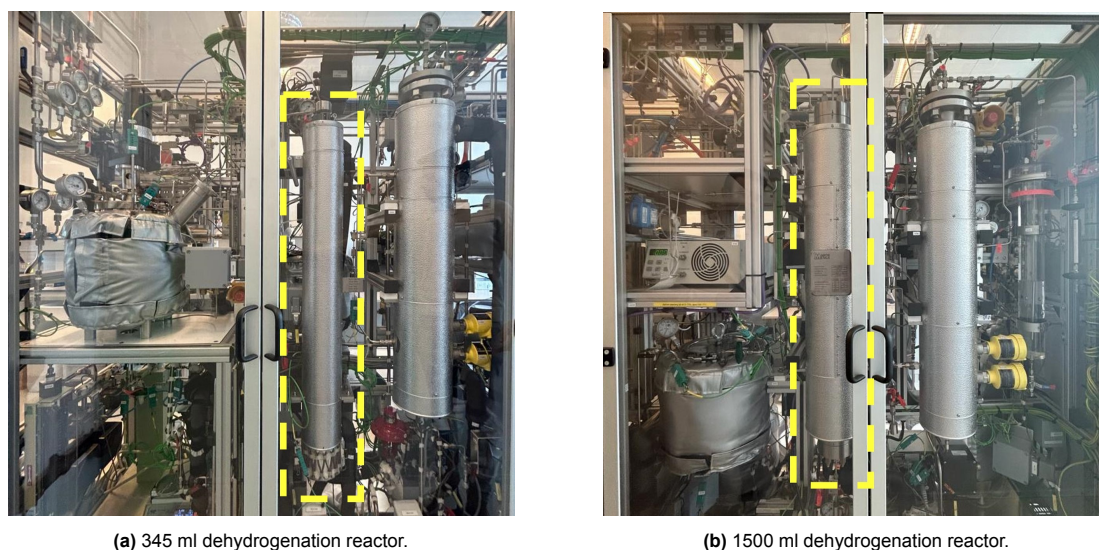
Figure 1.1: Experimental setups at Voyex with the LOHC dehydrogenation reactors framed in yellow.

The finalized model will provide insight into the inner flow and temperature fields so that reactor design improvements may be proposed. Furthermore, the validated model will not only help determine reactor design for the current setup but may also be used for future scale-up.

1.2. Research objective

Researchers have mainly explored LOHC dehydrogenation through experimental studies, focusing on catalyst testing, reaction modeling, and studying the impact of parameters like temperature and pressure for specific LOHC systems and specific reactor designs. No study, however, was found to simulate the LOHC dehydrogenation reaction through a computational fluid dynamics (CFD) model for a more comprehensive understanding of the flow, heat transfer and reaction progress within packed-bed reactors. Furthermore, most CFD simulations of packed-bed reactors are found to only study hydrodynamic aspects without involving heat transfer or chemical reactions.

To address this gap, this thesis aims to study LOHC dehydrogenation within a fixed-bed reactor through CFD simulations. This approach will offer insight into the hydrodynamic and heat transfer aspects within the dehydrogenation reactor as hydrogen bubbles are produced. A numerical model will be developed to predict the flow, temperature, and species concentration fields to relate reactor operating parameters with performance metrics, including degree of dehydrogenation and hydrogen yield. It will be important to understand the degree to which the large volumes of released hydrogen affect the reaction taking place and discuss ways to mitigate these effects. The numerical model will be validated step-by-step against other numerical and experimental tests found in literature to ultimately propose adequate choices for reactor design and operating conditions.

1.3. Thesis outline

First, chapter 2 provides a general background and literature review to understand the distinct aspects of this thesis project. Subsequent chapters 3 to 6 progressively develop the CFD model, focusing on individual aspects. In chapter 3, a non-reactive isothermal multiphase flow through a packed bed is modeled to understand hydrodynamics. Chapter 4 delves into material properties and chemical kinetics for the LOHC-H_2 system. Moving to chapter 5, material properties are integrated, and heat transfer models are discussed. This leads to chapter 6, where species transport and reaction kinetics are incorporated. These aspects converge in chapter 7, completing the LOHC dehydrogenation reactor model. Chapter 7 further uses the model to explore the impact of several design parameters on reactor performance. Final conclusions and recommendations for future work are included in chapter 8.

2

General background and literature review

This chapter provides background information and relevant findings from a literature review. It begins by presenting background information of LOHCs followed by specific details of two selected LOHCs similar to that developed by Voyex. The chapter moves on to discuss reactor designs considered for the dehydrogenation reactor followed by additional characteristics of multiphase fixed-bed reactors including hydrodynamic, mass transfer, and heat transfer aspects. Finally, the review discusses the different reactor modeling approaches and further details the selected Eulerian multiphase CFD modeling approach that will be used in this project. A high-level overview of the topics in this chapter is represented by Figure 2.1.

General background and literature review

LOHCs

- General background
- N-ethylcarbazole system
- Dibenzyltoluene system

Reactor design

- Design strategies
- Dehydrogenation reactor designs

Multiphase fixed-bed reactors

- Hydrodynamics
- Mass Transport
- Heat Transport

Reactor modeling

CFD Modeling

Euler-Euler approach
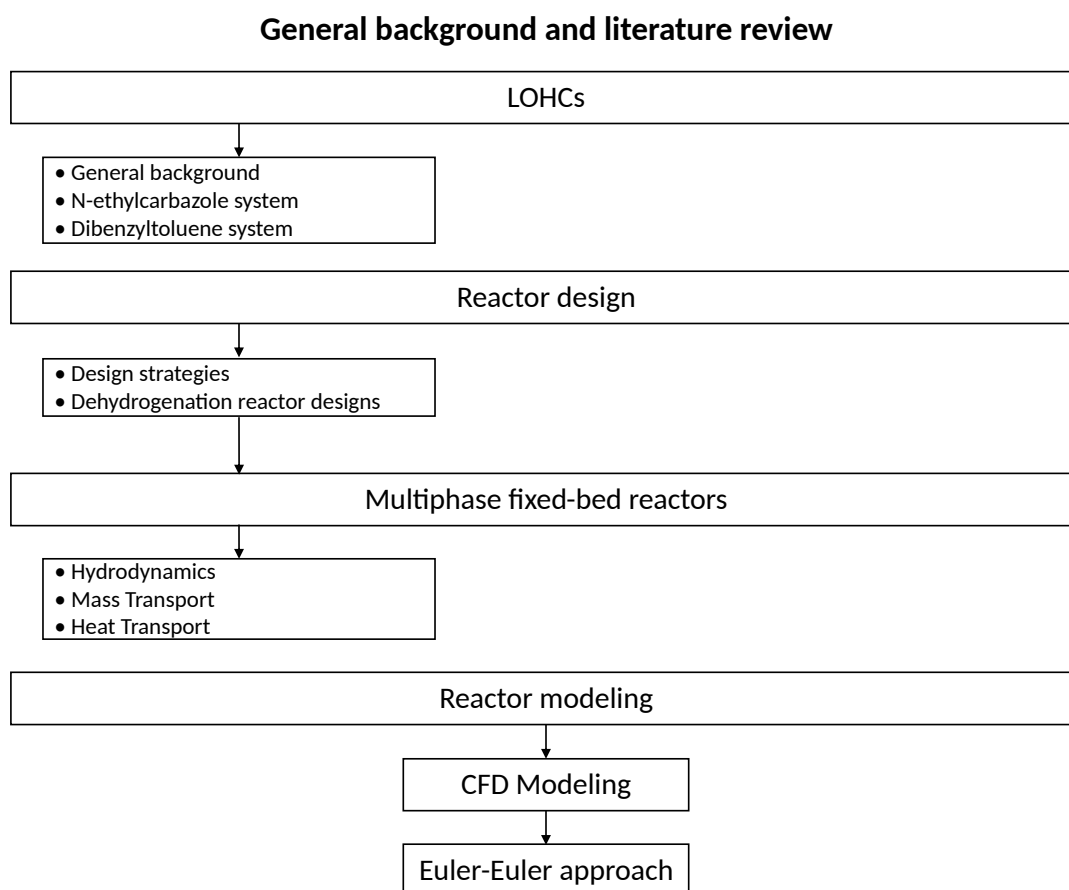
Figure 2.1: Overview of chapter 2.

2.1. Liquid organic hydrogen carriers

LOHCs provide a hydrogen storage method at ambient conditions, presenting a long-term energy storage solution without boil-off or hydrogen losses associated with other hydrogen storage methods. Since LOHCs are liquid at ambient conditions and have comparable properties to crude oil-based liquids, they

can be easily handled, transported, and stored using existing infrastructure. The principle behind LO-HCs' hydrogen storage lies in the reversible hydrogenation and dehydrogenation of carbon double bonds, as depicted in Figure 2.2.
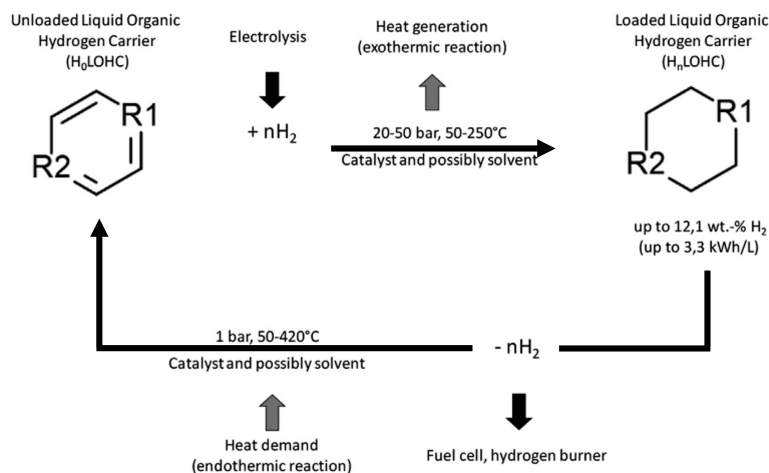
Figure 2.2: Concept of LOHC storage [110].

Initially, the dehydrogenated LOHC undergoes hydrogenation at temperatures in the range of 50-250°C and pressures of 10-50 bar in the presence of typically Ru, Pt, or Ni based catalysts. The hydrogenation reaction breaks the carbon double bonds in the LOHC, saturating them with hydrogen atoms and releasing excess heat which may be recovered for other processes. The loaded LOHC can then be stored at ambient conditions until needed, at which point hydrogen can be released again through a catalytic dehydrogenation reaction. In this case, the reaction occurs in the presence of Pt or Pd based catalysts, at low pressures and elevated temperatures in the range of 50 to 420°C [110]. The optimal combination of catalyst, temperature, and pressure depends on the specific LOHC in use.

Numerous compounds have been considered for their use as LOHCs including cyclic hydrocarbons, benzyl and dibenzyl-toluene, heterocyclic compounds, as well as some alicyclic and nonheterocyclic nitrogen containing compounds. However, the success of an LOHC does not only depend on its hydrogen storage capacity but also on other characteristics such as availability, toxicity, hydrogenation and dehydrogenation energy demand, material handling, stability, hydrogen release speed, and technology readiness level [110]. Niermann et al. [110] evaluated different substances for their potential use as LOHCs by assessing their properties against these required characteristics. They examined some of the most promising LOHCs including N-ethylcarbazole (NEC), dibenzyltoluene (DBT), toluene (TOL) and methylcyclohexane (MCH), formic acid (FA), and methanol to find that DBT is particularly well suited for energy transport and energy storage applications and NEC for mobility applications. Two of these LOHCs have already been tested at industrial scales including TOL by Chiyoda Corporation [121] and DBT by Hydrogenious Technologies and HySA Infrastructure [1].

The LOHC developed by Voyex has advantages over other LOHCs such as being on the higher range of hydrogen storage capacity (~6.0 wt%), requiring 20-25% less energy for dehydrogenation, remaining liquid at ambient conditions (melting point of about -20°C), having a relatively low dehydrogenation temperature (~220°C), and exhibiting low toxicity. This LOHC however, has not yet been fully characterized so the current LOHC dehydrogenation reactor model will not be developed with this LOHC but will instead select another more widely studied LOHC. Voyex's LOHC is expected to have properties between those of NEC and DBT, and therefore, more details concerning the dehydrogenation reaction of these LOHCs will be provided.

2.1.1. NEC system
N-ethylcarbazole, $C_{14}H_{13}N$ (0H-NEC), is a nitrogen substituted heterocycle that was first considered as an LOHC in the mid-2000s after discovering that by introducing nitrogen atoms into aromatic compounds, the hydrogenation/dehydrogenation thermodynamics and kinetics can be improved [110]. The hydrogenated form of 0H-NEC is called perhydro-N-ethylcarbazole, $C_{14}H_{25}N$ (12H-NEC), and a favor-

able point of 12H-NEC is that it has a relatively low energy demand for its dehydrogenation (50 kJ/mol). The hydrogen storage capacity of 12H-NEC is relatively high at 5.8 wt% and an energy density of 2.5 kWh/l. A drawback of the system, however, is that 0H-NEC is solid at room temperature with a melting point of 68°C. To assure the compound remains liquid at room temperature, the degree of hydrogenation can be kept above 10% thus decreasing the overall storage capacity of the system to 5.2 wt% or an energy density of 2.25 kWh/l [110]. The dehydrogenation reaction can occur in temperature ranges between 140°C and 270°C, with 270°C being an upper limit as above this temperature the compound is propense to dealkylation which results in creation of byproducts and LOHC degradation [98]. Otherwise, high purity (99.99%) hydrogen can be produced.

Several studies have been conducted on the different possible catalysts for 12H-NEC dehydrogenation. Pt was a common catalyst thanks to its good dehydrogenation efficiency, but its elevated price makes it difficult to apply in practical production [147]. Instead, recent years have focused on using Pd catalyst because of its high dehydrogenation activity and low price relative to Pt. At present, the dehydrogenation of 12H-NEC is most commonly performed with Pd catalysts sometimes in combination with a second component [147]. For example, studies using 4 wt% Pd/SiO$_2$ catalyst have achieved full dehydrogenation of 12H-NEC at 170°C at atmospheric pressure in only 1.6 hours [126]. Similarly, Wang et al. [139], propose a reduced graphene oxide (rGO) supported Pd catalyst (Pd/rGO) with excellent catalytic performance. The Pd/rGO catalyst shows an enhanced specific activity and uses half the amount of noble metals compared to commercial alumina supported Pd/Al$_2$O$_3$ catalysts.

The dehydrogenation of 12H-NEC is a stepwise reaction involving three steps as shown in Figure 2.3 in which two intermediates are formed: octahydro-N-ethylcarbazole, C$_{14}$H$_{21}$N (8H-NEC), and tetrahydro-N-ethylcarbazole, C$_{14}$H$_{17}$N (4H-NEC). Two H$_2$ molecules are released in each step, and from experimental observations, it noted that 12H-NEC and 8H-NEC are both rapidly consumed at the initial stage of the reaction, with then 4H-NEC taking the longest to dehydrogenate [139].

| | | | |
| 12H-NEC | 8H-NEC | 4H-NEC | 0H-NEC |
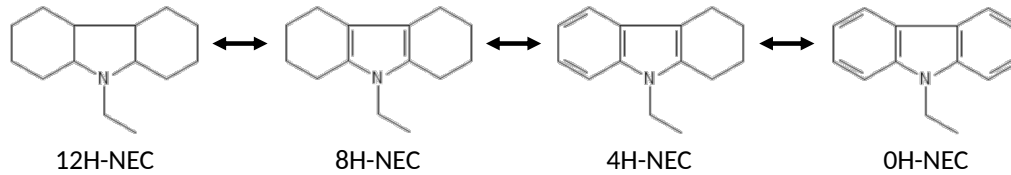
Figure 2.3: The dehydrogenation process of 12H-NEC.

Dehydrogenation of 12H-NEC is a heterogeneous catalytic process which involves molecular diffusion from the liquid phase LOHC to the surface of the catalyst, adsorption of the reactant and intermediates, surface reactions, and finally, product desorption from the catalyst surface [32]. Assuming that molecular diffusion in the liquid phase and surface adsorption are fast processes, surface reactions then dictate the overall reaction rates. Therefore, the kinetic model may be simplified as the following three consecutive elementary reactions:

$$12H-NEC \xrightarrow{k_1} 8H-NEC + 2\,H_2 \tag{2.1a}$$

$$8H-NEC \xrightarrow{k_2} 4H-NEC + 2\,H_2 \tag{2.1b}$$

$$4H-NEC \xrightarrow{k_3} 0H-NEC + 2\,H_2 \tag{2.1c}$$

Where k_1, k_2, and k_3 represent the reaction rate constants for each elementary reaction. The three stages of the process shown in Figure 2.3 are found to follow first-order kinetics. As an example, the local reaction rate equation applicable within a CFD cell for the first reaction can be expressed in terms of the concentration of 12H-NEC as:

$$r = -\frac{dC_{12H-NEC}}{dt} = k_1 C_{12H-NEC} \tag{2.2}$$

where:

r = Reaction rate [mol/(m^{3}s)]
k_1 = Reaction rate constant 1 [s^{-1}]
$C_{12H-NEC}$ = Concentration of 12H-NEC [mol/m^3]

The values for k_1, k_2, and k_3 will depend on the catalyst being used and the temperature at which the reactions occur. As an example, Dong et al. [32] conducted a kinetic study of 12H-NEC dehydrogenation over 5 wt% Pd/Al$_2$O$_3$ catalyst with Brunauer, Emmett and Teller (BET) surface area of 68.35 m^2/g and pore size of 11.89 nm. They experimentally derived values for k_1, k_2, and k_3 at temperatures between 140-170°C and at ambient pressure and noted that full dehydrogenation occurs in the order of 1.5-3 hours depending on reaction temperature [32].

Likewise, Wang et al. [139] conducted a kinetic study for 12H-NEC dehydrogenation but using a high efficiency 2.5 wt% Pd supported on reduced graphene oxide (Pd/rGO) catalyst. From the reaction rate constants provided by Dong et al. [32] and Wang et al. [139] at different temperatures, the reaction rate constants may be formulated in an Arrhenius approach as a function of temperature as:

$$k = Ae^{\frac{-E_a}{RT}} \tag{2.3}$$

where:

A　= Arrhenius pre-exponential factor [s^{-1}]
E_a = Activation energy [J/mol]
R　= 8.314 J/(K·mol), Universal gas constant
T　= Absolute temperature [K]

For reference, the thermophysical and thermochemical properties as a function of temperature of the four NEC species are provided by Stark et al. [128].

2.1.2. DBT system

Dibenzyltoluene, $C_{21}H_{20}$ (0H-DBT), is a heat transfer oil that has been produced commercially on a multi-thousand ton scale since the late 1960s [98]. The hydrogenated form of 0H-DBT is called perhydro-dibenzyltoluene, $C_{21}H_{38}$ (18H-DBT), and this system has several favorable properties including non-toxicity, non-flammability, and a high hydrogen storage capacity (6.2 wt% and energy density of 1.9 kWh/l). 0H-DBT has a low melting point (-39°C), high boiling point (390°C), high flash point (200°C), and similar viscosity to fuel oil, which makes it an intrinsically safe compound with easy handling. Another advantage is that from an economical viewpoint, 0H-DBT has a relatively low price (4 €/kg of DBT vs 40 €/kg of NEC) owing to its large-scale production. The 18H-DBT molecule, however, may undergo thermal cracking above temperatures of 290°C which results in byproduct formation that block catalyst active sites and degrade the DBT molecule [98].

The hydrogenation reaction of 0H-DBT may take place at temperatures between 80-180°C, pressures of 20-50 bar and is normally catalyzed by Pt and Ru catalysts [110]. The dehydrogenation reaction of 18H-DBT has been studied in temperature ranges between 250-320°C, pressures between 1-5 bar and Pt and Ru catalysts. Although higher temperatures imply faster dehydrogenation rates, it is recommended to maintain the temperature below 290°C to avoid DBT degradation [112]. A notable trait of 0H-DBT is its ability to undergo hydrogenation not only with pure hydrogen but also with hydrogen-containing gas mixtures. This may be economically attractive for industries generating such gas mixtures as byproducts from processes like reforming, gasification, or cracking reactions [98].

Studies have been conducted to screen possible catalysts for 18H-DBT dehydrogenation and Pt based catalysts have been found to be most suitable with catalyst support preference in the order C>Al$_2$O$_3$>SiO$_2$ [98]. Furthermore, Fikrt et al. [37] used a fixed-bed reactor loaded with 0.5 wt% Pt/Al$_2$O$_3$ to evaluate 18H-DBT dehydrogenation for dynamic power supply. They found that the fastest way of regulating the hydrogen production from the reactor was by changing the pressure level of the reactor as changes in temperature and flow rate result in long response times. Following Le Chatelier's principle, by adjusting the pressure of the system, the authors were able to shift the equilibrium of the reaction to control hydrogen production. For example, an increase in power of 16% in their 2.32 kW experimental setup was observed by reducing the pressure from 1.5 to 1.1 bar.

Similar to 12H-NEC dehydrogenation, 18H-DBT dehydrogenation is also a stepwise reaction involving two stable intermediates: 12H-DBT and 6H-DBT. Various authors have experimentally studied the reaction kinetics of 18H-DBT dehydrogenation and have all found that the multistep reaction may be simplified by an approximately second-order single-step reaction from 18H-DBT to 0H-DBT as represented by Figure 2.4 [114]. These authors have proposed kinetic models describing the reaction rate constants following the Arrhenius approach given by Equation 2.3, with the overall reaction rate given by:

$$r = -\frac{dC_{18H-DBT}}{dt} = kC_{18H-DBT}^n \qquad (2.4)$$

where:

n = Overall reaction order [-]

Peters et al. [114] proposed a kinetic model for 18H-DBT dehydrogenation at temperatures between 260-310°C, pressure of 1-5 bar and 0.5 wt% Pt/Al$_2$O$_3$ catalyst. Likewise, Park et al. [112] proposed a kinetic model valid for temperatures from 250-320°C with a 5 wt% Pt/Al$_2$O$_3$ catalyst. For reference, Müller et al. [105] and Aslam et al. [5] have characterized the thermophysical and thermochemical properties of both 0H-DBT and 18H-DBT as a function of temperature.
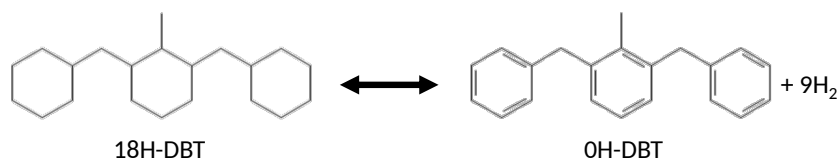
Figure 2.4: Simplified dehydrogenation process of 18H-DBT.

Selected LOHC for present model
The LOHC developed by Voyex is expected to have a reaction mechanism similar to that of NEC with consecutive elementary reactions involving a few intermediate species between the fully hydrogenated and dehydrogenated molecule. Thus, the present CFD model will focus on the NEC system including its four species (12H-NEC, 8H-NEC, 4H-NEC, 0H-NEC) along with the released H$_2$ gas.

2.2. Reactor design
2.2.1. Design strategies
Designing a chemical reactor from scratch can seem like a daunting task due to numerous design choices available. Initially, the question is what is the "ideal" reactor configuration that best meets a set of process requirements. To answer this question, it is important to first have a deep understanding of what the process requirements are, and then take a structured approach for proposing a reactor design. Ultimately, it is subjective to affirm that one reactor design is best, but rather different designs will each have their strengths and weaknesses and it will be up to the stakeholders to agree on a design.

There are various reactor types such as packed-bed, fluidized-bed, membrane reactors, or batch reactors, each with numerous variations. The selection process for reactor types can be aided by Krishna and Sie's three-level approach [64]. This approach entails formulating process requirements for catalyst design, injection and dispersion strategies, and flow regime choices to brainstorm ideas to meet each level's requirements. Combining decisions from these levels will help yield the most suitable reactor configuration.

Having selected a reactor configuration, the subsequent task involves sizing the reactor and selecting adequate operating conditions to achieve the desired output. This is a broad task that may involve experimental and numerical work on different scales to work towards a combination of design and operating parameters that optimize reactor performance.

Among the studied LOHC dehydrogenation reactor configurations are fixed-bed reactors, membrane reactors, and reactors with monolithic catalyst structures [87][98]. Among these, the fixed-bed reactor is the most studied and has past examples of use for LOHC dehydrogenation [121]. It is a relatively inexpensive reactor and as previously explained, Voyex has an experimental setup with a small-scale fixed-bed reactor on which experimental validation of the CFD model can be carried out. Thus, this work focuses on modeling the fixed-bed reactor type, while acknowledging the significance of other reactor configurations within the LOHC dehydrogenation field.

Considering a fixed-bed reactor design, various design and operating parameters still need study to complete the three steps of Krishna and Sie's approach [64] for LOHC dehydrogenation. From the first level regarding catalyst selection, the catalyst size and geometry are not yet defined. From the second level, decisions regarding product removal and heat input strategies should be made. Finally,

from the third level, the hydrodynamics and flow regime will need to be studied to understand the effect of parameters such as reactor dimensions or input LOHC mass flow rate on reactor performance.

2.2.2. Dehydrogenation reactors

The dehydrogenation reaction of LOHCs is complex as it is endothermic and creates large volumes of gaseous product. For example, complete dehydrogenation of 1 ml of 12H-NEC can produce 619 ml of hydrogen gas at standard temperature and pressure. The high volume of hydrogen can displace the LOHC causing a lower contact between the LOHC and the catalyst resulting in poor heat and mass transfer within the reactor. Modisha et al. [98] and Makaryan and Sedov [87] discuss the type of reactors that can be used for this reaction and, as they discuss, there is not one optimum reactor type or design but rather each reactor design will have its own set of advantages and drawbacks. Three of the most promising reactor types for the reaction under study are fixed-bed reactors, membrane reactors, and reactors with monolithic catalysts. There are other reactor types such as horizontal tube, suspended-catalyst, spray-pulsed, or radial flow reactors which may also have applications in LOHC dehydrogenation but are out of the scope of this project [98][34].

Fixed-bed reactor

Fixed-bed reactors (also known as packed-bed reactors) are the most studied for LOHC dehydrogenation. These reactors are vessels with randomly packed catalyst particles in which the particles are stagnant during operation. The particles may have varied sizes and shapes including spheres, cylinders, trilobes, rings or other more complex shapes. In these reactors a gas, liquid, or a combination of both, flows through the interstitial space between particles and react upon contact with the catalyst particles. These are amongst the simplest and least expensive reactor types and are well studied robust designs used for many chemical applications. However, there are drawbacks to this design such as high fluid pressure drops across the packed bed, moderate mass and heat transfer, partial catalyst wetting, and the need for service time to replace eroded or deactivated catalyst.

LOHC dehydrogenation reaction is a multiphase reaction as a liquid reactant reacts in the presence of a solid catalyst to produce both gaseous and liquid products. Multiphase fixed-bed reactors processing both gas and liquids can operate in three configurations according to the direction in which each of the fluid phases flow. They can operate in cocurrent downward flow, countercurrent flow, and in cocurrent upward flow as represented by Figure 2.5. Cocurrent downward and countercurrent flow fixed-bed reactors are both known as trickle-bed reactors (TBRs) while cocurrent upward flow fixed-bed reactors are known as flooded-bed reactors (FBRs). Each of these configurations will have distinct hydrodynamic behaviors and may each be better suited for different chemical reactions.

An important thing to note, however, is that unlike Figure 2.5 where both a gas and liquid phase are input, in an LOHC dehydrogenation reactor only a liquid LOHC stream is input and as the reaction progresses gas is produced. The input stream is hence only liquid, and the output streams are both gaseous and liquid.

a) Trickle bed   b) Trickle bed   c) Flooded bed
Cocurrent downflow   Countercurrent flow   Cocurrent upflow
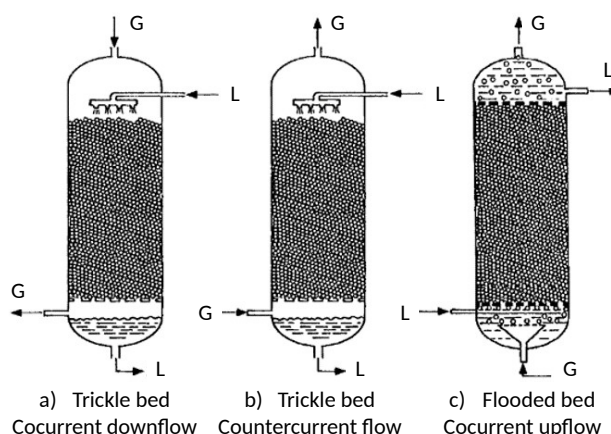
Figure 2.5: Packed-bed reactors for gas – liquid– solid catalyzed systems [34]. (a) Trickle-bed with cocurrent downflow; (b) trickle-bed with countercurrent flow; (c) flooded bed reactor with cocurrent upflow.

Fixed-bed reactors have been used in existing pilot installations for LOHC dehydrogenation such as the "SPERA Hydrogen" process developed by Chiyoda Corporation [121]. They have developed a demonstration plant with a capacity of 50 Nm^3 H$_2$/h for toluene hydrogenation and MCH dehydrogenation, with the MCH dehydrogenation reaction occurring in a fixed-bed of partially sulfidized Pt/Al$_2$O$_3$ catalyst at 350-400°C and a pressure of <10 MPa [87].

Membrane reactor

Membrane catalytic reaction systems employing hydrogen-selective membranes can be used to produce high-purity hydrogen, eliminating additional purification steps in the process [87]. Chen et al. [27] studied MCH dehydrogenation in membrane catalytic reactors through simulations validated with experiments to understand the velocity, temperature, and concentration profiles within the reactor. They studied design parameters including feed flow rate, mass of catalyst, and pressure to optimize the performance of the reactor for hydrogen production.

Studies have been conducted on the possible hydrogen selective membranes that could be attractive options for hydrogen separation technologies. These include polymer membranes and their composites, hybrid membranes (silicon-based membranes, metal organic frameworks), and metal alloy membranes [141]. In the area of metal alloy membranes, dense Pd-based membranes have been proposed for hydrogen purification due to the very high hydrogen selectivity, high thermal stability, and mechanical resistance [2]. Alique et al. [2] present a review of relevant advances in Pd-based membranes for hydrogen production.

Overall, membrane reactors combine the chemical reaction for hydrogen production and the purification step in a single device as a process intensification strategy. They offer a high yield of high purity hydrogen and a compact system design [87]. Byun et al. [22] developed a techno-economic and carbon footprint analysis of MCH dehydrogenation in a membrane reactor by simulating the process using Aspen Plus process simulation software. They developed the study for both a fixed-bed reactor and membrane reactor to compare both technologies at different production capacities. Overall, they found that the economic efficiency of the membrane reactor was higher, and the CO$_2$ emissions were lower as a result of the lower resource and power consumption required by the membrane reactor process.

Reactors with monolithic catalysts

A final reactor type of interest are reactors with structured catalysts. Catalyst particles in a monolithic block volume can be distributed in a structured way such as foams, fibers, or honeycomb structure. Monolithic catalysts are often used in applications in which large volumetric flows must be handled as monoliths offer the advantage of a low pressure drop and high mechanical strength.

In conventional fixed-bed reactor packings, there is a coupling between catalyst particle size and hydrodynamic diameter. Smaller particles are preferred for increased catalyst surface area and activity. However, smaller particle sizes lead to higher pressure drops across the packed bed. This conflict can be mitigated through the use of structured monolithic packings. Monolithic structures enable the separation of catalyst particle size (determined by channel wall thickness) and hydrodynamic diameter (controlled by channel width). These two dimensions can be individually optimized providing an additional degree of freedom for design to achieve low pressure drops without compromising catalyst activity. Monolith channels can take various geometries, such as square, hexagonal, triangular, or finned square, influencing flow patterns and reactor performance.

The main advantages of using monolithic reactors for multiphase reactions such as LOHC dehydrogenation include a very low pressure drop, excellent mass transfer properties, low axial dispersion, good contact area between phases, ease of reactor scale-up, and ease of catalyst handling [28]. Cybulski et al. [28] identify that the pressure drop in monolithic reactors can be up to two orders of magnitude lower than that in packed-bed reactors. However, they also identify high catalyst manufacturing costs, short residence time, poor heat transfer and difficulty of assuring fluid uniformity over reactor cross section as the main drawbacks of monolith reactors.

As an example, Peters et al. [115] studied the dehydrogenation reaction of 12H-NEC in a 25 ml tubular reactor with a titanium alloy monolithic structure coated with 5 wt% Pt/Al$_2$O$_3$ catalyst. The monolithic structure was optimized for optimal heat conductivity and efficient hydrogen gas removal through a diamond structure. They tested the dehydrogenation reaction in a single tubular reactor and then created a parallel ten tubular reactor system to provide a total reactor volume of 250 ml. The

authors were able to demonstrate a hydrogen generation of 9.8 normal liters per minute (NLPM) which corresponds to a thermal capacity of 1.75 kW.

2.3. Multiphase fixed-bed reactors

Having identified various reactor types suitable for LOHC dehydrogenation, this project will now narrow its focus to the study and simulation of fixed-bed reactors. As previously shown, packed-bed reactors can operate in cocurrent downflow, countercurrent flow and cocurrent upflow. Among these, cocurrent downflow, or trickle-bed reactors (TBR), are widely used in the chemical industry due to their capability to accommodate various flow regimes and adapt to various throughput requirements. Countercurrent flow is often used for catalytic distillation or enhancing gas-liquid mass transfer in absorbers. Cocurrent upflow reactors are primarily used to ensure complete external wetting of the catalyst and have increased liquid holdup compared to the other configurations [34].

For LOHC dehydrogenation, the cocurrent upflow configuration has particular advantages. As a high volume of gas is expected to be produced, which may displace the LOHC and reduce catalyst wetting, a cocurrent upflow configuration may be beneficial as this configuration can help improve external wetting of the catalyst particles [34]. For liquid-limited reactions such as LOHC dehydrogenation, an upflow reactor should be preferred as it provides high catalyst wetting allowing for faster transport of the liquid reactant to the catalyst. Cocurrent upflow reactors typically exhibit higher liquid holdup than the other configurations, offering benefits for conversion, selectivity, and interfacial mass transfer [17].

2.3.1. Hydrodynamics

When studying the hydrodynamic characteristics of multiphase flow systems in packed beds, several aspects should be considered. The following subsections introduce the main parameters related to the hydrodynamics within fixed-bed reactors.

Flow regimes

Different flow regimes or flow patterns can occur as gas and liquid flow through a packed bed. The type of flow regime depends on the flow direction of each phase, flow rates, physical properties of each phase and geometric properties of the packing [118]. Each flow regime has specific hydrodynamic properties which can benefit a particular application. Therefore, the identification of the flow regime within a reactor is important to determine for better design and control the reactor.

For two-phase downflow in TBRs the flow regimes can be categorized as low and high interaction regimes. The low interaction regime, also known as trickle flow, occurs at low gas and liquid velocities and is known as a low interaction regime because of the weak gas-liquid interfacial forces that occur [53]. In the trickle flow there are low shearing forces between the gas and liquid, and the flow is mainly gravity driven. This results in a continuous gas phase with liquid rivulets flowing downward along the particles [34]. The gas-liquid interfacial forces increase as the flow rates increase and this leads to the high interaction flow regimes. Low gas flow rates and high liquid flow rates leads to the bubble flow regime which consists of a continuous liquid phase with small bubbles within. As the gas flow increases, the bubbles coalesce and gas flows in the form of elongated bubbles (dispersed bubble flow regime). At even higher gas flow rates, the pulse flow regime is observed in which gas-rich and liquid-rich zones accumulate in horizontal regions in the bed and travels through the medium in the form of pulses or slugs. Finally, high gas flow rates but low liquid flow rates results in a spray flow in which the gas is the continuous phase and liquid droplets travel through it. These TBR flow regimes are represented by the schematic in Figure 2.6. These flow regimes are typical for TBR with coalescing liquids; non-coalescing liquids can develop two additional high interaction flow regimes: foaming flow and foaming-pulsing flow regimes [53].

Studies have been conducted to help identify the transition between the flow regimes. Flow maps have been developed to help predict flow regimes, but these tend to oversimplify the problem as it has been found that the flow regime depends on several factors including particle size, bed porosity, flow rates, liquid density, liquid viscosity, liquid surface tension, gas density, gas surface tension and operating pressure [53]. Since numerous variables affect the flow regime transition, many of the existing correlations are based on empirical and phenomenological approaches and can each only be interpolated for conditions falling within those used to develop them. As such, there is no one universal flow chart or correlation to predict the flow regime in a TBR. One of the most flexible approaches,

however, is an artificial neural network (ANN) correlation by Iliuta et al. [56] developed to determine the trickle-to-pulse flow transition.
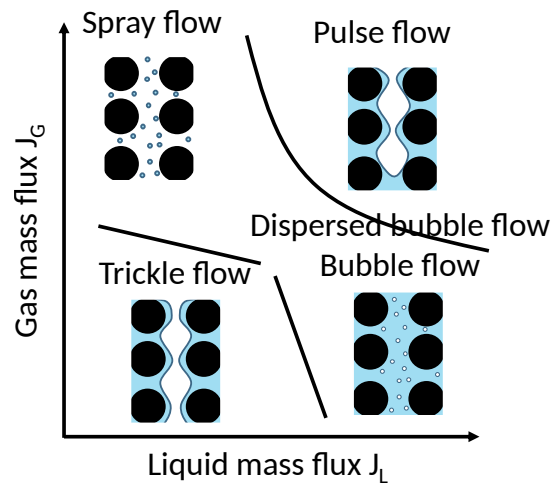
Figure 2.6: Schematic representation of flow regimes in a TBR with respect to gas and liquid phase mass fluxes for non-foaming liquids [108].

For two-phase cocurrent upflow in FBRs, three main hydrodynamic flow regimes have been identified: bubble flow, pulse flow, and spray flow, each manifesting with increasing gas flow rates. The transition depends on the flow rates, fluid properties, and the characteristics of the packing. As for TBRs, no generalized quantitative criteria for identifying flow regimes in FBRs is available. One of the more recent studies on flow regimes in FBRs, however, is that of Raghavendra Rao et al. [118] where an overview of existing correlations for flow regime transitions is presented and their own correlation is developed. Their correlations are based on experimentation of three different gas-liquid systems through packed beds of four packing types with liquid and gas mass fluxes, L and G, of 3.536$\leq L \leq$ 36.567 kg/m^{2}s and 0.176$\leq G \leq$ 1.768 kg/m^{2}s. As an example, Figure 2.7a graphs the equation developed by Raghavendra Rao et al. [118] to predict the transition from bubble flow to pulse flow in FBRs. A previous study of flow regimes through multiphase upflow through packed bed is that of Murugesan and Sivakumar [106]. Figure 2.7b shows the flow map they developed based on experimental results with a lower gas mass flux range of 0.0065$\leq G \leq$ 0.391 kg/m^{2}s and 4.5$\leq L \leq$ 135.4 kg/m^{2}s with the x and y axis corresponding to Equations 2.5a and 2.5b.
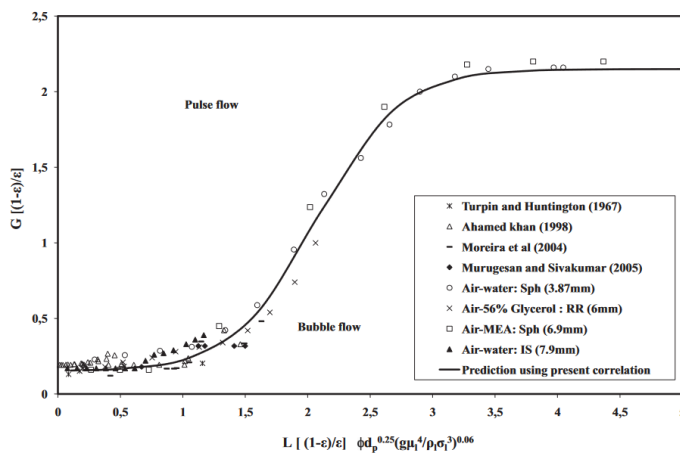
(a) Bubble to pulse flow regime transition by Raghavendra Rao et al. [118].
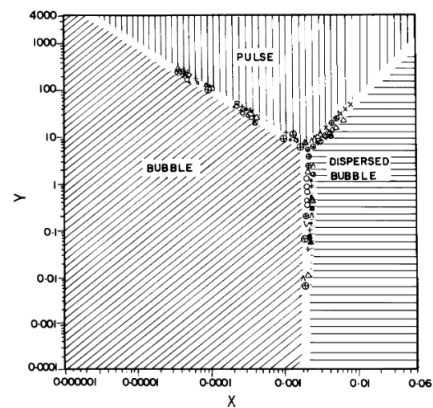
(b) Flow regime map by Murugesan and Sivakumar [106]. X and Y coordinate given by Equation 2.5a and Equation 2.5b.

Figure 2.7: Two-phase cocurrent upflow flow regime maps.

$$X = \frac{Fr_{\mathsf{L}}(d_{\mathsf{p}}/D)\psi}{\epsilon_{\mathbf{B}}} \tag{2.5a}$$

$$Y = \frac{(Fr_{\mathsf{G}}/Fr_{\mathsf{L}})(\varphi d_{\mathsf{p}}/D)^{0.75}}{\epsilon_{\mathbf{B}}\psi} \tag{2.5b}$$

$$Fr_q = \frac{|\boldsymbol{U}_q|^2}{d_{\mathsf{p}}g} \tag{2.5c}$$

$$\psi = \left(\frac{\sigma_{\mathsf{H_2O}}}{\sigma_{\mathsf{L}}}\right)\left[\left(\frac{\mu_{\mathsf{L}}}{\mu_{\mathsf{H_2O}}}\right)\left(\frac{\rho_{\mathsf{H_2O}}}{\rho_{\mathsf{L}}}\right)^2\right]^{0.33} \tag{2.5d}$$

where:

X $= X$ coordinate of Figure 2.7b [-]
Y $= Y$ coordinate of Figure 2.7b [-]
$Fr_q =$ Froude number of the qth phase [-]
d_{p} $=$ Particle diameter [m]
D $=$ Reactor diameter [m]
ϵ_{B} $=$ Mean bed porosity [-]
$\boldsymbol{U}_q$ $=$ Interstitial (local velocity) of the qth phase [m/s]
σ $=$ Surface tension [N/m]
μ $=$ Dynamic viscosity [Pa·s]
ρ $=$ Density [kg/m^3]

Heublein et al. [48] performed a series of experimental tests to compare the hydrogen yield of 12H-NEC dehydrogenation and heat requirements in different packed-bed reactor configurations. These included vertical cocurrent upwards reactor, vertical countercurrent reactor with and without intermediate gas separation, and horizontal cocurrent reactor. They found that a similar hydrogen yield can be reached in both horizontal and vertically orientated reactors. However, the vertical design was superior for heat integration as an easier heat transfer to the bed was found. In addition, between the vertical cocurrent and countercurrent configuration, the countercurrent configuration had greater limitations due to catalyst dewetting. From these observations and the discussion presented above, this project will focus on a vertical cocurrent upwards flow reactor. Heublein et al.'s [48] study employed an inlet liquid mass flux of 0.6 kg/m^{2}s, and using the dimensions of their reactor, their hydrogen yield corresponds to a hydrogen mass flux of 0.03 kg/m^{2}s. In relation to the flow regime, these mass fluxes are out of range of both Raghavendra Rao et al. [118] and Murugesan and Sivakumar [106] studies. No study was found in literature looking into the flow regimes at such low mass fluxes dealt with in this application. However, both of the above mentioned flow maps would predict a bubble flow for this reactor.

Pressure drop

Pressure drop is one of the main hydrodynamic characteristics in packed-bed reactors as is used to determine energy losses, sizing of compression and pumping devices, and to assess other parameters such as liquid holdup, catalyst wetting efficiency and mass transfer coefficients [53]. The total pressure drop consists of three components: friction due to the interaction between phases, acceleration as a result of uneven longitudinal distribution of fluid velocities, and the hydrostatic head related to the weight of the fluid in the reactor. Pressure drop across a packed bed depends factors such as fluid velocities, fluid properties and bed characteristics. Much work has been conducted to study pressure drop across packed beds and several general observations are obtained. For example, pressure drop tends to increase with increasing fluid velocity, viscosity, density, pressure, molecular weight, and with decreasing particle size and bed porosity. It is also affected by particle shape and liquid surface tension, but no clear trend can be drawn for these parameters [73].

The approach many authors have followed to predict hydrodynamic characteristics such as pressure drop and liquid holdup in different flow regimes for packed-bed reactors relies on empirical correlations and phenomenological observations based on dimensional analysis. As a result, most of the correlations developed are restricted for use in the narrow ranges of process conditions, fluid properties, and packing geometries considered by each researcher. Duduković et al. [34] present a comprehensive list of correlations and models developed for prediction of two-phase pressure drop in TBRs and FBRs.

Among the broadest correlations to predict pressure drop in TBRs is the ANN correlation developed by Iliuta et al. [54] generated from an extensive database encompassing wide range of fluid properties, operating conditions, and packing characteristics. Similarly, Larachi et al. [73] provide an ANN correlation for FBRs. Other simpler correlations, still with a relatively wide range of applicability, for pressure drop across FBRs are those proposed by Larachi et al. [75] and by Molga and Westerter [103].

Liquid holdup

Liquid holdup is another fundamental hydrodynamic parameter in packed-bed reactors, representing the liquid phase volume fraction within the bed. Its significance lies in its relation to other parameters such as pressure drop, interfacial mass transfer parameters, catalyst wetting, liquid residence time, liquid axial dispersion, radial thermal conductivity, and heat transfer coefficients [53]. As with for pressure drop, a series of empirical and phenomenological correlations have been proposed for both TBRs and FBRs many of which are summarized by Duduković et al. [34].

The ANN correlation by Iliuta et al. [54] is a recent and flexible correlation for estimating pressure loss and liquid holdup in TBRs. A comparable ANN correlation was developed from a database of 2600 experiments using six dimensionless groups to predict the liquid holdup [17]. A simpler empirical correlation for liquid holdup in FBRs is proposed by Lara Márquez et al. [68] using the liquid Weber number, We_L, liquid Reynolds number, Re_L, and the modified Lockart-Martinelli parameter, X_G, to estimate the liquid holdup.

It is important to note that the previously presented correlations are based on packed-bed reactors with both a gas and liquid inlet. In LOHC dehydrogenation, only liquid is introduced, and the gas will be produced within the reactor. Consequently, these correlations might not exactly apply to LOHC dehydrogenation but may serve as a guide or apply to local sections with similar behavior to reactors with both liquid and gas feeds.

Catalyst wetting

Catalyst wetting is an important parameter in fixed-bed reactors, particularly for those like LOHC dehydrogenation where the reaction relies on liquid-catalyst interaction. Catalyst wetting encompasses both external and internal wetting, where external wetting pertains to the outer surface and internal wetting involves the pores within porous particles. In steady-state operation, the internal liquid-catalyst contacting efficiency (fraction of pore volume filled with liquid) is generally unity due to capillary effects. However, incomplete external wetting may occur at low liquid flow rates when the available liquid is insufficient to cover all catalyst particles with a continuous liquid film [34]. The reaction rate over an incomplete external wetted packing can be different than that observed over completely wetted packing and it is therefore important to predict when partially externally wetted particles may exist.

External catalyst wetting can be measured by the external liquid-solid contacting efficiency (or external wetting efficiency), η_{WE}, which is defined as the fraction of the external catalyst surface area covered by the flowing liquid film. For TBRs, partially externally wetted particles ($\eta_{WE} < 1$) may especially occur in the trickle flow regime when low liquid flow rates exist as is represented by Figure 2.8. In FBRs however, the contacting efficiency is expected to be high as the liquid floods the bed. Correlations to predict liquid-solid contacting efficiency have been summarized by Duduković et al. [34] where one of the most recent and widely used is that of Al-Dahhan and Duduković [30] as it is applicable for both low and high-pressure trickle-bed reactor operation. This correlation is for use in the trickle flow regime where partial wetting can be of most concern.
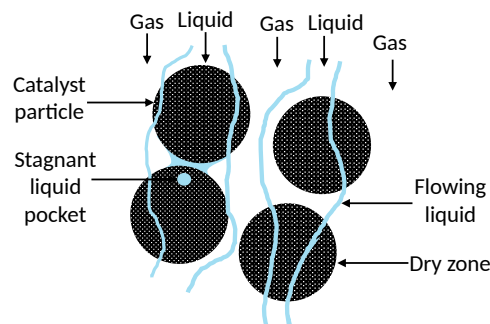
Figure 2.8: Partially externally wetted particles.

Capillary pressure

Capillary pressure effects are an important phenomenon to consider when modeling multiphase packed-bed reactors. The capillary pressure is defined as the volume average pressure difference between the gas and liquid phase and may be written as:

$$P_c = P_G - P_L = \sigma \left(\frac{1}{R_1} - \frac{1}{R_2} \right) \tag{2.6}$$

where:

P_c = Capillary pressure [Pa]
P_G = Gas pressure [Pa]
P_L = Liquid pressure [Pa]
σ = Surface tension [N/m]
R_1 = Principal radii of interface curvature 1 [m]
R_2 = Principal radii of interface curvature 2 [m]

Capillary pressure is then a result of surface tension forces that depend on the average curvature of the gas-liquid interfaces as described by R_1 and R_2 in Equation 2.6. In a porous media such as a packed bed, the interface curvature depends on the contact angle at the gas-liquid-solid contact lines, the bed porosity, and the liquid saturation [25]. In packed beds, capillary pressure along with packing wettability can be responsible for liquid flow maldistribution as well as for hysteresis effects when loading and unloading a bed with liquid [61].

The significance of capillary pressure effects in a packed-bed reactor depends on characteristics such as particle size and flow regime. For example, as catalyst particle diameter increases, the dimension of the interstitial space also increases, and capillary pressure effects become less dominant. Similarly, in low interaction flow regimes (trickle flow), the interaction between gas and liquid phases is so low that capillary pressure may be neglected [8]. When capillary pressure force is neglected, the pressure for both gas and liquid phases is assumed to be equal at any point in time and space. Furthermore, prewetted beds have demonstrated uniform liquid distributions with minimal gradients of liquid holdup, suggesting that the macroscale capillary pressure effect is also negligible when the particles are fully externally wetted [61]. As a result, several packed bed models in literature neglect capillary pressure effects for steady-state operation when a prewetted or completely externally wetted bed is assumed [13][43][42][61].

A few correlations have been developed to quantify the capillary pressure in packed beds for cases when capillary pressure effects should be considered such as in partially wetted beds or when studying liquid maldistribution in a reactor. One correlation is derived from a momentum balance analysis to estimate the characteristic gas-liquid interface curvature dimensions along with a correction factor determined from experimental observations for high-pressure operation [12]. This correlation proposed by Attou and Ferschneider shown in Equation 2.7 [12] is valid for both atmospheric and high-pressure operation.

$$P_c = 2\sigma \left(\frac{1 - \epsilon_B}{1 - \varepsilon_L} \right)^{1/3} \left(\frac{5.416}{d_p} \right) F \left(\frac{\rho_G}{\rho_L} \right) \tag{2.7a}$$

$$F \left(\frac{\rho_G}{\rho_L} \right) = 1 + 88.1 \frac{\rho_G}{\rho_L} \quad \text{for } \frac{\rho_G}{\rho_L} < 0.025 \tag{2.7b}$$

where:

ϵ_B = $1 - \varepsilon_S$ Mean bed porosity [-]
ε_L = Liquid volume fraction [-]
d_p = Particle diameter [m]
ρ = Density [kg/m^3]

Another way to express capillary pressure is through the permeability concept and Leverett's J function [79] which have been extensively used to analyze capillary pressure of multiphase flow through porous media. These concepts were further developed by Grosser et al. [40] for flow through packed beds in the trickle flow regime and proposed the following empirical correlation:

$$P_c = \sigma \frac{\varepsilon_S E_1^{0.5}}{(1 - \varepsilon_S) d_p} \left(0.48 + \frac{0.036 \ln(1 - \beta_L)}{\beta_L} \right) \tag{2.8}$$

where:

ε_{S} = Solid volume fraction [-]
E_1 = Ergun constant [-]
$\beta_{\mathsf{L}} = \frac{\varepsilon_{\mathsf{L}}}{1-\varepsilon_{\mathsf{S}}}$ = Liquid saturation [-]

As Jiang et al. [61] note, the capillary pressure effect on liquid distribution is related to the degree of particle wetting. For the modeling of macroscale flow they propose incorporating the external particle wetting efficiency, η_{WE}, into the capillary pressure formulation in Equation 2.6 as:

$$P_{\mathsf{G}} - P_{\mathsf{L}} = (1 - \eta_{\mathsf{WE}})P_{\mathsf{c}} \tag{2.9}$$

In CFD simulations, the wetting efficiency can be calculated locally at each cell using the previously presented correlation of Al-Dahhan and Duduković [30] for trickle beds.

Turbulence

The packing structures in fixed-bed reactors have characteristics such as complex geometries and large specific areas that ensure high gas-liquid contact areas and intensify mixing. This may contribute to turbulence developing within the reactor which may be important to model. A way to classify the degree of turbulence in flow through porous media is suggested by Dybbs and Edwards [35] by means of a particle Reynolds number given by:

$$Re_{\mathsf{p}} = \frac{\rho_q \varepsilon_q |\boldsymbol{U}_q| d_{\mathsf{p}}}{\mu_q (1 - \varepsilon_q)} \tag{2.10}$$

where:

Re_{p} = Particle Reynolds number [-]
ε_q = Volume fraction of the qth phase [-]
$\boldsymbol{U}_q$ = Interstitial or local velocity of the qth phase [m/s]
μ_q = Dynamic viscosity of the qth phase [Pa·s]

Dybbs and Edwards [35] conducted a series of experiments involving single-phase flow through porous media and identified four flow regimes. The first is Darcy or creeping flow, occurring at $Re_{\mathsf{p}} < 1$, where viscous forces dominate and the flow adheres to Darcy's law. Here, the pressure drop is a linear function of the interstitial velocity. The subsequent regime is the steady laminar inertial flow for $1 < Re_{\mathsf{p}} < 150$. At these higher flow rates, energy dissipation becomes the sum of viscous and inertia drag. To correlate pressure drop with flow conditions, the well-known Ergun equation is often employed as it incorporates both viscous and inertial terms where the latter scales with the square of velocity. The next flow regime is the unsteady laminar inertial flow occurring at $150 < Re_{\mathsf{p}} < 300$. Beyond Re 150, signs of unsteady flow may be observed through the formation of laminar wakes. Vortices commence forming at Re 250, leading to the final flow regime. For $Re_{\mathsf{p}} > 300$, the flow is considered turbulent, characterized by an unsteady and chaotic flow. Although Dybbs and Edwards' [35] criteria were determined for single-phase flow, the same criteria has been used for multiphase applications [140].

Numerical investigation of turbulent flow can employ macroscopic models such as the the $k - \varepsilon$ turbulence model. This model has been used in numerous CFD simulations of multiphase flow in packed-bed reactors [81][83][130][7][82]. It describes turbulence by including the effects of transport, production, and dissipation of turbulence through an equation for turbulent kinetic energy, k, and an equation for turbulent dissipation energy rate, ε. Within the context of the $k - \varepsilon$ turbulence model, there are three variations: standard $k - \varepsilon$ (SKE), renormalization-group $k - \varepsilon$ (RNG), and realizable $k - \varepsilon$ (RKE), with the major difference between them being the calculation of turbulent viscosity and turbulent Prandtl numbers [82].

Furthermore, in multiphase flow simulations, each variation may be applied as a mixture model, dispersed model, or as a per-phase model. When applied as a mixture model, a single set of equations is used for all phases using mixture properties (ρ_{m}, μ_{m}) and mixture velocities ($\boldsymbol{U}_{\mathsf{m}}$). This may be applicable in cases when the phases have similar properties between them. Applying the turbulence model as a dispersed model may be possible when there is one clear continuous phase and the other is a dispersed secondary phase. The turbulence of the continuous phase is modeled with the two k

and ε equations, and the dispersed phase is treated with other Tchen-theory correlations [57]. Finally, in a per-phase model, a set of k and ε transport equations are defined for each phase individually. This model is the most general and computationally intensive.

In the case of LOHC dehydrogenation, the liquid and gas phases have distinct physical properties so a mixture model may not be applicable. Furthermore, since large volumes of gas are expected to be produced, it would be inaccurate to say that the liquid remains a continuous phase throughout the entire reactor. As the volume proportions of liquid and gas change significantly along the reactor, the turbulence model should be applied as a per-phase model and not a dispersed one. Lopes and Quinta-Ferreira [82] performed a study comparing the three $k - \varepsilon$ models finding that the increasing order of relative error was SKE<RNG<RKE. However, Atta et al. [7] argue that the intensive computational demands necessary for turbulent model simulations in industrial-scale TBRs might outweigh the accuracy improvement in the overall macroscale reactor model gained from including a turbulence model.

Another perspective for the macroscopic flow modeling in packed beds, is that the contribution of turbulence stress on the fluid momentum equation is not significant. This is attributed to a smoothing effect from averaging numerous random local signals within a representative elementary volume, which attenuates the microscopic turbulence generated between particles[61]. Thus, in macroscopic CFD simulations where the cell sizes are larger than microscale turbulent structures, Jiang et al. [61] argue that the turbulence stress term is not important in determining macroscale flow patterns and may be neglected in packed beds with particle size of 10^{-4} to 10^{-2} m. This rationale is also employed by Atta et al. [9] to exclude turbulence modeling from their high-pressure TBR CFD simulation.

As will be seen further on in this work, initial simulations revealed that the particle Reynolds number of both gas and liquid phases in LOHC dehydrogenation remains below 150 thanks to the low velocity at which the LOHC is enters the dehydrogenation reactor. This indicates that the flow is in the steady laminar inertial flow regime and no turbulence model will be required.

Mean bed porosity

The mean bed porosity, quantifies the interstitial space within a reactor after the solid packing has been put in place. The bed porosity depends upon geometric aspects of the particles, reactor diameter, and of the packing procedure. A comprehensive understanding of the mean bed porosity in packed beds is important as hydrodynamic properties such as pressure drop are highly influenced by it.

Except for beds of mono-sized spherical particles, the mean bed porosity in randomly packed beds can only be obtained experimentally for which correlations have been developed [18]. Benyahia and O'Neill [18] present an overview of correlations developed to predict mean bed porosity for four different particle shapes. They also propose a general correlation applicable for spherical, solid cylinders, hollow cylinders, and 4-hole cylinders particle shapes by employing a sphericity parameter to describe the shape of the particles.

In addition, due to a significant difference in curvature radius between the surface of packing particles and the reactor wall, the value of porosity in the reactor wall region is generally higher than that in the main body of packed beds [130]. The correlations previously referred to are for calculating the mean porosity in the bed and the porosity variations in the wall region will be discussed further on.

2.3.2. Mass transfer
Interphase mass transfer coefficients

An important aspect in the design of multiphase reactors is the mass transfer between phases. In heterogeneous catalyzed reactions (when the catalyst is in a different phase from the reactants) such as LOHC dehydrogenation, the rate of reaction can be limited by interphase mass transfer instead of by the intrinsic reaction kinetics. In a general three-phase reactive system, distinct mass transfer resistances exist: gas-liquid mass transfer, liquid-solid mass transfer, and intraparticle diffusion as described by Figure 2.9. Depending on the system, one of these mass transfer resistances may be the reaction rate limiting step and can affect the overall conversion and selectivity of the process [53].
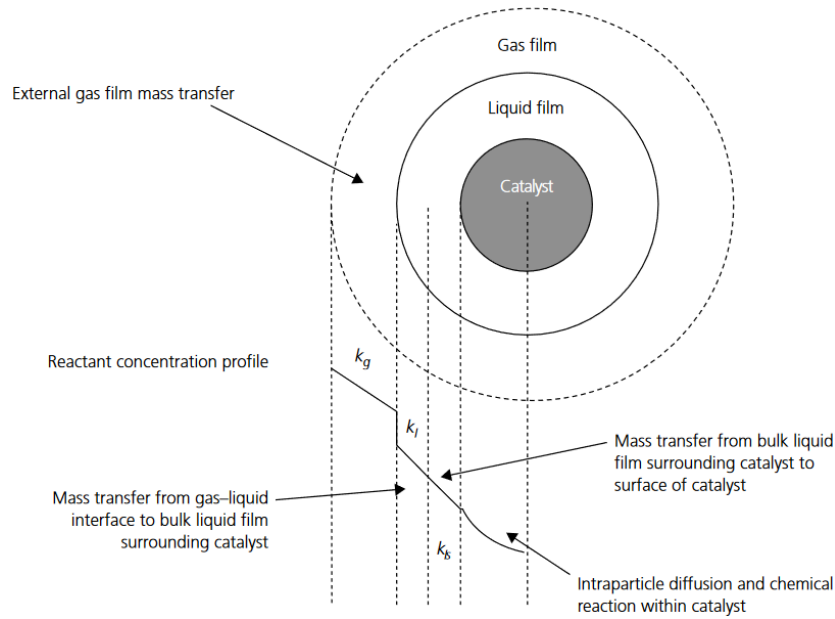
Figure 2.9: Mass transfer resistances in three-phase fixed-bed reactors [53].

Gas-liquid mass transfer is relevant for processes in which both gaseous and liquid reactants need to reach the solid catalyst particle for the reaction to occur. This is the case of many absorption, desorption, and distillation applications. For this purpose, correlations have been developed to estimate the gas-liquid interfacial areas and gas-liquid mass transfer coefficients [68][76][69][74]. However, in LOHC dehydrogenation, the reaction occurs uniquely from liquid reactants and the gas is instead a product. Therefore, only liquid-solid mass transfer should be considered.

Liquid-solid mass transfer can become a limiting factor for fast reactions with highly active catalysts. In these cases, reactions can influenced by the rate of liquid-solid mass transfer and it becomes important to know the liquid-solid mass transfer coefficient. As Iliuta and Larachi [53] explain, liquid-solid mass transfer resistance is significant when the following inequality is satisfied [122]:

$$\frac{10d_{\mathsf{p}}}{c_{\mathsf{sat}}} r_{\mathsf{v}} (1 - \epsilon_{\mathsf{B}}) > k_{\mathsf{ls}} \tag{2.11}$$

where:

$c_{\mathsf{sat}} =$ Concentration of saturation [mol/m^3]
$r_{\mathsf{v}} \quad =$ Volumetric reaction rate [mol/m^{3}s]
$\epsilon_{\mathsf{B}} \quad =$ Mean bed porosity [-]
$k_{\mathsf{ls}} \quad =$ Liquid-solid mass transfer coefficient [m/s]

Several studies have focused on predicting mass transfer coefficients in packed-bed reactors for which Duković et al. [34] provide an extensive list. Among the correlations that have been proposed to estimate the liquid-solid mass transfer coefficient for TBRs, one of the most advanced is the ANN correlation proposed by Larachi et al. [70]. This correlation embeds both the heat and mass transfer information into a Péclet number, Pe, to predict either Nusselt, Nu, or Sherwood, Sh, numbers to obtain liquid-solid heat and mass transfer coefficients.

For FBRs, the number of studies addressing the estimation of the liquid-solid particle mass transfer coefficient remains limited. One of these is presented by Mochizuki [97] which provides correlations to determine the liquid-solid mass transfer coefficient across a broad spectrum of liquid Reynolds numbers.

For this project, any mass transfer limitations that could affect the reaction rate will be accounted for through the reaction rate equations input to the CFD model. As previously discussed, experimental studies have been conducted to obtain the reaction kinetics for NEC and DBT dehydrogenation. The reaction rates derived from these studies inherently include any mass transfer limitations. Consequently, employing one of these reaction kinetics equations in the CFD model would adequately capture the overall reaction rates, including the influence of mass transfer limitations.

2.3.3. Heat transfer

Given that LOHC dehydrogenation is an endothermic reaction, an efficient heat supply system is necessary for the reaction to take place. Analogous to mass transfer, there are also various heat transfer resistances within a three-phase catalytic reactor such as thermal resistance at the wall, within particles, at contact points between particles, between particles and fluids, between fluids and, within each fluid [142]. The design of the reactor and heat supply system requires a thorough understanding of the heat transfer properties of the packed bed.

The models used to analyze heat transfer in multiphase packed beds can be categorized in two main groups: heterogeneous and pseudo-homogeneous [53]. Heterogeneous models describe the temperature and heat transfer of each phase using individual energy conservation equation. On the other hand, pseudo-homogeneous models treat the phases as a homogeneous medium and make no distinction between the phases' temperature. In this approach, a single energy conservation equation suffices to treat all phases.

Heat transfer in fixed-bed reactors has mainly been investigated through two-dimensional pseudo-homogeneous models. One way to represent heat transfer with a pseudo-homogeneous model is through two key parameters: the bed radial effective conductivity, Λ_e, and the wall heat transfer coefficient, h_w. The radial effective conductivity represents the global radial heat transfer coefficient within the bed, while the wall heat transfer coefficient accounts for relatively weaker heat transfer near the wall due to reduced mixing [67]. By neglecting an axial conduction term (a valid approximation for beds with sufficient length-to-particle diameter ratios, leading to near plug flow conditions [94]), the two-dimensional axisymmetric steady-state pseudo-homogeneous heat transfer model in a non-reacting cylindrical fixed-bed is formulated as:

$$(\rho_L c_{p,L} V_L + \rho_G c_{p,G} V_G) \frac{\partial T}{\partial z} = \Lambda_e \left(\frac{1}{r} \frac{\partial T}{\partial r} + \frac{\partial^2 T}{\partial r^2} \right) \tag{2.12a}$$

subject to boundary conditions at the wall ($r = R$) and at the reactor axis ($r = 0$):

$$\text{At } r = R, \qquad -\Lambda_e \frac{\partial T}{\partial r} = h_w (T - T_w) \tag{2.12b}$$

$$\text{At } r = 0, \qquad \frac{\partial T}{\partial r} = 0 \tag{2.12c}$$

$$\text{At } z = 0, \qquad T = T_0 \tag{2.12d}$$

where:

c_p = Specific heat capacity [J/(kg·K)]
V = Superficial velocity [m/s]
T = Temperature [K]
Λ_e = Radial effective thermal conductivity [W/(m·K)]
h_w = Wall heat transfer coefficient [W/(m²K)]

By fitting the analytical solution of Equation 2.12a to experimental temperature profiles, researchers have been able to calculate values for radial effective thermal conductivity and wall heat transfer coefficients and propose empirical correlations for them. It has been noted that these heat transfer parameters are highly influenced by hydrodynamics such that proposed correlations are often specific for either cocurrent upflow or downflow at specific hydrodynamic flow regimes.

Larachi et al. [72] provide a thorough literature review discussing the different correlations developed to calculate the radial effective thermal conductivity and wall heat transfer coefficient for multiphase cocurrent downwards TBRs and upwards FBRs. For the radial effective thermal conductivity in TBRs, Larachi et al. [72] compare four correlations and ultimately propose their own artificial neural network correlation based on an extensive database of past experimental data. Their ANN correlation is valid for all flow regimes in cocurrent downflow operation. For cocurrent upflow operation, Larachi et al. [72] recommend using the correlation by Lamine et al. [66] for the bubble flow regime and that of Gutsche [44] for low gas and liquid flow rates.

For the wall heat transfer coefficient in TBRs, Larachi et al. [72] also compare existing correlations and ultimately propose a more flexible ANN correlation valid for all flow regimes. For FBRs however, only the correlation of Sokolov and Yablokova [125] is identified and recommended for use. As a

general trend, the effective radial thermal conductivity and wall heat transfer coefficient increase with decreasing particle size, and with increasing liquid velocity. Larachi et al. [72] also show the effect of the liquid viscosity and surface tension on both heat transfer parameters and demonstrate that bed porosity has only minimal effects on these parameters.

In addition to the radial effective thermal conductivity, which serves as a comprehensive heat transfer coefficient within the bed, several studies have delved into local heat transfer coefficients within packed beds. For example, Marcandelli et al. [90] studied local particle-fluid heat transfer coefficients which can be important for exothermic reactions catalyzed by the particles as ensuring an adequate particle-fluid heat transfer coefficient is crucial to prevent particle overheating. They found that no correlation exists for this coefficient, but a rough estimate of the particle-fluid heat transfer coefficient can be obtained by using the Chilton-Colburn analogy with existing particle-fluid mass transfer correlations. Larachi et al. [70] however, took this a step further and developed an ANN correlation to find both Nusselt and Sherwood numbers for liquid-particle heat and mass transfer in TBRs. Additionally, Heidari and Hashemabadi [46] developed a model to predict the gas-liquid interfacial heat transfer in TBRs.

To have a better idea of the different heat transfer phenomena within fixed-beds, Mears [94] studied the main heat transfer resistances and their relative importance. He identified that temperature gradients can develop in three domains within fixed-bed reactors with heat exchange at the wall: intraparticle within a catalyst particle, interphase between external surface of the particle and adjacent fluid, and interparticle between fluids and the wall. Temperature gradients present in these three domains can disrupt the reactor's performance from achieving ideal isothermal conditions. Hence it is important to know the relative magnitude of the heat transfer resistances to model heat transfer through the reactor accurately.

For intraparticle temperature gradients, Mears [94] proposes using the criteria given by Equation 2.13 to determine if the deviation in the reaction rate due to intraparticle temperature gradients varies more than 5% than from an isothermal reaction rate.

Condition to neglect intraparticle temperature gradient:

$$\frac{|\Delta H| r_{p,v} r_p^2}{\lambda_p T_0} < 0.75 \frac{R T_0}{E_a} \tag{2.13}$$

where:

$|\Delta H|$ = Absolute value of heat of reaction [J/mol]
$r_{p,v}$ = Reaction rate per unit particle volume [mol/(m^{3}s)]
r_p = Particle radius [m]
λ_p = Particle thermal conductivity [W/(m·K)]
R = Universal gas constant [J/(mol·K)]
T_0 = Temperature of bulk fluid adjacent to a particle [K]
E_a = Activation energy for catalytic reaction [J/mol]

If the criteria in Equation 2.13 is met, the temperature gradients within a particle are negligible and the temperature of the particle can be considered equal throughout the volume of the particle. Mears [94] argues that the heat transfer resistance in the boundary layers adjacent to the particle could considerably surpass the resistance within the particle itself, justifying the treatment of the particle as isothermal in many cases.

Mears [94] introduced an analogous criteria to determine the significance of fluid-particle interphase heat transfer. To ensure that the reaction rate does not deviate more than 5% from an isothermal rate of reaction, the condition specified by Equation 2.14 must be met.

Condition to neglect fluid-particle temperature difference:

$$\frac{|\Delta H| r_{p,v} r_p}{h_{fs} T_0} < 0.15 \frac{R T_0}{E_a} \tag{2.14}$$

where:

h_{fs} = Fluid-particle heat transfer coefficient [W/(m^{2}K)]

If the above criteria is satisfied, fluid-particle heat transfer resistance may be considered low and the catalyst surface temperature may be assumed equal to that of the adjacent fluid. Furthermore, by comparison of Equation 2.13 and Equation 2.14, Mears [94] shows that fluid-particle heat transfer becomes limiting before intraparticle heat transfer provided Equation 2.15 is satisfied.

$$Bi_\mathsf{p} = \frac{h_\mathsf{fs} d_\mathsf{p}}{\lambda_\mathsf{p}} < 10 \qquad (2.15)$$

where:

$Bi_\mathsf{p} =$ Particle Biot number [-]

Lastly, for interparticle heat transfer, Mears [94] derives Equation 2.16 which enables the recognition of quasi-isothermal behavior across the radius of the bed.

Condition to neglect reactor scale radial temperature gradient:

$$\frac{|\Delta H| r_\mathsf{v} R_\mathsf{r}^2}{\Lambda_\mathsf{e} T_\mathsf{w}} < 0.4 \frac{R T_\mathsf{w}}{E_\mathsf{a} \left[1 + 8 r_\mathsf{p}/R_\mathsf{r} Bi_\mathsf{w}\right]} \qquad (2.16)$$

where:

$r_\mathsf{v} \quad =$ Average reaction rate per unit bed volume [mol/(m^{3}s)]
$R_\mathsf{r} \quad =$ Reactor radius [m]
$T_\mathsf{w} \quad =$ Wall temperature [K]
$Bi_\mathsf{w} = h_\mathsf{w} d_\mathsf{p}/\Lambda_\mathsf{e} =$ Biot number at the wall [-]

If this criteria is met, the radial temperature across the bed can be considered constant. This criteria, however, is often not fulfilled and a parabolic radial temperature distribution develops with a maximum or minimum temperature at the reactor axis depending depending on whether the reaction is exothermic or endothermic. From these criteria, Mears [94] concludes that heat transfer resistances are generally in the order: interparticle>interphase>intraparticle. Furthermore, an examination of these criteria can help identify that, for example, reducing the reactor radius will help minimize interparticle and interphase heat transport limitations, and decreasing the catalyst particle diameter reduces interphase and intraparticle heat transport resistances.

For the LOHC dehydrogenation reactor, it will be important to study these criteria and understand the main heat transfer resistances. Understanding the strength of each resistance will be important to then select an appropriate heterogeneous or homogeneous heat transfer model. The dehydrogenation reactors in Voyex's experimental setups are equipped with jacketed walls to provide the necessary heat for the reaction. This approach will serve as the initial basis for constructing the numerical model, although alternative heating methods could be explored in the future.

2.4. Reactor modeling

Modeling the performance of any multiphase reactor involves developing relations to connect productivity, conversion, and selectivity to input and operating parameters. This process involves formulating a set of conservation equations for mass, momentum, and energy, along with constitutive equations for species transport and chemical reactions, and solving them for the reactor. There are different levels at which these governing equations can be applied, each with varying degrees of sophistication. Dudukovic et al. [33] explain that modern reaction engineering requires handling phenomena over a multitude of scales: molecular scale (kinetics), eddy or particle scale (local transport phenomena), and at a reactor scale (flow patterns, contacting and flow regime). Figure 2.10 represents these three levels as well as different modeling approaches for each.

Molecular scale (rate forms)

Strictly empirical	Mechanism based	Fundamental elementary

├ ─ ─ ─ ─ ─ ─ ─ ─ ┤─ ─ ─ ─ ─ ─ ─ ┤

Eddy or particle scale transport

Empirical	Micromixing models	DNS CFD

├ ─ ─ ─ ─ ─ ─ ─ ─ ┤─ ─ ─ ─ ─ ─ ─ ┤

Empirical part of rate equation	Thiele modulus	Rigorous

Reactor scale

Ideal reactors	Empirical models	Phenomenological models	**CFD models**

├ ─ ─ ─ ─ ─ ─ ─ ─ ┤─ ─ ─ ─ ─ ─ ─ ┤─ ─ ─ ─ ─ ─ ─ ─ ┤

PFR, CSTR	Axial dispersion
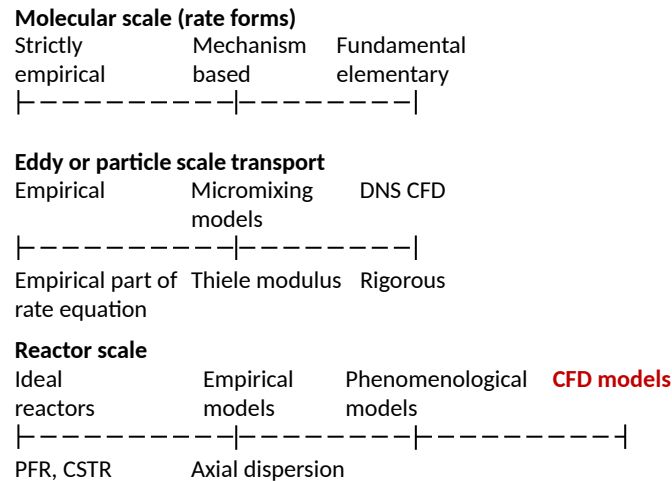
Figure 2.10: Levels of multiphase reactor modeling [33]

2.4.1. Macroscopic modeling

In this project, the primary focus will be on reactor-scale modeling of the dehydrogenation reactor as the aim is to obtain a macroscopic understanding of the hydrodynamics, heat transfer, and chemical reaction to evaluate the overall reactor performance. The simplest reactor-scale models are those assuming either perfect mixing or plug flow within the reactor. These models are known as the continuous stirred-tank reactor model (CSTR), and plug flow reactor model (PFR). CSTR and PFR models are considered ideal reactor models due to precisely defined transport and mixing processes. Deviations from the plug flow reactor model are often accounted for using axial dispersion coefficients to consider axial mixing along the reactor. The most sophisticated models are those that resolve the hydrodynamics by numerical solution of the Navier-Stokes equations and superimpose the reaction kinetics on it. As Duduković et al. [34] explain, the level of sophistication used to model reactor hydrodynamics should be commensurate with the level of modeling used to understand the reaction kinetics since kinetics ultimately drives the reactor.

Most of the correlations referenced in section 2.3 of this report are empirical or phenomenological models using experimental data, dimensionless number analysis, and in some cases artificial neural networks which can be useful to predict global properties relevant in multiphase reactor design such as pressure drop and liquid holdup. However, these correlations do not provide further insight into the multidimensional effects within the reactor such as the gas-liquid distribution, velocity, temperature, or concentration fields, and have limited use for reactive multiphase flows where the flow rates of liquid and gas phases change throughout the reactor. Despite the research that has been performed in understanding the multiple parameters of packed beds, two-phase flow is not well understood engineers often have to look through mostly empirical equations to evaluate design parameters. Engineers have to find suitable correlations that are applicable for the operating conditions and physical properties of the system of interest, but the overall discrepancy in predictions can remain large [34].

With the rapid advancement of computational techniques, the focus of reactor modeling and design has shifted towards computational models to gain deeper insight into phenomena within packed-bed reactors across different scales. As mentioned earlier, predicting the performance of multiphase reactors involves solving a set of conservation equations for mass, momentum, and energy, along with constitutive equations for species transport and chemical reaction. However, an incomplete understanding of the physics along with the highly coupled, and nonlinear nature of these equations, makes it a difficult task to obtain a complete solution. In this context, CFD has proved to be a useful tool in helping solve the multidimensional flow equations coupled with heat transfer, species transport, and reaction kinetics.

CFD is an advanced technique based on the finite volume method to solve a system of partial differential equations (PDEs) representing the conservation of several quantities. More specifically, it involves solving the Navier-Stokes equations, which account for the conservation of mass and momentum, as well as conservation equations for energy and species transport. In the finite volume method, the flow domain is discretized into small control volumes referred to as cells. over which the PDEs

are integrated to result in a system of algebraic equations. The PDEs are integrated over these cells, resulting in a system of algebraic equations. The system of equations is then discretized and solved numerically over multiple iterations until convergence is achieved. This versatile method facilitates analyzing complex flows and provides a numerical solution to the governing equations while adhering to an appropriate set of boundary conditions.

To simplify the complex problem of reactor modeling comprising of flow, heat transfer, and reaction phenomena, each of these aspects will be discussed separately and ultimately united in a single model.

2.4.2. CFD Modeling

Within CFD, there are various methods to approach the problem as described by the macroscopic modeling methods listed in Figure 2.11 with one of the main differences being how each of the phases is understood and modeled. The overall problem can be divided into two key parts: modeling of the fluid phases, and modeling of the solid phase.
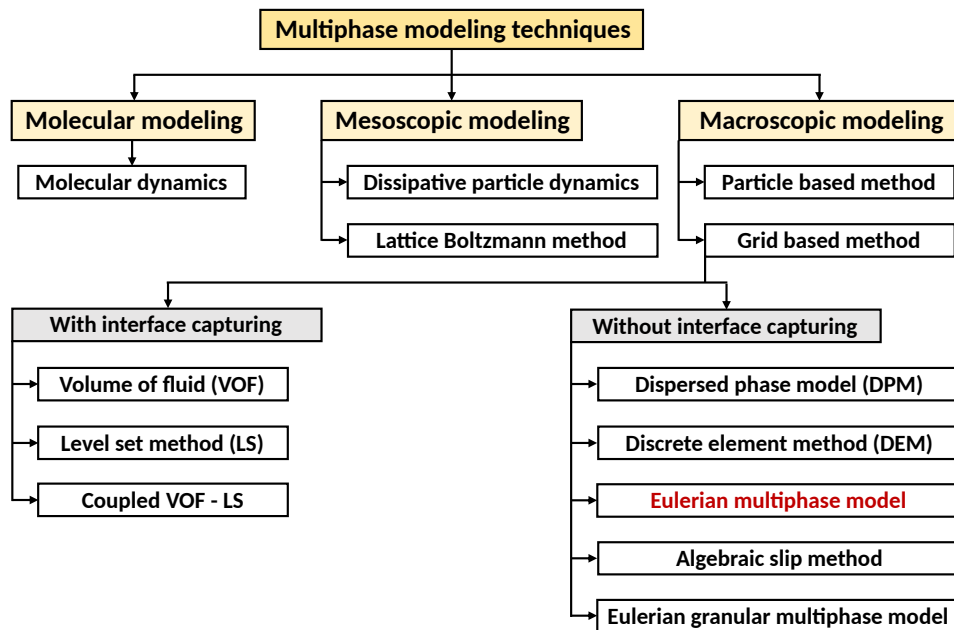
Figure 2.11: Multiphase flow modeling techniques [111].

Fluid phase modeling

Volume of fluid method

When modeling the fluid phases in multiphase CFD, a distinction can be made between models that track fluid interfaces and those that do not. The main interface tracking method for multiphase modeling is the volume of fluid (VOF) method in which the interfaces between fluids are well defined. VOF can be useful to study interaction processes between fluids and can be applied for any number of phases. It works by establishing a volume fraction variable that indicates the proportion of each fluid within each cell of the CFD simulation, ensuring that the sum of all volume fractions in a cell amounts to one.

The interface between phases is then tracked by solving a continuity equation for the volume fraction of each phase, and subsequently a single momentum equation is solved using volume-weighted average fluid properties. As a result, the velocity and pressure fields are shared by the phases and represent volume-averaged values. As an example, Lopes and Quinta-Ferreira [83] developed a VOF model for a high-pressure TBR as their goal was to study liquid distribution and surface tension phenomena for which accurate knowledge of the fluid phase interface was required. VOF is used when the knowledge of fluid interface position is of interest as can be for free flows, stratified flows, flows with large bubbles, or as in the case of Lopes and Quinta-Ferreira [83] when surface tension and capillary effects at the fluid interface are of interest.

Eulerian multiphase model
The main method of treating the fluid phases without interface tracking is the Eulerian multiphase model. It is referred to as the Euler-Euler approach because the motion of all fluid phases is analyzed from an Eulerian perspective in that no fluid elements or interfaces are followed, but rather fixed control volumes are defined through which fluid flows. Each cell within a CFD simulation is a control volume and in this approach all fluid phases are treated mathematically as interpenetrating continua. The amount of each phase in each cell is determined by its volume fraction, and each of the different fluids has its own set of governing equations that interact through additional force, source, and sink terms to achieve closure. This method applies a continuum approximation to all phases and solves the hydrodynamic aspects by using volume averaged mass and momentum conservation equations for each phase. The equations are coupled through the pressure field and additional terms corresponding to interphase interactions. More details of this method will be presented in subsection 2.4.3. As a reference, Wang et al. [140] provide an overview of the simulation choices and details used in multiphase CFD modeling for TBRs.

Solid phase modeling
Modeling the solid particles in a packed-bed reactor is less restrictive and can be divided into Eulerian and Lagrangian categories.

Porous medium approach
An Eulerian approach for treating the solid particles in a packed bed is the effective porous approximation in which the bed is represented as an effective porous medium. The domain for multiphase flow is defined as an isotropic or non-isotropic porous media and is characterized by a few lumped parameters [119]. To represent the porous region, a source or sink term is added in the conservation equations for fluid flow and heat transfer. This can be included into the Eulerian multiphase model framework where the varying porosity due to particles can be incorporated through a porosity correlation as will be described further on.

Three-fluids approach
Another Eulerian approach for treating the solid particles is known as the three-fluids approach in which the Eulerian multiphase model is applied to the solid phase as well. This way all three phases are treated through the Eulerian multiphase model simultaneously with the velocity of the solid phase fixed at 0 m/s such that it remains stationary. In addition, the volume fraction for the solid phase, ε_S, is defined at the beginning of the simulation and remains invariant throughout. The volume fraction may be taken equal to the mean bed porosity with spatial variations incorporated through the use of porosity correlations. This approach is used by several authors including Jiant et al. [61], Gunjal et al. [42], and Janecki et al. [60].

The Lagrangian solid phase modeling approach consists in modeling discrete particles so that the CFD simulation may fully resolve the interstitial flow through the bed. This approach accounts for the geometric complexities of the packing structure to achieve a more fundamental understanding of the effects of bed geometry on transport and reaction phenomena [140]. Bed non-uniformities can be especially significant in low tube-to-particle diameter ratio reactors, and modeling discrete particles may be beneficial for these cases. Although precise results are achieved, explicitly modeling individual particles and the interstitial space requires complex geometric modeling, grid generation, and is computationally expensive. This approach is too computationally demanding and impractical for routine design of full scale fixed-bed reactors and instead has been restricted to small reactors with a limited number of particles.

Discrete element method
Several methods have been used to model discrete random packing structures including the discrete element method (DEM), Monte-Carlo methods, image-based methods such as magnetic resonance imaging (MRI) and computer tomography (CT), and rigid body dynamic (RBD) tools [101]. One frequent approach in literature is the discrete element method (DEM) where individual particles are described by Newton's laws of motion in which inter-particle contact forces and particle-fluid interaction forces come into play. The contact model for particle-particle interactions is a core aspect of DEM. Depending on whether particles are treated as soft or hard, the resulting deformations and forces are captured

[20][148]. DEM can also be integrated with CFD to describe particle-fluid flow. For example, Baniasadi and Peters [13] utilized the DEM method for particle modeling combined with the Eulerian multiphase model for flow modeling to simulate a TBR. By using DEM, the authors were able to study the porosity distribution in the bed, and observe the three-dimensional effects it causes. Likewise, Vångö et al. [137] proposed a CFD-DEM model utilizing the VOF method for fluid phase modeling to study multiphase flow through packed beds.

Rigid body dynamics

A second approach for discrete particle modeling is rigid body dynamics (RBD). A packing algorithm for synthesizing three-dimensional packing models was recently developed by Moghaddam et al. [102]. This algorithm is founded on the equation of motion for rigid bodies, and hard contacts between particles are defined. This methodology can take into account the pellet shape, physio-mechanical properties, and loading methods when building a packing structure. A thorough description of the model formulation as well as the packing algorithm is provided by Moghaddam et al. [102]. They have used the RBD packing algorithm along with CFD to study packing structures, hydrodynamics, and heat transfer in narrow fixed-bed reactors [102][99][100][101]. They have found that for low tube-to-pellet fixed-bed reactors, sharp velocity, temperature, and composition profiles develop because of the nonuniform topography that is accentuated near the walls of the reactor. For narrow reactors it then becomes especially important to consider the bed porosity spatial variation and discrete particle models are an effective way of doing this. Additional details of discrete particle models and their recent use for packed-bed hydrodynamics studies are reviewed by Moghaddam et al. [99].

2.4.3. Eulerian multiphase model

In this study focused on macroscopic modeling of LOHC dehydrogenation in a packed-bed reactor, a two-dimensional Eulerian multiphase approach is selected to model fluid phases. The precise fluid interface position is not critical, ruling out the VOF method. Rather than tracking individual bubbles or gas-liquid regions, the main objective is understanding overall hydrodynamics, heat transfer, and reaction processes in the reactor. Hence, the Eulerian multiphase model is the preferred approach for simulating flow in the reactor under investigation.

Moreover, the solid particles will also be modeled through an Eulerian approach as Lagrangian approaches such as DEM or packing modeling through RBD are computationally expensive and provide details beyond the scope of this work. This work does not aim to study packing structures or develop a fully resolved flow field through interstitial spaces in the packed bed. Instead, the aims is to develop a macroscopic model that accurately considers interphase interaction, providing overall results for general reactor parameters. Therefore, an Eulerian approach for the solid phase, specifically the three-fluid approach, is selected considering the solid phase as a third interpenetrating continuum with a velocity of zero and fixed volume fraction profile.

Conservation equations

In the Eulerian multiphase method, a continuum approximation is applied to all three phases and the hydrodynamic equations consist of mass and momentum conservation equations for the qth phase which can be written as follows:

Mass conservation:

$$\frac{\partial}{\partial t}\left(\varepsilon_q \rho_q\right) + \nabla \cdot \left(\varepsilon_q \rho_q \boldsymbol{U}_q\right) = \sum_{p=1}^{n}(\dot{m}_{pq} - \dot{m}_{qp}) + S_{\text{mass},q} \tag{2.17}$$

Momentum conservation:

$$\frac{\partial}{\partial t}\left(\varepsilon_q \rho_q \boldsymbol{U}_q\right) + \nabla \cdot \left(\varepsilon_q \rho_q \boldsymbol{U}_q \boldsymbol{U}_q\right) = -\varepsilon_q \nabla P + \nabla \cdot \left(\varepsilon_q \mu_q \nabla \boldsymbol{U}_q\right) + \varepsilon_q \rho_q \boldsymbol{g} + \sum_{p=1}^{n} K_{pq}(\boldsymbol{U}_p - \boldsymbol{U}_q) + \boldsymbol{S}_{\text{momentum},q}$$
$$\tag{2.18}$$

Volume fraction constraint:

$$\sum_{q=1}^{n} \varepsilon_q = 1 \tag{2.19}$$

where:

ε_q	= Volume fraction of the qth phase [-]
ρ_q	= Density of the qth phase [kg/m³]
$\boldsymbol{U}_q$	= Interstitial velocity of the qth phase [m/s]
$\dot{m}_{pq}$	= Mass transfer from the pth phase to the qth phase [kg/s]
$S_{\text{mass},q}$	= Mass source for the qth phase [kg/s]
P	= Mean pressure shared by all phases [Pa]
μ_q	= Viscosity of the qth phase [Pa·s]
$\boldsymbol{g}$	= Acceleration due to gravity [m/s²]
K_{pq}	= Interphase momentum exchange coefficient [kg/m³s]
$\boldsymbol{S}_{\text{momentum},q}$	= Momentum source for the qth phase [kg/m²s²]

The right-hand side of Equation 2.17 represents mass transfer among phases and a source or sink term, $S_{\text{mass},q}$. For LOHC dehydrogenation, the terms for mass transfer between phases are expected to be negligible compared to the other terms as the only reactant is the liquid LOHC. There may be small amounts of H$_2$ dissolving in the liquid phase but is considered negligible. Furthermore, the term $S_{\text{mass},q}$ will depend on the reaction rate and accounts for the mass of liquid consumed by the reaction and gas produced by the reaction.

The left-hand side of Equation 2.18 represents the rate of change of momentum for the qth phase, while the right-hand side represents pressure forces, shear stresses, gravitational acceleration, and interphase momentum exchange. Particular attention is needed for the interphase momentum exchange coefficients, K_{pq}, as these couple the flow equations between phases and allow the Eulerian multiphase model to function. These terms provide closure to the flow equations by describing the forces arising from fluid-fluid and fluid-solid interactions. Similar to the mass conservation equation, the momentum conservation equation includes a source term, $\boldsymbol{S}_{\text{momentum},q}$, which becomes relevant during the reaction as momentum is conserved from reactants to products.

In the context of heat transfer, the energy conservation equation within an Eulerian multiphase method can be written in terms of enthalpy as presented in Equation 2.20.

Enthalpy based energy conservation:

$$\frac{\partial}{\partial t}(\varepsilon_q \rho_q h_q) + \nabla \cdot (\varepsilon_q \rho_q \boldsymbol{U}_q h_q) = -\varepsilon_q \frac{DP_q}{Dt} + (\bar{\bar{\tau}}_q : \nabla \boldsymbol{U}_q) - \nabla \cdot \boldsymbol{q}_q + \sum_{p=1}^{n}(Q_{pq} + \dot{m}_{pq}h_{pq} - \dot{m}_{qp}h_{qp}) + S_{\text{energy},q}$$

(2.20)

where:

h_q	= Specific enthalpy of the qth phase [J/kg]
$\boldsymbol{q}_q$	= Heat flux of the qth phase [W/m²]
$\bar{\bar{\tau}}_q$	= Shear stress tensor of the qth phase [Pa]
Q_{pq}	= Intensity of heat exchange between p^{th} and q^{th} phases [J/s]
h_{pq}	= Interphase enthalpy [J/kg]
$S_{\text{energy},q}$	= Energy source for the qth phase [J/s]

In Equation 2.20, heat exchange between phases must comply with local balance conditions ($Q_{pq} = -Q_{qp}$ and $Q_{\text{qq}} = 0$). The energy equation can be applied to each qth phase individually, or a pseudo-homogeneous approach can be adopted by considering a single temperature field for both gas and liquid phases, or even the same temperature for all three phases. Furthermore, Equation 2.20 considers a source or sink term, $S_{\text{energy},q}$, that in the case of LOHC dehydrogenation corresponds to the energy consumed by the endothermic reaction. When a single energy equation is utilized for the three phases, this source term becomes related to the reaction rate, r_{v}, as follows:

$$S_{\text{energy}} = \Delta H r_{\text{v}} \tag{2.21}$$

where ΔH is the heat of reaction. Alongside the mass conservation equation that monitors the mass of each phase, it is also important to track the concentration or mass fraction of individual chemical species within each phase. This is relevant because multiple liquid species are present in the reactor (loaded and unloaded LOHC). This is achieved by additional conservation equations for each species. In an Eulerian multiphase model, the general species conservation equation can be written as Equation 2.22.

Species conservation:

$$\frac{\partial}{\partial t}\left(\varepsilon_q\rho_q y_q^i\right) + \nabla\cdot\left(\varepsilon_q\rho_q\boldsymbol{U}_q y_q^i\right) = -\nabla\cdot\left(\varepsilon_q\boldsymbol{J}_q^i\right) + S_{\text{species},q} \tag{2.22}$$

where:

y_q^i = Mass fraction of species i in phase q [-]
$\boldsymbol{J}_q^i$ = Hydrodynamic dispersive flux of species i in phase q [kg/m^{2}s]
$S_{\text{species},q}$ = Species source for the qth phase [kg/m^{3}s]

In Equation 2.22, the source term, $S_{\text{species},q}$, is directly related to the volumetric reaction rate and the stoichiometric coefficients of the reaction taking place. An equation of this form is solved for $n-1$ species where n is the total number of chemical species present in the qth phase. Then, as the sum of mass fractions must equal one, the last mass fraction is calculated as one minus the sum of the remaining mass fractions. To minimize numerical error, the species with the largest mass fractions should be selected as the species for which a species balance equation is not solved; rather, its mass fraction is calculated as one minus the sum of the remaining mass fractions.

As previously mentioned, turbulence will not be initially taken into account. If it becomes necessary to consider, then two additional conservation equations for turbulent kinetic energy, k, and turbulent energy dissipation rate, ε, will be required.

Momentum interaction models

Various models have been developed to provide interphase momentum exchange coefficients, K_{pq}, used in the momentum conservation equation within Eulerian multiphase packed-bed reactor simulations. Three of the most commonly used will be discussed: the relative permeability model [120], the single-slit model [49][50], and the two-fluid interaction model [10][11].

Relative permeability model
The relative permeability model begins from one-dimensional averaged equations to formulate an expression for the drag force of single-phase flow through a packed bed. This expression is then rescaled to account for the second phase through a parameter known as the relative permeability, k_q. The relative permeability is defined as the ratio of the drag force under single-phase flow to that under two-phase flow at the same superficial velocity of a given phase. This way, the relative permeability accounts for the flow obstruction caused by the presence of a second phase [140]. To describe two-phase flow, the relative permeability model uses an Ergun-type equation and incorporates the relative permeability terms k_L and k_G for the liquid and gas phases. These terms were experimentally determined by Saez and Carbonell [120] and written as functions of liquid volume fraction, mean bed porosity, and static liquid volume fraction, ε_L^0. The static liquid volume fraction represents the portion of void fraction occupied by stagnant liquid and can be calculated using Equation 2.23f [120].

$$F_q = \frac{\varepsilon_q}{k_q}\left[E_1\frac{Re_q}{Ga_q} + E_2\frac{Re_q^2}{Ga_q}\right]\rho_q g \tag{2.23a}$$

$$Re_q = \frac{\rho_{\text{q}}|\boldsymbol{U}_{\text{q}}|d_{\text{p}}}{\mu_{\text{q}}(1-\epsilon_{\text{B}})} \tag{2.23b} \qquad Ga_q = \frac{\rho_{\text{q}}^2 g d_{\text{p}}^3\epsilon_{\text{B}}^3}{\mu_{\text{q}}^2\varepsilon_{\text{S}}^3} \tag{2.23c}$$

$$k_{\text{L}} = \left(\frac{\varepsilon_{\text{L}}-\varepsilon_{\text{L}}^0}{\epsilon_{\text{B}}-\varepsilon_{\text{L}}^0}\right)^{2.43} \tag{2.23d} \qquad k_{\text{G}} = \left(1-\frac{\varepsilon_{\text{L}}^0}{\epsilon_{\text{B}}}\right)^{4.8} \tag{2.23e}$$

$$\varepsilon_{\text{L}}^0 = \frac{1}{20+0.9Eo} \tag{2.23f} \qquad Eo = \frac{\rho_{\text{L}} g d_{\text{p}}^2\epsilon_{\text{B}}^2}{\sigma_{\text{L}}\varepsilon_{\text{S}}^2} \tag{2.23g}$$

where:

F = Drag force per unit volume [N/m^3]
E = Ergun constants: $E_1 = 180$, $E_2 = 1.8$ [-]
k_q = Relative permeability of the qth phase [-]
Re = Reynolds number [-]
Ga = Galileo number [-]

ε_S = Solid volume fraction [-]
ε_L = Liquid volume fraction [-]
ε_L^0 = Static liquid volume fraction [-]
ϵ_B = Mean bed porosity [-]
Eo = Eötvos number [-]

Using the previous set of equations and rearranging them to obtain interphase momentum exchange coefficients for use in the momentum conservation equation, the coefficients result as follows:

$$K_{GS} = \frac{\varepsilon_G}{k_G}\left[\frac{E_1\mu_G\varepsilon_S^2}{d_p^2\epsilon_B^3} + \frac{E_2\rho_G|U_G|\varepsilon_S}{d_p\epsilon_B^3}\right] \tag{2.24a}$$

$$K_{LS} = \frac{\varepsilon_L}{k_L}\left[\frac{E_1\mu_L\varepsilon_S^2}{d_p^2\epsilon_B^3} + \frac{E_2\rho_L|U_L|\varepsilon_S}{d_p\epsilon_B^3}\right] \tag{2.24b}$$

$$K_{GL} = 0 \tag{2.24c}$$

This model has been further studied by other authors to result in distinct relations for the relative permeability values. Wang et al. [140] summarize these efforts performed for the relative permeability model. Although this model derives from a one-dimensional analysis, it is recognized to provide good estimates of pressure drop and liquid holdup in multidimensional TBR simulations [140]. This model has been implemented in Eulerian multiphase CFD TBR simulations by several authors yielding good results in agreement with experimental data [8][127]. This model does not take into account gas-liquid interactions which may be a reasonable assumption at low interaction regimes such as the trickle flow regime. Overall, this method can be incorporated without much complexity and is able to capture the major hydrodynamic trends.

Single-slit model
The single-slit model is a phenomenological model proposed by Holub et al. [49][50]. It begins by resembling the cocurrent downward flow in a TBR in the trickle flow regime to the flow inside an inclined rectangular slit, as illustrated in Figure 2.12a. In the trickle flow regime, the liquid phase flows over the catalyst bed in the form of films or rivulets, while the gas phase flows continuously through the voids. This is represented by the slit model where a liquid film flows on the packing's surface while the gas phase flows in the space between. The width of the slit is related to the void fraction in the bed, and the angle of the slit to a tortuosity factor for the bed. This model considers complete wetting of the packing and is based on local momentum and mass balances for both liquid and gas phases. The resulting interphase momentum exchange coefficients take the form of a modified Ergun equation:

$$K_{GS} = \frac{E_1\mu_G\varepsilon_S^2}{\varepsilon_G^2 d_p^2} + \frac{E_2\rho_G|U_G|\varepsilon_S}{\varepsilon_G^2 d_p} \tag{2.25a}$$

$$K_{LS} = \frac{E_1\mu_L\varepsilon_S^2}{\varepsilon_L^2 d_p^2} + \frac{E_2\rho_L|U_L|\varepsilon_S}{\varepsilon_L^2 d_p} \tag{2.25b}$$

$$K_{GL} = 0 \tag{2.25c}$$
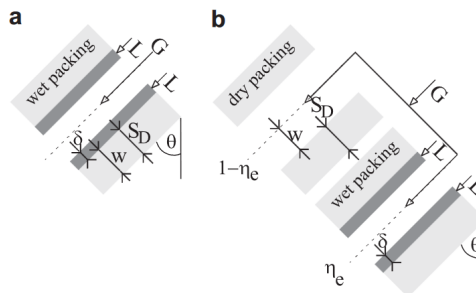
Figure 2.12: Geometry and phase distribution for slit flow models: (a) single-slit and (b) double-slit [140].

Holub et al. [49][50] were successful in fitting pressure drop and liquid holdup data in literature for trickle flow regime at atmospheric pressure with their single-slit model using the measured Ergun constants for each case. It is important to recognize that this model does not consider gas-liquid interfacial interactions, which are expected to be insignificant in the low interaction trickle flow regime. Consequently, the model did not perform well in high-interaction and high-pressure flow regimes. To address this limitation, Al-Dahhan et al. [29] further developed the model to account for gas-liquid interactions. This enhanced model is known as the extended single-slit model.

Further developments to the single-slit model have been made by Iliuta and Larachi [55][52] to consider partial wetting conditions. To achieve this, they add a dry slit to the single-slit model as shown in Figure 2.12b, resulting the what is known as the double-slit model. Iliuta et al. [52] test this model and show it can be used to accurately predict behavior of partially and fully wetted trickle flow at both atmospheric and high pressure.

Two-fluid interaction model

The two-fluid interaction model was developed by Attou et al. [10][11] taking a more physical approach to avoid the empiricism of the relative permeability and single-slit models. The model is derived from a momentum balance on trickle flow around fully wetted particles, considering that the total drag force on each phase arises from contributions due to particle-fluid and fluid-fluid interactions. The flow pattern is idealized as represented by Figure 2.13a, showing the presence of annular flow within the trickle flow regime Furthermore, Figure 2.13b indicates the force components considered. These force components are considered to have both viscous and inertial contributions. The viscous contribution is due to the slip motion between two phases, while the inertial contribution is a result of the gas pressing the liquid film against the solid particles thanks to the changing flow path geometry. The interphase momentum exchange coefficients are given by Equations 2.26a, 2.26b, and 2.26c [10][42].
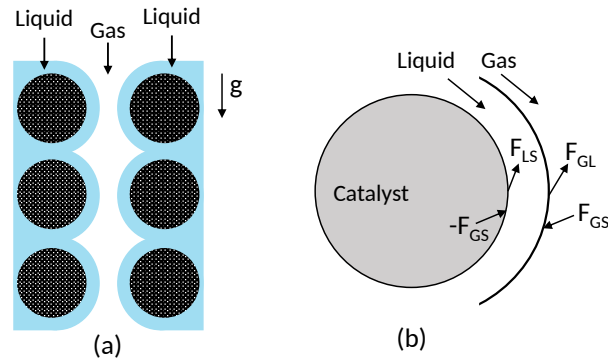
Figure 2.13: Representation of cocurrent gas–liquid flow through the interstitial space of the packed bed: (a) trickle flow idealization; (b) force components acting on the two-phase flow over catalyst particles [140].

$$K_{\text{GL}} = \frac{E_1 \mu_{\text{G}}(1-\varepsilon_{\text{G}})^2}{\varepsilon_{\text{G}} d_{\text{p}}^2} \left[\frac{\varepsilon_{\text{S}}}{1-\varepsilon_{\text{G}}} \right]^{2/3} + \frac{E_2 \rho_{\text{G}} |\boldsymbol{U}_{\text{G}} - \boldsymbol{U}_{\text{L}}|(1-\varepsilon_{\text{G}})}{d_{\text{p}}} \left[\frac{\varepsilon_{\text{S}}}{1-\varepsilon_{\text{G}}} \right]^{1/3} \tag{2.26a}$$

$$K_{\text{GS}} = \frac{E_1 \mu_{\text{G}}(1-\varepsilon_{\text{G}})^2}{\varepsilon_{\text{G}} d_{\text{p}}^2} \left[\frac{\varepsilon_{\text{S}}}{1-\varepsilon_{\text{G}}} \right]^{2/3} + \frac{E_2 \rho_{\text{G}} |\boldsymbol{U}_{\text{G}}|(1-\varepsilon_{\text{G}})}{d_{\text{p}}} \left[\frac{\varepsilon_{\text{S}}}{1-\varepsilon_{\text{G}}} \right]^{1/3} \tag{2.26b}$$

$$K_{\text{LS}} = \frac{E_1 \mu_{\text{L}} \varepsilon_{\text{S}}^2}{\varepsilon_{\text{L}} d_{\text{p}}^2} + \frac{E_2 \rho_{\text{L}} |\boldsymbol{U}_{\text{L}}| \varepsilon_{\text{S}}}{d_{\text{p}}} \tag{2.26c}$$

The model has shown good agreement between its predictions and experimental data for both pressure drop and liquid holdup over a wide range of operating conditions. Although the model was developed considering a low interaction flow regime, the model has been found applicable for high interaction regimes such as bubble flow in both cocurrent downward and upward flow [11]. This model is advantageous for high interaction flow regimes due to its explicit consideration of the gas-liquid momentum interaction term, absent in other models. Numerous authors have used the two-fluid interaction model for CFD simulations of multiphase flow in packed-bed reactors [61][43][42][84][16].

Momentum interaction model comparison

Larachi et al. [71] assessed the various momentum interaction models including the relative permeability model, variants of the slit model, and the two-fluid interaction model to understand their accuracy in predicting pressure drop and liquid holdup for TBRs in the trickle flow regime. This evaluation involved comparing the model predictions against an extensive experimental database and calculated the relative errors between predicted and experimental values. The results for the relative errors, presented in Table 2.1, demonstrated that the variants of the slit model yielded favorable results for liquid holdup prediction but were less effective for pressure drop forecasts. Meanwhile, the simpler relative permeability model had the best relative errors among the studied models, but had the highest values for standard deviation.

Overall, Carbonell [25] indicates that the results show that the models fit the available data to a similar degree of accuracy, but only those based on fundamental equations have the potential of modification for more complex behavior associated with chemical reactions and mass transfer. Carbonell concludes that the relative permeability model and the two-fluid interaction model are based on solid hydrodynamic principles, can predict hydrodynamic parameters with acceptable accuracy, and have the potential to include more complex phenomena. Considering this rationale and the fact that the two-fluid interaction model explicitly considers gas-liquid interactions, the two-fluid interaction model is selected for implementation in the present work.

Table 2.1: Mean relative errors [%] calculated by Larachi et al. [71] for pressure drop and liquid holdup in trickle flow regime using distinct momentum interaction models.

Momentum interaction model	Pressure drop mean relative error [%]	Liquid holdup mean relative error [%]
Relative permeability model	53	19
Single-Slit model	70	18
Extended single-slit model	68	13
Two-fluid interaction model	61	20

Ergun constants

An important aspect to highlight applicable to discussed momentum interaction models relates to the selection of Ergun constants E_1 and E_2. These constants originate from the Ergun equation for single-phase flow through packed beds, where Ergun proposed universal values of $E_1 = 150$ and $E_2 = 1.75$ irrespective of packing shape or dimensions. However, a further study by Macdonald et al. [86] concluded that although the form of the Ergun equation represents data well, using the constants proposed by Ergun can lead to significant errors, especially for non-spherical packings. They instead proposed modified values of 180 and 1.80 as more acceptable values for particles of different shapes. Another study by Nemec and Levec [109] focused on single-phase flow through packed beds and found that the original Ergun constants of 150 and 1.75 yielded an excellent fit for spherical packings. They additionally proposed correlations to modify these values for other packing shapes. While these correlations may be used for initial estimates of Ergun constants, it is recommended to empirically determine the Ergun constants for each packed bed whenever possible.

The single-phase flow Ergun constants are used for the multiphase flow momentum interaction models discussed above. Saez and Carbonell [120], and Attou et al. [10] both recommend the values proposed by Macdonald et al. [86] of 180 and 1.8 for their relative permeability model and two-fluid interaction model, respectively. On the other hand, Holub et al. [50] acknowledge the need to determine the Ergun constants for the packing of interest when presenting their single-slit model. Later CFD studies employing the two-fluid interaction model have both used the values of 180 and 1.80 [61] and have also used determined Ergun constants specific to their particular packed bed [42].

Porosity correlations

As previously described, the random packing of pellets in packed beds leads to a nonuniform porosity distribution. The variation in porosity causes nonuniform flow resistance and often results in a preferential flow of fluid towards the reactor wall where porosity tends to be higher than that in the bulk of the bed [130]. One of the main advantages of using a discrete particle modeling approach to handle

the solid phase in packed beds is that the exact porosity distribution and hence solid volume fraction for each cell in the CFD domain is defined [13]. In other words, the exact uneven topology of the solid particles is modeled and no assumptions for the bed porosity distribution need to be made. However, is very computationally expensive and instead an Eulerian multiphase model approach will be taken for solid phase modeling. To still account for the influence of spatially varying bed porosity, correlations for porosity distribution can be incorporated into the CFD model.

The distribution of porosity within packed beds has been thoroughly researched and various empirical correlations have been proposed to describe the radial variation of porosity. These correlations exhibit either oscillatory or exponential forms, and a review of these correlations is presented by Wang et al. [140]. Among the exponential correlations, Vortmeyer and Schuster [138] offer one for spherical packings, while Sun et al. [130] provide one applicable to packings of any shape. However, Mueller [104] explains that experimental research has shown that the radial porosity distribution shows oscillations near the wall which die away into the packed bed. The smoothed exponential porosity functions neglect this behavior and instead Mueller [104] proposes an oscillating function to capture this phenomenon. His correlation can be used for beds with uniformly sized spherical packing, and an important finding is that the porosity variation beyond 5 particle diameters is less than 5% so the porosity beyond this point can effectively be considered constant. All of these correlations predict a porosity value of 1 at the wall and drop to the mean porosity value within a few particle diameters. As an example, the referenced correlations are plotted in Figure 2.14 for a packed bed of spherical pellets with particle diameter d_p of 5 mm in a 30 cm diameter reactor.
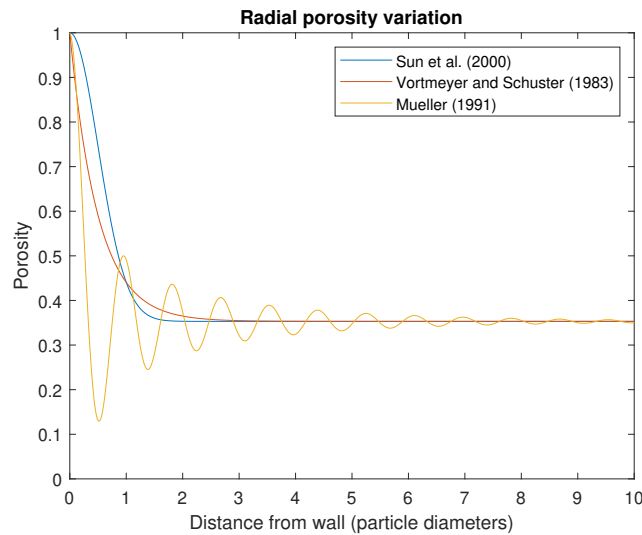
Figure 2.14: Comparison between porosity prediction models for a spherical packing ($D = 0.30$ m, $d_\mathrm{p} = 0.005$ m).

In addition to the radial porosity variation predicted by the correlations in Figure 2.14, researchers have also incorporated a global statistical variation of porosity [61][42]. This is achieved by superimposing a Gaussian probability density function of a specified standard deviation (e.g. 5% [42]) onto the oscillating radial porosity profile by Mueller [104]. This superposition introduces random fluctuations, resulting in a porosity distribution with both radial and axial variations.

3

CFD model development: Hydrodynamics

After understanding the different aspects of multiphase reactors and having selected a 2D Eulerian multiphase approach for simulating a packed-bed LOHC dehydrogenation reactor, the building blocks for this model can be further developed. There are a number of phenomena occurring simultaneously within the reactor and to include them all at once in a CFD simulation would be difficult and highly vulnerable to mistakes. Instead, each aspect of the CFD simulation will be looked at independently and having developed each one, they will be integrated to model their combined effect. These aspects specifically include hydrodynamics, material properties, chemical kinetics, heat transfer and species transport. These components along with the material properties of the three phases in the reactor will be discussed in chapters 3 to 6 for their implementation in a CFD model using ANSYS Fluent 2021 R2 commercial software.

This chapter focuses on packed-bed reactor hydrodynamics. In addition to the fluid inlet conditions, the hydrodynamics in an Eulerian multiphase simulation is mainly determined by the selection of an adequate momentum interaction model, the bed porosity distribution, and capillary pressure effects. Figure 3.1 outlines the chapter structure. The chapter begins by discussing these three aspects, followed by constructing a CFD model for non-reacting, isothermal flow to isolate and test the hydrodynamics of a multiphase packed-bed reactor. The CFD model will then be validated against experimental data and correlations for cocurrent upflow and downflow reactors.

CFD model development: Hydrodynamics
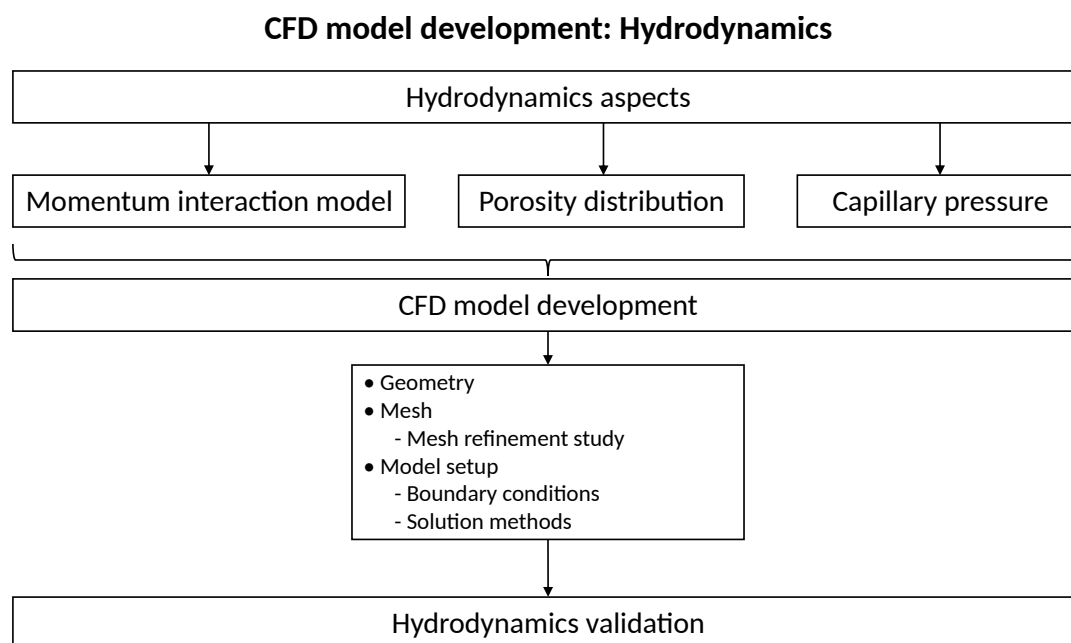
Figure 3.1: Overview of chapter 3.

3.1. Momentum interaction model

The two-fluid interaction model [10] given by Equations 3.1a to 3.1c will be used as it is based on solid hydrodynamic principles and has proven to be applicable in a variety of flow regimes [25]. To implement this into the ANSYS Fluent software environment, a user-defined functions (UDF) were written as separate code files in C programming language to calculate each of the three interface momentum exchange terms, K_{pq}. These UDFs calculate local values of K_{pq} at every cell within the CFD domain by evaluating Equations 3.1a to 3.1c with local flow properties.

$$K_{\mathsf{GL}} = \frac{E_1 \mu_{\mathsf{G}}(1-\varepsilon_{\mathsf{G}})^2}{\varepsilon_{\mathsf{G}} d_{\mathsf{p}}^2} \left[\frac{\varepsilon_{\mathsf{S}}}{1-\varepsilon_{\mathsf{G}}}\right]^{2/3} + \frac{E_2 \rho_{\mathsf{G}} |\boldsymbol{U}_{\mathsf{G}} - \boldsymbol{U}_{\mathsf{L}}|(1-\varepsilon_{\mathsf{G}})}{d_{\mathsf{p}}} \left[\frac{\varepsilon_{\mathsf{S}}}{1-\varepsilon_{\mathsf{G}}}\right]^{1/3} \tag{3.1a}$$

$$K_{\mathsf{GS}} = \frac{E_1 \mu_{\mathsf{G}}(1-\varepsilon_{\mathsf{G}})^2}{\varepsilon_{\mathsf{G}} d_{\mathsf{p}}^2} \left[\frac{\varepsilon_{\mathsf{S}}}{1-\varepsilon_{\mathsf{G}}}\right]^{2/3} + \frac{E_2 \rho_{\mathsf{G}} |\boldsymbol{U}_{\mathsf{G}}|(1-\varepsilon_{\mathsf{G}})}{d_{\mathsf{p}}} \left[\frac{\varepsilon_{\mathsf{S}}}{1-\varepsilon_{\mathsf{G}}}\right]^{1/3} \tag{3.1b}$$

$$K_{\mathsf{LS}} = \frac{E_1 \mu_{\mathsf{L}} \varepsilon_{\mathsf{S}}^2}{\varepsilon_{\mathsf{L}} d_{\mathsf{p}}^2} + \frac{E_2 \rho_{\mathsf{L}} |\boldsymbol{U}_{\mathsf{L}}| \varepsilon_{\mathsf{S}}}{d_{\mathsf{p}}} \tag{3.1c}$$

An important aspect to consider is that the momentum interaction exchange models for TBRs were developed for both gas and liquid input. This implies that the mass of gas and liquid remains constant throughout the reactor and their volume fractions do too, only varying slightly because of the changing porosity profile. In LOHC dehydrogenation, however, the inlet of the reactor will be purely liquid LOHC, and as a large volume of gas is produced, the gas is expected to take up a large amount of the available interstitial space, leaving only a small amount of space for the liquid. Looking at equations 3.1a and 3.1b it becomes apparent that as the gas volume fraction ϵ_{G} tends to 0 (as would be expected at the pure liquid reactor inlet), the first term of these equations tends to infinity. A similar effect happens with Equation 3.1c where the first term is divided by the liquid volume fraction, ϵ_{L}, such that as it tends to 0 (as would occur in a space dominated by gas), the value of K_{LS} will tend to infinity. This unrealistic inflation at single-phase flow can cause numerical instabilities and cause the CFD solution to diverge.

As the two-fluid interaction model fails to give a reasonable value for K_{pq} at single-phase flow through a packed bed, the respective UDFs will alter the value below 5% gas or liquid volume fraction to instead evaluate the function with a constant volume fraction of 5%. As an example, the gas-liquid interface momentum exchange coefficient, K_{GL}, can be calculated for a representative set of parameters in an NEC dehydrogenation reactor as given in Table 3.1. Calculating K_{GL} from these parameters using the unaltered Equation 3.1a and then the modified version results in the values plotted in Figure 3.2. The same modification will be applied to the gas-solid, K_{GS}, and liquid-solid, K_{LS}, coefficients to avoid unrealistic drag terms at low fluid volume fractions and avoid divergence in the numerical solution. For reference, the three UDFs are annexed in section A.1.

Table 3.1: Example parameters for H_2 - NEC dehydrogenation reactor for calculating interface momentum exchange coefficients.

Parameter	Symbol	Value
Particle diameter [m]	d_{p}	0.003
Ergun constant 1 [-]	E_1	215
Ergun constant 2 [-]	E_2	1.8
Temperature [K]	T	490
Gas viscosity [kg/(m·s)]	μ_{G}	1.26E-05
Gas density [kg/m^3]	ρ_{G}	0.054
Gas interstitial velocity [m/s]	u_{G}	0.241
Liquid viscosity [kg/(m·s)]	μ_{L}	6.66E-04
Liquid density [kg/m^3]	ρ_{L}	808.8
Liquid interstitial velocity [m/s]	u_{L}	0.006
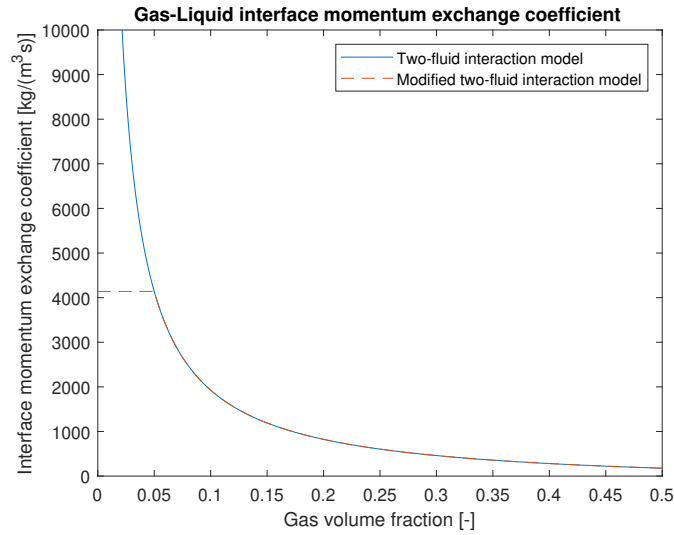
Figure 3.2: Gas-Liquid momentum exchange coefficient for parameters shown in Table 3.1.

3.2. Porosity distribution

In an Eulerian multiphase simulation, catalyst particles are not individually modeled but instead volume fractions of the solid, liquid, and gas are tracked. As individual catalyst particles are not modeled, it is important to define a solid volume fraction profile throughout the CFD domain that can represent the effect of solid particles on the hydrodynamics. This is done by creating a porosity profile that represents the packed bed including radial and axial variations.

3.2.1. Radial distribution

In the radial direction, oscillatory and exponential correlations have been proposed to describe the varying bed porosity as was shown in Figure 2.14. These correlations reflect the increasing porosity near the reactor walls and an average porosity towards the bulk of the reactor. The oscillating function proposed by Muller [104] will be used as it captures the oscillations in porosity near the wall. This porosity function is given as a function of radius as:

$$\epsilon(r) = \epsilon_\mathsf{B} + (1 - \epsilon_\mathsf{B})J_0(ar^*)\mathsf{exp}(-br^*) \tag{3.2a}$$

$$a = 8.243 - \frac{12.98}{D/d_\mathsf{p} + 3.156}, \quad \text{for } 2.61 \leq D/d_\mathsf{p} \leq 13.0 \tag{3.2b}$$

$$a = 7.383 - \frac{2.932}{D/d_\mathsf{p} - 9.864}, \quad \text{for } 13.0 < D/d_\mathsf{p} \tag{3.2c}$$

$$b = 0.304 - \frac{0.724}{D/d_\mathsf{p}} \tag{3.2d}$$

$$r^* = \frac{r}{d_\mathsf{p}}, \quad \text{for } 0 \leq r/d_\mathsf{p} \tag{3.2e}$$

where:

ϵ = Porosity [-]
ϵ_B = Mean bed porosity [-]
J_0 = Bessel function of the first kind of order zero [-]
r = Radial coordinate [m]
D = Reactor diameter [m]
d_p = Particle diameter, or particle equivalent diameter d_pe for non-spherical catalyst pellets [m]

The mean bed porosity, ε_B, can be estimated by Equation 3.3 by Benyahia and O'Neill [18] applicable to spherical, solid cylinders, hollow cylinders, and 4-hole cylinders particle shapes.

$$\epsilon_{\mathrm{B}} = \left(0.1504 + \frac{0.2024}{\varphi}\right) + \frac{1.0814}{\left(\frac{D}{d_{\mathrm{pe}}} + 0.1226\right)^2} \tag{3.3}$$

$$\varphi = \frac{\pi d_{\mathrm{pe}}^2}{A_{\mathrm{p}}} \tag{3.4}$$

where:

φ = Sphericity parameter [-]
d_{pe} = Equivalent sphere particle diameter [m]
A_{p} = Particle surface area [m^2]

The sphericity parameter accounts for pellet shape deviation from a sphere. The equivalent sphere particle diameter, d_{pe}, is the diameter of a sphere with the same volume as the actual pellet. It is important to note in Figure 3.3 that within the first two particle diameters from the wall, the porosity calculated from Mueller's profile [104] reaches values below 0.3. However, the recognized maximum random close packing of spheres is 0.64, corresponding to a minimum porosity of 0.36. This would suggest that the first two minima from Mueller's equation result inaccurate. Li et al. [80] explain that the maximum packing density of equal shape objects depends on the shape with values of 0.72 for cylinders and 0.64 for spheres. While catalyst pellets may not all be of identical shape and have a certain particle size distribution that may contribute to a denser packing, the value for porosity of 0.15 observed in the first minimum of Mueller's correlation is unrealistic. Using this radial porosity distribution would lead to cells with high solid volume fractions near the wall, causing additional flow resistance and unrealistically inflating pressure drop. To mitigate this, a minimum porosity of 0.3 (or maximum solid volume fraction of 0.7) will be imposed on Equation 3.2 to represent a realistic upper limit on catalyst pellet packing density.

Furthermore, Mueller's correlation [104] assigns a porosity of 1.0 at the wall. However, assigning values close to 1.0 to cells near the wall can create unrealistically low-resistance pathways, allowing fluid to bypass the reactor's bulk. While this does occur to some extent, using a value of 1.0 for cells adjacent to the wall is not reflective of reality, as particles come into contact with the wall, forming a tortuous path with some flow resistance. Kuzeljevic and Dudukovic [65] characterized the porosity distribution of a packed-bed reactor with spherical particles using CT imaging by dividing the reactor into cells and found maximum porosity values of around 0.65. Following this observation, an upper limit to the porosity of 0.65 will be applied. These adjustments lead the limited radial porosity profile, observed in Figure 3.3.
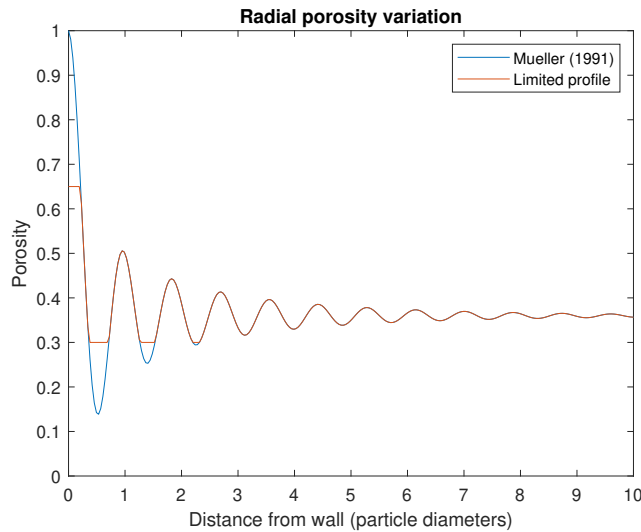
Figure 3.3: Radial porosity profile by Muller [104] and limited profile for a spherical packing ($D = 0.114$ m, $d_{\mathrm{p}} = 0.003$ m).

3.2.2. Axial distribution

Porosity variations in the axial direction should also be considered for the model to be as close to reality as possible. Jiang et al. [61] have shown that the axial porosity variation is close to a Gaussian distribution function and several authors have used this to specify an axial porosity variation. In the TBR 2D-CFD simulation performed by Jiang et al. [61][62], they subdivide the flow domain into sections of 1x1 cm (considering their particle diameter size of 3mm) and impose a constant solid volume fraction in each section by taking a random number from the Gaussian distribution of a specified standard deviation centered around the value obtained from a radial porosity correlation. For sections in the bulk of the reactor they take a standard deviation of 10% and for sections next to the wall a standard deviation between 10 and 20%. Gunjal et al. [42][43] also add axial porosity variation by means of a Gaussian distribution in their TBR CFD model. However, in their case they impose the random variation on each individual CFD cell. They tested imposing variations with standard deviations of 5 and 10% and observed that the results with a 5% standard deviation were closer experimental data. Additionally, Kuzeljevic and Dudukovic [65] characterized the porosity distribution of a packed-bed reactor with spherical particles using CT imaging and found that the resulting porosity for the entire domain resembles a Gaussian distribution with a standard deviation of roughly 5%.

To incorporate the axial porosity variation into the current model at first the approach of Gunjal et al. [42] was followed in that at each cell a number was drawn from the Gaussian distribution with a 5% standard deviation around the value calculated by Mueller's radial porosity correlation. Although this solid fraction distribution represents the oscillatory radial profile described previously, with the additional 5% axial porosity standard deviation, the resultant solid volume fraction field was highly discontinuous as the volume fraction of adjacent cells was not at all related to each other. Figure 3.5a shows an example of the solid volume fractions along a line in the axial direction obtained through this procedure. The random behavior leads to nonphysical volume fraction variations with very high volume fraction gradients between adjacent cells that could affect the results.

To overcome this limitation, this work proposes describing the axial variations through a Fourier series that will allow obtaining the desired standard deviation through a continuous function prevent abrupt changes in volume fractions between neighboring cells. A general Fourier series can be expressed as follows:

$$f(z) = A_0 + \sum_{n_{\min}}^{N_{\max}} \left[A_n \cos\left(\frac{2\pi n z}{L}\right) + B_n \sin\left(\frac{2\pi n z}{L}\right) \right] \tag{3.5}$$

where z is the axial coordinate, L the length of the reactor, A_0 the function's average value, $n_{\min}$ and $N_{\max}$ are the number of terms to be considered, and A_n and B_n the coefficients for each cycle denoted by integer n. The number of cycles given by $n_{\min}$ and $N_{\max}$ correspond to the number of harmonics that shall be taken into account by the function with the wavelength of each harmonic given by L/n. The harmonic with the shortest wavelength is given by $N_{\max}$ and this should correspond to the fastest change in solid volume fraction that is expected. The wavelength of this harmonic can be taken as 4 times the particle diameter, d_{p}, and therefore the value of $N_{\max}$ can be given as:

$$N_{\max} = \frac{L}{4 d_{\mathrm{p}}} \tag{3.6}$$

The desired value of standard deviation, σ, can be calculated from its definition:

$$\sigma^2 = \frac{\sum (f(z) - A_0)^2}{N} \tag{3.7}$$

Using Equation 3.5, Equation 3.7 can be rewritten as:

$$\sigma^2 = \frac{1}{L} \int_0^L \left(\sum_{n_{\min}}^{N_{\max}} \left[A_n \cos\left(\frac{2\pi n z}{L}\right) + B_n \sin\left(\frac{2\pi n z}{L}\right) \right] \right)^2 dz \tag{3.8}$$

Expanding Equation 3.8 and observing that the cross terms equal zero, the equation is simplified to:

$$\sigma^2 = \frac{1}{L} \int_0^L \sum_{n_{\min}}^{N_{\max}} \left[A_n^2 \cos^2\left(\frac{2\pi n z}{L}\right) + B_n^2 \sin^2\left(\frac{2\pi n z}{L}\right) \right] dz \tag{3.9}$$

Observing the trigonometric identity, simplifies the equation to:

$$\sigma^2 = \frac{1}{2} \sum_{n_{\min}}^{N_{\max}} \left(A_n^2 + B_n^2 \right) \tag{3.10}$$

If the values for A_n and B_n are both chosen as a random value from a normal distribution centered at 0 with standard deviation σ_i, the previous equation simplifies to:

$$\sigma^2 = \frac{1}{2}(N_{\max} - n_{\min} + 1)2\sigma_i^2 \tag{3.11}$$

such that standard deviation, σ_i, to select the values for A_n and B_n becomes:

$$\sigma_i = \frac{\sigma}{\sqrt{N_{\max} - n_{\min} + 1}} \tag{3.12}$$

With all the parameters of the Fourier series established, a continuous function is generated exhibiting a random-like behavior. This function's harmonic range is regulated, and the desired function standard deviation is obtained. As an example, Figure 3.4 shows the function's values for a 3 mm particle diameter and a 5% standard deviation in the first 0.1 m of the reactor.
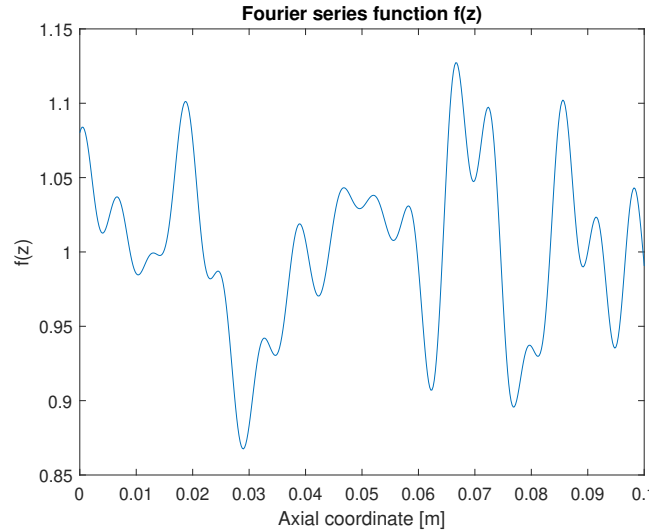
Figure 3.4: Fourier series function for $d_{\mathrm{p}} = 0.003$ m and 5% standard deviation.

Having functions to describe the radial and axial solid volume fraction variations, the solid volume fraction for each cell in the domain can be obtained by multiplying the two. As an example, Figure 3.5b gives the resulting solid volume fraction for a line in the axial direction. Compared to the previous profile obtained directly through a random distribution in Figure 3.5a, the new distribution is more realistic and maintains the desired standard deviation. This new solid volume fraction profile is continuous and cell size independent, both of which will aid in obtaining a more stable simulation and realistic solution. Following the findings of Kuzeljevic and Dudukovic [65] of an average of 5% standard distribution, this value will be used. The solid volume fraction profile described is written in a UDF referenced in section A.2, and will be used to initialize the value of solid volume fraction at the beginning of the CFD simulation.

(a) Solid volume fraction obtained through a Gaussian distribution.

(b) Solid volume fraction obtained through a Fourier series.
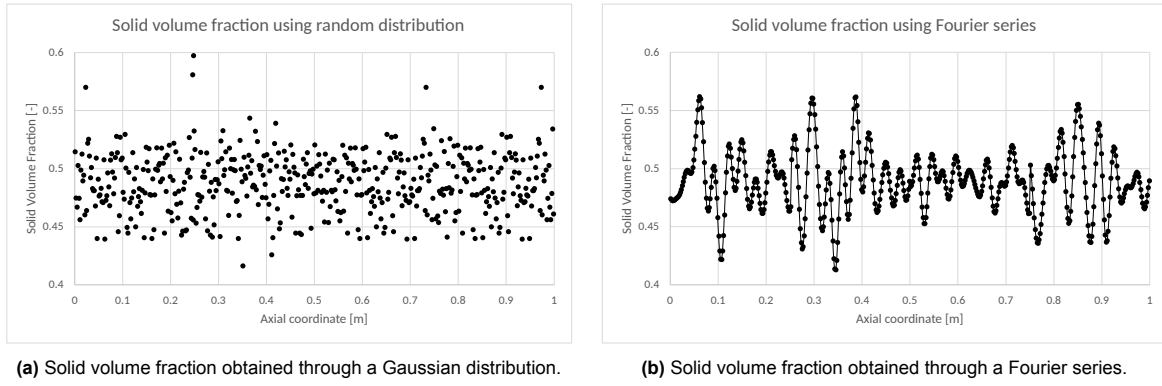
Figure 3.5: Solid volume fraction along a line in the axial direction with 5% standard deviation.

3.3. Capillary pressure

It is important to consider capillary pressure effects in multiphase flow through packed beds as they contribute to the liquid distribution and can cause gradients of liquid holdup within the packed bed [42]. One of the correlations used to quantify capillary pressure in packed beds, previously shown in Equation 2.7, is that of Attou and Ferschneider [12] derived from a momentum balance analysis around the gas-liquid interface. This equation will be used because of Gunjal et al.'s [42] reasoning that its formulation includes geometric parameters rather than liquid saturation like the correlation by Grosser [40] in Equation 2.8 making it easier to implement in the CFD model.

As noted by Jiang et al. [61], the capillary pressure effect on liquid distribution is related to the degree of particle wetting. The magnitude of the capillary pressure calculated with Equation 2.7 can be multiplied by an external particle wetting efficiency, η_{WE}, as was shown in Equation 2.9. This wetting efficiency can be calculated at every CFD cell using the following correlation by Al-Dahhan and Duduković [30]:

$$\eta_{\mathsf{WE}} = 1.104 Re_{\mathsf{L}}^{1/3} \left(\frac{1 + \frac{\Delta P}{z} \frac{1}{\rho_{\mathsf{L}} g}}{Ga_{\mathsf{L}}} \right)^{1/9} \tag{3.13a}$$

$$Re_{\mathsf{L}} = \frac{|\boldsymbol{U}_{\mathsf{L}}| \varepsilon_{\mathsf{L}} \rho_{\mathsf{L}} d_{\mathsf{p}}}{\mu_{\mathsf{L}} (1 - \epsilon_{\mathsf{B}})} \tag{3.13b}$$

$$Ga_{\mathsf{L}} = \frac{d_{\mathsf{p}}^3 \rho_{\mathsf{L}}^2 g \epsilon_{\mathsf{B}}^3}{\mu_{\mathsf{L}}^2 (1 - \epsilon_{\mathsf{B}})^3} \tag{3.13c}$$

where:

η_{WE} = Particle wetting efficiency [-]
$\frac{\Delta P}{z}$ = Pressure gradient [Pa/m]
Re_{L} = Liquid Reynolds number [-]
Ga_{L} = Liquid Galileo number [-]

To obtain the particle wetting efficiency throughout the CFD domain, a UDF (found for reference in section A.3) was written to calculate Equation 3.13a at each cell and write the value of wetting efficiency in a user defined memory slot (UDM).

Given that in an Eulerian multiphase model the pressure field is shared by both gas and liquid phases, the capillary pressure can be added as a source term to the liquid phase momentum conservation equation. To incorporate the capillary pressure as a source term to the momentum conservation equation, gradients of the capillary pressure need to be formulated to match the units of the momentum conservation equation. Differentiating the capillary pressure formulation in Equation 2.7 in the axial and radial directions give the following equations:

$$\frac{\partial P_G}{\partial z} - \frac{\partial P_L}{\partial z} = \frac{2}{3}\sigma \frac{5.416}{d_p} \left(\frac{\varepsilon_S}{1-\varepsilon_G}\right)^{-2/3} \left[\left(\frac{1}{1-\varepsilon_G}\right)\frac{\partial \varepsilon_S}{\partial z} + \left(\frac{\varepsilon_S}{(1-\varepsilon_G)^2}\right)\frac{\partial \varepsilon_G}{\partial z}\right] F\left(\frac{\rho_G}{\rho_L}\right) \tag{3.14a}$$

$$\frac{\partial P_G}{\partial r} - \frac{\partial P_L}{\partial r} = \frac{2}{3}\sigma \frac{5.416}{d_p} \left(\frac{\varepsilon_S}{1-\varepsilon_G}\right)^{-2/3} \left[\left(\frac{1}{1-\varepsilon_G}\right)\frac{\partial \varepsilon_S}{\partial r} + \left(\frac{\varepsilon_S}{(1-\varepsilon_G)^2}\right)\frac{\partial \varepsilon_G}{\partial r}\right] F\left(\frac{\rho_G}{\rho_L}\right) \tag{3.14b}$$

While Gunjal et al. [42] only apply the capillary pressure effect as a source term in the axial direction, it is important to consider the capillary pressure effect in the radial direction as well since gradients of capillary pressure in the radial direction also exist thanks to the solid volume fraction variation this direction. To implement this into the CFD model, the UDF found in section A.4 was written to calculate the value of the capillary pressure per equations Equation 2.7 and to calculate the axial and radial momentum source terms per Equations 3.14a and 3.14b. In these equations, the gradients of solid and gas volume fractions are obtained with the help of an additional UDF annexed in section A.5.

3.4. Hydrodynamics model validation

To bring the aspects influencing hydrodynamics together and validate this section, a CFD model will be set up to replicate the work conducted by Gunjal et al. [42]. In their study, Gunjal et al. developed an Eulerian multiphase CFD model to simulate the behavior of cocurrent downward flow in a non-reactive, isothermal trickle bed reactor, using the parameters listed in Table 3.2. They then compared the results of their model to experimental data. By simulating the same setup, the hydrodynamic aspect of the present CFD model can be isolated and assessed.

Table 3.2: Parameters used by Gunjal et al. [42] for a TBR CFD model

Parameter	Value
Flow configuration	Cocurrent downward flow
Reactor diameter [m]	0.114
Reactor length [m]	1
Fluid system	air-water
Inlet gas superficial velocity [m/s]	0.22
Inlet liquid mass flux [kg/m^{2}s]	$2-10$
Packing	Spherical glass beads
Particle diameter [m]	0.003, 0.006
Ergun constant 1 [-]	215, 500
Ergun constant 2 [-]	1.8, 2.4

3.4.1. Geometry

A 2D axisymmetric flow domain is constructed, as depicted in Figure 3.6. To prevent numerical effects originating from the domain's inlet and outlet affecting the results, additional inlet and outlet sections, each extending ten times the reactor diameter are added. The sections of the domain, labeled in Figure 3.6, are referred to as cell zones. The 'inlet' and 'outlet' sections will serve the purpose of monitoring the mass flow across the 'packed bed' and determine when the solution has converged. Furthermore, the outlet section will also be used to calculate the amount of produced hydrogen and other pertinent output variables. This way, everything before and after the 'packed bed' section is only to obtain stable numerics and to read the inlet and outlet conditions of the packed bed.
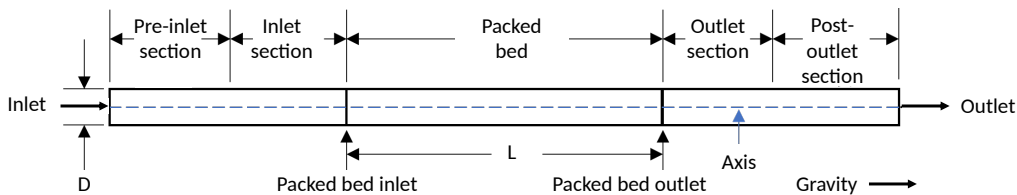
Figure 3.6: Trickle bed reactor CFD 2D axisymmetric solution domain.

3.4.2. Meshing

Having defined the flow domain, the next step involves discretizing it into a mesh that has both a sufficient cell count and quality, as this will affect the numerical solution and accuracy of the results. Thanks to the symmetry and basic shape of the domain, a uniform mesh can be applied. A uniform mesh composed entirely of quadrilateral elements is chosen to ensure a high mesh quality with no skewed elements and an orthogonal quality of one. To ensure a uniform mesh is produced, an edge sizing mesh control is applied along each edge as represented by Figure 3.7. The elements are assigned a certain length that can be controlled. Subsequently, an inflation mesh control is implemented along the wall boundary to generate thinner elements near the wall. Figure 3.3 showed that the porosity profile has the largest variation within the first two particle diameters from the wall. To accurately represent this variation, the inflation mesh control is defined to have eight layers and a thickness of two times the particle diameter. Considering the increased porosity adjacent to the wall, a significant portion of the flow is expected to be directed towards this region. Consequently, finer meshing near the wall is essential to capture the flow details accurately.
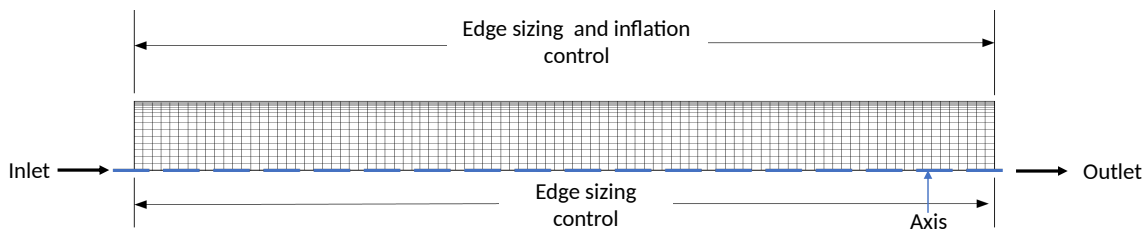
Figure 3.7: Packed bed meshing controls.

Gunjal et al. [42] discretized their packed-bed domain into a grid of 25 x 500 equal cells after conducting a mesh refinement study. However, given that the behavior of the flow is likely influenced by the particle diameter, it is important for the cell size to adequately reflect this influence. To achieve this, the mesh element size is scaled as a function of the particle diameter, so the same level of detail is obtained across different particle diameters. Following this approach, Gunjal et al.'s mesh size corresponds to 0.76 times the particle diameter for 3 mm particles and 0.38 times the particle diameter for their 6 mm particle simulations.

To select a cell size that balances accurate results with computational demand, a mesh refinement study is conducted using a single flow configuration. For an inlet liquid mass flux of 4 kg/m²s and a particle diameter of 6 mm, various cell sizes were evaluated, and the resulting pressure drop and liquid holdup recorded. As an example, Figures 3.8 (a) and (b) show a segment of the meshed domain with mesh sizes equivalent to 0.4 and 1 times the particle diameter, respectively. It is important to note that the radial dimension of the cells within the first two particle diameters from the wall remains constant thanks to the inflation mesh sizing control.
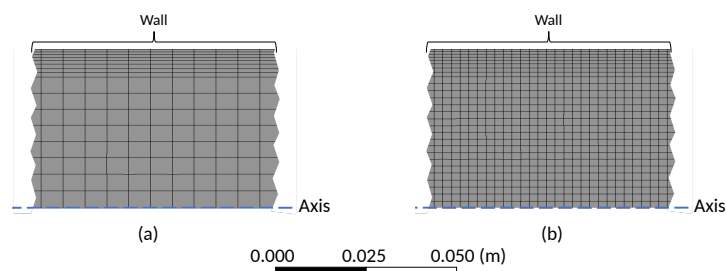
Figure 3.8: Mesh in a section of the domain. (a) Mesh size = 1.0 x d_p. (b) Mesh size = 0.4 x d_p.

Figures 3.9a and 3.9b show the result of this mesh independence study, alongside the experimental value presented by Gunjal et al. [42] for the same flow configuration. To offer a reference point, lines indicating deviations of ±5% from the experimental value are included.

(a) Pressure drop   **(b)** Liquid holdup
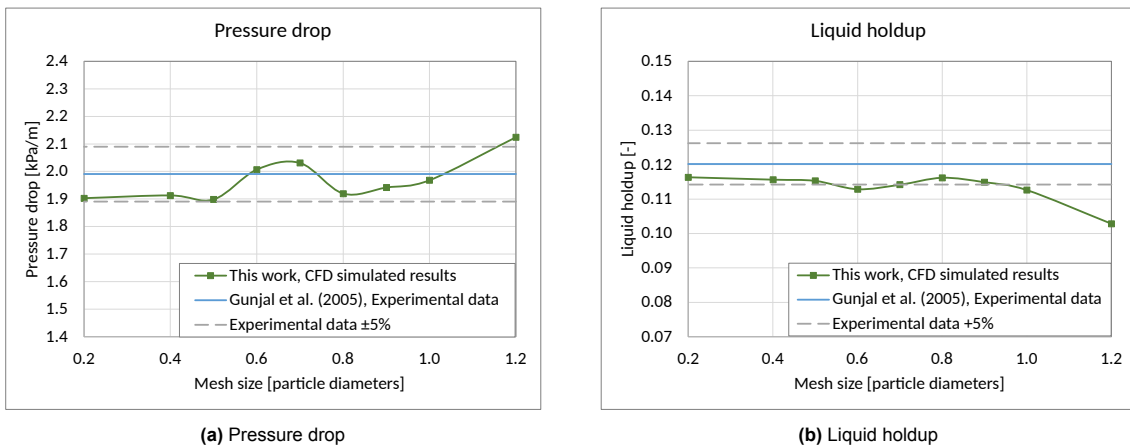
Figure 3.9: Mesh refinement study for air-water flow through TBR ($d_\mathrm{p} = 6$ mm, $V_\mathrm{G} = 0.22$ m/s, $J_\mathrm{L} = 4$ kg/m^{2}s).

In Figure 3.9, results for pressure drop and liquid holdup remain stable under a mesh size of one time the particle diameter. Pressure drop varies less than 5% and liquid holdup less than 3% for smaller mesh sizes. The variability observed in these figures, particularly in Figure 3.9a, can be attributed to the randomness in the porosity profile. If the simulations were rerun, these values would likely shift while maintaining the same trend. The low sensitivity of pressure drop and liquid holdup with mesh size can be attributed to the inflation layer mesh control which allows for a fine resolution of the wall section across all mesh sizes. This is visualized in Figure 3.10 showing the radial solid volume fraction profile for two mesh sizes.
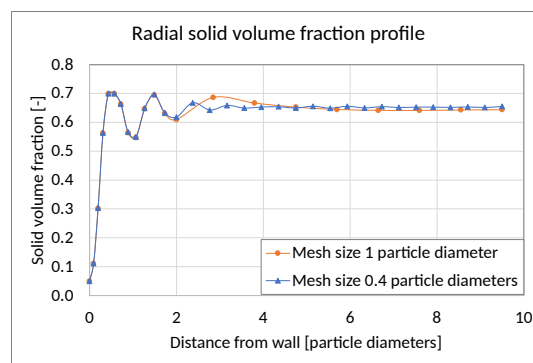
Figure 3.10: Radial solid volume fraction profile at arbitrary height for two mesh sizes.

A mesh size of 0.7 times the particle diameter is selected, as further refinement does not provide increased accuracy but does significantly increase the number of cells, consequently prolonging computational demand. It is important to note that for small particle diameters and large reactor diameters, selecting the mesh size as a function of particle diameter may quickly cause the number of elements to rise and thus require high computational resources. In these cases, it may be necessary to consider a larger mesh element size and assess its accuracy.

3.4.3. Model setup
Physical model setup
To solve the mass and momentum conservation equations in an Eulerian multiphase model framework, a three-phase simulation is adopted. In this approach, a primary phase is selected with the remaining two phases treated as secondary phases within the software. The liquid phase is selected as primary, while the gas and solid phases are both treated as secondary. It is important to select the liquid as the primary phase and not the gas because of how the balances are solved. Although the choice of primary phase might not be critical in this simulation involving both air and water inlets, further on when the inlet is pure liquid LOHC with no gas, the 'inlet' section of the domain will contain only liquid and no

gas. If the gas were selected as the primary phase in such a scenario, the software would result in an error and not calculate properly.

Once the phases are designated, the next step involves assigning materials to each phase. For this hydrodynamics validation study, the gas phase is defined as air with ideal gas properties, and the liquid phase as incompressible water. The ideal gas and incompressible water assumptions are valid for this test as an isothermal flow is considered at ambient pressure and temperature. Furthermore, the momentum exchange interactions are defined for each of the phase pairs with the previously defined UDFs. A laminar flow is also defined.

Boundary conditions

The solid phase is treated as stationary, with its axial and radial velocity components fixed to zero across the entire computational domain. Additionally, the solid phase's volume fraction profile is calculated as previously described and patched onto the domain at the beginning of each calculation. While the solid volume fraction within the 'packed bed' cell zone adheres to the earlier discussion, the three volume fraction profiles presented in Figure 3.11 were tested for the remaining cell zones before and after the 'packed bed' zone. The purpose behind utilizing distinct profiles for the inlet and outlet zones is to promote flow stabilization before and after the packed bed.
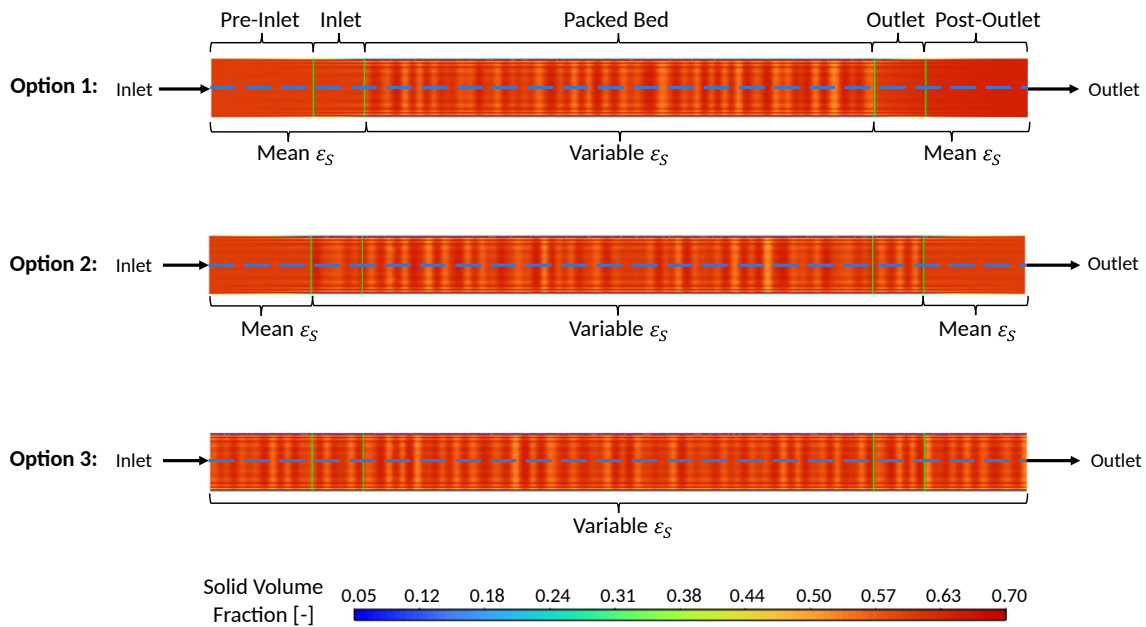
Figure 3.11: Solid volume fraction in 'packed bed', 'inlet', and 'outlet' sections.

In option 1 of Figure 3.11, a constant solid volume fraction equal to 1-ϵ_B is applied before and after the packed bed with a smooth transition at the section boundaries given by an exponentially decaying function. Option 2 extends the variable porosity section to include the 'inlet' and 'outlet' sections. The rationale behind this option is to replicate the same hydrodynamic behavior in the 'inlet' and 'outlet' section as the packed bed and be able to retrieve representative values from these cell zones at the end of the simulation. Finally, option 3 extends the variable porosity to the entire domain.

After initial tests, abrupt shifts in flow variable parameters were found near the interfaces between distinct solid volume fraction profiles. These jumps required a substantial number of cells and solution iterations to stabilize. As a result, option 3 was found to maintain the flow variables the most stable throughout the domain. Although in this option all cell zones have the same solid volume fraction profile, it remains important to maintain the domain divided as represented by Figure 3.6. The 'pre-inlet' and 'post-outlet' cell zones help maintain any inlet and outlet effects away from the central packed bed region. Then, the chemical reaction will only be applied within the 'packed bed' section, and the 'inlet' and 'outlet' sections will be non-reactive sections. As the flow variables are expected to have some level of variation due to the non-uniform solid volume fraction profile, the 'inlet' and 'outlet' sections will be used to obtain average values of flow input and output parameters from the reactor.

An axis boundary condition is set on the centerline of the axisymmetric geometry and a wall boundary condition is set at the reactor wall to impose a no slip and no penetration boundary condition. The boundary conditions are shown in Figure 3.12 for further clarity. At the inlet of the domain, flat velocity inlet profiles normal to the boundary are defined. Since the solid volume fraction at the inlet of the domain is set to a value of $1 - \epsilon_B$, the fluid inlet velocities should be interstitial velocities, U, rather than superficial velocities, V.

For the gas phase in this example, a fixed superficial velocity of 0.22 m/s is used. The interstitial velocity is defined as $U = V/\varepsilon$, so this value of superficial velocity needs to be divided by the gas phase volume fraction. As the gas phase volume fraction is not known beforehand, an estimated liquid or gas holdup is used to calculate the inlet interstitial velocity. For example, estimating a liquid holdup of 0.12 for the system described by Table 3.1, and a mean bed porosity of 0.36, the gas volume fraction results to be 0.24. With this information, the inlet gas interstitial velocity is estimated as well as the volume fraction of the gas at the inlet.

For the liquid phase, a mass flux, J, between 2-10 kg/m^{2}s is used by Gunjal et al. [42] as shown in Table 3.1. Again, the estimated liquid holdup is used as the input inlet liquid volume fraction and the inlet liquid interstitial velocity is then calculated as

$$U = \frac{J}{\rho_L \varepsilon_L} \tag{3.15}$$

where:
J = Mass flux [kg/m^{2}s]

Although an estimated liquid holdup is used to define the inlet velocities of either fluid, the solution is expected to stabilize within the 'inlet' section. The actual liquid holdup will subsequently be read from the 'packed bed' region.

At the outlet boundary, a zero gauge pressure boundary condition is defined. Additionally, it is necessary to provide a backflow volume fraction for the secondary phases (gas and solid) in case there is flow reversal at the boundary during the solution process. The designated backflow volume fraction is read from neighboring cells, such that no gradients in volume fractions at the outlet boundary are present.
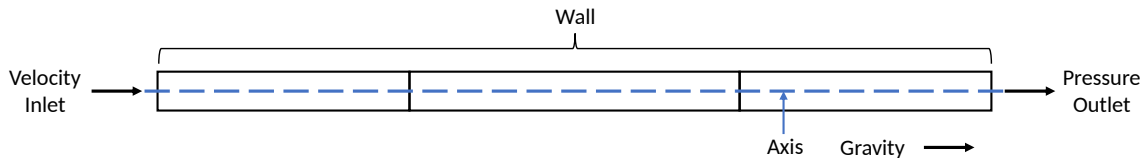
Figure 3.12: Boundary conditions applied on solution domain.

Solution methods

The simulation is performed using ANSYS Fluent 2021 R2 pressure-based CFD solver. A steady-state method is selected as relatively stable flow variables and negligible time-dependent changes are expected. For the parameters given in Table 3.2 a low-interaction flow regime is expected to develop in which no periodic or unsteady flow features should develop. For this reason, this study is only interested in obtaining a steady-state solution.

In multiphase flow, the phase momentum and continuity equations are highly interconnected, and they can either be solved sequentially or in a coupled manner. The chosen approach in this study is the Phase Coupled SIMPLE (PC-SIMPLE) algorithm, which employs a segregated approach meaning that it solves each equation separately in a sequential manner. It begins by solving for the velocity of each phase independently and subsequently introduces a pressure correction term derived from the momentum equations. Notably, this methodology is more numerically stable compared to the coupled solution approach, and its successful application has been demonstrated in previous trickle bed reactor CFD simulations [8][130].

Moreover, the method employed for calculating gradients is the least squares cell-based approach, which is less computationally expensive than other methods and maintains similar accuracy to the

Green-Gauss node-based method. For pressure interpolation, the body force weighted scheme is selected. This scheme is recommended for scenarios with high body forces, which is anticipated for the case for LOHC dehydrogenation as the released hydrogen will accelerate within the surrounding liquid due to buoyancy forces. Furthermore, for density, momentum, and energy, the second-order upwind spatial discretization schemes are selected for improved accuracy. For the volume fraction spatial discretization, however, a first-order upwind scheme is applied. Since the volume fractions of the phases are expected to vary widely from one cell to another due to the uneven porosity profile imposed throughout the domain, it may be difficult for the solution to stabilize using of a higher-order discretization scheme for this parameter. Thus, to maintain numerical stability and facilitate convergence, a first-order upwind scheme is employed for the spatial discretization of the volume fraction.

For this initial test, the default under-relaxation factors proposed by the software will be used except for volume fraction and momentum both of which are decreased. Under-relaxation factors are used to limit the amount that each variable changes from one iteration to the next. Because of the high coupling and non-linearities in the equations, it may be necessary to limit the change in each variable between iterations to help with numerical stability. The under-relaxation factors take values less than 1 meaning that they slow down the steps which variables can take. This slows down the solution's convergence speed but increases its stability. The under-relaxation factor for momentum is reduced from 0.7 to 0.3 and for volume fraction is also reduced from 0.5 to 0.1 for the same reason that a first-order spatial discretization scheme is selected for this parameter. Given the high changes in volume fraction, it can easily become unstable, so a low under-relaxation factor will help prevent overshooting values and maintaining a stable solution. The used under-relaxation factors are shown in Table 3.3.

Table 3.3: Under-relaxation factors for hydrodynamic aspect model validation.

Under-Relaxation Factor	Value
Pressure	0.3
Density	1.0
Body Forces	1.0
Momentum	0.3
Volume Fraction	0.1
Energy	1.0

As a means of monitoring the solution's progress, the mass flow rate through the 'inlet' and 'outlet' sections in Figure 3.6 are measured to assist in determining the mass flow rate imbalance across the reactor. This measurement is conducted by means of the UDF in section A.6 which calculates the mass flow rate at each cross-sectional plane based on local flow parameters and then computes the average mass flow rates across all cell planes. Figure 3.13 illustrates this calculation, where the mass flow rate of each qth fluid phase at the ith cell is determined using Equation 3.16. The mass flows of each cell within a plane are summed to obtain the mass flow rate at each jth cell plane. Due to variations in the solid volume fraction profile, the mass flow rate calculated at each plain varies slightly. To mitigate noise and obtain a more accurate value for mass flow rate within the 'inlet' and 'outlet' sections, an average is taken across all plane calculations within these sections. This procedure is done for both gas and liquid phases, and the overall mass flow rate imbalance is quantified using Equation 3.17.

By plotting this mass imbalance against the number of iterations, it becomes possible to monitor the evolution of the imbalance and determine convergence of the solution. Another way to monitor the progress of the solution is to also plot the pressure drop across the packed bed as the solution advances and observe as it stabilizes. In this specific setup, between 20000 and 25000 iterations are found to be enough for the residuals, mass imbalance, and pressure drop to stabilize. The exact iteration count required depends on the particle size and flow input parameters.

$$\dot{m}_{i,q} = \rho_{i,q}\varepsilon_{i,q}U_{\text{axial},i,q}\pi(r_{\text{upper},i}^2 - r_{\text{lower},i}^2) \tag{3.16}$$

where:

$\dot{m}_{i,q}$ = Mass flow rate of qth phase through cell i in the axial direction [kg/s]
$r_{\text{upper},i}$ = Radial distance of cell i's innermost wall from the reactor axis [m]
$r_{\text{lower},i}$ = Radial distance of cell i's outermost wall from the reactor axis [m]
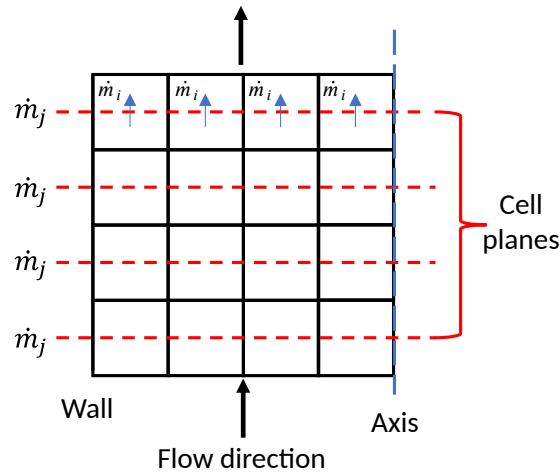
Figure 3.13: Section mass flow rate calculation

$$\dot{m}_{\text{imbalance}} = \frac{\dot{m}_{\text{G,inlet}} + \dot{m}_{\text{L,inlet}} - \dot{m}_{\text{G,outlet}} - \dot{m}_{\text{L,outlet}}}{\dot{m}_{\text{G,inlet}} + \dot{m}_{\text{L,inlet}}} \times 100\% \tag{3.17}$$

As an example, Figure 3.14a and Figure 3.14b display the mass imbalance and pressure drop monitors for a specific simulation run. These figures demonstrate that as the number of iterations grows, the monitored parameters progressively stabilize, indicating the achievement of a converged result.

(a) Mass imbalance monitor.

(b) Pressure drop monitor.
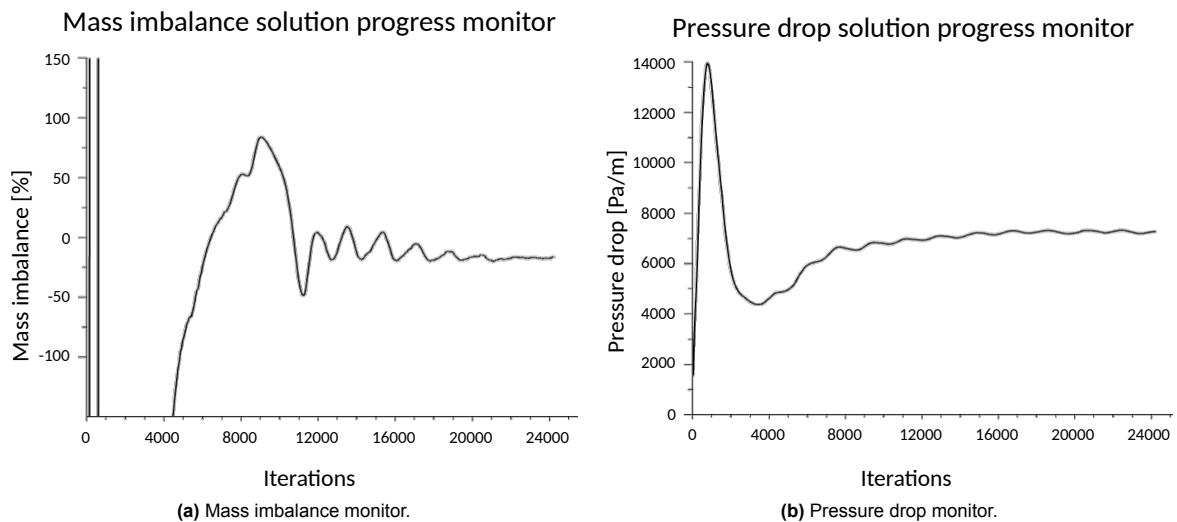
Figure 3.14: Example of mass imbalance and pressure drop monitor showing evolution of these variables over the number of iterations.

3.4.4. Hydrodynamic validation study results

The main outputs of this hydrodynamic study are the pressure drop across the reactor and the liquid holdup. Figures 3.15 and 3.16 present the results for pressure drop and liquid holdup for air-water downflow through a packed bed with 3 and 6 mm particles respectively with the parameters previously detailed in Table 3.2. The figures show the results of this work, experimental measurements by Gunjal et al. [42], predictions by Gunjal et al.'s CFD model [42], predictions by Jiang et al.'s CFD model [62], and experimental data from Szady and Sundaresan [132]; all for the same system.

(a) Pressure drop.   **(b)** Liquid holdup
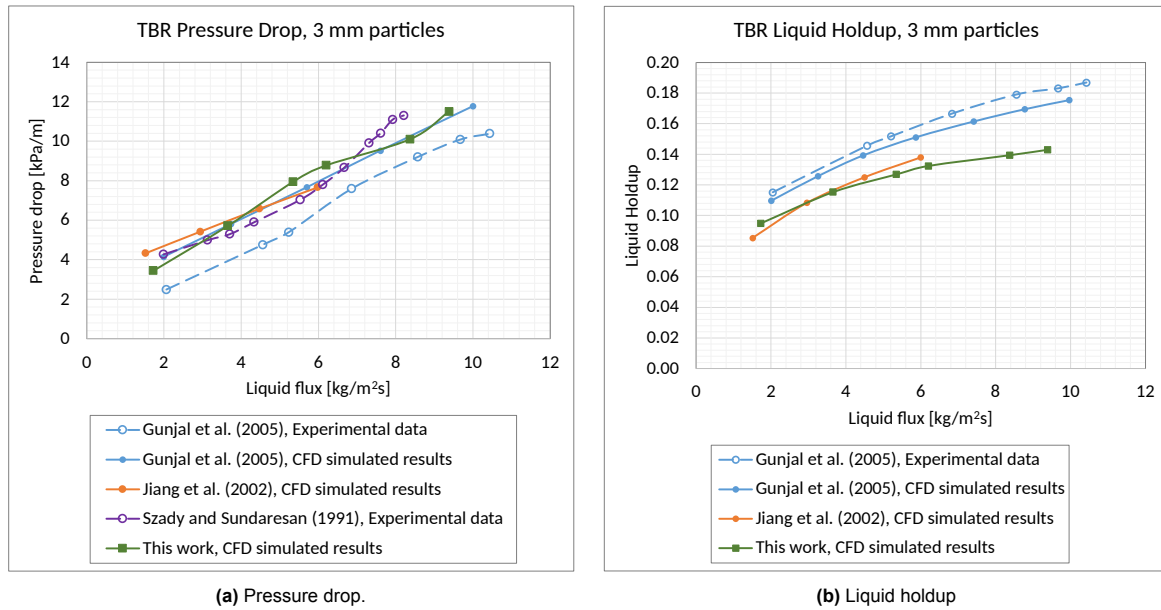
Figure 3.15: Comparison of CFD results with experimental data and other authors' CFD models for TBR with $d_\mathrm{p} = 3$mm.

(a) Pressure drop.   **(b)** Liquid holdup
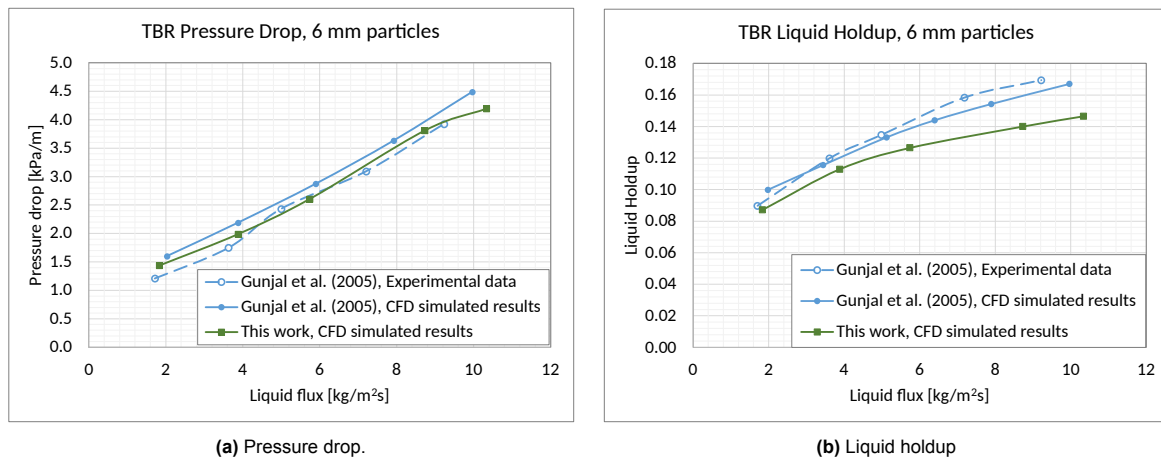
Figure 3.16: Comparison of CFD results with experimental data and other authors' CFD models for TBR with $d_\mathrm{p} = 6$mm.

From the figures above, it is possible to observe that the results from this work's CFD simulation are close to the experimental results and follow the same trend.

3.4.5. Cocurrent upwards configuration

The LOHC dehydrogenation reaction may benefit from a cocurrent upward configuration over a cocurrent downward configuration as catalyst wetting efficiency is expected to be higher. To assess the CFD model in the upwards configuration, the same setup will be used but with the gravity vector defined in the opposite direction. The same parameters as shown in Table 3.2 and solution methods will be used.

In this upwards configuration, no experimental data was found in literature with reactors of characteristics similar to those in Table 3.2. Instead, empirical correlations developed for pressure drop and liquid holdups in FBRs will be used for validation. Larachi et al. [75] propose a correlation for pressure drop across FBRs, based on a broad experimental database covering columns of 23 to 225 mm diameter and particle diameters of 1 to 6 mm. Their correlation in Equation 3.18a yields a friction factor f_LG to calculate the frictional pressure drop across the reactor using Equation 3.18b.

$$f_{LG} = \frac{1}{\chi^{1.5}(Re_L We_L)^{0.375}} \left(45.6 + \frac{15.9}{\chi^{0.5}(Re_L We_L)^{0.125}} \right) \tag{3.18a}$$

$$\left(\frac{\Delta P}{L} \right)_{\text{Frictional}} = \frac{2 f_{LG} \rho_G V_G^2}{d_H} \tag{3.18b}$$

$$d_H = d_P \left(\frac{16 \epsilon_B^3}{9\pi (1 - \epsilon_B)^2} \right)^{1/3} \tag{3.18c}$$

$$\chi = \frac{V_G}{V_L} \left(\frac{\rho_G}{\rho_L} \right)^{0.5} \tag{3.18d}$$

$$Re_L = \frac{V_L d_p \rho_L}{\mu_L} \tag{3.18e}$$

$$We_L = \frac{V_L^2 d_p \rho_L}{\sigma} \tag{3.18f}$$

where:

f_{LG} = Two-phase friction factor [-]
χ = Inertial Lokhart-Martinelli factor [-]
Re = Reynolds number [-]
We = Webber number [-]
d_H = Hydraulic diameter [m]

The CFD simulations however, result in values of total pressure drop which includes the frictional pressure drop, the liquid head, and gas head. Molga and Westerterp [103] propose that for multiphase flows through packed beds, the liquid and gas heads can be calculated as the product of the fluids' density, gravity, and saturation. The total pressure drop per unit length is then given by Equation 3.19.

$$\left(\frac{\Delta P}{L} \right)_{\text{Total}} = \left(\frac{\Delta P}{L} \right)_{\text{Frictional}} + \rho_L \beta_L g + \rho_G \alpha_G g \tag{3.19}$$

where:

β_L = $\varepsilon_L / \epsilon_B$ = Liquid saturation [-]
α_G = $\varepsilon_G / \epsilon_B$ = Gas saturation [-]

For predicting the liquid saturation, β_L, in cocurrent upward packed-bed reactors, Lara Márquez et al. [68] propose Equation 3.20. From the liquid saturation, the liquid holdup, ε_L, can be calculated as $\varepsilon_L = \beta_L \epsilon_B$.

$$\log_{10} \left(\frac{1}{1 - \beta_L} \right) = \frac{0.93 We_L^{0.08}}{Re_L^{0.20} \chi^{0.15}} \tag{3.20}$$

In addition to these empirical correlations, artificial neural network correlations have also been proposed. Larachi et al. [73] propose an ANN correlation to estimate the pressure drop in FBR and Bensetiti et al. [17] propose one to estimate the liquid saturation.

During the upflow simulations, a ripple effect became apparent within the domain, and the pressure drop values exhibited no variations in response to changes in the inlet mass flows. For example, Figure 3.17a shows the liquid velocity contour plot for an upflow simulation and the ripple behavior can be seen throughout the domain. This is a nonphysical effect caused by numerical instabilities, and it was found that by reducing the volume fraction under-relaxation factor from its default value of 0.5 to 0.1, the effect was eliminated. Furthermore, as the inlet liquid flow rate decreased among simulations, it was observed that the solution became unstable with more ease and as such other under-relaxation factors were slightly reduced to end up with those in Table 3.3. The higher propensity for numerical instabilities in the upflow configuration and at lower flow rates can be attributed to the increasing importance of buoyancy forces and relative effect of gravity. After adjusting the under-relaxation factors, the instabilities were minimized as shown in Figure 3.17b where the ripples are eliminated and the pattern observed mimics the varying porosity profile.

(a) Liquid velocity contours for upflow simulation at L = 6 kg/m^{2}s with volume fraction under-relaxation factor = 0.5.

(b) Liquid velocity contours for upflow simulation at L = 6 kg/m^{2}s with volume fraction under-relaxation factor = 0.1.
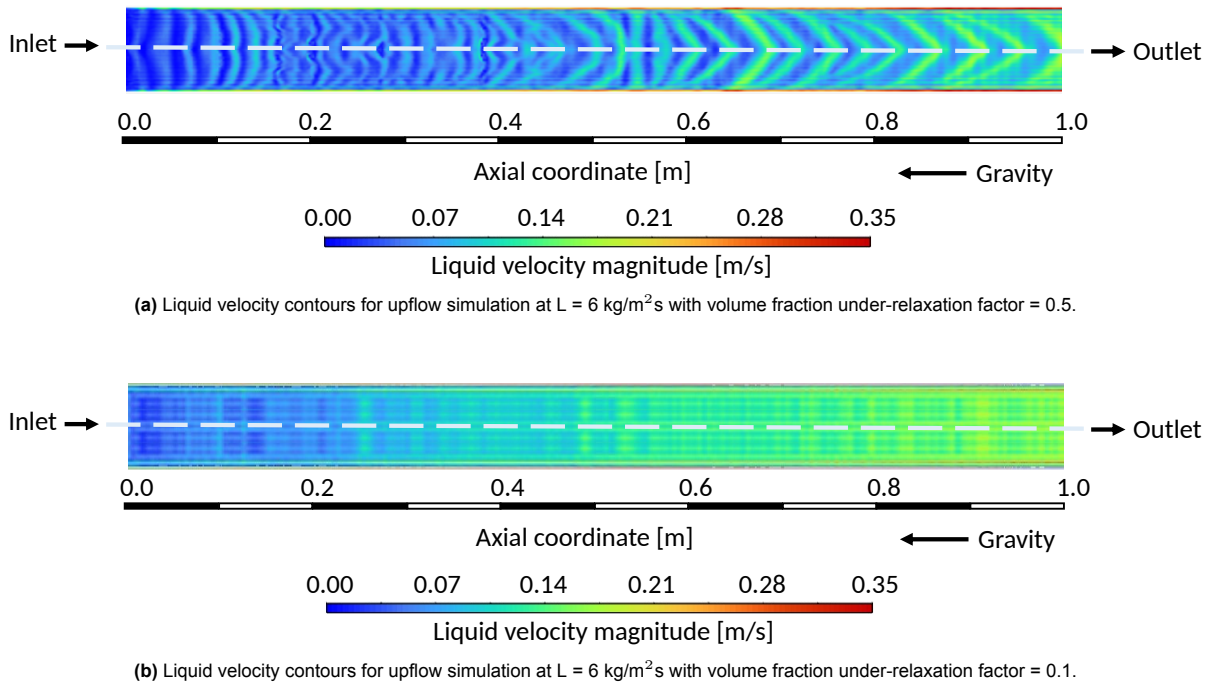
Figure 3.18 shows the results for the cocurrent upwards flow simulations with 6 mm particle diameter. As for cocurrent downflow, the resulting values for pressure drop and liquid holdup are close to those predicted by the other correlations described.

(a) Pressure drop.

(b) Liquid holdup
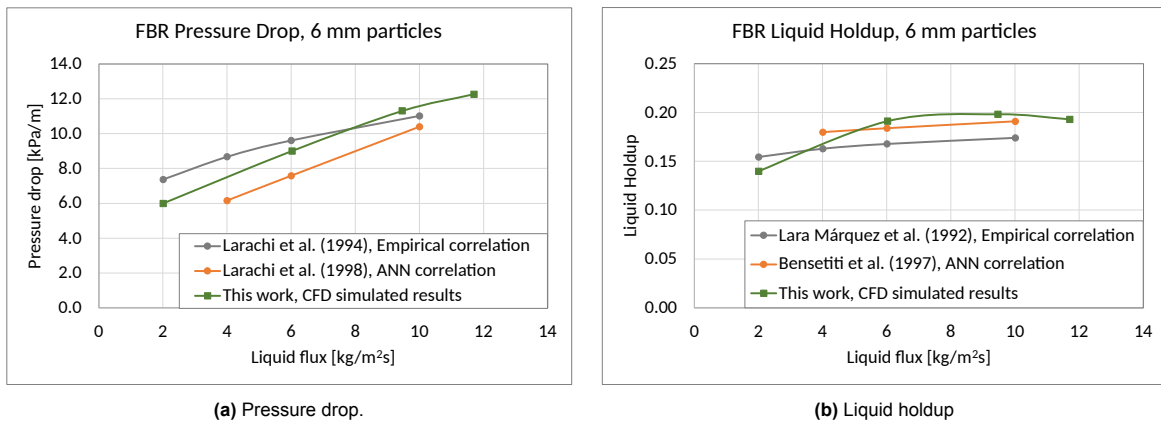
Figure 3.18: Comparison of CFD results with experimental data and other authors' CFD models for FBR with $d_p = 6$mm.

CFD model development: Material properties and chemical kinetics

Before discussing heat and species transport in the reactor, it is important to determine the material properties and chemical kinetics of the LOHC dehydrogenation reactor under study. This work will simulate the dehydrogenation of 12H-NEC as the NEC LOHC system is expected to have similar properties to the LOHC developed by Voyex. As represented by Figure 4.1, this chapter will discuss the material properties of the H_2 gas, the liquid NEC individual species and mixture, and solid catalyst particles. Afterwards, chemical kinetic models for 12H-NEC dehydrogenation will be discussed and one selected for implementation in the CFD simulation.

CFD model development: Material properties and chemical kinetics
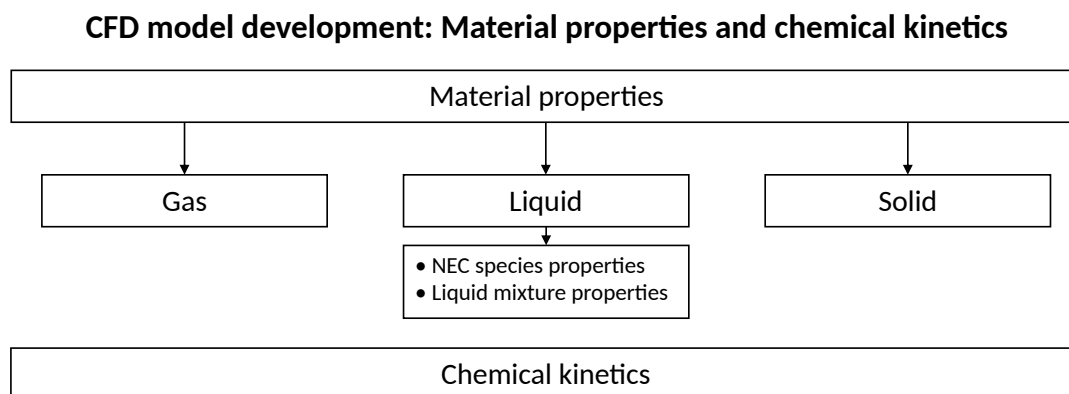
Figure 4.1: Overview of chapter 4.

4.1. Material properties

Since an appropriate definition of material properties is key for a successful numerical simulation, this section will discuss the relevant material properties that need to be defined as well as the values and models that will be used to define them.

4.1.1. Gas

An assumption that will be made in this model is that the gas phase is comprised solely of hydrogen gas. Liquid LOHC is input into the reactor and as the reaction takes place, hydrogen is formed. At the operating temperatures of the reactor, the LOHC is expected to remain in liquid form as the heat input to the reactor is not expected to be enough to boil the LOHC. In addition to the gaseous hydrogen produced from the dehydrogenation reaction, there may, however, be trace amounts of LOHC that evaporate into the gas phase. Heublein et al. [48] developed a model to predict NEC dehydrogenation in a packed bed reactor at equilibrium conditions. In other words, they calculate the amount of NEC dehydrogenation at certain temperature and pressure if the reactor were to reach thermodynamic equilibrium. For their equilibrium calculations, they do consider that each intermediate species of NEC (12H-NEC, 8H-NEC, 4H-NEC, and 0H-NEC) is in vapor-liquid equilibrium (VLE) and calculate phase equilibrium for each species using Raoult's law. Given the dynamic nature of the process, it is unlikely that vapor-liquid equilibrium will be reached so calculating the LOHC in the gas phase through VLE calculations could

overestimate the amount of LOHC in the gas phase. Furthermore, the amount of LOHC in the gas phase would remain very small compared to that of hydrogen and as such it will be neglected.

Considering the gas to be 100% H_2, the properties of the gas are thus equal to the properties of H_2. The density of H_2 can be described by an equation of state. Leachman et al. [77] developed fundamental equations of state for parahydrogen, normal hydrogen, and orthohydrogen explicit in Helmholtz free energy. In their equation of state, the Helmholtz free energy is composed of an ideal gas contribution and a residual contribution estimated from experimental data. Their elaborate equation of state can be particularly valuable for predicting thermophysical properties near the critical region and in liquid states where other conventional equation of state formulations may result in significant errors. The operating conditions of the dehydrogenation reactor, however, are far from hydrogen's critical or liquid regions, so the use of a simpler equation of state is sufficient. Therefore, the Peng-Robinson [113] cubic equation of state will be employed. This equation requires knowledge of the fluid's critical properties and acentric factor shown in Table 4.1.

Table 4.1: Critical point properties [77] and acentric factor [78] of normal hydrogen.

T_c [K]	P_c [MPa]	ρ_c [mol/dm^3]	Acentric Factor [-]
33.145	1.2964	15.508	-0.219

Other hydrogen properties that will be needed for this model include the specific heat capacity, thermal conductivity, and dynamic viscosity. Elaborate correlations have also been developed for these properties to accurately predict them over a wide range of conditions. Such is the case of the correlation for viscosity for normal hydrogen by Munzy et al. [107] which considers different contributions for viscosity to develop a 13-coefficient correlation. Similarly, Assael et al. [6] develop a correlation for the thermal conductivity of hydrogen considering three contributions. While these correlations may be highly accurate, they are also complex to implement and would not necessarily increase the accuracy of the CFD model under development. Instead, piecewise polynomial functions by Andrews and Biblarz [3] will be used as they are simple to implement and still provide accurate values for each property as a function of temperature.

Specific heat capacity c_p [J/(kg·K)] [3]:

<div align="center">100-365 K</div>

$$c_p = 6436.5105 + 63.161307T - 0.1685728T^2 + 1.5229265 \times 10^{-4}T^3 \tag{4.1a}$$

<div align="center">365-475 K</div>

$$c_p = 29616.405 - 51.4939245T + 0.304123881T^2 - 4.2495904 \times 10^{-3}T^3 +$$
$$1.9472701 \times 10^{-5}T^4 - 3.55632306 \times 10^{-8}T^5 + 2.30568584 \times 10^{-11}T^6 \tag{4.1b}$$

<div align="center">475-1255 K</div>

$$c_p = 15009.352 - 2.2923455T + 2.8969303 \times 10^{-3}T^2 - 5.937169 \times 10^{-7}T^3 \tag{4.1c}$$

Thermal conductivity k [W/(m·K)] [3]:

<div align="center">100-500 K</div>

$$k = 2.009705 \times 10^{-2} + 3.234622 \times 10^{-4}T + 2.1637249 \times 10^{-6}T^2 - 6.49151204 \times 10^{-9}T^3 +$$
$$5.52407932 \times 10^{-12}T^4 \tag{4.2a}$$

500-1500 K

$$k = 0.1083105 + 2.21163789 \times 10^{-4}T + 2.26380948 \times 10^{-7}T^2 - 1.74258636 \times 10^{-10}T^3 +$$
$$4.6468625 \times 10^{-14}T^4 \quad \text{(4.2b)}$$

1500-2000 K

$$k = -0.28107269 + 1.09703479 \times 10^{-3}T - 5.27318283 \times 10^{-7}T^2 + 1.2403865 \times 10^{-10}T^3 \quad \text{(4.2c)}$$

Dynamic viscosity μ [N·s/m^2] [3]:

10-500 K

$$\mu = -0.135666 \times 10^{-6} + 6.84115878 \times 10^{-8}T - 3.928747 \times 10^{-10}T^2 + 1.8996 \times 10^{-12}T^3 -$$
$$5.23104 \times 10^{-15}T^4 + 7.4490972 \times 10^{-18}T^5 - 4.250937 \times 10^{-21}T^6 \quad \text{(4.3a)}$$

500-2000 K

$$\mu = 2.72941 \times 10^{-6} + 2.3224377 \times 10^{-8}T - 7.6287854 \times 10^{-12}T^2 + 2.92585 \times 10^{-15}T^3 -$$
$$5.2889938 \times 10^{-19}T^4 \quad \text{(4.3b)}$$

The gas properties are defined in the CFD model using the software's built in user interface with the exception of the thermal conductivity which is calculated through an external UDF shown for reference in section A.7.

4.1.2. Liquid

The fully hydrogenated form of NEC is perhydro-N-ethylcarbazole (12H-NEC) and the dehydrogenation of 12H-NEC includes two intermediate species, 8H-NEC and 4H-NEC, before reaching its fully dehydrogenated form, 0H-NEC. Therefore, the liquid phase in the reactor consists of a liquid mixture of these four species and the composition of the liquid phase will change as the reaction progresses. Furthermore, the CFD simulation will assume that no hydrogen is dissolved in the liquid and no other byproducts or impurities are present. As such, the material properties of the four NEC species and of the overall liquid mixture need to be defined.

General properties

General properties of the four carbazole species include their molecular weight, melting point and boiling point at atmospheric pressure are given in Table 4.2. These will be needed further on for calculating other material properties.

Table 4.2: General properties of NEC species.

Chemical Formula	Abbreviation	Molecular weight [g/mol]	Melting Point [K][129]	Boiling Point [K]
$C_{14}H_{13}N$	0H-NEC	195.2597	342.4	621
$C_{14}H_{17}N$	4H-NEC	199.2915	282.4	624
$C_{14}H_{21}N$	8H-NEC	203.3232	316.0	
$C_{14}H_{25}N$	12H-NEC	207.3550	188.0	553

Density

The density of the NEC species was characterized by Stark et al. [128] and found to decrease upon hydrogenation of the NEC molecule such that the density of 0H-NEC > 4H-NEC > 8H-NEC > 12H-NEC. The temperature dependency of density, ρ, is described with the following linear approach:

$$\rho = A + BT \tag{4.4}$$

where A and B are parameters given in Table 4.3 and T is the fluid temperature in Kelvin.

Table 4.3: Parameters for calculating the density, ρ [kg/m^3], of NEC species at different temperatures using Equation 4.4 [128].

	0H-NEC	4H-NEC	8H-NEC	12H-NEC
A	1313.467	1255.3362	1210.127	1148.2329
B	−0.7238	−0.6966	−0.6907	−0.7092

Specific heat capacity

The specific heat capacities of 0H-NEC and 12H-NEC were measured by Stark et al. [128] and found to increase upon hydrogenation. They propose a linear relation of the following form:

$$c_{\mathrm{p}} = A + BT \tag{4.5}$$

Following the approach used by Heublein et al. [48], the specific heat capacity parameters for 4H-NEC and 8H-NEC can be interpolated between those reported by Stark et al. [128] for 0H-NEC and 12H-NEC. The resulting parameters for use with Equation 4.5 are shown in Table 4.4 below.

Table 4.4: Parameters for calculating the specific heat capacity, c_{p} [J/(kg·K)], of the NEC species at different temperatures using Equation 4.5 [128].

	0H-NEC	4H-NEC	8H-NEC	12H-NEC
A	1037.490071	1096.333762	1007.361678	613.24781
B	1.703372483	2.374411352	3.018347144	3.6377227

Dynamic viscosity

The dynamic viscosity of the four NEC species was measured by Stark et al. [128] between 283.15 K and 408.15 K and observed to increase upon hydrogenation. The viscosity can be described by Equation 4.6 with the corresponding parameters given in Table 4.5.

$$\ln(\mu) = A + \frac{B}{T} + C\ln(T) + DT^2 \tag{4.6}$$

Table 4.5: Parameters for calculating the dynamic viscosity, μ [mPa·s)], of the NEC species at different temperatures using Equation 4.6 [128].

	0H-NEC	4H-NEC T < 323.15K	4H-NEC T > 323.15 K	8H-NEC	12H-NEC
A	−198.5107397	54.77739118	−8.474341421	−51.67196212	−121.3831627
B	14092.471	14646.3196	5607.607	5951.08459	8035.86187
C	27.4111475	−21.0444126	−1.46520555	6.23125641	16.8924989
D	6.94×10^{-13}	2.35×10^{-4}	2.42×10^{-5}	-6.10×10^{-8}	-3.65×10^{-9}

Using the parameters above yields a value for dynamic viscosity in mPa·s which should then be converted to Pa·s. It is important to note that these parameters were obtained from measurements up to 408.15 K. However, NEC dehydrogenation can be conducted at temperatures up to 550 K after which byproduct formation can become significant. The CFD simulations will thus also be conducted at temperatures of up to 550 K. Plotting the above correlations for viscosity in Figure 4.2, shows that

the viscosity has a steep decrease from ambient temperature up to about 400 K after which the values for viscosity remain approximately constant until the each of the NEC species' boiling temperatures. Therefore, it remains appropriate to extrapolate these equations up to 550 K for the CFD simulations.
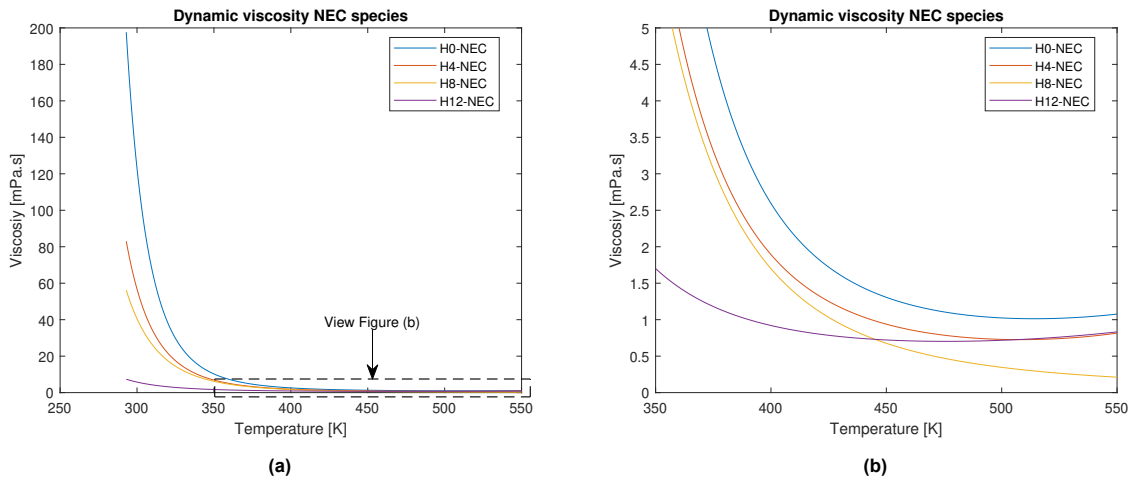
Figure 4.2: Dynamic viscosity of NEC species.

Surface tension

The surface tension of the liquid will come into play when calculating the capillary forces within the reactor. Surface tension of 4H-NEC, 8H-NEC, and 12H-NEC was measured by Stark et al. [128] between 293.23 K and 353.75 K and found that with increasing degree of hydrogenation the surface tension of the carbazole decreases. Furthermore, the temperature dependency of surface tension, σ, can be described by a linear equation of the form:

$$\sigma = A + BT \tag{4.7}$$

Table 4.6: Parameters for calculating the surface tension, σ [N/m], of the NEC species at different temperatures using Equation 4.7 [128].

	4H-NEC	8H-NEC	12H-NEC
A	0.071176	0.0631091	0.0593586
B	-0.0000996	-0.000085	-0.0000881

As no measurements for 0H-NEC surface tension were found, the surface tension of 4H-NEC will be assumed. Moreover, as the 4H-NEC to 0H-NEC reaction is the slowest among the three dehydrogenation steps, a small amount of 0H-NEC is expected to be formed in the reactor. By using the values of surface tension of 4H-NEC for 0H-NEC as well, no large source of error is expected. Similar to the previous properties, the parameters given in Table 4.6 were obtained from measurements only up to 353 K whereas the CFD simulations will be at higher temperatures up to 550 K. Plotting the values of surface tension from the above parameters in Figure 4.3 shows that surface tension drops to values of around 0.01 N/m around boiling point of the species. Given that these are still reasonable values, and in general surface tension tends to follow a linear relation even past the boiling point of many organic liquids, the parameters presented above will be used.
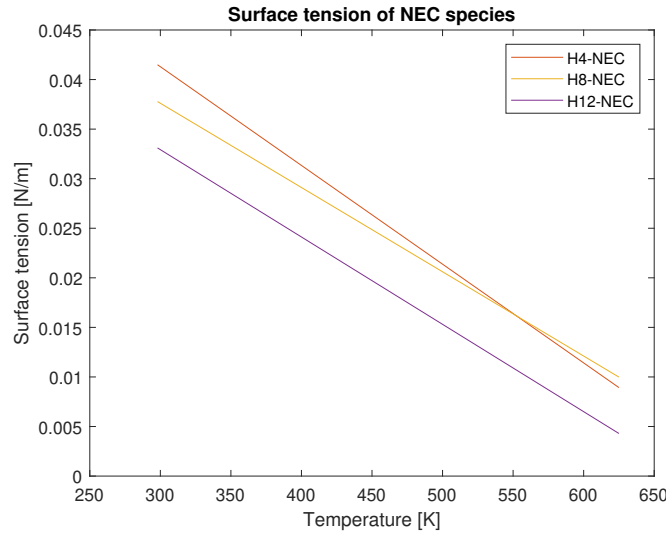
Figure 4.3: Surface tension of NEC species.

Thermal conductivity

No experimental data was found on the thermal conductivity of the NEC species. However, Berger Bioucas et al. [19] studied the thermal conductivity of the DBT system and developed a model to estimate the thermal conductivity of LOHCs. They developed their model from measurements of DBT thermal conductivity as well as from data of other cyclic hydrocarbons such as diphenylmethane, and benzyltoluene which can also be hydrogenated for their use as LOHCs. Their model shown in Equation 4.8 predicts the thermal conductivities, λ, of these LOHCs and was also shown to predict the thermal conductivities of other similar substances like benzene, toluene, xylene, cyclohexane and methylcyclohexane.

$$\lambda = \left(A\rho_{T_{\text{ref}}} + B\frac{\rho_{T_{\text{ref}}}^2}{M} \right) \left(\frac{\rho_T}{\rho_{T_{\text{ref}}}} \right)^{C \cdot \rho_T} \tag{4.8}$$

where:

A $= 0.1083$ W·cm^3/(K·m·g)
B $= 4.823$ W·cm^6/(K·m·mol·g)
C $= 2.2$ or 2.0 cm^3/g for dehydrogenated or hydrogenated substances
M $=$ Molecular weight [g/mol]
T_{ref} $= 303.15$ K, Reference temperature
$\rho_{T_{\text{ref}}}$ $=$ Density calculated at reference temperature [g/cm^3]
ρ_T $=$ Density calculated at temperature of interest [g/cm^3]

Given the flexibility of this model, it will be applied in the current simulation to predict the thermal conductivities of the four NEC species. The value of parameter C depends on the degree of hydrogenation of the molecule of interest. For the case of NEC, C will be taken as 2.2 for 0H-NEC, 2.0 for 12H-NEC and interpolated to 2.13 and 2.07 cm^3/g for 4H-NEC and 8H-NEC, respectively. The values of thermal conductivity predicted by this model for the NEC species are shown in Figure 4.4. This figure additionally shows the thermal conductivity reported for 2,6-diisopropyl-N,N-dimethylaniline (C$_{14}$H$_{23}$N) [145] which has a composition and molecular weight close to that of the NEC species. It can be observed that the thermal conductivity given for C$_{14}$H$_{23}$N is in the range of thermal conductivities predicted for the NEC species.
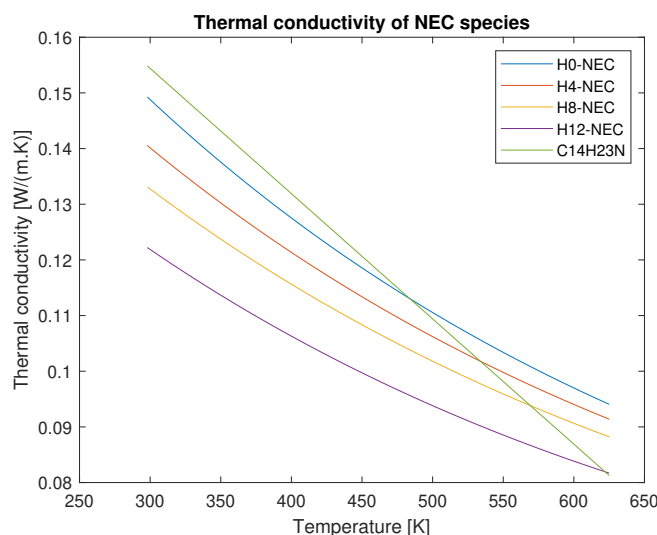
Figure 4.4: Thermal conductivity of NEC species.

Liquid mixture properties

Having defined the properties of each of the four individual NEC species, it is now important to consider what the overall liquid phase properties will be. The liquid phase in the reactor will be a mixture of these four species and the composition of the liquid phase will change throughout the reactor. Therefore, the overall liquid properties will depend on temperature as given by the previous correlations and on composition.

When multiple liquid species are combined, interactions between each pair of compounds come into play. In a thermodynamically ideal case, the interaction of substances upon mixing will not cause energy to be liberated or absorbed such that the enthalpy of mixing is zero. In this case the mixture is considered to be ideal, which also means that other thermodynamic excess properties such as volume are also zero. On the other hand, the deviation from ideal behavior of real mixtures can be quantified by parameters such as activity coefficients.

Stark et al. [129] studied the binary mixture of 0H-NEC and 12H-NEC by measuring the melting point of the mixture with different compositions to plot the liquidus line in a binary phase diagram. From this information, the authors were able to obtain activity coefficients and fit them to the non-random two-liquid (NRTL) activity coefficient model. This frequently used model correlates the activity coefficients to the mole fractions of each component in the liquid phase. For binary mixtures, the NRTL model takes the following form:

$$\ln(\gamma_1) = x_2^2 \left[\tau_{21} \left(\frac{G_{21}}{x_1 + x_2 G_{21}} \right)^2 + \frac{G_{12}\tau_{12}}{(x_2 + x_1 G_{12})^2} \right] \tag{4.9a}$$

$$\ln(\gamma_2) = x_1^2 \left[\tau_{12} \left(\frac{G_{12}}{x_2 + x_1 G_{12}} \right)^2 + \frac{G_{21}\tau_{21}}{(x_1 + x_2 G_{21})^2} \right] \tag{4.9b}$$

$$G_{ij} = \exp(-\alpha \tau_{ij}) \tag{4.9c}$$

$$\tau_{ij} = a_{ij} + \frac{b_{ij}}{T} \tag{4.9d}$$

$$\alpha = c + d(T - 273.15 \text{ K}) \tag{4.9e}$$

$$\tag{4.9f}$$

For the 0H-NEC and 12H-NEC binary mixture, Stark et al. [129] propose the NRTL model parameters shown in Table 4.7. The resultant activity coefficients for this binary mixture are shown in Figure 4.5 as a function of mole fraction. Given that 0H-NEC and 12H-NEC are molecules with very similar structures and molecular weights with the difference being the saturated and unsaturated carbon rings, it

may be expected that the activity coefficients be close to one suggesting an ideal mixture. However, from Figure 4.5 it can be observed that activity coefficients greater than one up to around three are expected indicating positive deviations from an ideal mixture.

Table 4.7: NRTL parameters for a 0H-NEC and 12H-NEC binary mixture at atmospheric pressure [129].

NRTL Parameter	i = 0H-NEC, j = 12H-NEC
a_{ij}	0
a_{ji}	0
b_{ij}	-3274.28415
b_{ji}	4100.5343
c	9.87×10^{-3}
d	0
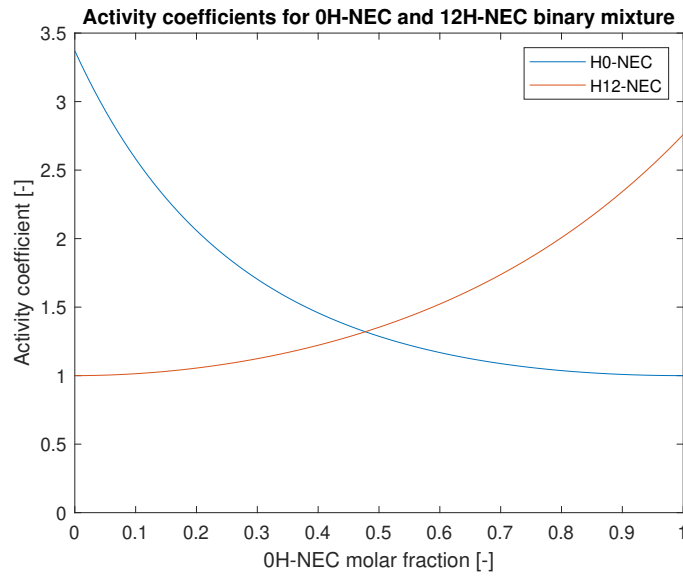
Figure 4.5: Activity coefficients for a 0H-NEC and 12H-NEC binary mixture.

These activity coefficients represent the mixture's deviation from ideal behavior and can be used to more accurately calculate the mixture's thermophysical properties. In the NEC dehydrogenation reactor under study, however, there are four species so an activity coefficient between each pair of species would be needed. The NRTL model shown in Equation 4.9 can be extended for more than two species, it becomes complex, requiring numerous parameters for each species pair. Despite a certain level of non-ideality being shown by these values of activity coefficients, having only the activity coefficients for the 0H-NEC and 12H-NEC pair makes it difficult to consider the non-ideal behavior of the liquid mixture involving four species. Thus, in this CFD model, the liquid phase will be treated as an ideal mixture of the four NEC species.

Density
As shown by the species transport equation, the mass fractions of each species are tracked by the CFD simulation and these can then be used to calculate the mixture properties. The density of each individual species, ρ_i, is calculated from Equation 4.4 and the mixture density is a function of each species' mass fraction and density. Considering an ideal mixture, the volume change on mixing is equal to zero meaning that the liquid mixture density is a volume-weighted density that is calculated as:

$$\rho = \frac{1}{\sum_i \frac{y_i}{\rho_i}} \tag{4.10}$$

Specific heat capacity

The specific heat capacity of a liquid mixture is recommended to be computed through an arithmetic mole or mass fraction average [134]. As Teja explains [134], this method neglects any contribution to the temperature change from mixing the enthalpy of mixing, but considering an ideal mixture where the enthalpy of mixing is zero, the liquid mixture specific heat capacity will be calculated from a mass-weighted average as follows:

$$c_{\mathsf{p}} = \sum_i y_i c_{\mathsf{p},i} \tag{4.11}$$

Dynamic viscosity

Liquid mixture viscosity should not be calculated directly from a volume or mass weighted average as density or specific heat capacity. As Grunberg and Nissan explain [41], Arrhenius instead proposed Equation 4.12 based on mole fractions, x_i.

$$\ln(\mu) = \sum_i x_i \ln(\mu_i) \tag{4.12}$$

Grunberg and Nissan [41] built on this equation to include interaction parameters for either positive or negative deviations from ideal behavior. Other viscosity blending equations have been developed particularly in the petroleum industry such as the Refutas equation [89] which calculates what is known as the viscosity blending index for each component. For this simulation however, as an ideal mixture is considered, Equation 4.12 will be used. The liquid mixture viscosity is implemented in the CFD simulation by an external UDF found for reference in section A.9. This UDF, reads the mass fraction and viscosity of each species in each cell, and then converts the mass fractions to mole fractions to evaluate Equation 4.12.

Surface tension

The surface tension of a liquid mixture is not a simple function of the surface tension of the individual components. As Escobedo and Mansoori explain [36], when liquid species mix, a region of distinct composition develops at the vapor-liquid interface compared to the composition in the bulk of the liquid. The species with the lowest surface tension tends to migrate towards the surface of the liquid creating a surface layer rich in this component. As the species with the lowest surface tension enriches the surface region, non-linearities in the liquid surface tension can develop. Tjahjono and Garland [135] explain that this difference in composition between the bulk liquid region and surface region could even have repercussions in heat and mass transfer properties of the liquid mixture. Escobedo and Mansoori [36] and Tjahjono and Garland [135] both provide models to predict the liquid mixture's surface tension which includes calculating surface and bulk properties, and interaction parameters. For the Eulerian multiphase CFD model being developed, no fluid interfaces are explicitly modeled meaning it is not possible to track the possible enrichment of liquid surface with molecules of lower surface tension.

In their study, Tjahjono and Garland [135] identify mixtures with distinct behaviors including organic-organic mixtures with slight negative deviation or close to ideal behavior. While most organic-organic mixtures present negative deviations, some systems are close to ideal in which case the surface tension can be calculated from a mole fraction weighted average. In the case of NEC, the fully hydrogenated molecule 12H-NEC has a 20% lower surface tension than the fully dehydrogenated 0H-NEC molecule at 298 K [128] so some migration of this species to the surface region could occur. However, assuming an ideal liquid mixture for this model, no composition changes due to surface enrichment will be considered and the mixture's surface tension will be calculated as:

$$\sigma = \sum_i x_i \sigma_i \tag{4.13}$$

In the CFD simulation, the surface tension is used to calculate the capillary forces at each cell and is calculated by a UDF found in section A.10. This UDF calculates the surface tension of each species per Equation 4.7, and then calculates the liquid mixture surface tension from Equation 4.13.

Thermal conductivity
Numerous methods have been proposed to estimate the thermal conductivity of liquid mixtures, with most of them involving the component's mass fractions, individual conductivities, interaction parameters and other empirical parameters. Maloka [88] discusses a series of empirical mixture thermal conductivity models that have been proposed in the past and provides his own model based on a large database of experimental data. Most of these empirical equations are limited to binary mixtures so cannot be applied to the four species NEC mixture. Matsuda et al. [93] look into four different formulations for ideal mixture thermal conductivity including mass weighted average, mole weighted average, and two logarithmic average formulations. After assessing these formulations with experimental data, the following equation gave the best predicted results:

$$\ln(\lambda M) = \sum_i x_i \ln(\lambda_i M_i) \tag{4.14}$$

In Equation 4.14 M represents the liquid's mean molecular weight and M_i the molecular weight of species i. The mixture thermal conductivity of the liquid phase is calculated in the CFD model through a UDF provided in section A.8. This UDF first calculates the thermal conductivity of each NEC species in every cell using Equation 4.8. It then reads the mole fraction of each species and calculates the liquid mixture thermal conductivity for every cell using Equation 4.14. Thus, a profile of the liquid thermal conductivity is obtained that updates with every solution iteration.

4.1.3. Solid
The solid phase in the CFD simulation under study refers to the catalyst particles that are fixed within the packed-bed reactor. There are several catalyst particle characteristics that will each play a role in the hydrodynamics, heat transfer, and chemical kinetics of the reactor. Some of these basic characteristics include their shape, size, porosity, surface area, and material.

As previously discussed, the particles may have different shapes and can have diameters ranging from a few tenths of a millimeter to around 1 cm. As an example, Heublein et al. [48] study the 12H-NEC dehydrogenation reaction in a FBR with cylindrical pellets of 3.2 mm in diameter and 3.6 mm length. Similarly, Peters et al. [115] study the 12H-NEC dehydrogenation reaction in a small TBR with spherical 3 mm catalyst pellets. The shape and size of the pellets will be explicitly input into the CFD simulation by indicating the pellet diameter and sphericity. These will affect the hydrodynamics of the reactor since they are used to model the solid volume fraction profile and the interphase momentum exchange coefficients. From a chemical kinetics point of view, the catalyst pellet's dimensions, porosity, surface area, and material all contribute to determine the rate of the chemical reaction. In general, a higher metal loading and higher active surface area will increase the active sites on the catalyst's surface and allow for a faster reaction. In the current CFD model, the catalyst active material (e.g. Pd, Pt, Ni), surface area, and porosity are not explicit inputs but are instead considered when specifying a model for the reaction rate. The reaction rates for NEC dehydrogenation and its formulation for this CFD model will be discussed further on.

Finally, additional characteristics related to the material of the catalyst particles will come into play to define the heat transfer characteristics within the packed bed. These include the pellet's density, specific heat capacity, and thermal conductivity.

Density
The density of the catalyst particles will depend on the support material and the porosity of the pellet. Considering the support material to be alumina (Al_2O_3), the density of the pellet will be a function of the pellet density or pore volume fraction. Mischke and Smith [95] studied the thermal properties of alumina pellets by manufacturing and testing pellets of different densities. As they explain, the density of solid $\alpha - Al_2O_3$ is 2450 kg/m^3 but when pellets are formed from alumina powder, the resultant pellet density can be controlled as the pore fraction within the pellet changes. Mischke and Smith [95] prepared pellets with densities ranging from 1121 kg/m^3 to 672 kg/m^3 corresponding to total void fractions of 0.543 to 0.725, respectively. The void fraction and pellet density are both characteristics that would be given by the catalyst manufacturer, and as an example for this CFD simulation the catalyst pellet properties given by commercial catalyst product number 195082500 from Thermo Fisher Scientific [59] will be used. The product specification for this catalyst pellet is shown in Table 4.8 including the density

value of 700 kg/m^3. A constant value of 700 kg/m^3 for the solid phase density will be used for the simulation.

Table 4.8: Product specification of Thermo Fisher Scientific 0.5 wt% Pd on alumina catalyst pellets [59].

Product name	Palladium on 1/8-inch alumina pellets, 0.5% Pd, Thermo Scientific Chemicals
CAS number	1344-28-1, 7440-05-3
Specific surface area [m^2/g]	230
Total pore volume [ml/g]	0.54
Color	Grey
Form	Pellets
Loading	0.5% Pd
Density [kg/m^3]	700
Loss on drying	1%
Loss on abrasion	3%

Specific heat capacity

Considering the support material of the catalyst particles is alumina with about 0.5 to 5 wt% loading of a usually noble metal such as Pd, Pt, or Ru, the specific heat capacity of the pellet will be assumed to be equal to that of pure alumina. Chase [26] provides an equation for the specific heat capacity of alumina in the following form:

$$c_{\mathrm{p}} = A + BT + CT^2 + DT^3 + \frac{E}{T^2} \tag{4.15}$$

where parameters A through E were given to calculate specific heat capacity in J/(mol·K). These can be converted to yield the specific heat capacity in J/(kg·K) leading to the parameters in Table 4.9 below.

Table 4.9: Parameters for calculating the specific heat capacity, c_{p} [J/(kg·K)], of α-alumina as a function of temperature (T [K]) using Equation 4.15 [26].

	$\alpha - \mathbf{Al_2O_3}$
A	1004.587034
B	0.380044
C	-1.560484×10^{-4}
D	2.577626×10^{-8}
E	-2.949699×10^{7}

Thermal conductivity

Like density, the thermal conductivity of catalyst pellets is not only dependent on the thermal conductivity of the support material but also on the void fraction of the pellet. As the pellets can be highly porous, the surrounding fluid will fill these voids and contribute to the effective thermal conductivity of the pellet. Therefore, the thermal conductivity of a catalyst pellet depends on its void fraction, the thermal conductivity of the support material, and the thermal conductivity of the fluid that fills the pellet's pores. Mischke and Smith [95], studied the thermal conductivity of alumina pellets in a vacuum, air, and helium. They found that as the pellet's void fraction increases, the thermal conductivity of the pellet decreases since the thermal conductivity of the fluid is much lower than that of pure alumina. It was also found that as the surrounding medium changes from vacuum to air to helium, the thermal conductivity of the pellet increases as is expected by the increasing thermal conductivities of these mediums.

In the present CFD simulation, the catalyst pellets will be surrounded by a mixture of LOHC liquid and hydrogen gas at varying proportions and temperatures as the reaction progresses through the reactor. Although Mischke and Smith [95] demonstrate a clear trend between void fraction, surrounding fluid, and pellet thermal conductivity, no correlation between the thermal conductivity of the pellet and that of the surrounding fluid is provided. Although in the present CFD simulation the surrounding liquid and gas

volume fractions and thermal conductivities will be known, without such correlation it becomes difficult to estimate the pellet's thermal conductivity. For the accuracy of this model, it is sufficient to assume that the thermal conductivity of the alumina supported catalyst pellets will be close to that reported by Mischke and Smith [95] for alumina pellets in helium. Among the three mediums tested (vacuum, air, and helium), hydrogen has a slightly higher thermal conductivity than helium and NEC has a thermal conductivity between that of air and helium.

Using Thermo Fisher Scientific [59] 0.5 wt% Pd/Al_2O_3 pellets detailed in Table 4.8, the pellets have a pore volume of 0.54 ml/g and density of 0.7 g/ml which can be multiplied to result in a void fraction of 0.378. For a pellet with this void fraction in helium, Mischke and Smith's [95] measurements result in a pellet thermal conductivity of 0.185 W/(m·K).

Furthermore, Mischke and Smith [95] measured the thermal conductivity of the pellets in a vacuum at different temperatures and found a slight decrease in thermal conductivity with increasing temperature due to the decrease in thermal conductivity of the alumina itself. While the thermal conductivity slightly decreases with temperature, that of hydrogen increases with temperature and that of the LOHC decreases with temperature. Without any relation provided to estimate the catalyst pellet conductivity as a function of the thermal conductivity of the surrounding fluid, it is difficult to take the temperature dependence of the pellet's thermal conductivity into account. Instead, in this CFD simulation, a constant thermal conductivity value for the solid phase of 0.185 W/(m·K) will be used.

It is important to note that the thermal conductivity of the catalyst pellets will be used in calculating a no flow (pure conduction) component λ_{s0} of the effective thermal conductivity that will be further described in section 5.1.3.2. In terms of practical impact, a 10% variation in the pellet thermal conductivity would correspond to only a 1% alteration in the overall effective thermal conductivity of the packed bed under the anticipated operating conditions. Given the relative insensitivity of the effective bed thermal conductivity to changes in catalyst pellet thermal conductivity, using a constant value of 0.185 W/(m·K) is considered sufficient for the purpose of this model.

4.2. Chemical kinetics

LOHC dehydrogenation is a heterogeneous catalytic process. The process first requires molecular diffusion of hydrogenated LOHC species from the bulk of the liquid to the surface of the catalyst, adsorption of the reactant onto the catalyst surface, surface reactions, and finally product desorption from the catalyst surfaces [32]. Among these, the surface reaction is understood to be the slowest process and thus dictates the overall reaction rate. The dehydrogenation of 12H-NEC is a three-step process and may be represented by three consecutive elementary reactions shown by Equations 4.16a through 4.16c. Each of these three steps have been studied individually to provide reaction rate constants for each.

$$12H-NEC \xrightarrow{k_1} 8H-NEC + 2H_2 \tag{4.16a}$$

$$8H-NEC \xrightarrow{k_2} 4H-NEC + 2H_2 \tag{4.16b}$$

$$4H-NEC \xrightarrow{k_3} 0H-NEC + 2H_2 \tag{4.16c}$$
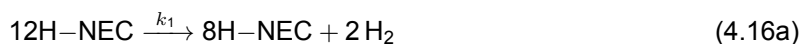
Dong et al. [32] identified the three NEC dehydrogenation step reactions to be of first order and measured the reaction rate constants and activation energy for the three steps at temperatures between 140 and 170°C using a 5 wt% Pd/Al_2O_3 catalyst with a BET surface area of 68.35 m^2/g and pore size of 11.89 nm. The values of reaction rate constants given by Dong et al. may be plotted and fitted to an Arrhenius equation in the form $k = Ae^{\frac{-E_a}{RT}}$. Likewise, Wang et al. [139] studied NEC dehydrogenation reaction rates using a 5 wt% Pd/Al_2O_3 catalyst of unspecified BET surface area or pore size. Figures 4.6a through 4.6c plot the experimental data points measured by Dong et al. [32] and Wang et al. [139] as well as the fitted Arrhenius equation using the data points of Dong et al. Furthermore, Table 4.10 shows the values for each of the three step reaction's enthalpy of reaction ΔH [128], activation energy E_a [32], and the calculated Arrhenius pre-exponential factor A.

(a) Reaction rate 1

(b) Reaction rate 2
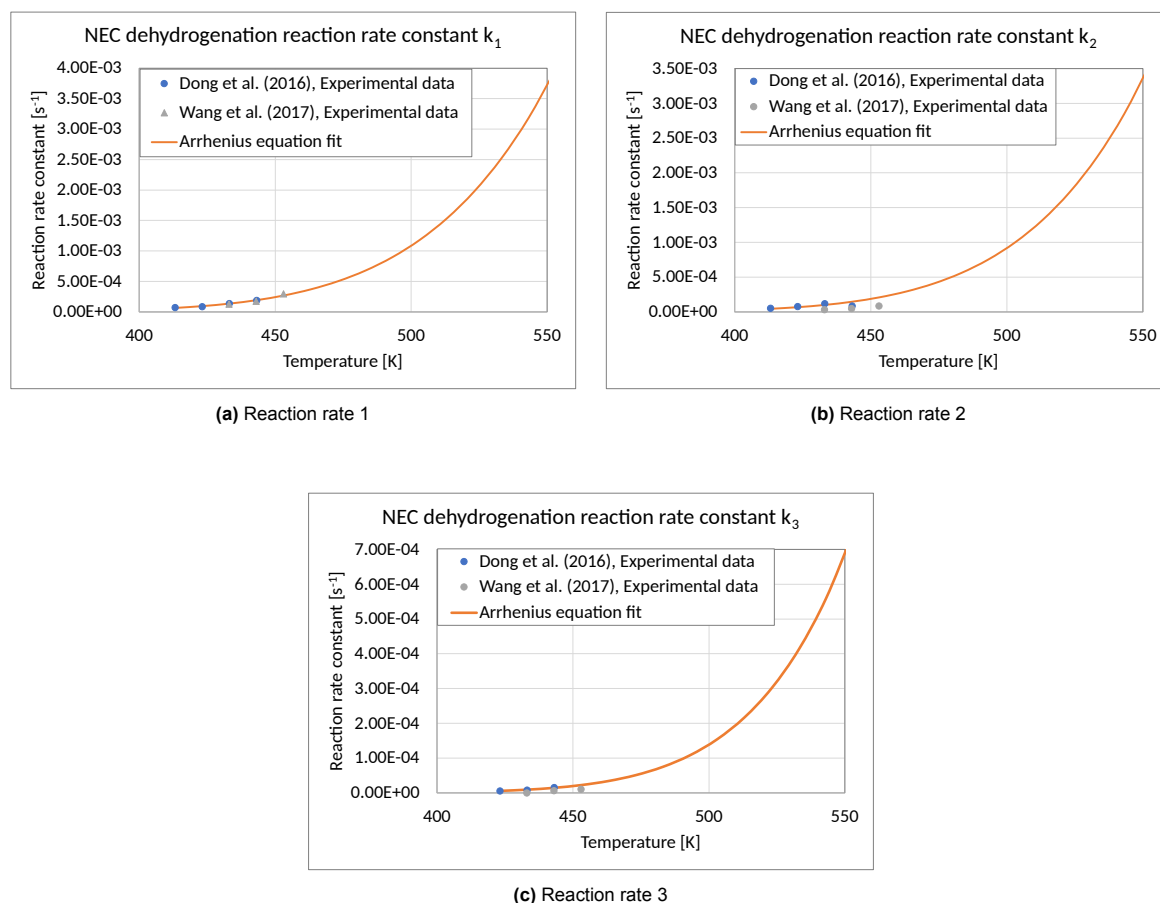
(c) Reaction rate 3

Figure 4.6: NEC dehydrogenation reaction rate constants

Table 4.10: NEC dehydrogenation kinetics.

Step reaction number	ΔH [kJ/mol]	E_a [kJ/mol]	A [s^{-1}]
1	89.3	56.3	826
2	105.2	59.2	1406
3	108.9	73.1	6007

It is important to note that the reaction rate constants provided by Dong et al. [32] and Wang et al. [139] were measured at temperatures between 413 and 453 K. However, the Arrhenius equations shown in Figures 4.6a through 4.6c are extrapolated until 550 K. In literature, authors have conducted 12H-NEC dehydrogenation tests through packed beds at temperatures between 493 and 553 K [48][115]. Additionally, Yang et al. [144] conducted a numerical study of 12H-NEC dehydrogenation in temperatures between 481 and 523 K. The experimental setup of Heublein et al. [48] will be simulated to test the current CFD model and therefore temperatures in those ranges will be used. Without any other data for the reaction rates at higher temperatures, the extrapolated values from the fitted Arrhenius equations will need to be used with caution.

It is also important to understand that the above kinetics presented by Dong et al. [32] and Wang et al. [139] are specific to the catalyst they have used with its specific metal loading, metal particle size, BET surface area, pore volume distribution, operating temperature and pressure. The catalyst activity and selectivity depend on the combined effect of these catalyst properties and operating conditions which makes it difficult to extrapolate a certain set of reaction kinetics to another set of conditions. For example, Sotoodeh et al. [126] studied the effect of Pd loading and particle size on silica supported catalyst in 12H-NEC dehydrogenation. They found that catalyst activity is structure dependent and that Pd particle size plays a significant role. The reaction rates are not a direct function of Pd loading

but depend on the number of catalytic sites for the adsorption of the hydrogenated molecules. In their research, Sotoodeh et al. [126] found that among the catalyst they evaluated, the 4 wt% Pd/SiO_2 catalyst with small Pd particle diameters of ~9 nm produced from calcination of the metal in He, resulted in the maximum NEC dehydrogenation.

From the point of view of the particle porosity and BET surface area, a higher particle porosity or BET surface area does not inherently correspond to faster reaction kinetics. The pores of a catalyst pellet have a range of sizes and can be classified by their size as macro, meso and micropores where micropores are those with a pore size of roughly 0.9 nm or less [146]. The BET surface area of a catalyst particle is determined by measuring the adsorption of N_2 gas onto the surface of all its pores. As N_2 has a small kinetic diameter of 0.36 nm, it can get into the micropores of the particles such that the reported BET surface area of particles includes the surface area of micropores as well. The kinetic diameter of LOHC molecules such as 12H-NEC, however, is more in the range of 1.0 to 1.5 nm impeding them from reaching the micropores' surface. As a result, if a catalyst particle has a high BET surface area but a high fraction corresponds to micropores, it may not necessarily be more effective in LOHC dehydrogenation than a catalyst particle with a lower BET surface area but with more meso or macropore surface area. What is important then is the number of catalytic sites that are available for the hydrogenated molecule to adsorb on which will depend on these factors.

As an example, Dong et al. [32] reported a BET surface area of 68.35 m^2/g and pore size of 11.89 nm for the catalyst used in their study. This pore size is an order of magnitude larger than the NEC molecules' diameter, making it likely that most of the surface area is effective. Given that the reaction kinetics are highly dependent on the catalyst characteristics, which are often not fully detailed in literature, it is difficult to directly compare results among studies or between different catalysts. In the current CFD model, all of these catalyst properties including metal loading, metal particle size, metal particle distribution, porosity, pore volume distribution, and BET surface area are not individually modeled but come together to define the reaction kinetics. The input to the current Eulerian multiphase CFD model under development is the chemical kinetics in form of Arrhenius equations as defined by Table 4.10. For this CFD model, the reaction kinetics reported by Dong et al. [32], specific for the catalyst characteristics they describe, will be used. Within the computational domain previously described by Figure 3.6, the reaction will only be active within the 'packed bed' cell zone . This distinction is done through a UDF found in section A.11 which takes the parameters from Table 4.10 and reads the concentration of reactants to give back the rate of reaction within the 'packed bed' section. Once Voyex has defined the catalyst to be used, it will be important to characterize the reaction kinetics and update the CFD model accordingly.

CFD model development: Heat transfer

Given that LOHC dehydrogenation is an endothermic reaction with a reaction rate sensitive to temperature, it is important that the CFD simulation accurately models the heat transfer taking place. Heat transfer within packed-bed reactors can be modeled by either heterogeneous or pseudo-homogeneous models. The heterogeneous model describes the temperature and heat transfer of each phase with its own energy conservation equation, whereas a pseudo-homogeneous model uses a single energy conservation equation for both fluid phases and one for the solid phase, or a single equation for all three phases. While the most realistic model would be describing the energy of each phase individually and considering interphase heat transfer resistances, the aim here is to select the simplest model that maintains accurate.

This chapter will follow the structure represented by Figure 5.1. First, the three heat transfer resistance criteria by Mears [94] will be explored for the current LOHC reactor along with the heat transfer parameters needed to evaluate them. Having analyzed the three criteria, an adequate heat transfer model will be selected, and its functionality will be discussed. The heat transfer model will then be incorporated into the CFD model and validated against the analytical solution of the selected model.

CFD model development: Heat transfer
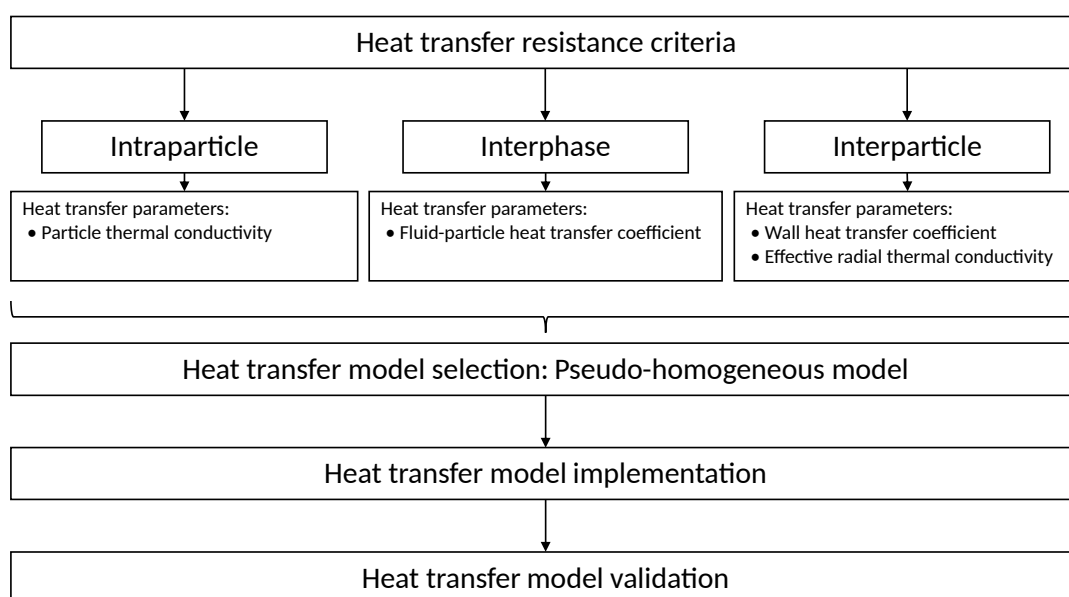
Figure 5.1: Overview of chapter 5.

5.1. Heat transfer resistances

To help select an adequate heat transfer model, it is important to study the main heat transfer resistances in the system and their relative strengths. These can be studied through Mears' [94] three heat transfer resistance criteria presented in chapter 2 which include looking at the intraparticle, interphase, and interparticle heat transfer. To evaluate these three criteria, the details for fluid properties and chemical kinetics presented in chapter 4 will be used.

5.1.1. Intraparticle heat transfer resistance

The first heat transfer resistance identified by Mears [94], is the intraparticle heat gradient that can develop within a porous catalyst particle. He suggests criteria given by Equation 5.1 where if met, the temperature gradients within the particles can be considered negligible and temperature of the particle assumed equal throughout its entire volume.

Condition to neglect intraparticle temperature gradient:

$$\frac{|\Delta H| r_{\mathsf{p,v}} r_{\mathsf{p}}^2}{\lambda_{\mathsf{p}} T_0} < 0.75 \frac{RT_0}{E_{\mathsf{a}}} \tag{5.1}$$

To evaluate Equation 5.1 one of the three reactions in the 12H-NEC dehydrogenation mechanism needs to be selected. In practice, it is expected that 12H-NEC will be input into the reactor and will be the dominant species throughout. Hence, Equation 5.1 will be evaluated with the first step reaction given by Equation 5.2. Furthermore, a temperature for the reactor needs to be selected as it will impact the values of reaction rate, $r_{\mathsf{p,v}}$, and bulk fluid temperature, T_0. Heublein et al. [48] studied the 12H-NEC dehydrogenation reaction in a packed-bed reactor with temperatures between 230 and 280°C. This temperature range will therefore be considered to evaluate Mears' heat resistance criteria. Table 5.1 summarizes the values for the parameters required for evaluating this criteria.

$$12\mathrm{H-NEC} \xrightarrow{k_1} 8\mathrm{H-NEC} + 2\,\mathrm{H}_2 \tag{5.2}$$

Table 5.1: Properties for calculating Equation 5.1 for 12H-NEC dehydrogenation

Parameter	Symbol	Value
Heat of reaction [J/mol]	ΔH	89300
Particle radius [m]	r_{p}	≤ 0.005
Particle thermal conductivity [W/(m·K)]	λ_{p}	0.185
Bulk fluid temperature [K]	T_0	503, 553
Universal gas constant [J/(mol·K)]	R	8.314
Activation energy [J/mol]	E_{a}	56300
Molecular weight [kg/mol]	$M_{\mathrm{12H-NEC}}$	0.207335
Density at T_0 [kg/m^3]	$\rho_{\mathrm{12H-NEC},T_0}$	Calculated with Equation 4.4
Liquid volume fraction [-]	ε_{L}	≈ 0.36
Concentration of 12H-NEC [mol/m^3]	$C_{\mathrm{12H-NEC}}$	$C = \frac{\rho \varepsilon_{\mathsf{L}}}{M}$
Arrhenius pre-exponential factor [s^{-1}]	A	826
Reaction rate constant [s^{-1}]	k_1	$k_1 = A e^{\frac{-E_{\mathsf{a}}}{RT_0}}$
Reaction rate per unit particle volume [mol/(m^{3}s)]	$r_{\mathsf{p,v}}$	$r_{\mathsf{p,v}} = k_1 C_{\mathrm{12H-NEC}}$

The concentration of 12H-NEC, $C_{\mathrm{12H-NEC}}$, which is required to calculate reaction rate, $r_{\mathsf{p,v}}$, is calculated as:

$$C = \frac{\rho \varepsilon_{\mathsf{L}}}{M} \tag{5.3}$$

where the liquid volume fraction, ε_{L}, is estimated as the mean bed porosity considering that the case with highest concentration and thus highest reaction rate will be near the beginning of the reactor when the liquid saturation is one.
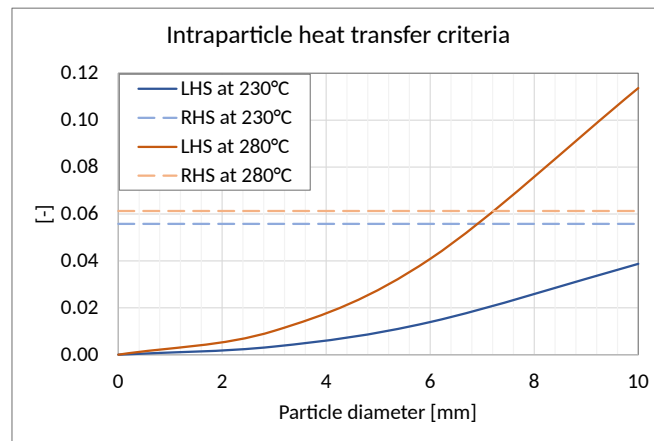
Figure 5.2: Intraparticle heat transfer criteria for parameters given by Table 5.1, comparing the left-hand side (LHS) and right-hand side (RHS) of Equation 5.1.

Figure 5.2 plots the left-hand side (LHS) and right-hand side (RHS) of Equation 5.1 evaluated at 230 and 280°C with parameters given by Table 5.1. The figure shows that at higher temperatures and particle diameters, the RHS comes closer to the LHS of the equation. For 280°C, the RHS of Equation 5.1 becomes greater than the LHS at a particle diameter of 7.2 mm such that the criteria is no longer met. Therefore, for particle diameters less than 7.2 mm, the criteria can be considered to be met and the temperature throughout the volume of the catalyst particles can be considered homogeneous.

5.1.2. Interphase heat transfer resistance

The subsequent heat transfer resistance identified by Mears [94] is the interphase resistance which refers to the temperature gradient that may exist between the external surface of the particle and the adjacent fluid. This criteria is given by Equation 5.4, where meeting this condition signifies that the heat transfer resistance between the fluid and particle is sufficiently low that the temperature of the solid particle surface and adjacent fluid phase can be considered equal.

Condition to neglect fluid-particle temperature difference:

$$\frac{|\Delta H| r_{\text{p,v}} r_{\text{p}}}{h_{\text{fs}} T_0} < 0.15 \frac{RT_0}{E_{\text{a}}} \tag{5.4}$$

Evaluating Equation 5.4 requires the knowledge of a fluid-particle heat transfer coefficient, h_{fs}. To estimate the value of this heat transfer coefficient, Larachi et al. [70] developed an ANN correlation based on a large database of fluid-particle heat transfer coefficients for multiphase flow through TBRs. This correlation requires knowledge of the properties of the three phases given in Table 5.2.

Table 5.2: Phase and reactor properties to calculate Mears' heat transfer resistance criteria.

Parameter	Symbol	Value
Liquid properties		
Superficial velocity [m/s]	V_L	0.00068
Density [kg/m^3]	ρ_L	Calculated with Equation 4.4
Viscosity [Pa·s]	μ_L	Calculated with Equation 4.6
Surface tension [kg/s^2]	σ	Calculated with Equation 4.7
Specific heat capacity [J/(kg·K)]	$c_{p,L}$	Calculated with Equation 4.5
Thermal conductivity [W/(m·K)]	λ_L	Calculated with Equation 4.8
Emissivity [-]	ϵ_L	0.85
Liquid saturation [-]	β_L	Calculated with ANN correlation by Bensetiti et al. [17]
Gas properties		
Superficial velocity [m/s]	V_G	0.61
Density [kg/m^3]	ρ_G	Calculated with Peng-Robinson equation of state [113]
Viscosity [Pa·s]	μ_G	Calculated with Equation 4.3b
Specific heat capacity [J/(kg·K)]	$c_{p,G}$	Calculated with Equation 4.1c
Thermal conductivity [W/(m·K)]	λ_G	Calculated with Equation 4.2a
Particles and bed properties		
Sphericity [-]	φ	1
Grain specific area [m^2/m^3]		A_p/V_p
Reactor diameter [m]	D	0.114
Mean bed porosity [-]	ϵ_B	Calculated with Equation 3.3
Thermal conductivity [W/(m·K)]	λ_G	0.185
Flattening coefficient [-]	ϕ	From Table 5.3
Shape factor for calculating λ_{s0} [-]	C_f	From Table 5.3
Shape factor for calculating Pe number [-]	f	From Table 5.3

The values for liquid and gas superficial velocities are taken from those reported by Heublein et al. [48] in their 12H-NEC dehydrogenation packed-bed reactor. They reported a hydrogen power output of up to 2.25 kW at a temperature of 280°C which can be converted to an outlet gas superficial velocity of 0.61 m/s using hydrogen's lower heating value (LHV) and the author's reactor dimensions. These values will serve as a starting point with which an estimate for the interphase heat resistance criteria can be made. Furthermore, the fluid-particle heat transfer ANN correlation requires the grain specific area which is defined as the particle surface area over the particle's volume. The values for fluid-particle heat transfer coefficient calculated for the above conditions are shown in Figure 5.3a. Having values for the fluid-particle heat transfer coefficient from Larachi et al.'s [70] ANN correlation, Equation 5.4 can now be evaluated using the parameters previously specified in Table 5.1.

(a) Fluid-particle heat transfer coefficient.

(b) Interphase heat transfer criteria comparing the LHS and RHS of Equation 5.4.
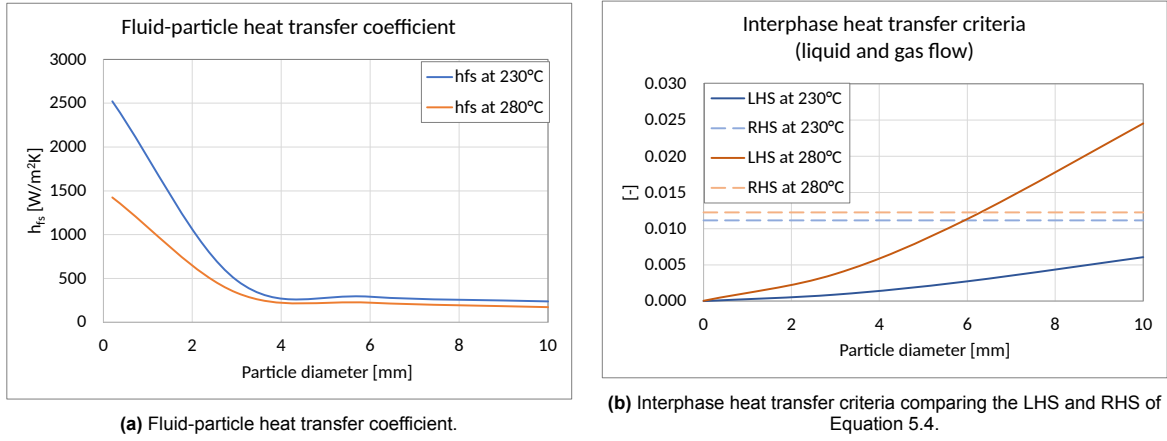
Figure 5.3: Fluid-particle heat transfer coefficient (a), and interphase heat transfer criteria (b) for conditions given by Table 5.1 and Table 5.2.

Figure 5.3b plots the LHS and RHS of Equation 5.4 evaluated at 230 and 280°C. The figure shows that as the temperature and particle diameter increases, the RHS of the equation approaches the LHS. At 280°C, the criteria is not met after a particle diameter of 6.2 mm. Therefore, for simulations with particle diameters below this value, the interphase heat resistance can be assumed to be sufficiently low such that the fluid and catalyst temperature can be taken as equal. This helps simplify the heat transfer model as now a single energy equation is needed to monitor the temperature of both fluid and solid phases.

5.1.3. Interparticle heat transfer resistance

The last main heat transfer resistance identified by Mears [94] is the interparticle resistance where temperature gradients occur between the fluid regions and the wall. This criteria is given by Equation 5.5 where if met, the radial temperature profile throughout the bed can be considered constant.

Condition to neglect reactor scale radial temperature gradient:

$$\frac{|\Delta H| r_\mathrm{v} R_\mathrm{r}^2}{\Lambda_\mathrm{e} T_\mathrm{w}} < 0.4 \frac{R T_\mathrm{w}}{E_\mathrm{a} \left[1 + 8 r_\mathrm{p}/R_\mathrm{r} B i_\mathrm{w}\right]} \tag{5.5}$$

$$Bi_\mathrm{w} = \frac{h_\mathrm{w} d_\mathrm{p}}{\Lambda_\mathrm{e}} \tag{5.6}$$

Evaluating Equation 5.5 requires knowledge of the wall heat transfer coefficient, h_w, and the effective radial thermal conductivity, Λ_e, both of which will also be important for implementing the heat transfer model in the CFD simulation further on. As previously presented, Larachi et al. [70] provide a review discussing different correlations that have been developed to estimate these two parameters for cocurrent downwards and upwards flow packed-bed reactors. The recommended models for a cocurrent upflow configuration, which will be used for the current CFD simulation, will be discussed in the following sections.

Wall heat transfer coefficient

For cocurrent upflow packed-bed reactors, Larachi et al. [70] recommend the correlation of Sokolov and Yablokova [125] given by the following equations:

$$h_\mathrm{w} = \frac{\lambda_\mathrm{L}}{d_\mathrm{ec}} 0.26 Re_\mathrm{L}^{0.43} Pr^{1/3} \tag{5.7a}$$

$$Re_\mathrm{L} = \frac{V_\mathrm{L} \rho_\mathrm{L} d_\mathrm{ec}}{\epsilon_\mathrm{B} \mu_\mathrm{L} \beta_\mathrm{L}} \tag{5.7b}$$

$$d_\mathrm{ec} = \frac{2\epsilon_\mathrm{B}}{3(1 - \epsilon_\mathrm{B})} d_\mathrm{p} \tag{5.7c}$$

At this point, the liquid saturation, β_L, required by Equation 5.7b is not yet known but may be estimated using the ANN correlation for cocurrent upflow fixed bed reactors by Bensetiti et al. [17]. This correlation was developed from a large database of experimental data and requires the same set of input parameters previously given by Table 5.2.

By utilizing the parameters outlined in Table 5.1 and Table 5.2, figures 5.4a through 5.4c depict the wall heat transfer coefficient's dependency on particle diameter, reactor diameter and liquid velocity. It can be noted observed that the wall heat transfer coefficient decreases with particle diameter, increases with reactor diameter but is most sensitive to liquid velocity. For the LOHC reactor, a high wall heat transfer coefficient is desirable to facilitate efficient reactor heating. From the previous graphs this would be achieved with a smaller particle diameter, and faster liquid velocities. A high liquid velocity, however, would reduce the LOHC's residence time in the reactor such that the combined effect of increasing liquid velocity reactor performance may be disadvantageous. Looking at the effect of reactor diameter, the wall heat transfer coefficient increases up to a reactor diameter of about 20 mm for the present conditions after which it remains relatively constant. Increasing the reactor diameter will also, however, affect the internal heat transfer so no conclusion on selecting reactor diameter can be taken at this point. It will be important to combine the effects of all phenomena to see the collective impact of these parameters on overall reactor performance.

(a) Wall heat transfer coefficients for varying particle diameter ($D = 114$ mm, $V_L = 0.68$ mm/s).

(b) Wall heat transfer coefficients for varying reactor diameter ($d_p = 3$ mm, $V_L = 0.68$ mm/s).

(c) Wall heat transfer coefficients for varying liquid superficial velocity ($d_p = 3$ mm, $D = 114$ mm).
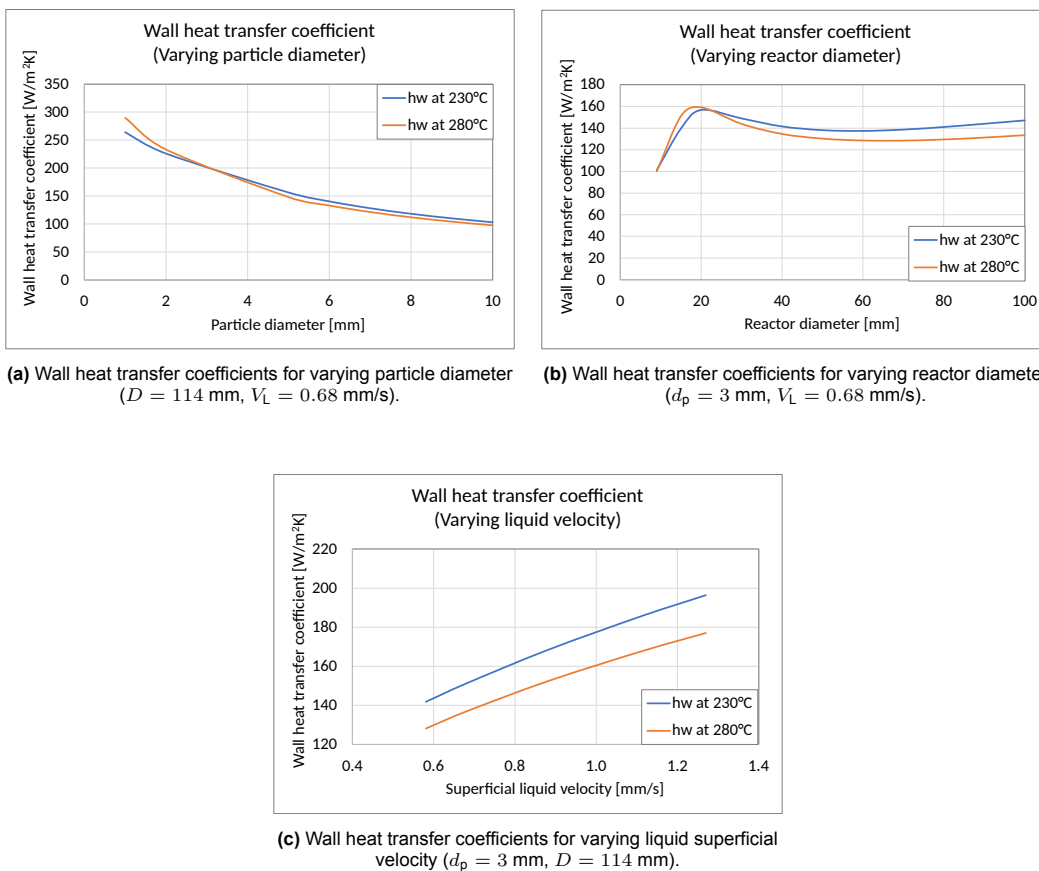
Figure 5.4: Wall heat transfer coefficients for conditions given by Table 5.1 and Table 5.2 at varying particle diameter, reactor diameter and liquid velocity).

Effective radial thermal conductivity

The effective radial thermal conductivity, Λ_e, is often correlated in a two-term form [45]:

$$\Lambda_e = \lambda_{s0} + \lambda_r \tag{5.8}$$

where:

$\lambda_{s0} =$ Pure conduction term [W/(m·K)]
$\lambda_r =$ Radial mixing term [W/(m·K)]

In this equation, λ_{s0} represents the pure conduction thermal conductivity of the packed bed as if the fluid within was stagnant. It is independent of hydrodynamics and represents the contribution of conduction through the solid particles and fluids in the void space to the effective radial heat transfer. The second term, λ_r, is a convective contribution to Λ_e caused by the radial cross-mixing of the fluid. The radial mixing term, λ_r, can be further subdivided into a term for liquid radial mixing, $\lambda_{r,L}$, and a term for gas radial mixing, $\lambda_{r,G}$. Some authors, however, ignore the gas radial mixing term as the most significant contribution is that of the liquid radial mixing term [133][67][91]. Authors have also disregarded the contribution of the pure conduction term which accounts for a small part of the effective radial thermal conductivity, especially in reactors with high liquid velocities. In the case of LOHC dehydrogenation, liquid velocity is expected to be low so the pure conduction term should take on a significant role and be considered.

Pure conduction term, λ_{s0}

The pure conduction term, λ_{s0}, should account for conductive mechanisms in the particle, gas, and liquid phases. In literature it is referred to as the "stagnant contribution" and is primarily a function of the thermal conductivities and volume fractions of all three phases. In addition, several secondary parameters also influence the pure conduction term. These include heat transfer by radiation, pressure dependence, heat transfer through flattened interparticle contacts, particle shape, and particle size distribution [136].

Diverse types of models to estimate the pure conduction term have been proposed. These include models that analytically or numerically solve the Laplace equation for heat conduction, models that represent the system as a combination of thermal resistances, and models that calculate the thermal conductivity of a unit cell which is then equated to that of the packed bed. For practical use, Tsotsas [136] recommends using models that calculate the thermal conductivity of a unit cell such as the model developed by Bauer and Schlünder [15] which is often recommended for use [45][91][133]. This model was developed for liquid flow through packed beds using the unit cell shown in Figure 5.5 and is a comprehensive model considering both primary and secondary contributions to the pure conduction term.
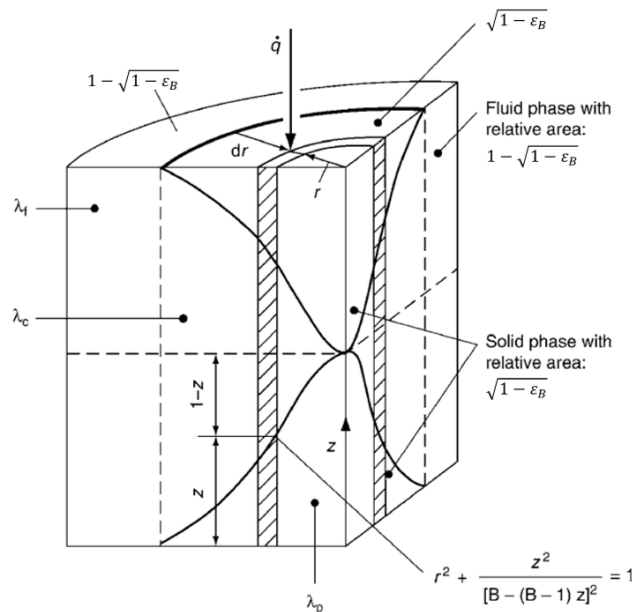
Figure 5.5: Unit cell of Bauer and Schlünder model for estimating the pure conduction term, λ_{s0} [136].

Mariani [92] proposed a modification to the Bauer and Schlünder model [15] for two-phase flow through a packed bed. He does this by assuming that the liquid forms rivulets surrounding each particle and the rest of the interstitial volume is filled by the gas phase. As a simplification, Mariani neglects the radiant heat transfer contribution, pressure effects, and the particle size distribution which are expected

to be minimal in most practical cases. For the LOHC reactor however, dehydrogenation occurs at elevated temperatures so it may be beneficial to include radiation effects. Extending Mariani's concept to encompass radiation effects yields the model delineated by the following equations:

$$\lambda_{s0} = \left(1 - \sqrt{1-\epsilon}\right)\left(1 + \lambda_{rad}\epsilon\right)\lambda_G + \sqrt{1-\epsilon}\left[\phi\kappa + (1-\phi)\Theta\right]\lambda_L \tag{5.9a}$$

$$\Theta = \frac{2}{N}\left[\frac{B(\kappa + \lambda_{rad} - 1)}{N^2\kappa}\ln\frac{\kappa + \lambda_{rad}}{B} + \frac{B+1}{2B}(\lambda_{rad} - B) - \frac{B-1}{N}\right] \tag{5.9b}$$

$$B = C_f\left(\frac{1-\epsilon}{\epsilon}\right)^{10/9} \tag{5.9c}$$

$$N = 1 + \frac{\lambda_{rad} - B}{\kappa} \tag{5.9d}$$

$$\kappa = \frac{\lambda_s}{\lambda_L} \tag{5.9e}$$

$$\lambda_{rad} = \frac{4\sigma_{SB}}{(2/\epsilon_L) - 1}T^3\frac{d_p}{\lambda_G} \tag{5.9f}$$

where:

λ_{s0} = Pure conduction term [W/(m·K)]
ϵ = Porosity [-]
λ_{rad} = Radiative heat transfer equivalent thermal conductivity [W/(m·K)]
ϕ = Flattening coefficient [-]
B = Deformation factor [-]
ϵ_L = Emissivity of liquid [-]
σ_{SB} = 5.67×10^{-8} [W/m²K⁴] = Stefan–Boltzmann constant
C_f = Shape factor [-]

Table 5.3: Shape factors and flattening coefficients for Equations 5.9a, 5.9c, and 5.10c [136][14][15].

Particle Shape	C_f	f	ϕ	Material
Spherical	1.25	1.15	0.0013	Steel
			0.0077	Ceramic
			0.0253	Copper
Irregular (broken)	1.4	1.55	0.0010	Sand
Cylindrical	2.5	1.75		
Raschig rings	$2.5[1 + d_i/d_o)^2]$	2.8		

Table 5.3 provides the shape factors, C_f, and flattening coefficients, ϕ, needed for calculating Equations 5.9a and 5.9c. For the LOHC dehydrogenation reactor, the flattening coefficient is taken as 0.0077 as the catalyst pellets are assumed to be of an alumina (ceramic) base. Furthermore, since the particles are assumed to be covered by a liquid layer, the emissivity of the liquid should be used in Equation 5.9f. While no data was found on the emissivity of the NEC species, the emissivity of a 0.5 mm thick sample of toluene was measured by Capelle et al. [24]. Over the narrow wavelength range of 3.0-3.6 μm, the average toluene emissivity was 0.85. Although emissivity could vary across different wavelengths and might differ for NEC, the value of 0.85 will be adopted as a reference point also considering that the expected contribution of radiative heat transfer is expected to be small. The remaining properties required to estimate the value of the pure conduction term, λ_{s0}, are detailed in Table 5.2.

Radial mixing term, λ_r
For the overall effective radial thermal conductivity, Λ_e, in cocurrent upflow FBRs, Larachi et al. [72] recommend using the correlation by Lamine et al. [66] for the bubble flow regime and that of Gutsche [44] for low gas and liquid flow rates. As the LOHC dehydrogenation reactor is expected to operate under low liquid and gas flow rates, the correlation of Gutsche [44] given by Equations 5.10a through

5.10c will be used. The first term of Equation 5.10a corresponds to the pure conduction term previously discussed, and the second and third term to the radial mixing contributions from the liquid and gas phase respectively.

$$\Lambda_e = \lambda_{s0} + \frac{Pe_L \lambda_L}{\beta_L K} + \frac{Pe_G \lambda_G}{(1 - \beta_L) K} \tag{5.10a}$$

$$K = 8 \left(2 - \left(1 - 2\frac{d_p}{D} \right)^2 \right) \tag{5.10b}$$

$$Pe = \frac{\rho c_p d_p V f}{\lambda} \tag{5.10c}$$

In Equation 5.10c, f is another shape factor with values given in Table 5.3. The value for the effective radial thermal conductivity can now be evaluated with the remaining properties taken from Table 5.2. Figures 5.6a through 5.6c show the values of Λ_e for varying parameters at two temperatures.
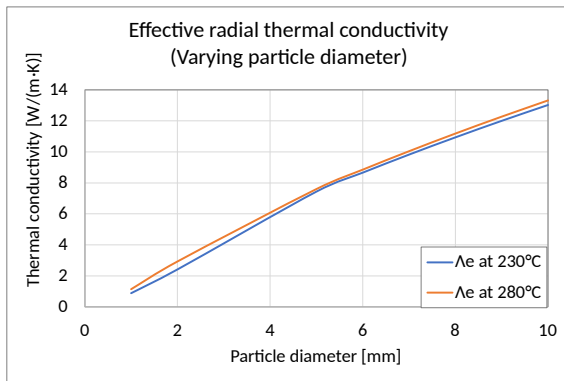
(a) Effective thermal conductivities for varying particle diameter ($D = 114$ mm, $V_L = 0.68$ mm/s).
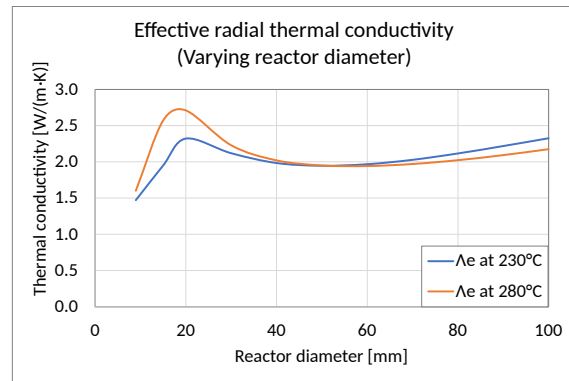
(b) Effective thermal conductivities for varying reactor diameter ($d_p = 3$ mm, $V_L = 0.68$ mm/s).
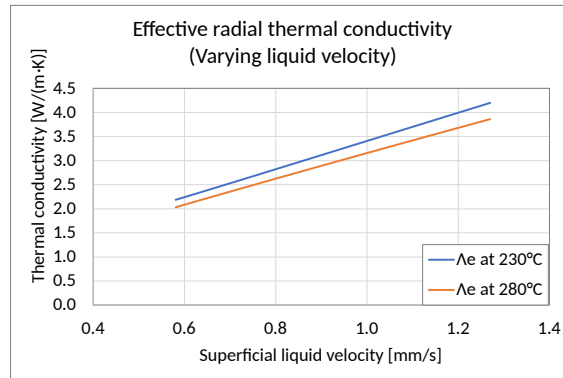
(c) Effective thermal conductivities for varying liquid superficial velocity ($d_p = 3$ mm, $D = 114$ mm).

Figure 5.6: Effective thermal conductivities for conditions given by Table 5.1 and Table 5.2 at varying particle diameter, reactor diameter and liquid velocity.

From the above figures, it can be appreciated that the effective radial thermal conductivity is most sensitive to particle diameter and liquid velocity. It is important to note that from the three terms in Equation 5.10a, the first term, λ_{s0}, corresponds to between 2-8% of the total value of the effective radial thermal conductivity, the second between 87-94% and the third between 4-6% depending on the conditions. This indicates that the liquid radial mixing term is the most dominating contribution towards the effective radial thermal conductivity, and it becomes understandable why at certain conditions authors may decide to neglect the pure conduction term or the gas radial mixing term.

Interparticle heat resistance criteria

With the appropriate models for estimating the wall heat transfer coefficient and the effective radial thermal conductivity now established, attention can be returned to the computation of the interparticle heat resistance criteria expressed in Equation 5.5. First, the wall Biot number, Bi_w, is evaluated with Equation 5.6, followed by the assessment of the interparticle heat resistance criteria.

Figure 5.7 plots the LHS and RHS of the interparticle heat resistance criteria for varying particle and reactor diameters at 230 and 280°C. Unlike the previous two criteria, the LHS of Equation 5.5 is always greater than the RHS. At very small tube-to-particle diameter ratios, the LHS comes closer to the RHS of the equation but still does not fall below it. This indicates that the wall heat resistance is non-negligible, and the effective bed thermal resistance is also significant. Therefore, a constant radial temperature profile cannot be assumed but instead, the bed's effective radial thermal conductivity should be used to calculate the packed bed's internal temperature profile.

It is important to realize that the evaluation of the previous criteria was done based on the experimental conditions from Heublein et al.'s [48] NEC dehydrogenation study and the material and chemical kinetics properties detailed in chapter 4. These are the most realistic conditions for the NEC dehydrogenation reaction from which the preceding conclusions were made. If, however, the LOHC material or operating conditions differ significantly from those used in this study, it would be important to re-evaluate Mears' [94] heat transfer resistance criteria and determine what simplifications to the heat transfer model can be made.

(a) Interparticle heat transfer criteria for varying particle diameter ($D = 114$ mm).

(b) Interparticle heat transfer criteria for varying reactor diameter ($d_\mathsf{p} = 3$ mm).
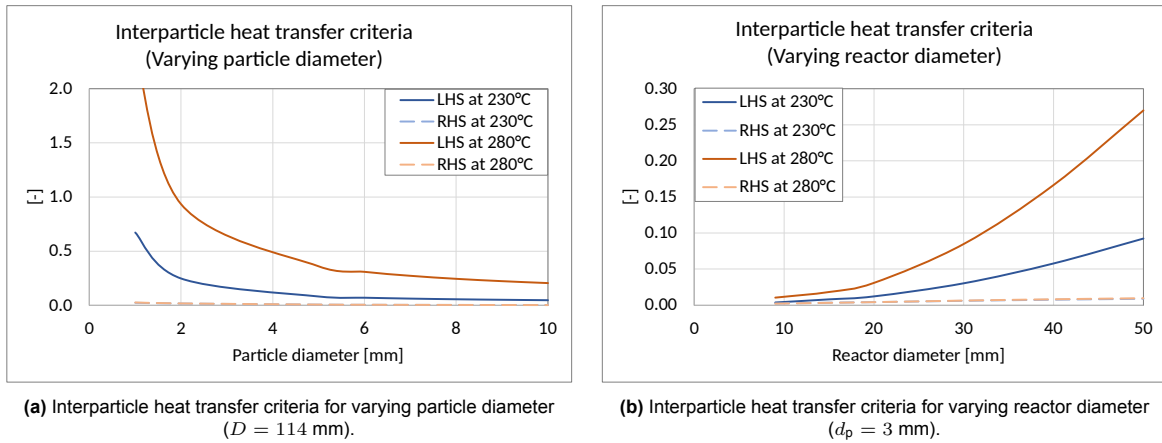
Figure 5.7: Interparticle heat transfer criteria for conditions given by Table 5.1 and Table 5.2 comparing the LHS and RHS of Equation 5.5.

5.2. Pseudo-homogeneous heat transfer models

Having evaluated Mears' [94] heat transfer resistance criteria, an adequate heat transfer model can be selected to implement into the CFD simulation. From evaluating these criteria, it was found that in 12H-NEC dehydrogenation, the temperature gradients within catalyst particles, and between particle surface and adjacent fluid are small for particle diameters less than 6.2 mm. In addition, the interparticle heat transfer resistance criteria was not met indicating that the temperature gradients throughout the reactor are important to consider. This suggests that a pseudo-homogeneous heat transfer model using a single energy equation to track the temperature of all three phases can be used. All phases will share the same temperature field, and no heat transfer resistance between phases will be considered.

Flávio Pinto Moreira et al. [38] evaluated five of the most used pseudo-homogeneous models to study heat transfer in packed beds. The difference between them lies in the heat transfer parameters used to describe the models, the wall boundary conditions, and the inlet boundary conditions. The general pseudo-homogeneous formulation is given by:

$$(\rho_\mathsf{L} c_{p,\mathsf{L}} V_\mathsf{L} + \rho_\mathsf{G} c_{p,\mathsf{G}} V_\mathsf{G}) \frac{\partial T}{\partial z} = \lambda_\mathsf{r} \left[\frac{1}{r} \frac{\partial}{\partial r} \left(r \frac{\partial T}{\partial r} \right) \right] + \lambda_\mathsf{a} \frac{\partial^2 T}{\partial z^2} \tag{5.11}$$

where λ_r is the radial thermal conductivity and λ_a the axial thermal conductivity. At the column wall ($r = R$) the possible boundary conditions suggested by Flávio Pinto Moreira et al. [38] include

considering a constant temperature ($T = T_\mathsf{w}$), or considering convective heat transfer at the bed of the walls as suggested by Equation 5.12 below.

$$\text{At } r = R, \qquad -\Lambda_\mathsf{e}\frac{\partial T}{\partial r} = h_\mathsf{w}(T_{\mathsf{r=R}} - T_\mathsf{w}) \tag{5.12}$$

Furthermore, at the reactor inlet ($z = 0$) Flávio Pinto Moreira et al. [38] suggest that either a constant temperature profile ($T = T_0$) or a parabolic temperature profile can be assumed as would be expected for fully developed pipe flow. Flávio Pinto Moreira et al. [38] evaluated the different combination of boundary conditions by considering deviations between calculated and measured temperatures and by studying the values of thermal parameters alongside their associated confidence intervals. They found that estimating an axial thermal conductivity value, λ_a, is problematic as it is highly sensitive to operating conditions. The axial thermal conductivity in packed beds was found to be an inconsistent parameter and the authors suggest discarding it from the heat transfer model. Furthermore, models considering a convective heat transfer boundary condition at the walls instead of a constant wall temperature resulted in a better fit to experimentally measured temperatures. Finally, as for the inlet boundary condition, a constant temperature profile is suggested as it presented better confidence intervals and no guess for a parabolic temperature profile is required. Considering these insights, the selected pseudo-homogeneous heat transfer model to be applied in the current CFD simulation is:

$$(\rho_\mathsf{L}c_{p,\mathsf{L}}V_\mathsf{L} + \rho_\mathsf{G}c_{p,\mathsf{G}}V_\mathsf{G})\frac{\partial T}{\partial z} = \Lambda_\mathsf{e}\left[\frac{1}{r}\frac{\partial}{\partial r}\left(r\frac{\partial T}{\partial r}\right)\right] \tag{5.13a}$$

subject to boundary conditions at the wall ($r = R$) and at the reactor axis ($r = 0$):

$$\text{At } r = R, \qquad -\Lambda_\mathsf{e}\frac{\partial T}{\partial r} = h_\mathsf{w}(T_{\mathsf{r=R}} - T_\mathsf{w}) \tag{5.13b}$$

$$\text{At } r = 0, \qquad \frac{\partial T}{\partial r} = 0 \tag{5.13c}$$

$$\text{At } z = 0, \qquad T = T_0 \tag{5.13d}$$

5.3. Implementation and validation

To implement the selected pseudo-homogeneous heat transfer model in the present CFD model, the radial thermal conductivity, λ_r, in Equation 5.13a is replaced by the effective radial thermal conductivity, Λ_e, previously presented. This parameter can be calculated from the pure conduction term contribution and the radial mixing term using Equations 5.9 and 5.10. While in subsection 5.1.3 the values of Λ_e and h_w were calculated once for the average operating parameters expected throughout the bed, in the CFD model these will be calculated locally at each cell by means of UDFs. The effective radial thermal conductivity, Λ_e, will be calculated at each cell using local flow parameters as the solution progresses such that its value will update for each cell at every solution iteration. This calculation is done by the UDF found in section A.12 for reference.

Similarly, the wall heat transfer coefficient, h_w, can be calculated using the correlation of Sokolov and Yablokova [125] previously written in Equation 5.7. For its implementation in the CFD model, the wall heat transfer coefficient will also be calculated locally as it too depends on the flow parameters. The wall heat transfer coefficient calculation requires a value for liquid superficial velocity, V_L, which can be rewritten in terms of local interstitial velocity, U_L, as $V_\mathsf{L} = U_\mathsf{L}\varepsilon_\mathsf{L}$. At the wall however, the liquid interstitial velocity $U_\mathsf{L} = 0$ m/s because of the no-slip condition, and the velocity will vary significantly in the radial direction because of the uneven porosity profile. Therefore, to have a representative value of h_w that can be used at each cell face on the wall, the value of h_w will be calculated at every cell in the domain, and a mass-weighted average will be taken at each cell plain. To better exemplify this, Figure 5.8 represents a few cells of the domain with the dotted lines representing planes at adjacent cell in the axial direction. The value for h_w is calculated using the local flow parameters at each cell and then averaged along each plane to have a value of h_w that can be used for the convective heat transfer boundary condition at the wall cell of that plane. This calculation is also conducted done by an external UDF found in section A.13.
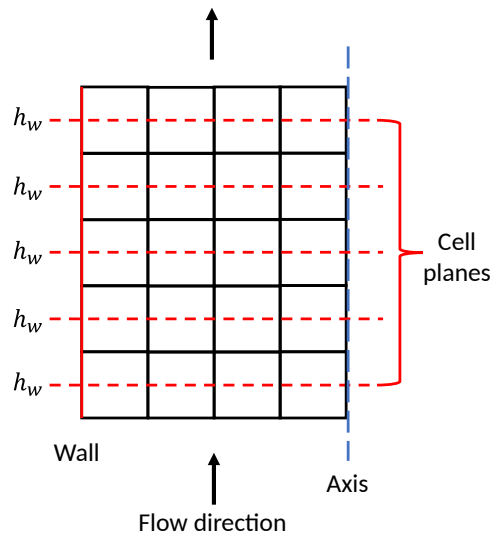
Figure 5.8: Mass weighted plane-average calculation of wall heat transfer coefficient h_w

5.3.1. Geometry and mesh

The CFD model built for validation of the hydrodynamic aspects in section 3.4 will now be further developed to incorporate the material properties discussed in chapter 4 and the heat transfer model discussed in this chapter. For this test, the same CFD domain from Figure 3.6 will be used. Furthermore, as the mesh refinement study was already conducted, the same mesh with an inflation layer near the wall and the remaining cells with a size of 0.7 times the particle diameter will be used.

5.3.2. Model setup

To build on the Eulerian multiphase CFD model framework from chapter 3, the same phases and phase interactions are maintained but now the liquid phase is set to 12H-NEC, the gas phase to H_2, and the solid phase to alumina. Material properties for these three phases are updated according to the information presented in chapter 4. It is important to note that CFD software ANSYS Fluent 2021 R2 automatically assigns and solves an energy conservation equation for each of the three phases which includes terms for interphase heat transfer. However, the aim is to describe the energy of the reactor through a shared temperature field by means of a pseudo-homogeneous heat transfer model. To ensure that the three phases share the same temperature field, the interphase heat transfer coefficient, h_{pq}, between the pth phase and the qth phase defined in the energy conservation equation (Equation 2.20)is set to a very high number. By setting a very high interphase heat transfer coefficient between each pair of phases, for example 1000 W/m^{2}K, the heat transfer resistance between phases is essentially set to 0 such that energy can freely transfer between phases. By assigning the thermal conductivity of the liquid, gas, and solid phases equal to the calculated effective radial thermal conductivity, Λ_e, and setting the interphase heat transfer coefficient between each pair of phases to 1000 W/m^{2}K, the same temperature field for the three phases is achieved.

Boundary conditions

In addition to the boundary conditions previously described for the inlet flow velocities, solid porosity profile, wall, axis, and pressure outlet boundary conditions, there are now additional boundary conditions to consider for the energy equation. At the inlet, a constant or flat temperature profile is given for the three phases. Here, it is important that the temperature of the three phases is equal. Furthermore, a convective wall boundary condition is defined at the 'packed-bed' cell zone wall and a zero heat flux boundary condition is set at the remaining 'inlet' and 'outlet' cell zone walls. For the convective wall boundary condition, the wall heat transfer coefficient is input from the corresponding UDF as well as a constant wall temperature T_w. At this point a constant wall temperature is assumed which may represent a sufficiently high heating oil mass flow through the reactor's heating jacket to maintain this temperature. Further on, it may be beneficial to improve the constant wall temperature assumption with a temperature profile that may closer imitate the actual wall temperature of a jacketed reactor.

Lastly, at the outlet boundary, it is necessary to specify a backflow temperature in the event of flow reversal occurring at the boundary during the solution process. To minimize the disturbance caused by such backflow to the main domain, a UDF is developed to read the temperature along the cells at the outlet boundary and provide this same temperature profile for the backflow. By reading the temperature of the cells at the outlet and using this temperature for the backflow, a zero normal derivative condition is enforced ($\frac{\delta T}{z} = 0$). The UDF providing this boundary condition is referenced in section A.14.

Solution methods

Regarding the pressure-velocity coupling method and spatial discretization schemes, the same schemes described earlier for the hydrodynamic aspect test will be employed. Additionally, a second-order upwind spatial discretization scheme for energy will be used. Furthermore, both the present and upcoming tests will focus on a cocurrent upflow configuration. While in theory, this only involves reversing the gravity vector used in the cocurrent downflow setup, practical implementation requires additional precautions to ensure simulation stability.

From the expected liquid and gas velocities within an LOHC dehydrogenation reactor (as depicted in Table 5.2, derived from Heublein et al.'s experiments [48]), it becomes evident that the gas velocity is expected to be 2-3 orders of magnitude higher than that of the liquid. As there is no gas at the reactor inlet but rather it forms throughout the reactor, the gas is expected to start from a velocity of zero at the particle surface where it is formed, and quickly accelerate due to buoyancy force and the fact that large volumes of gas are created which must travel upstream to escape. The buoyancy force effect is therefore significant in the reactor and special considerations should be taken.

In the Ansys Fluent User's Guide [58], special considerations are suggested for buoyancy driven flows. One strategy suggested for buoyancy driven flows found to be helpful for the current LOHC dehydrogenation model was to progressively change the value of gravitational acceleration. If the value for gravitational acceleration was set to -9.81 m/s^2 from the start (where the negative direction is downward), the solution presented numerical instabilities and diverged. Instead, it was first important to begin with a gravitational acceleration of 0.0 m/s^2, run some iterations, and progressively change the value until -9.81 m/s^2 was reached. Table 5.4 shows the values for gravitational acceleration and the number of iterations run found to give a steady solution for this heat transfer validation test.

Table 5.4: Progressive application of gravitational acceleration for cocurrent upward flow configuration.

Gravitational acceleration [m/s^2]	Iterations
0.00	2000
-2.00	1000
-4.00	1000
-6.00	1000
-8.00	1000
-9.81	8000

The Ansys Fluent User's Guide [58], also makes special reference to defining an operating density for a buoyancy-driven multiphase flows. When solving the mass conservation equation (2.17) and volume fraction constraint (2.19) for each phase in multiphase flows, the software represents these in either a mass or volumetric form. Furthermore, the software multiplies the whole mass conservation equation by the inverse of a reference density, ρ_{rq}. This setting is controlled in the software by the "reference density method" where the default option is to represent the volume fraction equation in a mass form, the continuity equation in a volumetric form, and calculate the phase reference density as an average density of the phase within the whole domain.

For the LOHC dehydrogenation reactor however, large volumes of gas are expected to be produced but its mass compared to the liquid phase will remain low. In addition, significant differences in temperature throughout the reactor may exist causing the density of the fluids to change. Therefore, representing the volume fraction equation in a mass form may cause difficulties in closing the mass balance, and using an average density of the whole reactor may be inadequate as it is expected to change throughout. Instead, the reference density option representing both the volume fraction and mass conservation equations in the volumetric form is used. This option further assigns the value of

the reference density, ρ_{rq}, to the density of the cell instead of an average density throughout the whole domain. This reference density option was found to have the best mass imbalance among the options and led to a more stable solution with improved convergence behavior.

Finally, given that compressible fluids are being considered, the energy and density under-relaxation factor is slightly reduced. The URFs to be used for this study are summarized in Table 5.5. Furthermore, a summary of the parameters used for this heat transfer model validation study is found in Table 5.6.

Table 5.5: Under relaxation factors for heat transfer model validation study.

Under-Relaxation Factor	Value
Pressure	0.3
Density	0.6
Body Forces	0.6
Momentum	0.2
Volume Fraction	0.1
Energy	0.6

Table 5.6: Parameters for heat transfer model validation.

Parameter	Value
Flow configuration	Cocurrent upward flow
Reactor diameter [m]	0.114
Reactor length [m]	1
Fluid system	H2 & 12H-LOHC
Inlet gas velocity [m/s]	0.61
Inlet liquid mass flux [kg/m^{2}s]	0.60
Packing	Spherical alumina particles
Particle diameter [m]	0.003
Ergun constant 1 [-]	15
Ergun constant 2 [-]	1.8
Mesh size	$0.7 \times d_{\mathrm{p}}$
Inlet Temperature [K]	400
Wall Temperature [K]	520

5.3.3. Heat transfer validation study results

To validate the implementation of this heat transfer model in the CFD simulation, the temperature profiles calculated by the CFD simulation can be compared to the analytical solution of Equation 5.13. This pseudo-homogeneous heat transfer model has an analytical solution which is provided by Flávio Pinto Moreira et al. [38] and is given by Equation 5.14.

$$\frac{T - T_{\mathrm{w}}}{T_0 - T_{\mathrm{w}}} = 2 \sum_{n=1}^{\infty} \frac{Bi J_0\left(a_n \frac{r}{R}\right) \exp\left[\frac{-\Lambda_{\mathrm{e}} a_n^2 z}{R^2\left(\rho_{\mathsf{L}} c_{p,\mathsf{L}} V_{\mathsf{L}} + \rho_{\mathsf{G}} c_{p,\mathsf{G}} V_{\mathsf{G}}\right)}\right]}{(Bi^2 + a_n^2) J_0(a_n)} \tag{5.14a}$$

$$Bi J_0(a_n) - a_n J_1(a_n) = 0 \tag{5.14b}$$

$$Bi = \frac{h_{\mathrm{w}} R_{\mathrm{r}}}{\Lambda_{\mathrm{e}}} \tag{5.14c}$$

where:

T = Temperature [K]
T_{w} = Wall temperature [K]
T_0 = Reactor inlet temperature [K]
J_0, J_1 = Bessel function of the first kind of order zero and one, respectively [-]
Bi = Biot number [-]

r = Radial coordinate [m]
R_r = Reactor radius [m]
z = Axial coordinate [m]

It is important to note, however, that this solution does not consider the effects of the varying porosity profile or capillary effects, both of which induce radial mixing within the reactor. The temperature profile given by Equation 5.14 would instead correspond to that of plug flow through the reactor. To try out the CFD model, a test is first conducted with parameters given in Table 5.6 with and without capillary pressure effects. Figure 5.9 gives the temperature profile in the packed-bed area for the test without capillary pressure effects, closer to a plug flow, and Figure 5.10 including capillary pressure effects. It is interesting to note here that the capillary effect aids in transferring the heat to the fluid faster thanks to the radial mixing induced by the capillary effect.
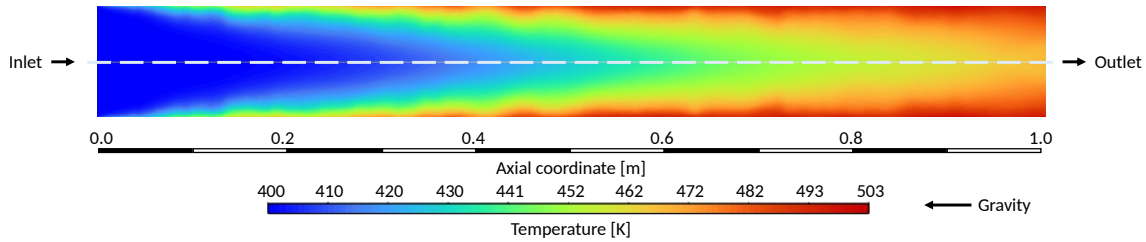
Figure 5.9: Temperature contour plot, without capillary pressure effects.
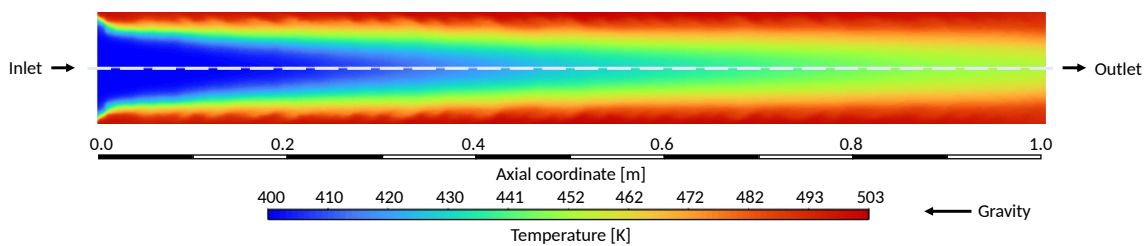
Figure 5.10: Temperature contour plot, with capillary pressure effects.

Evaluating the analytical solution for the temperature profile given by Equation 5.14 requires values for the fluid properties and heat transfer parameters. While these are changing throughout the reactor as the fluids are heated, as an estimate, volume average values will be taken from the CFD simulation performed to generate the contour plot in Figure 5.9. These average properties are shown in Table 5.7 and used to evaluate the analytical solution.

Table 5.7: Average flow and heat transfer parameters from the CFD simulation.

Parameter	Symbol	Value
Wall heat transfer coefficient [W/m^{2}K]	h_w	103.8
Effective radial thermal conductivity [W/(m·K)]	Λ_e	1.961
Liquid properties		
Mass flux [kg/m^{2}s]	J_L	0.6
Density [kg/m^3]	ρ_L	827.9
Specific heat capacity [J/(kg·K)]	$c_{p,L}$	2256
Gas properties		
Mass flux [kg/m^{2}s]	J_G	0.0267
Density [kg/m^3]	ρ_G	0.057
Specific heat capacity [J/(kg·K)]	$c_{p,G}$	14504

Figure 5.11a shows the temperature profile in the radial direction at the reactor outlet from both the CFD simulation and the analytical solution. Similarly, Figure 5.11b shows the temperature in the axial direction along the reactor's axis.

(a) Radial temperature profile along reactor outlet.   **(b)** Axial temperature profile along reactor axis.
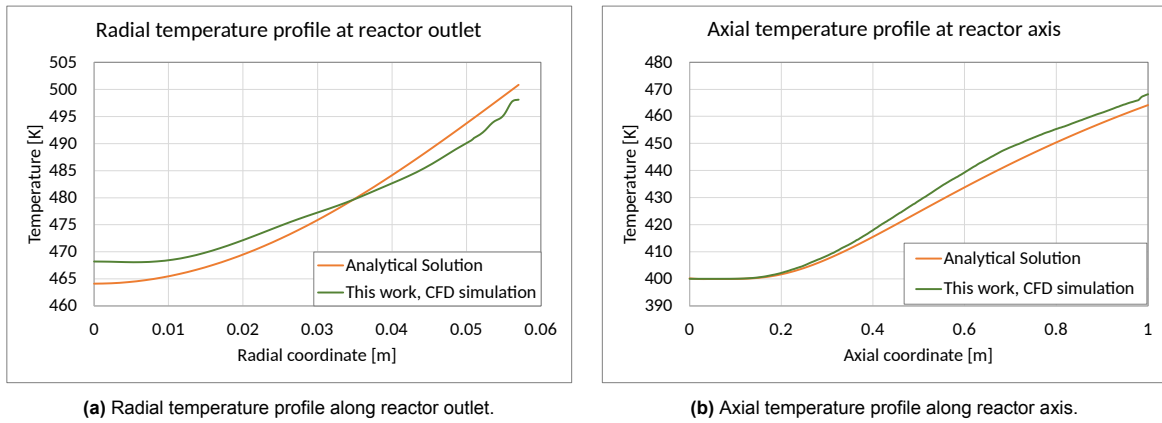
Figure 5.11: Comparison of CFD temperature result with pseudo-homogeneous heat transfer model analytical solution.

From Figure 5.11a and Figure 5.11b it can be observed that the temperature profiles resulting from the CFD simulation are very close to the analytical solution with differences within 1% for Figure 5.11a and 2% for Figure 5.11b. This gives confidence that the CFD model is correctly applying the two parameter pseudo-homogeneous heat transfer model that was selected. Moreover, as the CFD model calculates all flow parameters and heat transfer parameters locally at every cell, it will be able to describe the heat transfer in complex flow patterns more accurately than if the analytical solution was directly applied.

<div align="right">

6

</div>

CFD model development: Species transport

The last aspect to develop for the LOHC dehydrogenation reactor model is species transport. This chapter will follow the structure laid out in Figure 6.1 by discussing the species conservation equation and diving into the details of hydrodynamic dispersion. Hydrodynamic dispersion refers to the added effect of molecular diffusion and mechanical dispersion, both of which will be discussed and calculated for the application at hand. Species transport will then be implemented in the CFD model and visualized to observe the effect of hydrodynamic dispersion in the reactor.

CFD model development: Species transport
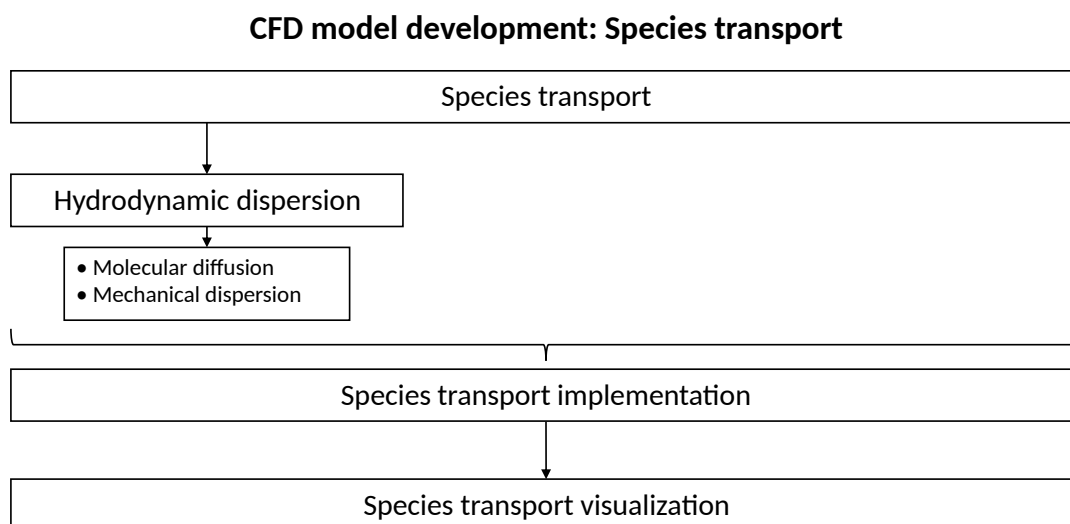
Figure 6.1: Overview of chapter 6.

6.1. Species transport

Species transport refers to the tracking of different chemical species throughout the CFD domain within each phase. In this case, the gas phase is assumed to be a single species (H_2) but the liquid phase does consist of multiple species. Specifically, 12H-NEC dehydrogenation includes four liquid species: fully hydrogenated 12H-NEC, two intermediate species, 8H-NEC and 4H-NEC, and fully dehydrogenated 0H-NEC. While the mass conservation equation shown is applied at a phase level, additional species conservation equations are required to track the mass fractions, y_q^i, of each species. The species conservation equation takes the following form:

$$\frac{\partial}{\partial t}\left(\varepsilon_q \rho_q y_q^i\right) + \nabla \cdot \left(\varepsilon_q \rho_q \boldsymbol{U}_q y_q^i\right) = -\nabla \cdot \left(\varepsilon_q \boldsymbol{J}_q^i\right) + S_{\text{species},q} \tag{6.1}$$

A species conservation equation is solved for $n-1$ species where n is the total number of chemical species present in the qth phase. To minimize numerical error, 12H-NEC is set as the last species so that its mass fraction is calculated as one minus the mass fraction of the other three liquid species. This is done because for a large part of the domain, it is expected that 12H-NEC will be the species with the largest mass fraction.

6.1.1. Hydrodynamic dispersion
Hydrodynamic dispersion is the spreading of chemical species as they are transported through the packed bed. It is driven by two mechanisms: molecular diffusion and mechanical dispersion which combined are called hydrodynamic dispersion [85]. In the species conservation equation, hydrodynamic dispersion is considered through the dispersive flux, $\boldsymbol{J}_q^i$, of each species. The following section will discuss the contributions to hydrodynamic dispersion and its implementation in the CFD model.

Molecular diffusion
Molecular diffusion is the spreading of a species within a single phase due to the random motion of molecules. Molecular diffusion occurs in all directions, is independent of the flow, and has the effect of transporting species from areas of high to low concentration. This can be described by Fickian diffusion in terms of mass fraction as:

$$\boldsymbol{J}_{\text{Diffusion}}^i = -\rho D_{i,\text{m}} \nabla y^i \tag{6.2}$$

where $D_{i,\text{m}}$ is the molecular diffusion coefficient of species i in the mixture. In a multicomponent system like NEC dehydrogenation, one method to derive the molecular diffusion coefficient involves calculating a mass average of binary molecular diffusion coefficients as follows [124]:

$$D_{i,\text{m}} = \frac{1 - x_i}{\sum_{j=1}^{n}(x_j/\mathcal{D}_{i,j})} \tag{6.3}$$

where:

$D_{i,\text{m}}$= Molecular diffusion coefficient of species i in the mixture [m^2/s]
x_i = Mole fraction of species i [-]
x_j = Mole fraction of species j [-]
$\mathcal{D}_{i,j}$ = Binary molecular diffusion coefficient of component i in component j [m^2/s]

Calculating Equation 6.3 requires knowledge of binary molecular diffusion coefficients, $\mathcal{D}_{i,j}$, between every pair of LOHC species. As an example, Heller et al. [47] experimentally studied the binary diffusion coefficients for the 0H-DBT and 18H-DBT LOHC system over a temperature range from 264 to 571 K. However, no data was found regarding the binary molecular diffusion coefficients among the four NEC species, and they will instead be estimated.

Poling et al. [117] explain various methods for predicting binary liquid molecular diffusion coefficients. These have been based on hydrodynamic theory, kinetic theory, statistical mechanics, and other concepts. One equation based on hydrodynamic theory is the Stokes-Einstein equation for diffusion which analyzes the diffusion of large spherical molecules in a dilute solution. The Stokes-Einstein equation has served as a starting point for other authors to develop correlations for molecular diffusion such as the Wilke-Chang equation which is one of the most recommended and used correlations [143][117][96]. This equation is an empirical modification of the Stokes-Einstein equation and is used to estimate binary liquid molecular diffusion coefficients at infinite dilution. For example, $\mathcal{D}_{i,j}^{\circ}$ refers to the diffusion coefficient of species i diffusing in an infinitely dilute solution of j. For practical purposes, $\mathcal{D}_{i,j}^{\circ}$ is assumed to be a representative diffusion coefficient for concentrations of species i up to 5 to 10 mol % [117]. The Wilke-Chang model is formulated as:

$$\mathcal{D}_{i,j}^{\circ} = \frac{7.4 \times 10^{-8}(\phi_j M_j)^{1/2}T}{\mu_j V_i^{0.6}} \tag{6.4}$$

where:

$\mathcal{D}_{i,j}^{\circ}$= Binary diffusion coefficient of component i in component j at infinite dilution [cm^2/s]
ϕ_j = Association factor of solvent j [-]
M_j = Molecular weight of solvent j [g/mol]
T = Temperature [K]
μ_j = Viscosity of solvent j [cP]
V_i = Molar volume of solute i at its boiling temperature [cm^2/mol]

The association factor, ϕ_j, represents the degree of aggregation which correlates with the physico-chemical properties of the solvent. Miyabe and Isogai [96] study the dependence of this association factor and propose values for various organic compounds. Among the studied compounds, toluene is expected to be most similar to other LOHCs for which an association factor of 1.0 is proposed. For the case of the NEC system, an association factor of 1.0 will also be assumed.

The Wilke-Chang equation results in diffusion coefficients at infinite dilution, but for the case of the LOHC dehydrogenation, it is expected that the no one species should be dominant for it to be considered an infinite dilution system. Instead, the mole fractions of the intermediate and dehydrogenated species should continuously rise as the reaction progresses. For non-dilute solutions such as this one, the binary diffusion coefficient will change as a function of the concentration of either species between two limiting values. For example, in the case of a binary mixture of species i and j, the binary diffusion coefficient, $\mathcal{D}_{i,j}$, will vary between infinite dilution coefficients $\mathcal{D}^{\circ}_{i,j}$ and $\mathcal{D}^{\circ}_{j,i}$ as the concentration of either species changes. The variation, however, may not necessarily be linear and may have positive or negative deviations. This deviation may be considered by means of an additional factor such as an activity coefficient.

As discussed in chapter 4, since little information exists regarding the activity coefficients of the four NEC species, the liquid phase is assumed to be an ideal mixture of these four species. Caldwell and Babb [23] studied diffusion in ideal binary liquid mixtures and found that accurate predictions for diffusion coefficients in the entire concentration region can be made by calculating two diffusion coefficients at infinite dilution and interpolating for intermediate concentrations by using Equation 6.5.

$$\mathcal{D}_{i,j} = \mathcal{D}^{\circ}_{i,j} + x_i(\mathcal{D}^{\circ}_{j,i} - \mathcal{D}^{\circ}_{i,j}) \tag{6.5}$$

Following this method to calculate all binary molecular diffusion coefficients among each species pair in an NEC liquid mixture, the mixture molecular diffusion coefficients can now be calculated per Equation 6.3.

Mechanical dispersion

In the context of flow through packed beds, mechanical dispersion refers to the spreading of solutes, or in this case LOHC species, thanks to the advection of flow through the packed bed. Mechanical dispersion plays a significant role because of the tortuous pore network within packed beds, which causes a variation of local flow velocities and hence spreading of the species. Since the current Eulerian multiphase CFD simulation does not explicitly model individual particles or the tortuous path, mechanical dispersion should be taken into account by a dispersion coefficient that contributes to the hydrodynamic dispersive flux, $\boldsymbol{J}^i_q$, in the species conservation equation. At a macroscopic level, the quantitative treatment of dispersion is based on Fick's law with the appropriate dispersion coefficients. In the radial direction, a radial dispersion coefficient, D_{r}, is used whereas an axial dispersion coefficient, D_{a}, is defined for the axial direction. Delgado [31] provides a review of these two dispersion coefficients, along with empirical correlations for their estimation.

In a broad sense, both radial and axial dispersion coefficients are functions of the dimensions of the packed column, tube-to-particle diameter ratio, particle size distribution, particle shape, packing density, fluid properties, fluid velocity, and temperature. Delgado [31] explains each of these dependencies and ultimately proposes his own correlations valid for a wide range of Peclet and Schmidt numbers. Equation 6.6 is the correlation proposed for estimating the radial dispersion coefficient and Equation 6.7 for the axial dispersion coefficient.

Radial dispersion coefficient:
For $Sc < 550$ and $Pe_{\mathrm{m}} > 1600$:

$$Pe_{\mathrm{r}} = (0.058Sc + 14) - (0.058Sc + 2)\mathsf{exp}\left(-\frac{352Sc^{0.5}}{Pe_{\mathrm{m}}}\right) \tag{6.6a}$$

For $Sc < 550$ and $Pe_{\mathrm{m}} \leq 1600$:

$$\frac{1}{Pe_{\mathrm{r}}} = \frac{1}{\tau Pe_{\mathrm{m}}} + \frac{1}{12} - \left(\frac{Sc}{1500}\right)^{4.8} (\tau Pe_{\mathrm{m}})^{3.83 - 1.3\log_{10}(Sc)} \tag{6.6b}$$

For $Sc > 550$ and $Pe_m > 1600$:

$$Pe_r = 45.9 - 33.9 \exp\left(-\frac{15Sc}{Pe_m}\right) \qquad (6.6c)$$

For $Sc > 550$ and $Pe_m \leq 1600$:

$$\frac{1}{Pe_r} = \frac{1}{\tau Pe_m} + \frac{1}{12} - 8.1 \times 10^{-3} \left(\tau Pe_m\right)^{0.268} \qquad (6.6d)$$

Axial dispersion coefficient:

$$\frac{1}{Pe_a} = \frac{Pe_m}{5}(1-p)^2 + \frac{Pe_m^2}{25}p(1-p)^3 \left[\exp\left(-\frac{5}{p(1-p)Pe_m}\right) - 1\right] + \frac{1}{\tau Pe_m} \qquad (6.7a)$$

$$p = \frac{0.48}{Sc^{0.15}} + \left(\frac{1}{2} - \frac{0.48}{Sc^{0.15}}\right)\exp\left(-\frac{75Sc}{Pe_m}\right) \qquad (6.7b)$$

where:

$Pe_r = Ud_p/D_r =$ Peclet number based on radial dispersion coefficient [-]
$Pe_a = Ud_p/D_a =$ Peclet number based on axial dispersion coefficient [-]
$Pe_m = Ud_p/D_m =$ Peclet number based on molecular diffusion coefficient [-]
$\tau \quad =$ Tortuosity factor [-]; $\tau = \sqrt{2}$ for spheres and 1.93 for cylinders [85].
$D_r \quad =$ Radial dispersion coefficient [m^2/s]
$D_a \quad =$ Axial dispersion coefficient [m^2/s]
$D_m \quad =$ Mixture molecular diffusion coefficient [m^2/s]
$Sc \quad = \mu/\rho D_m$ Schmidt number [-]

Hydrodynamic dispersion in a NEC dehydrogenation reactor

To have a better understanding of molecular diffusion and mechanical dispersion in the current application, a first estimate of their values will be made. As an example, with the conditions defined in Table 6.1 and material properties calculated per relations presented in chapter 4, the molecular diffusion and mechanical dispersion coefficients will be estimated.

Table 6.1: Parameters for calculating molecular diffusion and mechanical dispersion coefficients.

Parameter	Symbol	Value
Temperature [K]	T	500
Particle diameter [m]	d_p	0.003
Interstitial liquid velocity [m/s]	U	0.002
Association factor [-]	ϕ	1
Tortuosity factor [-]	τ	$\sqrt{2}$
Mole fraction of species 1 (0H-NEC) [-]	x_1	0.05
Mole fraction of species 2 (4H-NEC) [-]	x_2	0.20
Mole fraction of species 3 (8H-NEC) [-]	x_3	0.25
Mole fraction of species 4 (12H-NEC) [-]	x_4	0.50

Table 6.2 gives the values of the binary molecular diffusion coefficients at infinite dilution for the four NEC species and the value for the mixture molecular diffusion coefficient for each species at the conditions given in Table 6.1. Furthermore, Figure 6.2 shows the interpolated values for the binary molecular diffusion coefficients at different molar concentrations of the species considering ideal liquid mixtures.

Table 6.2: Molecular diffusion coefficients at infinite dilution and in mixture for four NEC species at 500 K (species 1: 0H-NEC; species 2: 4H-NEC; species 3: 8H-NEC; species 4: 12H-NEC).

Parameter	Value [m^2/s]
Binary molecular diffusion coefficient at infinite dilution	
$\mathcal{D}^{\circ}_{1,2}$	2.86×10^{-9}
$\mathcal{D}^{\circ}_{1,3}$	7.59×10^{-9}
$\mathcal{D}^{\circ}_{1,4}$	2.86×10^{-9}
$\mathcal{D}^{\circ}_{2,1}$	1.96×10^{-9}
$\mathcal{D}^{\circ}_{2,3}$	7.27×10^{-9}
$\mathcal{D}^{\circ}_{2,4}$	2.74×10^{-9}
$\mathcal{D}^{\circ}_{3,1}$	1.92×10^{-9}
$\mathcal{D}^{\circ}_{3,2}$	2.68×10^{-9}
$\mathcal{D}^{\circ}_{3,4}$	2.67×10^{-9}
$\mathcal{D}^{\circ}_{4,1}$	1.82×10^{-9}
$\mathcal{D}^{\circ}_{4,2}$	2.55×10^{-9}
$\mathcal{D}^{\circ}_{4,3}$	6.76×10^{-9}
Molecular diffusion coefficient in mixture	
$D_{1,m}$	3.24×10^{-9}
$D_{2,m}$	3.17×10^{-9}
$D_{3,m}$	4.42×10^{-9}
$D_{4,m}$	3.23×10^{-9}
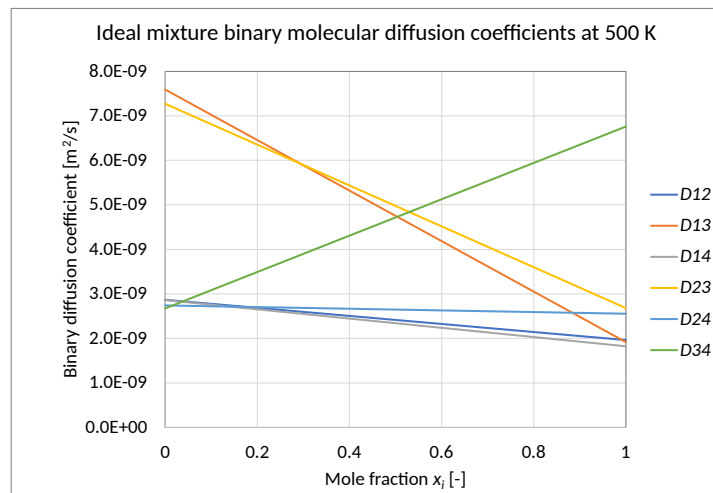
Figure 6.2: Ideal mixture binary molecular diffusion coefficients for four NEC species at 500 K (species 1: 0H-NEC, species 2: 4H-NEC, species 3: 8H-NEC, species 4: 12H-NEC).

Next, the axial and radial dispersion coefficients are estimated for the same conditions and presented in Table 6.3.

Table 6.3: Axial and radial dispersion coefficients for parameters in Table 6.1.

Parameter	Value [m²/s]
$D_{a,1}$	1.19×10^{-5}
$D_{a,2}$	1.13×10^{-5}
$D_{a,3}$	8.34×10^{-6}
$D_{a,4}$	1.16×10^{-5}
$D_{r,1}$	1.83×10^{-7}
$D_{r,2}$	2.13×10^{-7}
$D_{r,3}$	3.76×10^{-7}
$D_{r,4}$	1.97×10^{-7}

It is important to emphasize the magnitude of the above coefficients and observe that the mechanical dispersion coefficients are between 2 and 4 orders of magnitude higher than the molecular diffusion coefficients. This will be discussed further on.

6.2. Implementation

Model setup

Having understood the species conservation equation and the methodology to estimate both components of the hydrodynamic dispersion coefficient, species transport can now be implemented into the CFD model. First, the same geometry and mesh used in previous tests will be used. Then, species transport is enabled within the software and the liquid phase is defined as a mixture of the four LOHC species. Here, it is important to define the liquid phase properties per the mixing rules discussed in chapter 4. This way, the liquid phase material properties will be calculated from the four LOHC species properties and their mass fraction at every cell. Additionally, in order to account for hydrodynamic dispersion, a diffusion coefficient must be specified for the liquid mixture. The value for this coefficient will be discussed further on.

Boundary conditions and solution methods

In addition to the boundary conditions described in earlier tests, there are now additional boundary conditions to consider for species transport. At the domain inlet, the mass fraction of each species must be specified to fully define the liquid mixture entering the domain. Likewise, it is necessary to specify the species mass fractions at the outlet in case of liquid backflow. In the current study, the outlet mass fractions are not known beforehand as they will depend on the reaction's progress. A long outlet section is in place after the packed-bed section, intended to confine any liquid backflow to the vicinity of the outlet, where it can eventually be pushed out by the incoming flow. The solution of the CFD model should therefore not be too sensitive to the specified backflow species mass fractions. Nevertheless, to minimize any disturbance to the flow caused by the prescribed backflow species mass fractions, a UDF analogous to the one employed for the outlet temperature is used. This UDF will read the species mass fractions at the cells adjacent to the outlet boundary and use this profile for the backflow condition. Consequently, a zero normal derivative condition is imposed ($\frac{\delta x^i}{z} = 0$). The UDF providing this boundary condition is referenced in section A.14.

Lastly, by adding the species conservation equation to the model, a spatial discretization method for the equation of each species should be selected. As with other spatial discretization methods, a second-order upwind spatial discretization scheme is used.

Dispersion visualization

To verify the correct implementation of species transport in the model and to observe the effect of both molecular diffusion and mechanical dispersion, a test will be conducted where the inlet is divided in two sections and different species are input from either side. This is exemplified by Figure 6.3 where the inner half of the inlet is defined to introduce 12H-NEC and the outer half 0H-NEC. This will help observing how molecular diffusion and mechanical dispersion cause the species to mix throughout the reactor's length. The parameters used for this test will remain consistent with those employed in the previous heat transfer model validation test, as outlined in Table 5.6.
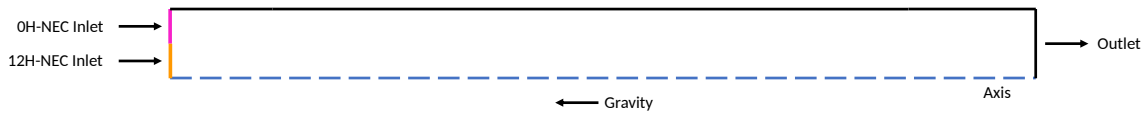
Figure 6.3: Inlet species boundary conditions for testing hydrodynamic dispersion.

The diffusion coefficient for the liquid mixture is first set to a constant value of 3.5×10^{-9} m²/s. This value is chosen to be in the same order of magnitude as the molecular diffusion coefficients previously calculated for the mixture, as provided in Table 6.2. The outcome of this test is depicted in Figure 6.4, where it is evident that minimal mixing occurs as 0H-NEC and 12H-NEC remain separate throughout the reactor. This result suggests that for the operating conditions expected in an NEC dehydrogenation reactor, molecular diffusion does not play a significant role.
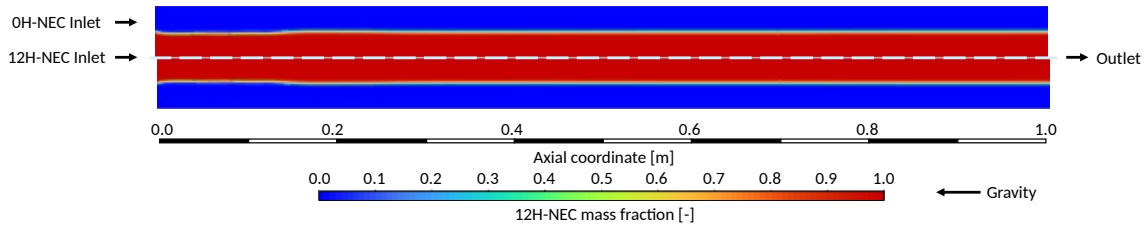
Figure 6.4: 12H-NEC mass fraction contour considering solely molecular diffusion.

The mechanical dispersion coefficients, nonetheless, were found to be a few orders of magnitude higher than the molecular diffusion coefficients. As a result, its effect is expected to be more noticeable. The diffusion coefficient in the CFD model is now set to a value of 3×10^{-7} m²/s, in line with the radial dispersion coefficients estimated in Table 6.3. The resulting 12H-NEC mass fraction contour plot is shown in Figure 6.5 where the mixing of species due to mechanical dispersion is now evident.
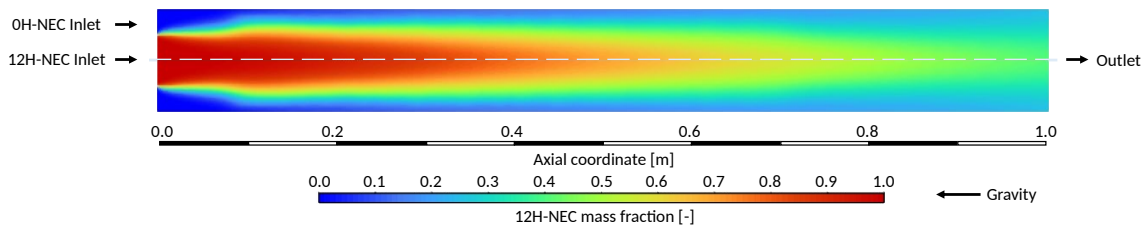
Figure 6.5: 12H-NEC mass fraction contour considering mechanical dispersion.

Given the considerable disparity in magnitude between the values of molecular diffusion and mechanical dispersion, it is reasonable to neglect the contribution of molecular diffusion to hydrodynamic dispersion. The coefficient used to solve for the hydrodynamic dispersive flux, $\boldsymbol{J}_q^i$, in the species transport equation should therefore be the axial and radial dispersion coefficients for each of the four species. In CFD software ANSYS Fluent 2021 R2, however, only a single coefficient can be specified for the entire liquid mixture. As the main objective of including hydrodynamic dispersion into the simulation is to model the radial spreading of the species within the reactor due to the tortuous path, a value for the radial dispersion coefficient will be used. By selecting a value for radial dispersion coefficient, the same value will also be applied in the axial direction. However, in the axial direction, species transport is dominated by advection, making the influence of mechanical diffusion minimal.

Furthermore, to obtain a single dispersion coefficient for the LOHC liquid mixture, a mass fraction weighted average coefficient of the four species will be calculated. This computation will be facilitated through a UDF referenced in section A.15. Although the contribution of the molecular diffusion coefficient will not be taken into account for the hydrodynamic dispersion coefficient, the UDF will initially calculate the molecular diffusion coefficients as they are required for evaluating Equation 6.7 and Equation 6.6 to calculate mechanical dispersion coefficients. After calculating radial dispersion coefficients for each species, the UDF reads the local mass fractions to calculate a mass-weighted average dispersion coefficient for each cell.

7

Comprehensive CFD model

Having developed the key aspects of the CFD model and verified them independently, they can now be integrated to obtain a comprehensive LOHC dehydrogenation model. This chapter will follow the structure represented by Figure 7.1. First, the model will be setup for a baseline case representing an experimental setup used in an NEC dehydrogenation study. The results of this case will be analyzed focusing on the various aspects studied in this thesis. Then a series of four sensitivity analyses will be conducted to understand the effect of four input parameters on the reactor behavior. Finally, with the insight gained from the sensitivity analyses, a reactor design will be proposed.

Complete CFD Model
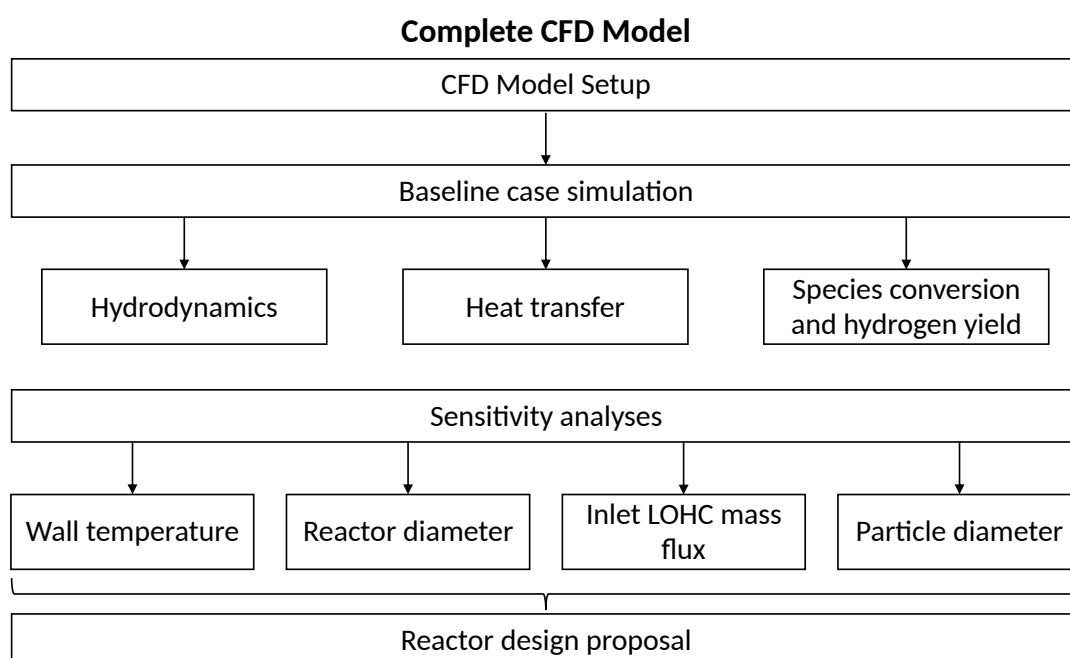
Figure 7.1: Overview of chapter 7.

7.1. CFD model setup

As a starting point, a CFD model will be created following the setup of a packed-bed NEC dehydrogenation reactor found in literature. Table 7.1 presents three studies concerning NEC dehydrogenation in packed-bed reactors. The investigations conducted by Heublein et al. [48] and Peters et al. [116] are two experimental studies using a Pd/Al$_2$O$_3$ catalyst. Heublein et al,'s research studies a 2 m long reactor, whereas Peters et al. focus on a short 6 cm long reactor. Additionally, Yang et al. developed a CFD simulation for a 2 m long reactor. In their simulation however, they have used a mixture model, the porosity profile is not contemplated, and a plug flow is assumed. Given these findings, the current CFD simulation will utilize the reactor geometry and inlet conditions employed by Heublein et al. [48].

Table 7.1: Fixed-bed reactor NEC dehydrogenation studies

	Heublein et al. [48]	Yang et al. [144]	Peters et al. [116]
Approach	Experimental	CFD simulation	Experimental
Reactor diameter [mm]	29.7	29.7	8
Reactor length	2 m	2 m	6 cm
Catalyst	0.5 wt% Pd/Al$_2$O$_3$	N/A	Pd/Al$_2$O$_3$ with different Pd weights
Pellet diameter [mm]	3.2 (Cylindrical)	N/A	3 (Spherical)
Reaction kinetics	Not measured	Estimated	Provides Arrhenius plots for overall reaction
Inlet temperature [K]	373	400	493−539
Inlet liquid mass flux [kg/m^{2}s]	0.6	0.50−1.10	0.05−0.21
Heating temperature [K]	503−553	481−523	493−539
Operating pressure [bar]	1−7	1	1

So far, the CFD model has been set up for an Eulerian multiphase simulation, with the NEC liquid mixture defined as the primary phase, H$_2$ gas a secondary phase, and alumina catalyst pellets as a stationary secondary phase. In chapter 3, interphase momentum exchange coefficients, capillary pressure effects, and the solid volume fraction profile were defined. Subsequently, all material properties were defined in section 4.1 and the chemical kinetics measured by Dong et al. [32] have been adopted. After quantifying the distinct heat transfer resistances in chapter 5, a pseudo-homogeneous heat transfer model was implemented in which a single temperature field is shared by all phases. Finally, species transport, including hydrodynamic diffusion effects, was integrated in chapter 6. With these aspects incorporated into the CFD model, a simulation following the input parameters detailed in Table 7.2 will now be conducted.

Table 7.2: Input parameters for complete NEC dehydrogenation CFD model.

Input parameter	Value
Flow configuration	Cocurrent upward flow
Fluid system	H2 - NEC
Reactor diameter [m]	0.0297
Reactor length [m]	2
Particle diameter [m]	0.003
Particle Shape	Spherical
Sphericity [-]	1
Mesh size	$0.7 \times d_p$
Ergun constant 1 [-]	215
Ergun constant 2 [-]	1.8
Inlet liquid mass flux [kg/m^{2}s]	0.6
Inlet temperature [K]	400
Inlet 12H-NEC mass fraction [-]	1
Wall temperature [K]	550
Reaction Kinetics	Dong et al. [32]
Operating pressure [bar]	5

The inlet temperature is set at 400 K, chosen as a preheating temperature for the LOHC before entering the reactor similar to that used by Heublein et al. [48]. Moreover, although the reaction kinetics established by Dong et al. [32] were determined under atmospheric pressure conditions, a higher

operating pressure of 5 bar is selected for the simulation. From a practical standpoint, operating the reactor at pressures above atmospheric is advantageous as it reduces the need for extensive compression of the hydrogen product for subsequent downstream processes. Heublein et al. [48] tested their experimental setup with pressures of up to 7 bar and found that up to 5 bar, similar hydrogen yields are obtained. Thus, assuming that the reaction kinetics have not been significantly impeded at 5 bar, an operating pressure of 5 bar is selected, retaining the reaction kinetics outlined by Dong et al. [32].

The boundary conditions for this complete model are recapped as follows:
Inlet boundary conditions:

- Inlet liquid mass flux
- Inlet temperature
- Inlet species mass fractions

Wall boundary conditions:

- No-slip boundary condition
- No-penetration boundary condition
- Zero heat flux at 'inlet' and 'outlet' section walls
- Convective boundary condition at the 'packed bed' section wall

Axis boundary condition.
Outlet boundary conditions:

- Zero gauge pressure outlet
- Zero temperature normal derivative boundary condition
- Zero species mass fraction normal derivative boundary condition

Solid phase conditions:

- Zero axial and radial velocity (fixed-bed)
- Predefined solid volume fraction profile

From this list, the only distinction from prior simulations is the inlet liquid mass flux boundary condition. While previous simulations employed a velocity inlet boundary condition for both gas and liquid input, now only a liquid input will be defined. By defining the liquid input through a mass flux inlet boundary condition, no estimate of liquid holdup or liquid interstitial velocity needs to be made. Imposing the desired liquid mass flux directly in kg/m^{2}s minimizes any discrepancy between the intended inlet mass flux and the applied value.

Furthermore, a summary of the solution methods and under-relaxation factors used for this simulation are given in Table 7.3.

Table 7.3: Solution parameters

Solution Method Setting	
Pressure-Velocity Coupling	SIMPLE
Solve N-phase Volume fraction equations	Yes
Gradient calculation method	Least squares cell based
Pressure spatial discretization	Body force weighted
Density spatial discretization	2nd order upwind
Momentum spatial discretization	2nd order upwind
Volume fraction spatial discretization	1st order upwind
Energy spatial discretization	2nd order upwind
Liquid species spatial discretization	2nd order upwind
Reference density method	Volumetric form (Ansys Fluent option 3)
Under-Relaxation Factors	
Pressure	0.3
Density	0.6
Body Forces	0.6
Momentum	0.2
Volume Fraction	0.1
Energy	0.6
Species	0.6

7.1.1. Visualization

Several UDFs were developed to facilitate solution monitoring and result visualization. The first UDF, introduced in chapter 3, calculates the mass flow rate of both fluids at every plane within the domain using Equation 3.16. This UDF is executed at each iteration to allow real-time tracking of mass flow rate imbalances throughout the solution process.

A second, found in section A.16, UDF was designed to help visualize the results and calculate volume-weighted average properties at every cell plane in the reactor axial direction. The UDF accesses property values along with the cell volume considering that since the domain is 2D axisymmetric, each cell represents a 3D ring-like element. The calculation procedure is depicted by Figure 7.2a where the volume-weighted average of any property ϕ at the jth plane for the qth phase is calculated per Equation 7.1.

Similarly, another UDF, presented in section A.17, focuses on calculating mass-weighted average properties, which may be more relevant for some properties compared to volume-weighted average values. The distinction lies in accounting for the mass of fluid within a cell, as opposed to relying on the cell's volume. This is calculated using Equation 7.2 and is represented by Figure 7.2a. The mass of each phase in this equation is calculated as previously discussed using Equation 3.16. Both the volume-weighted average and mass-weighted average UDFs can be executed at the end of the simulation procedure to provide insight into the final simulation results.

$$\phi_{j,q,\text{volume}} = \frac{\sum_{i=1}^{n} \phi_{i,q} V_i}{\sum_{i=1}^{n} V_i} \tag{7.1}$$

$$\phi_{j,q,\text{mass}} = \frac{\sum_{i=1}^{n} \phi_{i,q} \dot{m}_{i,q}}{\sum_{i=1}^{n} \dot{m}_{i,q}} \tag{7.2}$$

where:

$\phi_{j,q,\text{volume}}$ = Volume-weighted average of property ϕ at plane j
$\phi_{i,q}$ = Value of property ϕ at cell i for qth phase
V_i = Volume of cell i [m^3]
$\phi_{j,q,\text{mass}}$ = Mass-weighted average of property ϕ at plane j

(a) Volume-weighted property calculation.

(b) Mass-weighted property calculation.
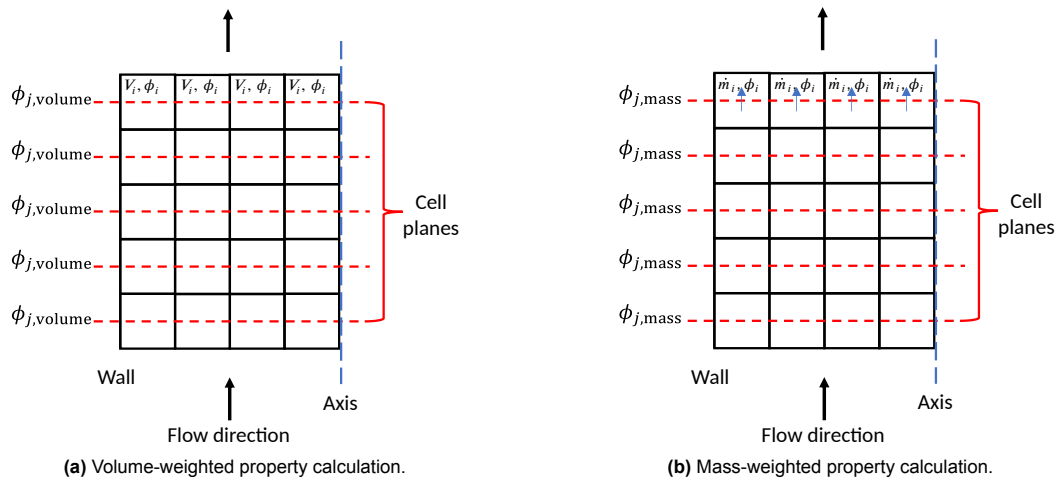
7.1.2. Stability and convergence

While running this simulation, several challenges were encountered regarding its stability and convergence. These difficulties manifested as high mass imbalances, reversed flow within the reactor, and oscillating flow parameters along the length of the reactor.

This CFD simulation models an intricately coupled system involving interacting effects that may trigger numerical instabilities. One of the primary sources of instability stems from the solid volume fraction profile, made to represent the packed bed. While it was carefully designed to combine a radial profile and axial variations through a continuous function, the resulting profile still exhibits variation across the domain's cells. This causes increased gradients in flow parameters between adjacent cells which can potentially lead to numerical instabilities. However, retaining this profile is vital, as it dictates the flow behavior within the reactor.

Another factor contributing to stability and convergence issues is the highly gas-producing nature of LOHC dehydrogenation. As previously mentioned, 1 ml of 12H-NEC can yield 619 ml of hydrogen gas at standard temperature and pressure upon complete dehydrogenation. Even at conditions expected in the reactor such as 550 K, 5 bar, and 20% hydrogen yield, a substantial volume of around 40 ml of hydrogen per ml of 12H-NEC is still produced. The present CFD simulations found that as soon as the temperature rises within the reactor, gas production rapidly increases, leading to a surge in the gas volume fraction. A visual representation in Figure 7.3 shows the plane volume-weighted average gas volume fraction along the reactor length. Notably, the graph demonstrates that shortly after the reaction begins, the gas volume fraction rapidly increases, also meaning that the liquid volume fraction rapidly decreases. Consequently, to conserve mass balance, the velocities of both fluids must quickly adapt, causing a rapid change in the interphase momentum exchange coefficient governed by the selected two-fluid momentum interaction model. This abrupt change in variables across a short distance was observed to induce instabilities.
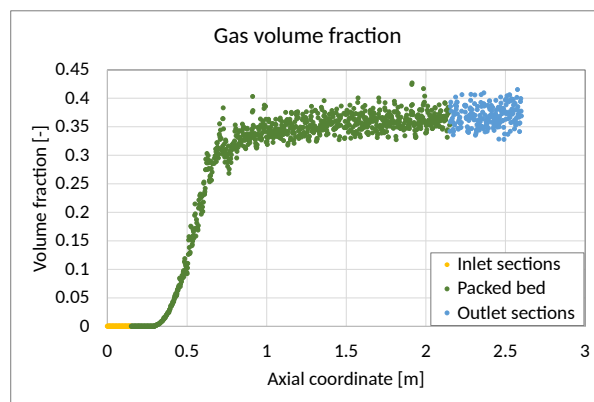
Figure 7.3: Plane averaged gas volume fraction along the length of the reactor for input parameters detailed in Table 7.2

Specifically, one of the issues observed was the occurrence of reversed flow within the domain, as depicted in Figure 7.4a and Figure 7.4b. Figure 7.4a plots the plane-average liquid mass flow rate in kg/s along the reactor's length. In an ideal scenario of mass conservation, this plot should a remain a nearly horizontal line with a low decline of up to 5.8%, corresponding to the hydrogen released during the dehydrogenation reaction. However, in Figure 7.4a, after the reaction rate increases and much gas is released, the mass flow of liquid experiences a sudden drop, thus disrupting mass conservation. Moreover, Figure 7.4b illustrates the liquid velocity vectors around this mass flow drop. It is noteworthy to observe that to the right of the drop, the liquid vectors point upstream, indicating a reverse flow. Further investigation revealed that this reversed flow was initiated by the sudden decrease in liquid volume fraction at this point which in turn meant a sudden increase in liquid-solid interphase momentum exchange coefficient, K_{LS}, and high capillary forces in this area.

(a) Plane liquid mass flow rate exhibiting significant backflow along the length of the reactor for input parameters detailed in Table 7.2.

(b) Liquid velocity vectors at the point of mass flow rate drop.
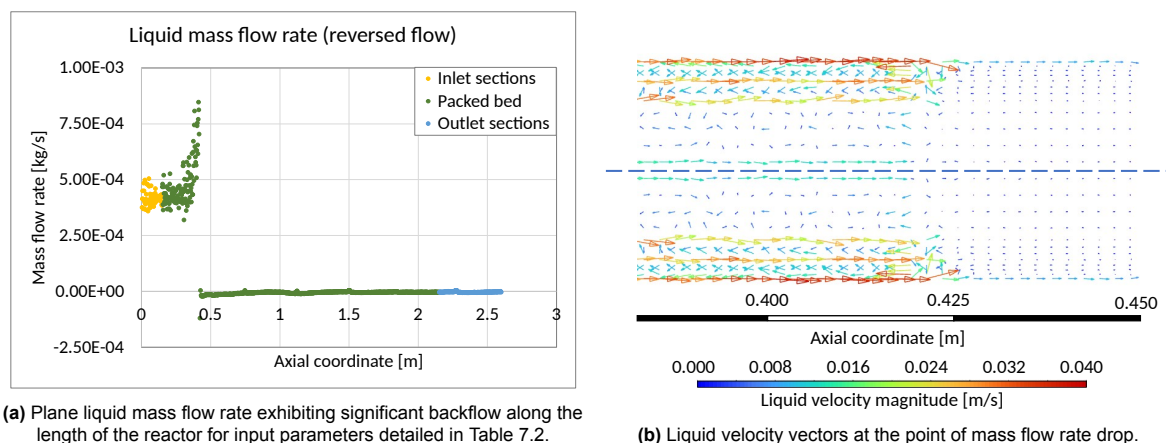
Figure 7.4: Simulation instability caused as seen by reversed flow within the reactor, and high mass imbalance.

When graphed as a function of liquid volume fraction for representative parameters, the liquid-solid interphase momentum exchange coefficient, as defined by Equation 3.1c, produces the curve shown in Figure 7.5. It becomes apparent that at low liquid volume fractions, ε_L, the value of K_{LS} spikes. This behavior was previously identified in chapter 3, and a minimum volume fraction limit of 5% had been set. However, when studying the hydrodynamics independently, the flow was non-reacting, and the volume fractions were approximately constant throughout the reactor. Now that the reaction has been added, when gas production begins in the simulation, the liquid mass fraction drops from around 36% to between 5-10% in a short distance, causing the value of K_{LS} to spike. In the simulation ending in reversed flow, this K_{LS} spike caused a very large momentum term of value $-K_{LS}U_L$, effectively stripping all of the liquid's upward momentum and causing it to instead change direction due to the downwards gravitational acceleration. This issue was found to occur at the low inlet liquid velocities expected for LOHC dehydrogenation. At such reduced speeds, the liquid does not have much momentum, so a sudden addition of negative momentum can cause the liquid to stall and redirection.

It is important to highlight that the behavior exhibited by the K_{LS} term plotted in Figure 7.5 is not unique to the two-fluid interaction model. The spike of K_{LS} at low liquid volume fractions is also observed by the relative permeability model [120], the single-slit model [49], and various drag models developed for single-phase flow through beds, such as the Gidaspow [39] and Syamlal-O'Brien [131] models. However, it is worth noting that in single-phase flow models, the liquid volume fraction would not drop below approximately 30% as dictated by the solid particle packing limit. Furthermore, even in the models specifically developed for trickle beds explored in this thesis, the liquid volume fraction would tend to remain relatively stable, as these models consider a constant gas and liquid input. Therefore, the change in gas and liquid volume fractions observed in this simulation is something unexplored by the aforementioned momentum interaction models.
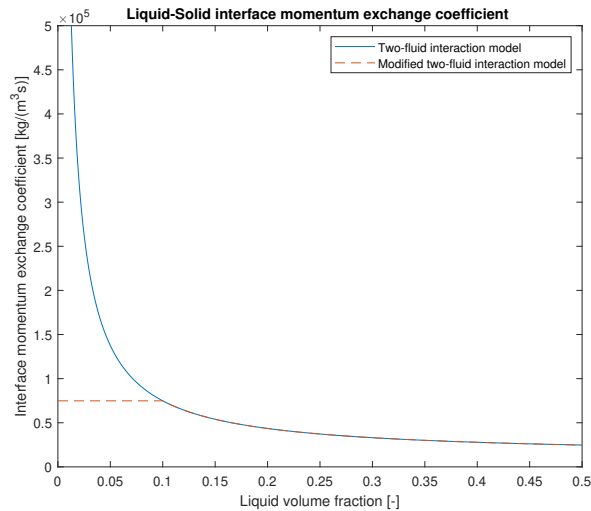
Figure 7.5: Liquid-solid interphase momentum exchange coefficient, K_{LS}, as a function of liquid volume fraction.

To mitigate these issues, a few measures were found to be effective. First, the limit imposed on the three interphase momentum exchange coefficients was increased to a liquid or gas volume fraction of 10% as represented by Figure 7.5. This helped avoid such an abrupt surge in the interphase momentum exchange coefficients triggered by the change in fluid volume fractions. Furthermore, in addition to the gas-liquid momentum exchange coefficient, K_{GL}, calculated from the two-fluid momentum interaction model, an additional value of 0.2 was added to this coefficient. As the gas phase is accelerated upstream due to buoyancy, adding this term to the gas-liquid momentum exchange coefficient had the effect of accelerating the liquid phase along with the gas. This prevented the liquid from stalling and reduced numerical instabilities. The value was brought down to 0.2 through iterative testing and could not be further reduced due to the occurrence of liquid stalling. This may be a limitation of the two-fluid momentum interaction model for this application involving low speeds and high changes in volume fractions. Further investigation may be warranted to understand this aspect more comprehensively.

Another issue encountered during the current CFD simulation was oscillating flow parameters along the reactor. As an example, Figure 7.6 shows the liquid mass flow rate along the reactor at a certain point during the solution process. Despite many iterations at this point, the oscillations persisted without damping. To improve this issue, the solution process was started with 1st order spatial discretization schemes and switched to 2nd order discretization schemes further along in the process.
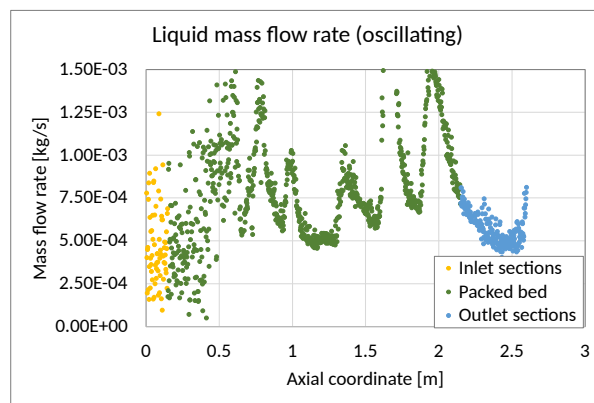
Figure 7.6: Plane liquid mass flow rate exhibiting oscillating features along the length of the reactor for input parameters detailed in Table 7.2.

For reference, Table 7.4 shows the solution procedure followed to obtain the results for the simulation with input parameters shown in Table 7.2. While there is potential for refining the sequence of

steps and number of iterations to reduce computational time, the current approach has proven to be satisfactory at this stage.

Table 7.4: Procedure followed to obtain solution for CFD model with input parameters shown in Table 7.2

Initialization	
Density, momentum, energy and liquid species spatial discretization	1st Order Upwind
Initialize flow and temperature fields from inlet values	
Patch solid volume fraction profile	
Remaining solution parameters per Table 7.3	
Iterations	35000
Further Modifications	
Density, momentum, energy and liquid species spatial discretization	2nd Order Upwind
Iterations	$15000 - 25000$

To assess the convergence of the simulation, several parameters were monitored: mass imbalance across the packed bed, pressure drop, hydrogen yield, and the sum of hydrogen yield and degree of dehydrogenation. To determine convergence, the hydrogen yield plus degree of dehydrogenation should remain within a range of 100%±2% for numerous iterations. This indicates that the species' mass fractions, and phase volume fractions are no longer changing. Furthermore, the pressure drop should also remain invariant, and the mass imbalance close to 0%. To exemplify these monitors and convergence criteria, Figures 7.7a through 7.7d plot the monitors for mass imbalance, pressure drop, hydrogen yield, and hydrogen yield plus degree of hydrogenation against the number of iterations in the solution process. Notably, the mass balance monitor presented the most fluctuations throughout the solution process as small oscillations developed. This, however, was found to have minor impact on the output parameter values as these remained stable despite the fluctuations.

(a) Mass imbalance calculated per Equation 3.17.

(b) Pressure drop across the packed-bed.

(c) Hydrogen yield at packed bed outlet.

(d) Hydrogen yield plus degree of hydrogenation at packed bed outlet.
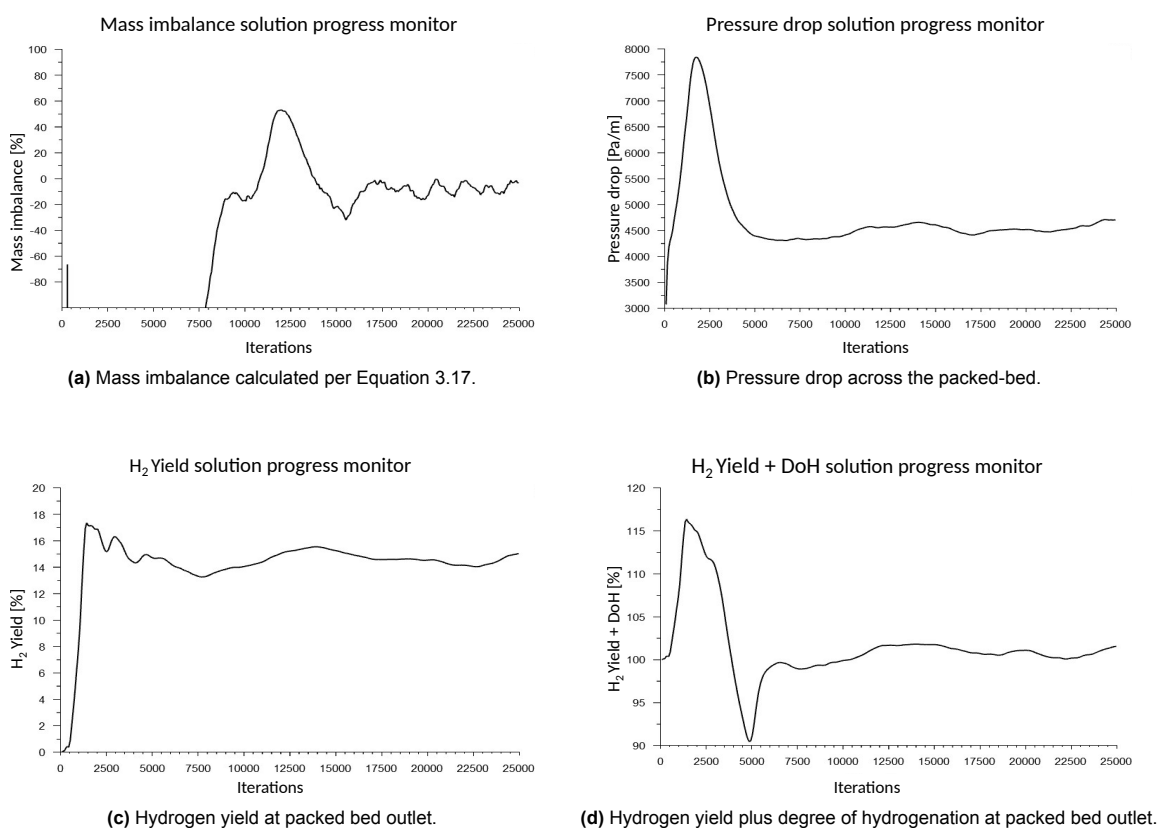
Figure 7.7: Monitors to help determine stability and convergence of the solution with input parameters detailed in Table 7.2.

Figure 7.8a plots the plane liquid mass flow rate along the reactor's length at the end of the solution process which can be compared to previously presented Figures 7.4a and 7.6. The liquid mass flow rate now remains approximately constant along the reactor, as expected to satisfy the mass balance. The noise observed in the plot arises from the varying porosity profile. This is why an average across both the 'inlet' and 'outlet' sections of the domain is computed to determine the output parameters and mass imbalance.
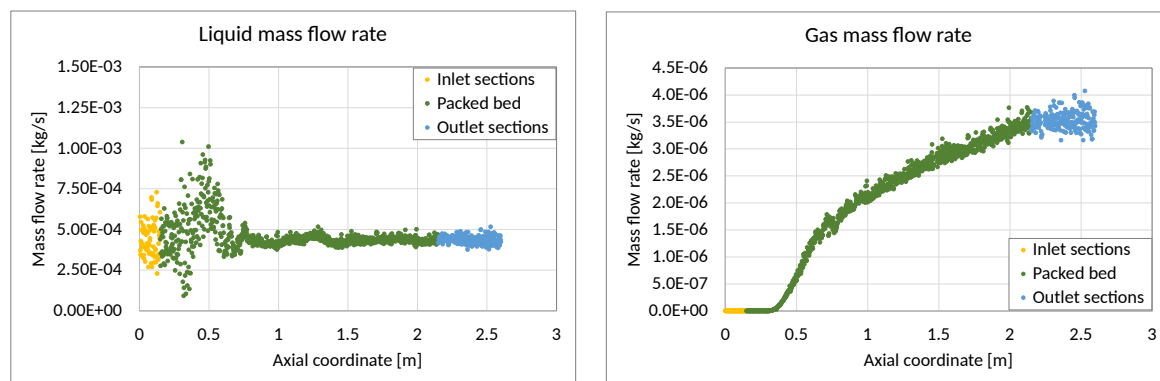
(a) Liquid mass flow rate exhibiting stable behavior along the length of the reactor.

(b) Gas mass flow rate monotonically increasing along the length of the reactor.

Figure 7.8: Plane mass flow rates along the length of the reactor for input parameters detailed in Table 7.2.

7.2. Baseline case results

The main output parameters of the baseline case simulation are summarized in Table 7.5. For a more structured approach, these results and further details will be discussed in the following sections focusing on the general themes discussed in this thesis.

Table 7.5: Main output parameters for simulation with input parameters detailed in Table 7.2

Output parameter	Units	Value
Pressure drop	[kPa/m]	4.94
Liquid holdup	[-]	0.091
Wetting efficiency	[%]	0.61
Outlet temperature	[K]	548.3
Hydrogen mass flow rate	[mg/s]	3.8
Hydrogen volumetric flow rate	[ml/s]	17.0
Hydrogen power output	[W]	451
Hydrogen yield	[%]	15.5
Outlet degree of hydrogenation	[%]	86.2
Heat of reaction	[W]	114
Wall heat transfer rate	[W]	275
Mass-average liquid axial velocity	[m/s]	0.032
Mass-average liquid residence time	[s]	62.3
Mass-average gas axial velocity	[m/s]	0.062
Gas mass flux	[kg/m^{2}s]	0.0054

7.2.1. Hydrodynamics

From a hydrodynamics perspective, the primary output parameters include pressure drop and liquid holdup. However, much can also be learned from examining the velocity and volume fraction fields. As indicated in Table 7.5, the recorded pressure drop is 4.9 kPa/m, and the average liquid holdup within the packed bed 9.1%. This value for liquid holdup is the bed average but it is important to understand how it evolves throughout the reactor. An alternative approach of visualizing liquid holdup is through liquid saturation, β_L, and gas saturation, α_G, which represent the proportion of either fluid in the interstitial

space. Figure 7.9 plots the plane volume-weighted average of liquid and gas saturation along the reactor. Notably, at the reactor inlet, liquid saturation equals unity in accordance with a pure liquid inlet boundary condition. Then, as the reaction begins, liquid saturation experiences a rapid decline as large volumes of gas are formed and displace the liquid. The rapid increase in gas saturation occurs in this reactor until an axial coordinate of around 0.75 m after which the gas saturation continues to slowly rise to a value of 0.94 at the reactor outlet meaning that only 6% of the interstitial space is left for the liquid phase.

Furthermore, Figure 7.10a and Figure 7.10b display the liquid and gas volume fraction contour plots, respectively. Near the reactor's entrance, a rapid decrease in the liquid volume fraction along the reactor length can be observed. Then, Figure 7.10a zooms in on at the last 0.1 m of the reactor where more stable liquid volume fractions between 2 and 4% are observed. The varying pattern in the figure can be attributed to the fluctuating solid volume fraction profile. It is important to notice, however, that the lower solid volume fraction near the reactor wall allows the fluids to take up more space, which as will be seen also corresponds to a higher fluid velocity in this region.
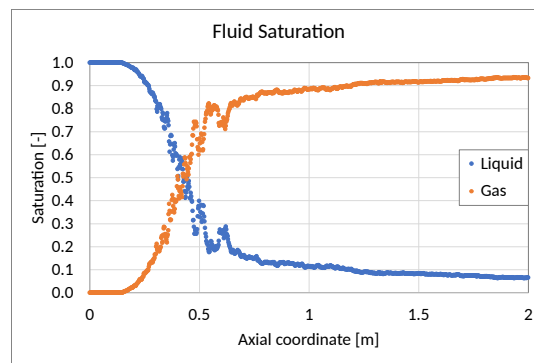
Figure 7.9: Plane volume-weighted average fluid phase saturation along reactor length for input parameters detailed in Table 7.2.
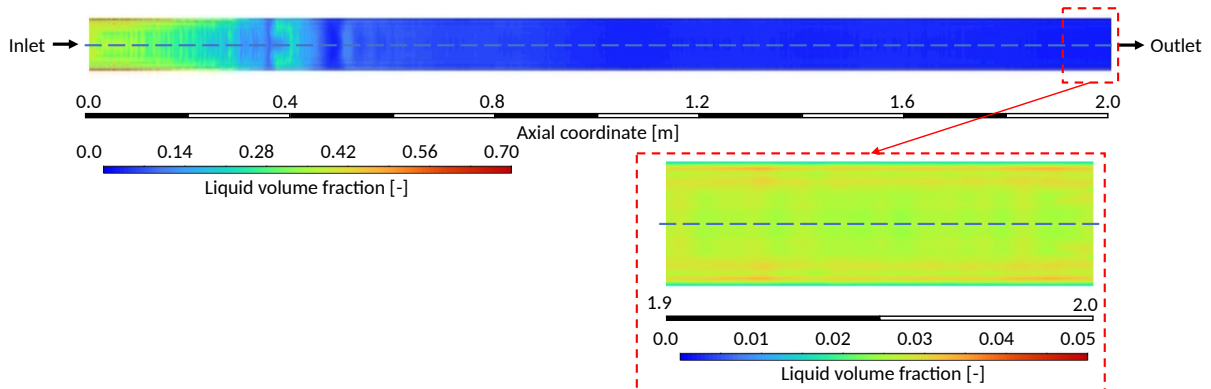
(a) Liquid volume fraction contour plot with zoomed section at the end of the packed bed.
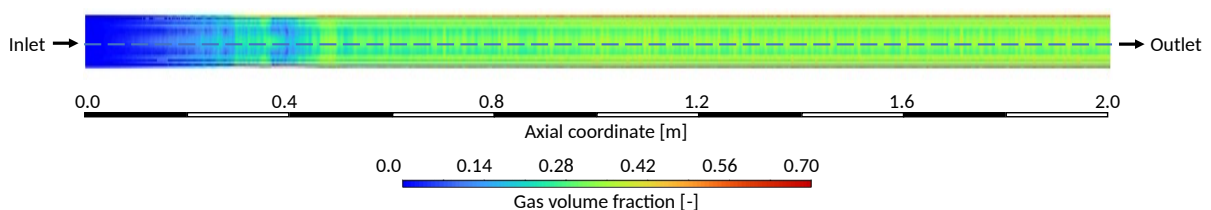
(b) Gas volume fraction contour plot.

Figure 7.10: Fluid volume fraction contour plots for input parameters detailed in Table 7.2.

The plots illustrating fluid saturation and volume fraction can be linked to fluid velocity contour plots and understood together. Figures 7.11a and 7.11b present the velocity magnitude contour plots of both phases. Notably, both phases exhibit an increase in velocity along the reactor. From the liquid's perspective, the rising velocity can be attributed to the declining volume fraction. In essence, the liquid must accelerate to maintain mass conservation as its volume fraction decreases. A faster flowing liquid means a shorter residence time in the reactor and as a result, less time for the LOHC to react.

From the gas phase's perspective, an increase in velocity can also be attributed to the continuous gas production which impulses the gas downstream. Additionally, due to the gas's lower density, the buoyancy force contributes to an upward acceleration of the gas. Figure 7.12 plots the radial profile of axial velocity for both fluid phases at the packed bed outlet. This figure shows the higher gas velocities compared to the liquid, and highlights the higher velocities of both fluids within the first two particle diameters from the reactor wall. The shape of these profiles aligns with the radial void fraction profile where in the vicinity of the wall, since solid volume fractions are lower, the fluids encounter less resistance and can speed up.
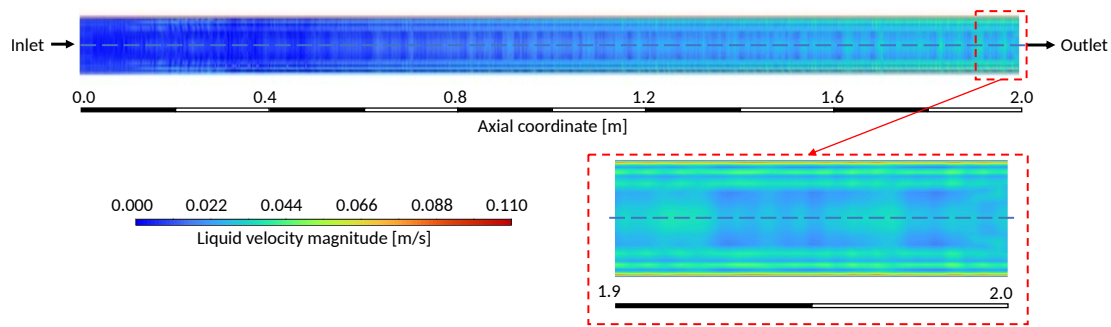
(a) Liquid velocity magnitude contour plot with zoomed section at the end of the packed bed.
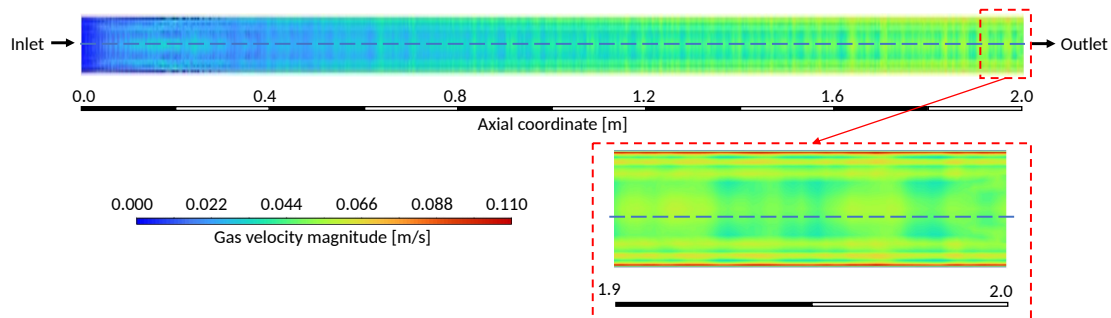
(b) Gas velocity magnitude contour plot with zoomed section at the end of the packed bed.

Figure 7.11: Velocity magnitude contour plots for input parameters detailed in Table 7.2.
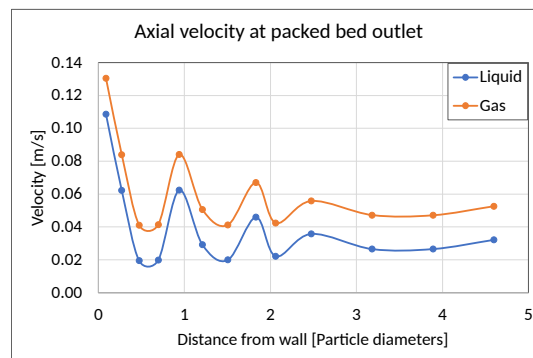
Figure 7.12: Liquid and gas radial velocity magnitude profile at packed bed outlet for input parameters detailed in Table 7.2.

To improve the understanding of the fluid's mass flow radial distribution, Figure 7.13a divides the radial length into equal sections of 0.5 times the particle diameter and shows the proportion of the total mass flow of liquid across each section along with the average axial velocity of the liquid at each of these sections on the secondary axis. The bars represent the proportion of liquid flowing through each section out of 100%, and the line represents the average axial velocity at each section. Likewise, Figure 7.13b shows the same information but for the gas phase. From these graphs, it can be observed that a significant amount of the fluid is channeled towards the wall. Figure 7.13a, shows that 25% of the liquid mass flows along the first half particle diameter from the wall at a velocity 140% higher than the average velocity across the rest of the cross-section. This means that more than a quarter of the liquid mass bypasses the bulk of the reactor at more than twice the speed, effectively reducing the residence time of this portion of liquid within the reactor and allowing less time for it to react and convert into the desired product. From the gas' perspective, 36% of mass flows within the first half particle diameter from the wall. In this case, the faster gas flow near the wall is beneficial as it releases the product from the bulk of the reactor, allowing more space for the liquid to contact the catalyst particles.

(a) Liquid mass flow proportions and axial velocities.

(b) Gas mass flow proportions and axial velocities.
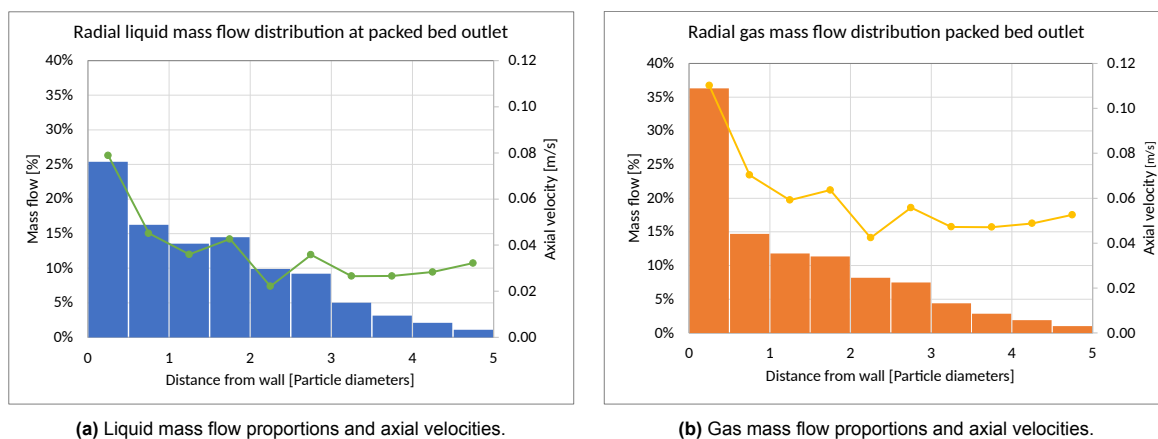
Figure 7.13: Proportion of fluid mass flow at a radial cross-section at the packed bed outlet as well as axial fluid velocities for input parameters detailed in Table 7.2.

By calculating a mass-average liquid axial velocity within the whole packed bed and dividing the length of the reactor by this velocity, an estimate can be made for the average residence time of the liquid within the reactor. As shown in Table 7.5, the mass-average liquid axial velocity for this simulation is 0.033 m/s which corresponds to an average liquid residence time of 60.5 s within the 2 m long reactor.

An interesting feature of the flow within this simulation becomes evident when visualizing the velocity vectors of both the liquid and gas phases. These vectors indicate both the direction and speed of the flow. Figures 7.14a through 7.14d show these vector plots at a section near the beginning reactor where the increase in gas saturation is most pronounced, as well as at a section at the reactor's end for both phases.

The gas velocity vectors, illustrated in Figure 7.14a and 7.14b, consistently point upstream with an increasing magnitude as the gas accelerates. In contrast, the behavior of liquid velocity vectors varies between the initial and final segments of the packed bed. In Figure 7.14c, during the reactor's early phase, the liquid velocity vectors display indications of altering direction and the emergence of minor vortex structures. As the liquid phase gains speed and momentum in the axial direction, these flow patterns dissipate, resulting in a more streamlined flow profile parallel to the reactor's axis.

It is worth noting that in a physical packed bed, the flow streamlines would not be perfectly straight as represented by the parallel velocity vectors in Figures 7.14b and 7.14d. Instead, the flow would follow a tortuous path around the catalyst particles. In the context of this Eulerian multiphase simulation, the fluid velocity values within each cell represent an averaged velocity within that segment, where the complexities of the tortuous paths are smoothed out, leaving the dominant axial velocity component. For this reason, radial mixing in this simulation is instead primarily considered through species dispersion.

(a) Gas velocity vectors zoomed towards the beginning of the packed-bed section.

(b) Gas velocity vectors zoomed towards the end of the packed-bed section.

(c) Liquid velocity vectors zoomed towards the beginning of the packed-bed section.

(d) Liquid velocity vectors zoomed towards the end of the packed-bed section.
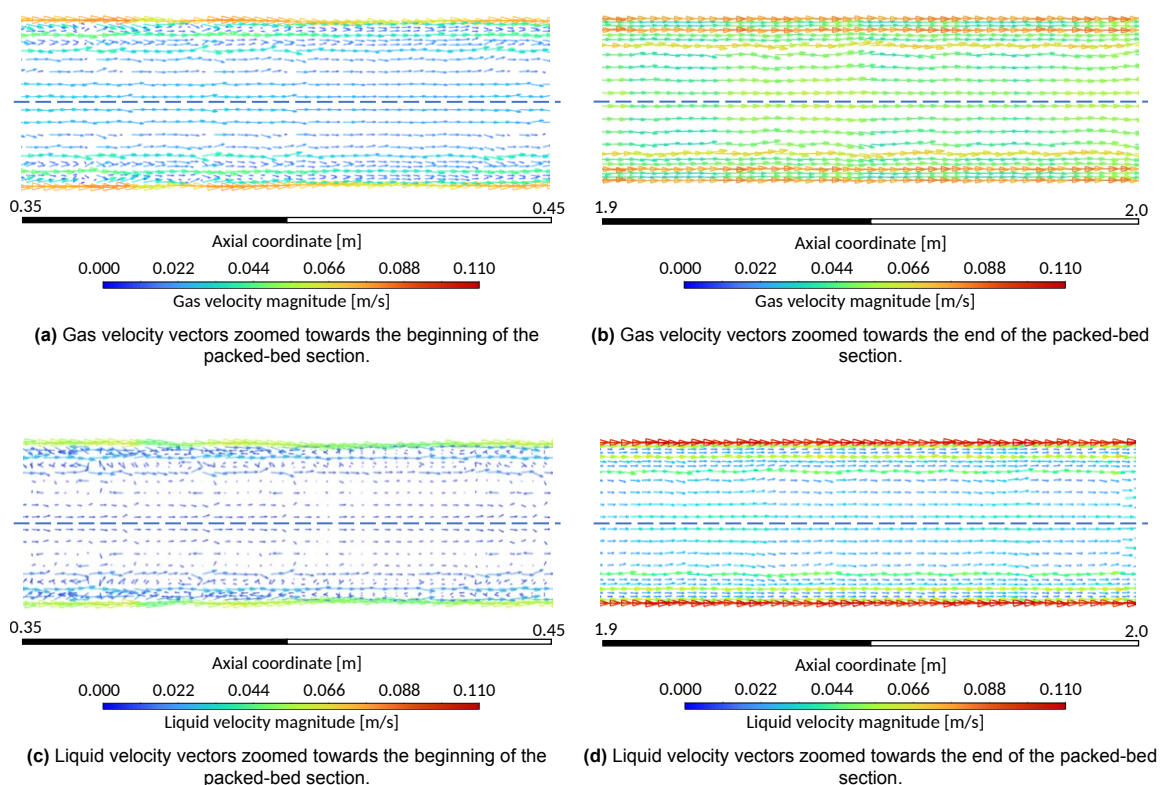
Figure 7.14: Velocity vectors for input parameters detailed in Table 7.2.

The average packed bed wetting efficiency is seen from Table 7.5 to be 57%. This can be further understood by plotting the wetting efficiency contour plot shown by Figure 7.15. This plot shows how the wetting efficiency transitions from 100% at the reactor inlet where no gas has been formed and quickly drops as would be expected in an environment with high gas saturation. A low wetting efficiency is undesired as it means much of the catalyst particles would not be in contact with the LOHC and their surface is not used to its maximum capacity. This graph, along with the preceding observations regarding fluid volume fraction and velocities leads to the conclusion that the high gas volumes produced reduce reactor efficiency and can lead to low hydrogen yields.
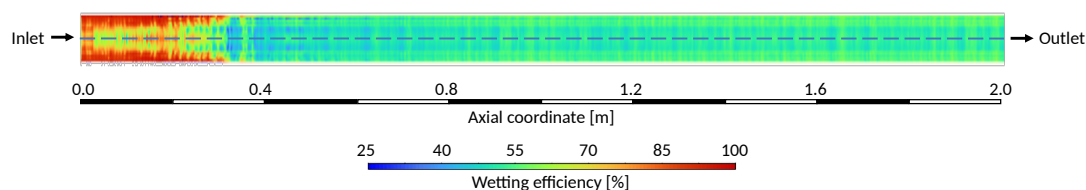
Figure 7.15: External particle wetting efficiency, η_{WE}, contour plot for input parameters detailed in Table 7.2.

Another important observation regarding hydrodynamics pertains to identifying the prevailing flow regime. As discussed in chapter 2, there is no universal criteria available to predetermine the flow regime in cocurrent packed-bed upflow reactors. Instead, the existing flow maps should be applied within the flow properties for which they were developed. In this case, the liquid mass flux, L, is 0.6 kg/m²s, and from Table 7.5, the gas mass flux, G, resulted in 0.0054 kg/m²s. Both of these fluxes fall below the values reported by the flow maps in the literature. The closest match, however, is the work by Murugesan and Sivakumar [106] introduced by their flow map in Figure 2.7b. In their criteria, the flow regime can either be bubble flow, dispersed bubble flow, or pulsed flow. Figure 7.16 evaluates Murugesan and Sivakumar's [106] criteria with local flow properties at every cell and determines which of these flow regimes would be present. The simulation's data indicates that bubble flow prevails up to a height of 1.2 m, as characterized by the relatively low fluid flow rates. However, as the flow speeds up towards the end of the reactor, the flow transitions into a pulsed flow.
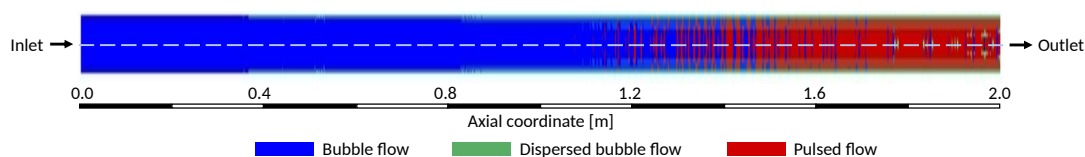
Figure 7.16: Flow regime calculated per Murugesan and Sivakumar's [106] flow map for input parameters given in Table 7.2.

An important assumption of this model is that of laminar flow, in that no turbulence model was incorporated to represent the effect turbulent structures in the flow. A way to review this assumption is by calculating the particle Reynolds number throughout the domain to determine whether the flow is turbulent. As Dybbs and Edwards [35] explain, the flow remains steady and laminar below a particle Reynolds number of 150. Figures 7.17a and 7.17b show contour plots for Reynolds number of the liquid and gas phase, respectively. The liquid's maximum Reynolds number is 105, localized near the wall where speed is greatest. However, across most of the reactor domain, the liquid Reynolds number ranges between 1 and 20, indicating a consistent laminar flow pattern. Similarly, the gas phase exhibits a maximum Reynolds number of 9 also suggesting a steady laminar flow. This supports the decision of opting for laminar flow modeling and avoiding turbulence flow models.
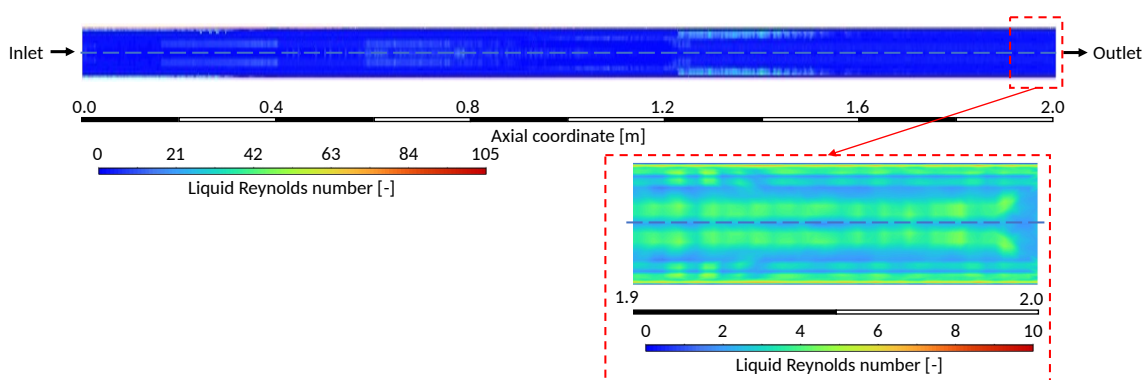
(a) Liquid Reynolds number contour plot with zoomed section at the end of the packed bed.
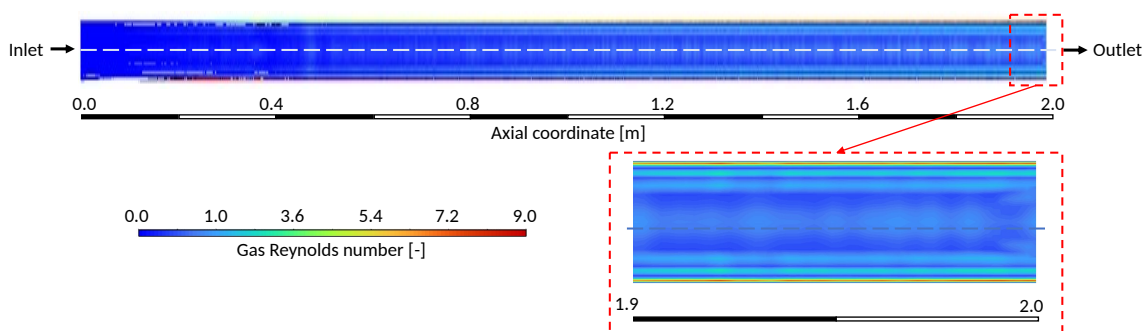
(b) Gas Reynolds number contour plot with zoomed section at the end of the packed bed.

Figure 7.17: Particle Reynolds number contour plots for input parameters detailed in Table 7.2.

7.2.2. Heat transfer

From the heat transfer perspective, this CFD model offers insight into the heat exchange process between the heated walls to the bulk of the reactor as energy is used for LOHC dehydrogenation. In the current simulation, the inlet temperature is set at 400 K and the reactor wall at 550 K, which could be attained through a jacketed reactor with sufficient circulating heating oil.

Figure 7.18a illustrates the temperature contour plot shared by all phases within the reactor. This plot demonstrates that after initial heating, temperature remains relatively stable throughout the reactor's length. This can further be observed by Figure 7.18b which plots the temperature along both the

axis and the fluid adjacent to the reactor wall. The temperature increases significantly in the first 0.5 m and then remains consistent throughout the remaining reactor length.

It is also important to recognize the difference between the wall and axis temperatures, as this informs how deep the energy is transferred and how fast this happens. In this simulation, the most significant temperature difference between the wall and axis arises within the first 0.5 m, with variations ranging from 3 to 10 K. Then, the difference gradually decreases until the end of the reactor where the difference is only 0.7 K. This is observed in Figure 7.18c which shows the radial temperature profile at the packed bed outlet. Ultimately, this analysis demonstrates that for this 29.7 mm diameter reactor, the flow and heating system prove effective in achieving a uniform temperature across the reactor's cross-section. It will be important to study how this heating behavior evolves as a larger diameter reactor is selected to increase reactor volume and hydrogen production.
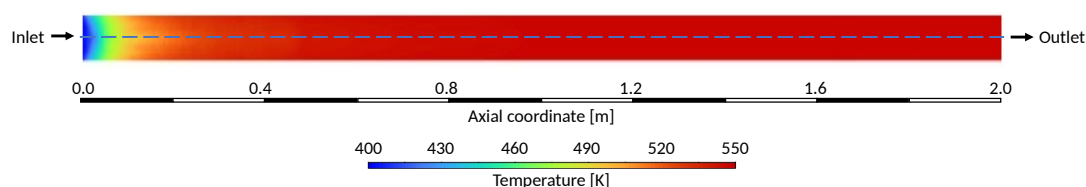
(a) Temperature contour plot for input parameters detailed in Table 7.2.
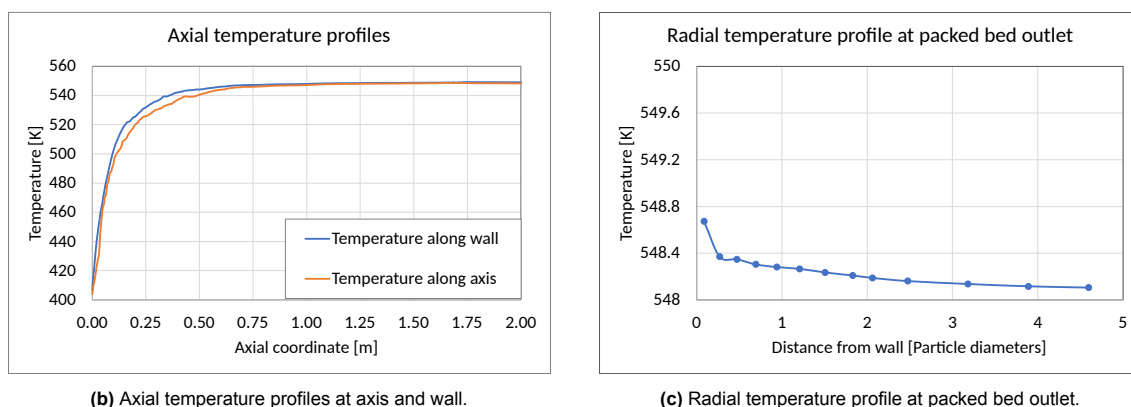
(b) Axial temperature profiles at axis and wall.

(c) Radial temperature profile at packed bed outlet.

Figure 7.18: Temperature plots for input parameters detailed in Table 7.2.

Within the pseudo-homogeneous heat transfer model, one of the heat transfer parameters is the wall heat transfer coefficient, h_w, plotted by Figure 7.19 along the reactor. The increasing trend in h_w can linked to earlier Figure 5.4c which showed how h_w increases with increasing liquid velocity. This pattern also holds true for the effective thermal conductivity, Λ_e, which also increases downstream as liquid velocity increases.
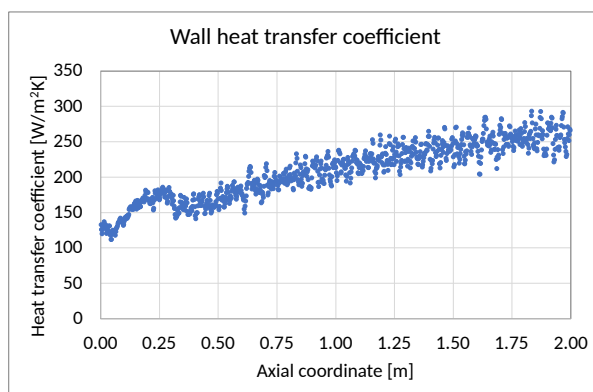
Figure 7.19: Wall heat transfer coefficient along reactor length for input parameters detailed in Table 7.2.

7.2.3. Species conversion and hydrogen yield

Finally, a valuable outcome of this simulation is to understand the chemical conversion and heat requirements.

Results from Table 7.5 show a 15.5% hydrogen yield and 451 W hydrogen power output, derived by multiplying the hydrogen mass flow rate by hydrogen's lower heating value (119960 kJ/kg). Additionally, the outlet degree of hydrogenation is 86.2%. Figure 7.20 presents NEC species mass fractions along the reactor, depicting the transition from fully hydrogenated 12H-NEC to a mixture of four NEC species. At the reactor's end, the mixture is still mostly 12H-NEC, with minimal 4H-NEC and 0H-NEC. This behavior can be explained by observing the reaction rates of each of the three consecutive reactions. The first reaction, 12H-NEC to 8H-NEC, is fastest due to high inlet 12H-NEC concentration and a high reaction rate constant, k_1. The next reaction from 8H-NEC to 4H-NEC has a reaction rate constant, k_2, in the same order of magnitude as k_1. However, since 8H-NEC first needs to be formed by the previous reaction, its concentration is low resulting in a lower reaction rate from 8H-NEC to 4H-NEC. The final reaction, 4H-NEC to 0H-NEC, has a significantly lower rate constant, k_3, and 4H-NEC concentration, resulting in minimal conversion. The three plane volume-average reaction rates are plotted in Figure 7.21 to show this behavior. Notably, the first reaction rate sharply rises within the initial 0.2 m which coincides with the LOHC heating from its inlet temperature towards the wall temperature.

Analyzing reaction rate distribution reveals areas of reactor underutilization. For example, the initial 0.15 m where the LOHC is not yet at high temperatures, and further upstream where the concentration of LOHC is low because of the high gas volume fraction, are underutilized. Figure 7.22 shows cumulative gas production along the reactor length. This figure shows that barely any gas is produced in the first 0.15 m of the reactor. At 0.15 m, the temperature at the center of the reactor reaches 510 K after which high gas production begins. Subsequently, from 0.15 to 0.65 m, the high reaction rates produce 50% of the total hydrogen production. The remaining 50% of the produced hydrogen is produced steadily between 0.65 m and the reactor outlet.

This insight can help propose ideas to improve reactor performance, such as preheating the LOHC to temperatures above 510 K before encountering the catalyst. To maximize catalyst efficiency, only heated LOHC should come in contact with the catalyst to avoid low reaction rates. This could be done before the reactor inlet by a preheating system or within the reactor in an initial section with inert particles such that the LOHC can be heated without spending valuable catalyst pellets. Another way to improve the reaction rate is by increasing the LOHC concentration upstream of the reactor which would imply reducing the gas volume fraction or, in other words, removing gas from the system.
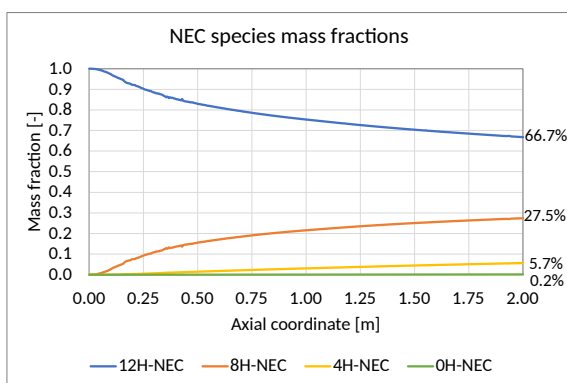
Figure 7.20: Plane mass-averaged LOHC species mass fractions along reactor length for input parameters detailed in Table 7.2.
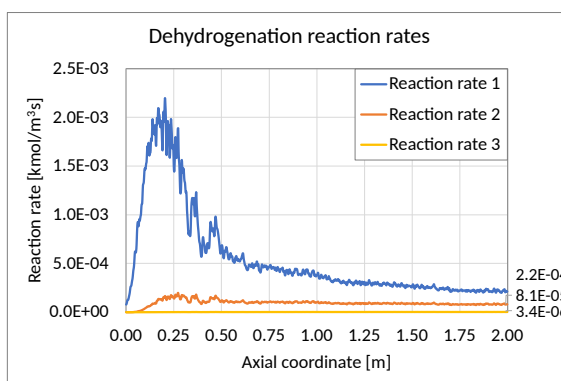
Figure 7.21: Plane volume-averaged reaction rates along reactor length for input parameters detailed in Table 7.2. Reaction rate 1 corresponds to 12H-NEC to 8H-NEC; reaction rate 2 corresponds to 8H-NEC to 4H-NEC; reaction rate 3 corresponds to 4H-NEC to 0H-NEC.
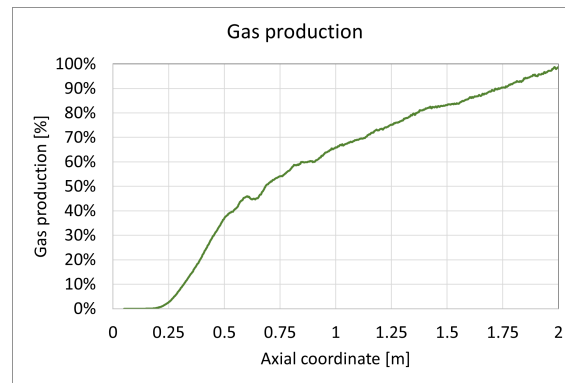
Figure 7.22: Cumulative gas production as a percent of total gas production for input parameters detailed in Table 7.2.

7.3. Sensitivity analyses

Having analyzed an initial case for this model, four sensitivity analyses will be done to understand the effect of some of the principal input parameters on the output parameters.

7.3.1. Wall temperature study

Given the exponential relationship between reaction rate constants and temperature, reactor temperature is one of the parameters that most easily impacts reactor performance. In this reactor design, key parameters influencing reactor temperature include the inlet liquid temperature, reaction kinetics, and reactor wall temperature. Assuming a consistent inlet temperature and reaction kinetics, adjusting the reactor wall temperature, or the associated heating system, can provide control over the reactor temperature. To understand the influence of wall temperature, a set of simulations will be executed with varying wall temperatures as outlined in Table 7.6.

Table 7.6: Input parameters for wall temperature sensitivity analysis.

Input parameter	Value
Flow configuration	Cocurrent upward flow
Fluid system	H2 - NEC
Reactor diameter [m]	0.0297
Reactor length [m]	2
Particle diameter [m]	0.003
Particle Shape	Spherical
Sphericity [-]	1
Mesh size	$0.7 \times d_p$
Ergun constant 1 [-]	215
Ergun constant 2 [-]	1.8
Inlet liquid mass flux [kg/m^{2}s]	0.6
Inlet temperature [K]	400
Inlet 12H-NEC mass fraction [-]	1
Wall temperature [K]	**510−570**
Reaction Kinetics	Dong et al. [32]
Operating pressure [bar]	5

This series of simulations were done following the same procedure and model settings described in section 7.1. The main output parameters are summarized in Table 7.7 and some of them graphed in Figures 7.23a through 7.23f.

Table 7.7: Main output parameters for wall temperature sensitivity analysis as described by Table 7.6

Input parameter	Units	Value	Value	Value	Value	Value	Value	Value
Wall temperature	[K]	510	520	530	540	550	560	570
Output parameter	**Units**	**Value**	**Value**	**Value**	**Value**	**Value**	**Value**	**Value**
Pressure drop	[kPa/m]	3.97	4.06	4.30	4.54	4.94	5.43	5.85
Liquid holdup	[-]	0.128	0.120	0.114	0.098	0.091	0.083	0.077
Wetting efficiency	[%]	0.58	0.60	0.61	0.60	0.61	0.62	0.62
Outlet temperature	[K]	509.2	518.2	528.8	538.5	548.3	558.1	568.0
Hydrogen mass flow rate	[mg/s]	2.5	2.7	3.1	3.4	3.8	4.2	4.5
Hydrogen volumetric flow rate	[ml/s]	10.3	11.8	13.4	15.0	17.0	19.4	20.9
Hydrogen power output	[W]	294	330	368	406	451	508	537
Hydrogen yield	[%]	10.1	11.3	12.7	13.9	15.5	17.4	18.5
Outlet degree of hydrogenation	[%]	88.9	88.8	88.2	87.7	86.2	84.1	83.1
Heat of reaction	[W]	67	82	94	100	114	128	138
Wall heat transfer rate	[W]	181	207	236	249	275	303	325
Mass-average liquid axial velocity	[m/s]	0.023	0.025	0.028	0.029	0.032	0.036	0.039
Mass-average liquid residence time	[s]	85.9	79.6	72.7	68.8	62.3	55.7	51.0
Mass-average gas axial velocity	[m/s]	0.045	0.050	0.057	0.057	0.062	0.068	0.073
Gas mass flux	[kg/m^{2}s]	0.0035	0.0040	0.0044	0.0049	0.0054	0.0061	0.0065
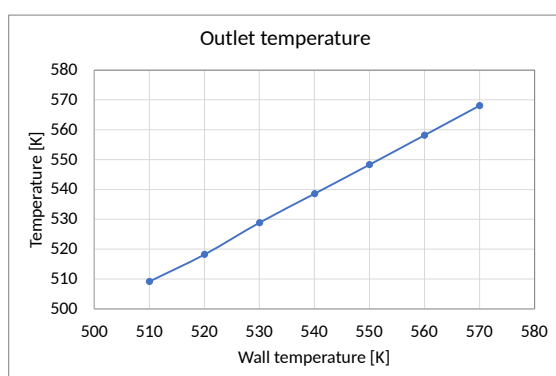
(a)
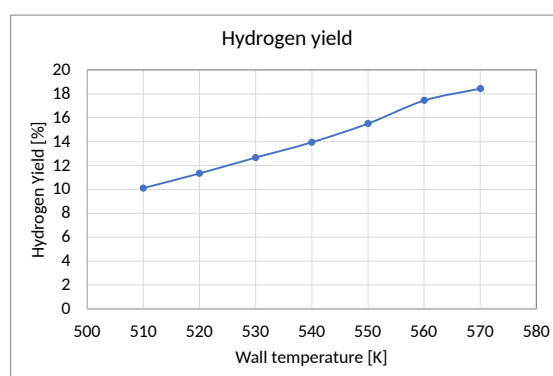
(b)

Figure 7.23: Output parameters for simulations with input parameters detailed in Table 7.6.
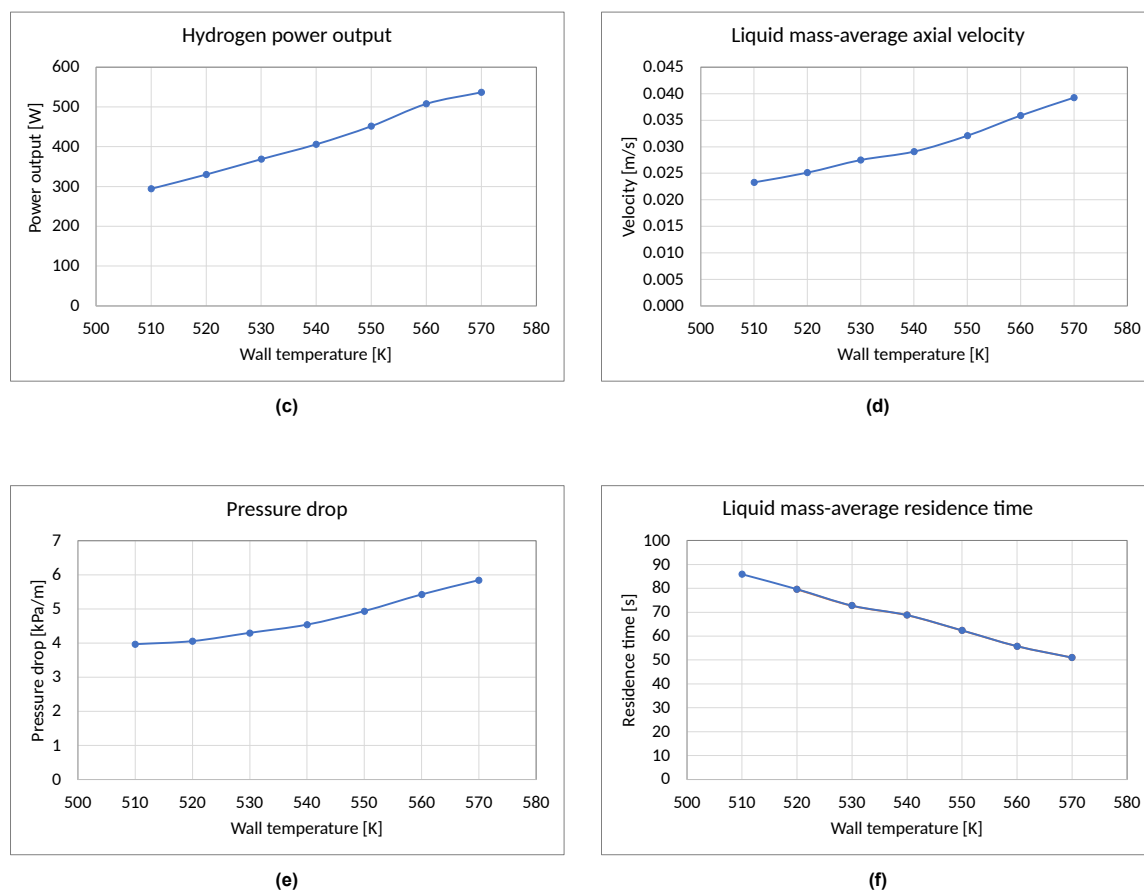
Figure 7.23: Output parameters for simulations with input parameters detailed in Table 7.6 (cont.).

The most evident trend observed in this study is the increase in wall heat transfer rate, as anticipated with rising wall temperatures. As wall heating increases, reactor temperature rises as is observed from the increase in outlet temperature shown in Figure 7.23a. Higher temperatures lead to accelerated reaction kinetics and consequently a higher hydrogen yield, as observed in Figure 7.23b. This correlates directly with the hydrogen produced, evident through the increased hydrogen mass flow rate and the corresponding hydrogen power graphed in Figure 7.23c.

The increased hydrogen production leads to an increased gas volume fraction, subsequently accelerating fluid flow. This acceleration results in higher mass-average liquid and gas velocities, as observed in Figure 7.23d, which plots the mass-average liquid velocity across the whole packed bed at varying wall temperatures. Faster moving fluids results in the increased pressure drop observed in Figure 7.23e. It is interesting to note that within the range of examined flow parameters, the pressure drop increases almost linearly to fluid velocity. This linear relationship aligns with the behavior of the viscous contribution to interphase momentum exchange coefficients, which are themselves linear functions of velocity. Examining the data reveals that, in fact, the viscous term dominates the interphase momentum exchange coefficients, with values ranging between one and two orders of magnitude higher than the inertial contribution. This observation is further supported by the low Reynolds numbers observed in previous Figures 7.17a and 7.17b, indicating that within the fluids, viscous forces dominate over inertial forces.

Finally, an increased velocity implies a lower residence time as is depicted by Figure 7.23f. While a reduced residence time might seem counterproductive, the higher temperatures and reaction rates counteract this effect, yielding an overall positive outcome with increased hydrogen yield and hydrogen power output. Although continuing to increase the wall temperature is beneficial for the hydrogen yield, an upper temperature limit exists due to byproduct generation and the thermal degradation of the LOHC. For NEC, these effects begin at 550 K, which should thus be regarded as the upper temperature limit [98]. Additionally, practical limitations related to the equipment and surrounding setup could also come into play at elevated temperatures.

7.3.2. Reactor diameter study

One of the main design parameters for packed-bed LOHC dehydrogenation reactors is the reactor diameter. A larger reactor diameter can accommodate a larger volume of LOHC and catalyst pellets to produce higher mass flows of hydrogen. The following set of CFD simulations will study the effect of reactor diameter on the output parameters while maintaining the remaining input parameters constant. Following the discussion of wall temperature, a constant wall temperature of 550 K will be used as this is the highest temperature that NEC can be dehydrogenated at without undesired byproduct formation or decomposition. Table 7.8 summarizes the set of input parameters for this study.

Table 7.8: Input parameters for reactor diameter sensitivity analysis.

Input parameter	Value
Flow configuration	Cocurrent upward flow
Fluid system	H2 - NEC
Reactor diameter [m]	**0.02−0.25**
Reactor length [m]	2
Particle diameter [m]	0.003
Particle Shape	Spherical
Sphericity [-]	1
Mesh size	$0.7 \times d_p$
Ergun constant 1 [-]	215
Ergun constant 2 [-]	1.8
Inlet liquid mass flux [kg/m^{2}s]	0.6
Inlet temperature [K]	400
Inlet 12H-NEC mass fraction [-]	1
Wall temperature [K]	550
Reaction Kinetics	Dong et al. [32]
Operating pressure [bar]	5

This series of simulations was done following the same procedure and model settings described in section 7.1. The main output parameters are summarized in Table 7.9 with some of them plotted in Figures 7.24a through 7.24f.

Table 7.9: Main output parameters for reactor diameter sensitivity analysis as described by Table 7.8

Input parameter	Units	Value	Value	Value	Value	Value	Value	Value	Value	Value
Reactor diameter	[m]	0.02	0.0297	0.045	0.06	0.08	0.1	0.15	0.2	0.25
Output parameter	**Units**	**Value**	**Value**	**Value**	**Value**	**Value**	**Value**	**Value**	**Value**	**Value**
Pressure drop	[kPa/m]	4.44	4.94	5.41	5.75	5.75	5.74	5.55	5.55	5.71
Liquid holdup	[-]	0.089	0.091	0.104	0.113	0.122	0.128	0.149	0.168	0.185
Wetting efficiency	[%]	0.61	0.61	0.64	0.65	0.66	0.64	0.62	0.62	0.64
Outlet temperature	[K]	548.7	548.3	547.4	547.1	544.7	542.6	536.5	529.4	511.4
Hydrogen mass flow rate	[mg/s]	1.8	3.8	8.6	14.2	23.3	34.7	61.0	87.0	115.1
Hydrogen volumetric flow rate	[ml/s]	8.2	17.0	38.9	64.1	104.7	155.3	270.2	381.7	488.9
Hydrogen power output	[W]	218	451	1036	1708	2800	4168	7321	10440	13804
Hydrogen yield	[%]	16.5	15.5	15.0	14.4	13.3	12.6	9.9	7.9	6.7
Outlet degree of hydrogenation	[%]	86.4	87.2	87.9	88.5	89.2	89.3	90.6	90.8	93.0
Heat of reaction	[W]	52	114	252	497	774	879	1405	1967	1719
Wall heat transfer rate	[W]	131	275	621	1111	1884	2608	5069	8133	10920
Mass-average liquid axial velocity	[m/s]	0.034	0.033	0.031	0.029	0.026	0.024	0.020	0.016	0.015
Mass-average liquid residence time	[s]	58.4	60.5	63.8	67.8	77.0	83.6	100.7	121.8	130.5
Mass-average gas axial velocity	[m/s]	0.059	0.060	0.056	0.054	0.050	0.051	0.043	0.035	0.033
Gas mass flux	[kg/m^{2}s]	0.0058	0.0054	0.0054	0.0050	0.0046	0.0044	0.0035	0.0028	0.0023
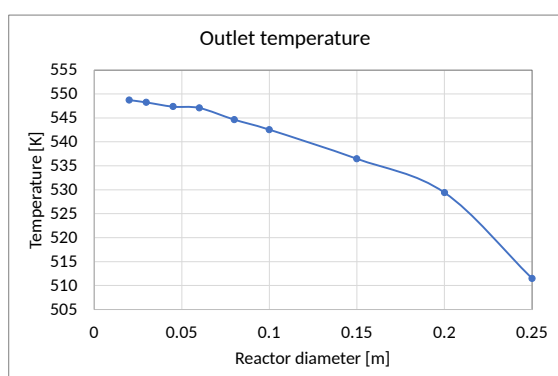
(a)
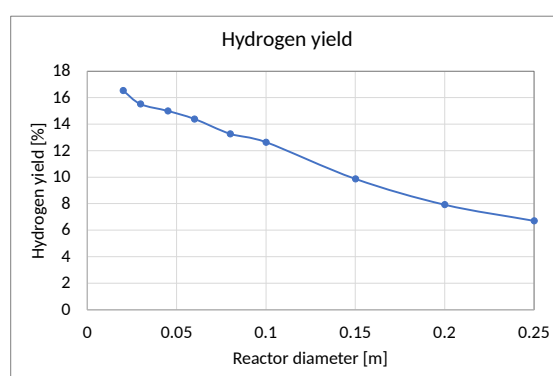
(b)

Figure 7.24: Output parameters for CFD simulations with input parameters given in Table 7.8.
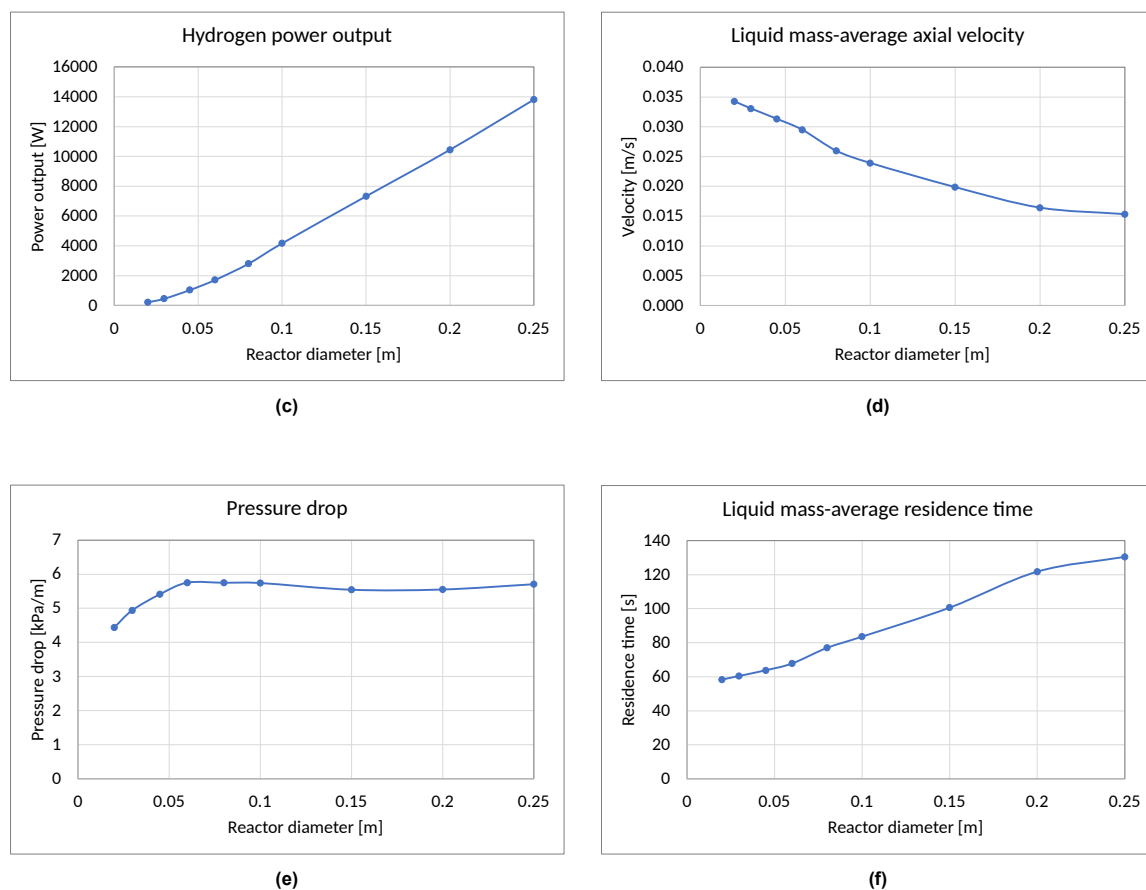
Figure 7.24: Output parameters for CFD simulations with input parameters given in Table 7.8 (cont.).

One important consequence of increasing the reactor diameter is its impact on the temperature field. With an enlarged diameter, heating the cross-section of the reactor requires more time. This results in lower average temperatures throughout the reactor and as Figure 7.24a plots, outlet temperature decreases. Lower temperatures lead to diminished hydrogen yields, as observed in Figure 7.24b. However, increased reactor diameters allow for a greater mass flow of LOHC, which in turn can result in higher hydrogen production. This dynamic is evident in Figure 7.24c where despite a lower hydrogen yield, hydrogen production and power output increase due to the increased mass of LOHC.

The reactor's temperature distribution can be visualized through the temperature contour plots shown in Figure 7.25, complemented by reactor axis temperature profiles depicted in Figure 7.26. These figures illustrate how, as the reactor diameter increases, the bulk of the reactor takes longer to reach higher temperatures. An interesting effect that becomes noticeable in larger diameter reactors is the formation of small eddies along the wall region.

To understand this phenomenon, the length of the reactor can be described in three sections. Focusing on the 0.20 m diameter reactor, the first section spans from the beginning up until roughly 0.5 m axial length where the liquid is at a too low temperature for the reaction to be observable. In this region, the bulk of the fluid moves at low velocities, while near the wall higher speeds are observed because of the higher bed porosity. Along the wall, a thermal boundary layer begins to develop. However, the higher fluid velocity near the wall quickly advects the heated fluid downstream resulting in a thin thermal boundary layer.

Furthermore, as the temperature increases from roughly 0.5 m to 1 m axial coordinate, reaction rates surge generating substantial volumes of gas. At this point, the thermal boundary layer along the wall has thickened and begun to form vortices due to temperature gradients between the relatively colder bulk region and the hot wall region. These fluid structures are better observed in Figure 7.27 which displays liquid velocity vectors over the temperature contour plot. These vectors delineate circulating paths, mirroring the patterns on the temperature contour plots. These paths facilitate hotter fluid from the wall region to penetrate towards the bulk of the reactor, enhancing mixing and heating of the bulk

region within the reactor. Given that in this section the velocity of the flow near the bulk region remains low, the buoyancy effects from the high thermal gradients can easily manifest in these circulating flow structures.

An interesting effect of this flow pattern can be observed in Figure 7.28 which plots the four NEC species contour plots for the 0.20 m diameter reactor. These plots show zones of higher concentration of the intermediate species such as 8H-NEC and 4H-NEC, particularly close to the center of the reactor. Some of the circulating flow structures have the effect of maintaining LOHC in place for longer periods of time which allows it to further react and increase the concentration of partially hydrogenated species. Next to the wall however, a consistently higher speed advects 12H-NEC further downstream.

Finally, from 1 m onward, the mixing caused by the circulating flow structures helps the temperature become more uniformly distributed, intensifying the reaction rate. The lower temperature gradients diminish buoyancy effects, and with the effect of an accelerated flow due to the increase in gas production, the vortices are dissipated.
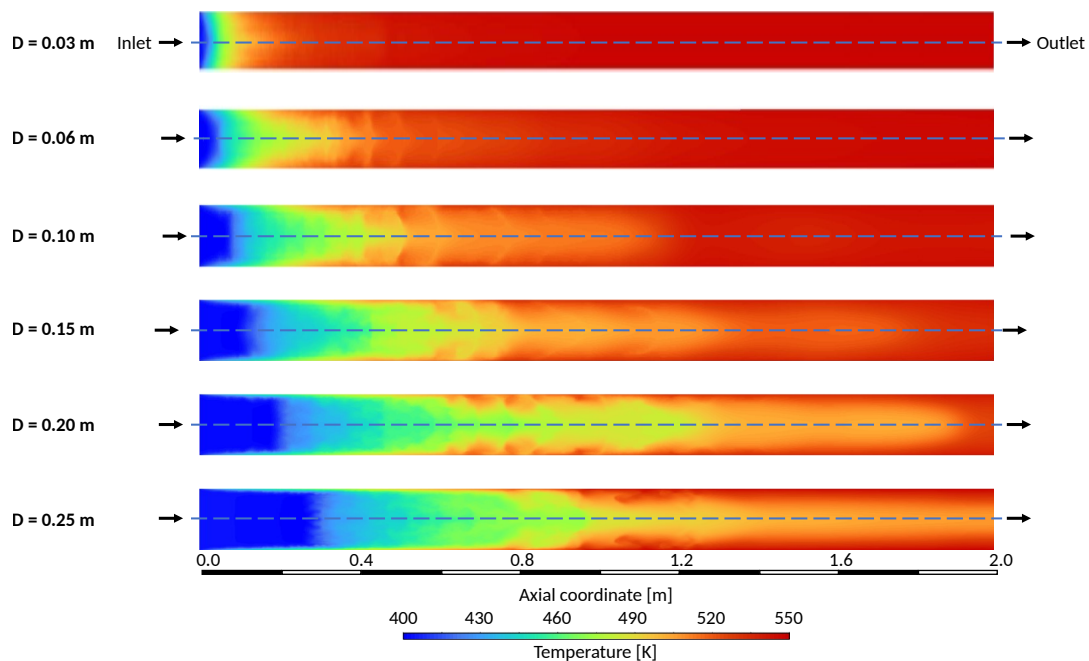
Figure 7.25: Temperature contour plots for different reactor diameters. Simulation performed with input parameters detailed in Table 7.8.
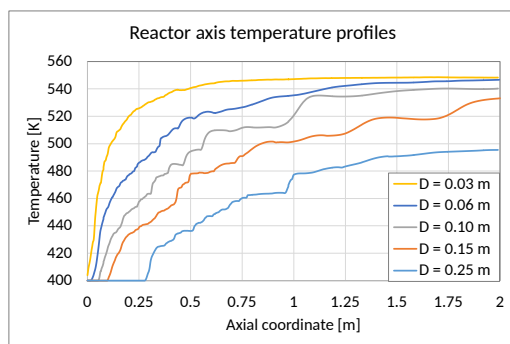
Figure 7.26: Reactor axis temperature profiles for different reactor diameters. Simulation performed with input parameters detailed in Table 7.8.
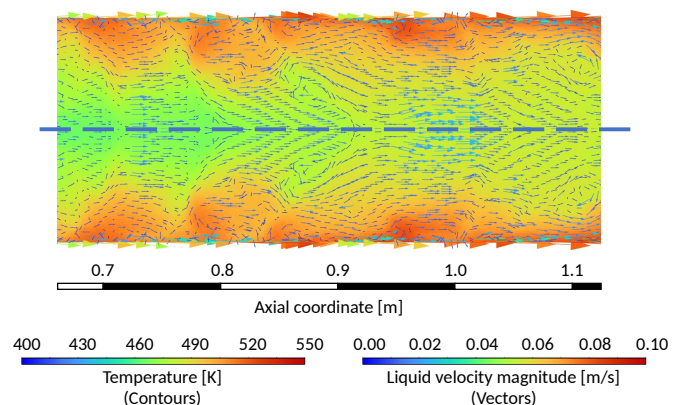
Figure 7.27: Temperature contour plots with superimposed liquid velocity vectors for reactor with 0.20 m diameter. Simulation performed with input parameters detailed in Table 7.8.
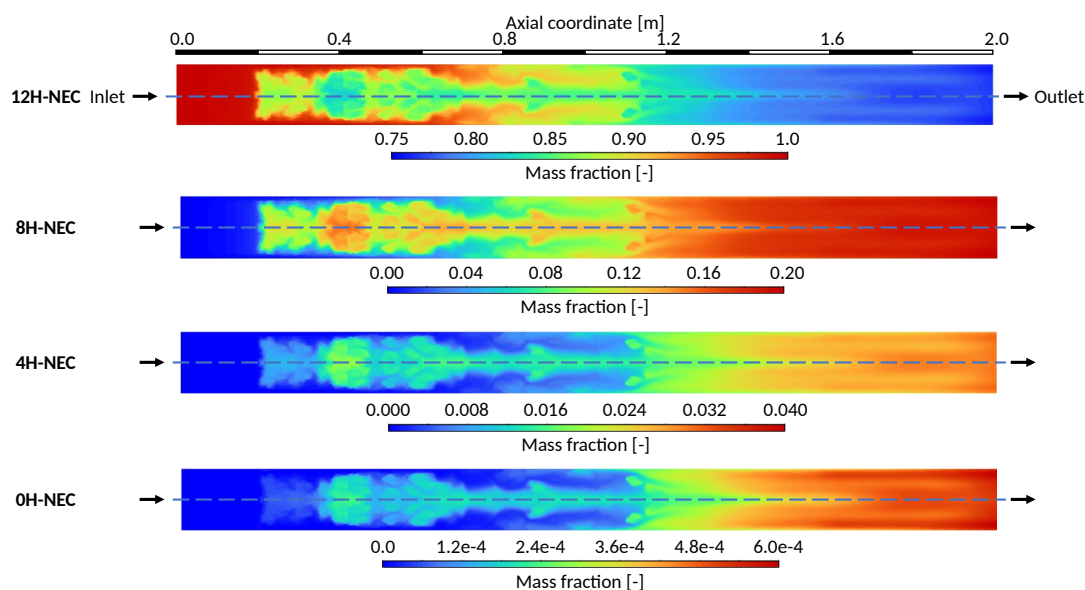
Figure 7.28: NEC species mass fraction contour plots for reactor with 0.20 m diameter, each with its own scale. Simulation performed with input parameters detailed in Table 7.8.

To gain a deeper understanding of the behavior exhibited in reactors with larger diameters, an additional simulation was conducted for the 0.20 m diameter reactor. This simulation was conducted with the same input parameters previously outlined in Table 7.8, except for the inlet temperature which was set at 550 K to match the wall temperature. This would simulate a scenario where the LOHC has been fully preheated. The objective of this simulation was to investigate whether the circulating zones would still emerge under these conditions. The resulting temperature and NEC species mass fraction contour plots can be observed in Figure 7.29, where no indications of circulating regions are found. Without the high thermal gradients, these flow structures do not form, resulting in a more uniform flow pattern. A lower temperature spot near the reactor's axis can be observed due to the endothermic nature of the reaction.
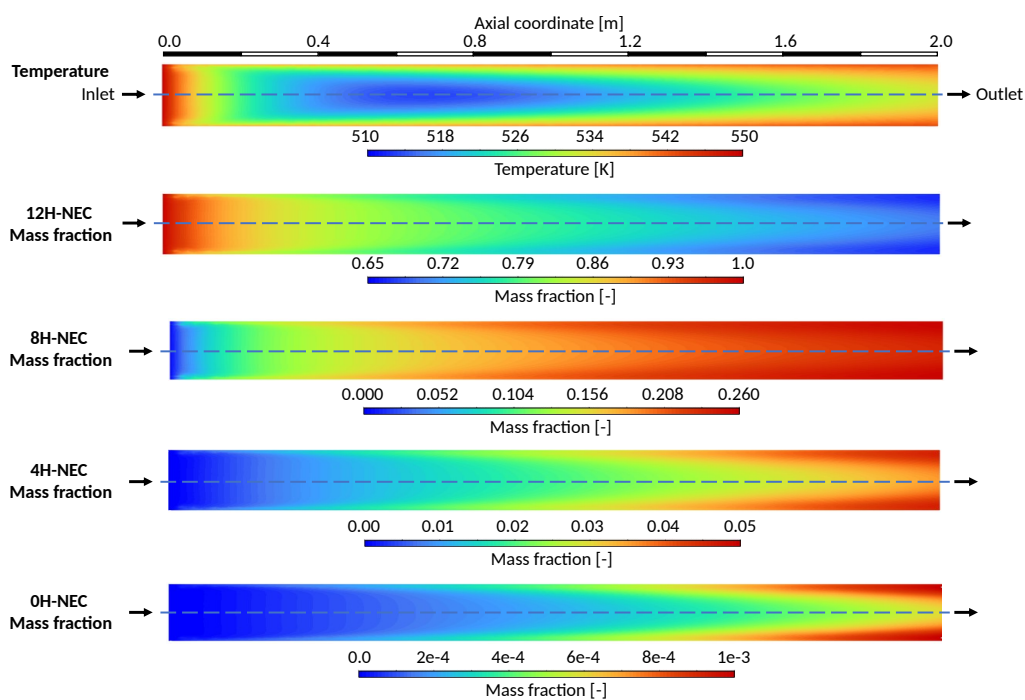
Figure 7.29: Temperature and NEC species mass fraction contour plots for 0.20 m diameter reactor and 550 K inlet temperature, each with its own scale.

Another important aspect to highlight with changing reactor diameter pertains to the impact of the high porosity region near the wall. With an increasing reactor diameter, the tube-to-particle diameter ratio rises, resulting in a diminishing impact of the previously observed effects near the wall because of the high porosity. This can be observed is through the pressure drop which is plotted in Figure 7.24e as a function of reactor diameter. For reactor diameters below 0.06 m, corresponding to a tube-to-particle diameter ratio of 20, the pressure drop can be observed to decrease as reactor diameter decreases. This trend can be attributed to the decreasing tube-to-particle diameter ratio which implies that the area with higher porosity along the wall is a larger proportion of the reactor's total cross-sectional area. Consequently, a greater fraction of fluid mass flows through the zone of lower porosity, leading to reduced flow resistance and yielding a lower pressure drop.

On the contrary, for reactors with diameter greater than 0.06 m, or tube-to-particle diameter ratios above 20, the pressure drop remains relatively constant. In these cases, the wall region constitutes a smaller proportion of the reactor area, meaning that its effects on the overall fluid flow and pressure drop are minimized. This can also be observed by plotting the proportion of mass flow across the radius of the reactor. Figure 7.30a divides the radial length into equal sections of 0.5 times the particle diameter and shows the proportion of the total mass flow of liquid across each section for the first 5 particle diameters from the wall for the 0.20 m diameter reactor. The secondary axis also plots the average axial velocity of the liquid at each of these sections. The same can be said for Figure 7.30b but for gas. These figures can be compared with Figure 7.13a and Figure 7.13b which plot the same information but for the thinner 0.0297 m diameter reactor. While in the thin reactor 42% of the liquid mass flows through the first particle diameter at higher speeds than the rest, for the 0.2 m diameter reactor this number is only 10% and a more homogeneous flow distribution can be observed.

(a) Liquid mass flow proportions and axial velocities.

(b) Gas mass flow proportions and axial velocities.
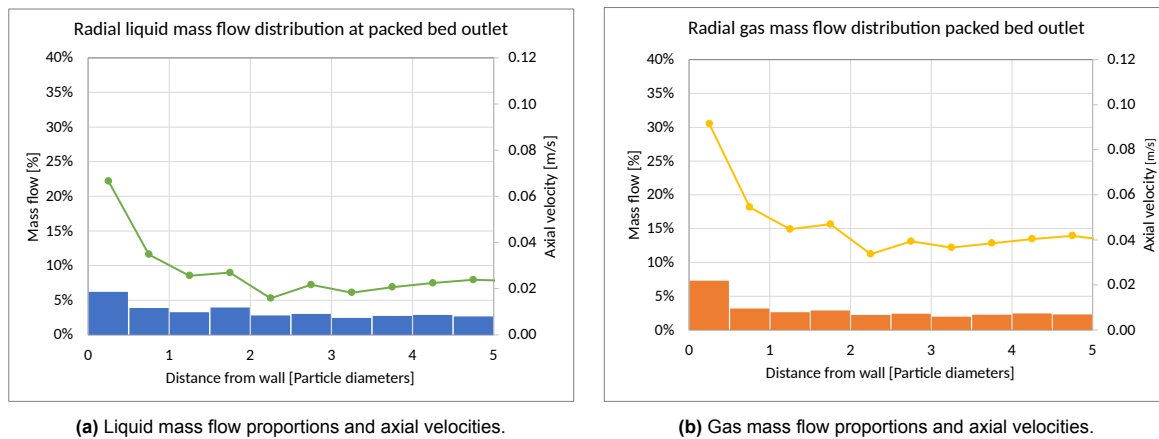
Figure 7.30: Proportion of fluid mass flow at a radial cross-section at the packed bed outlet as well as axial fluid velocities for a 0.20 m diameter reactor. Simulation performed per input parameters detailed in Table 7.8.

Finally, a comment can be made regarding the predicted flow regimes within reactors of different diameters. Figure 7.31 evaluates Murugesan and Sivakumar's [106] flow regime criteria throughout the domain for three reactor diameters to predict the prevailing flow regime. In the 0.02 m diameter reactor, a transition from bubble to pulsed flow occurs at the axial coordinate of 1 m. Similarly, the 0.0279 m diameter reactor exhibits this transition but further downstream at a location of 1.4 m. In contrast, reactors with diameters greater than 0.045 m showed a bubble flow only. This behavior correlates with the fact that the small diameter reactors present the highest liquid and gas velocities. Pulsed flow is particularly correlated with a higher gas mass flux, which, as observed in Table 7.9, is greatest in the smallest diameter reactor.
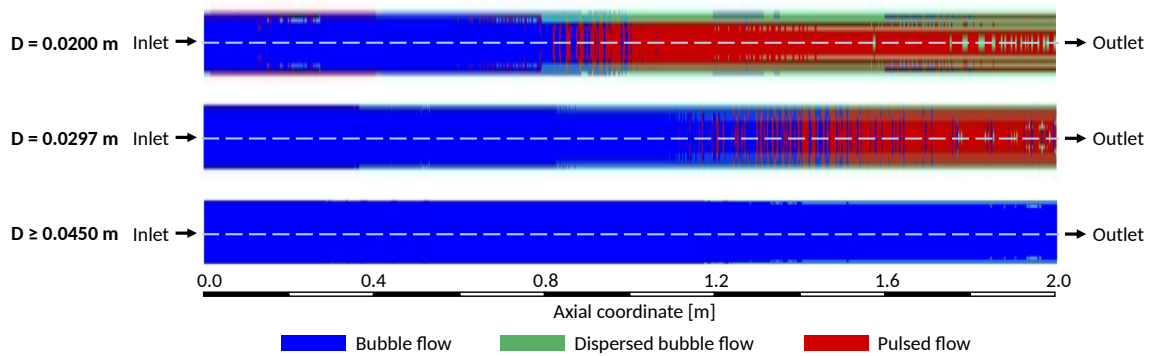
Figure 7.31: Flow regime calculated per Murugesan and Sivakumar's [106] flow map for different diameter reactors. Simulation performed per input parameters detailed in Table 7.8.

Overall, increasing reactor diameter has a negative effect with regards to heat transfer but has the positive effect of minimizing high porosity effects near the wall. A way to maintain a homogeneous temperature distribution and reduce the high porosity wall effect on the flow could be to maintain a thin reactor but reduce the particle size to increase the tube-to-particle diameter ratio. This will be explored in a following sensitivity analysis studying the effect of particle size.

7.3.3. Inlet liquid mass flux study

One of the input parameters that can most easily be regulated via a mass flow meter is the inlet liquid mass flux. The rationale behind adjusting the mass flow rate is to influence the LOHC velocity and consequently its residence time within the reactor. An increased residence time can yield a higher conversion, and thus an increased hydrogen production. To explore this phenomenon, a series of simulations will be conducted according to Table 7.10. In these simulations, all variables will remain constant except for the inlet liquid mass flux.

Table 7.10: Input parameters for inlet liquid mass flux sensitivity analysis.

Input parameter	Value
Flow configuration	Cocurrent upward flow
Fluid system	H2 - NEC
Reactor diameter [m]	0.0297
Reactor length [m]	2
Particle diameter [m]	0.003
Particle Shape	Spherical
Sphericity [-]	1
Mesh size	$0.7 \times d_p$
Ergun constant 1 [-]	215
Ergun constant 2 [-]	1.8
Inlet liquid mass flux [kg/m^{2}s]	**0.3−1.2**
Inlet temperature [K]	400
Inlet 12H-NEC mass fraction [-]	1
Wall temperature [K]	550
Reaction Kinetics	Dong et al. [32]
Operating pressure [bar]	5

This series of simulations was done following the same procedure and model settings described in section 7.1. The main output parameters are summarized in Table 7.11 with the inlet liquid mass flux input converted to inlet liquid interstitial velocities for reference. Additionally, some important trends are shown in Figures 7.32a through 7.32e.

Table 7.11: Main output parameters for inlet liquid mass flux sensitivity analysis as described by Table 7.10

Input parameter	Units	Value	Value	Value	Value	Value	Value	Value	Value
Inlet liquid mass flux	[kg/m^{2}s]	0.3	0.4	0.5	0.6	0.7	0.8	1.0	1.2
Inlet liquid interstitial velocity	[m/s]	0.0010	0.0013	0.0016	0.0019	0.0022	0.0026	0.0032	0.0039
Output parameter	**Units**	**Value**	**Value**	**Value**	**Value**	**Value**	**Value**	**Value**	**Value**
Pressure drop	[kPa/m]	3.95	4.38	4.71	4.94	5.39	5.54	5.72	6.23
Liquid holdup	[-]	0.073	0.078	0.086	0.091	0.097	0.100	0.105	0.115
Wetting efficiency	[%]	0.54	0.55	0.60	0.61	0.64	0.65	0.66	0.70
Outlet temperature	[K]	548.3	548.5	548.4	548.3	548.3	548.3	548.3	548.5
Hydrogen mass flow rate	[mg/s]	3.2	3.4	3.6	3.8	4.1	4.1	4.1	4.3
Hydrogen volumetric flow rate	[ml/s]	14.3	15.2	16.2	17.0	18.3	18.6	18.5	19.2
Hydrogen power output	[W]	380	405	431	451	487	495	493	511
Hydrogen yield	[%]	26.1	20.9	17.8	15.5	14.3	12.8	10.2	8.8
Outlet degree of hydrogenation	[%]	82.8	82.8	85.7	86.2	88.3	88.7	89.8	90.9
Heat of reaction	[W]	99	103	107	114	119	118	110	118
Wall heat transfer rate	[W]	188	212	247	275	309	329	371	429
Mass-average liquid axial velocity	[m/s]	0.0263	0.0282	0.0298	0.0321	0.0347	0.0361	0.0366	0.0386
Mass-average liquid residence time	[s]	76.0	70.9	67.0	62.3	57.6	55.3	54.6	51.8
Mass-average gas axial velocity	[m/s]	0.054	0.054	0.063	0.062	0.063	0.064	0.066	0.068
Gas mass flux	[kg/m^{2}s]	0.0046	0.0049	0.0052	0.0054	0.0059	0.0060	0.0059	0.0062
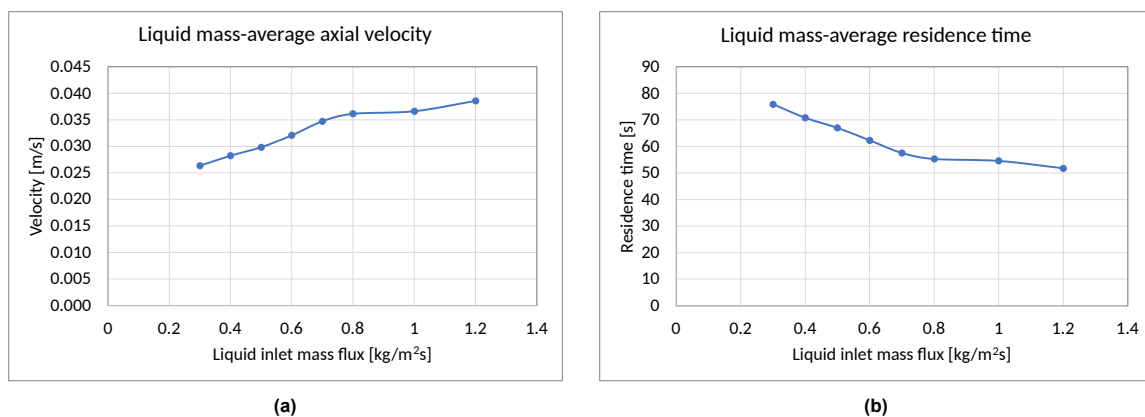
(a)

(b)

Figure 7.32: Output parameters as a function of inlet liquid mass flux for CFD simulations with input parameters given in Table 7.10.

(c)

(d)

(e)
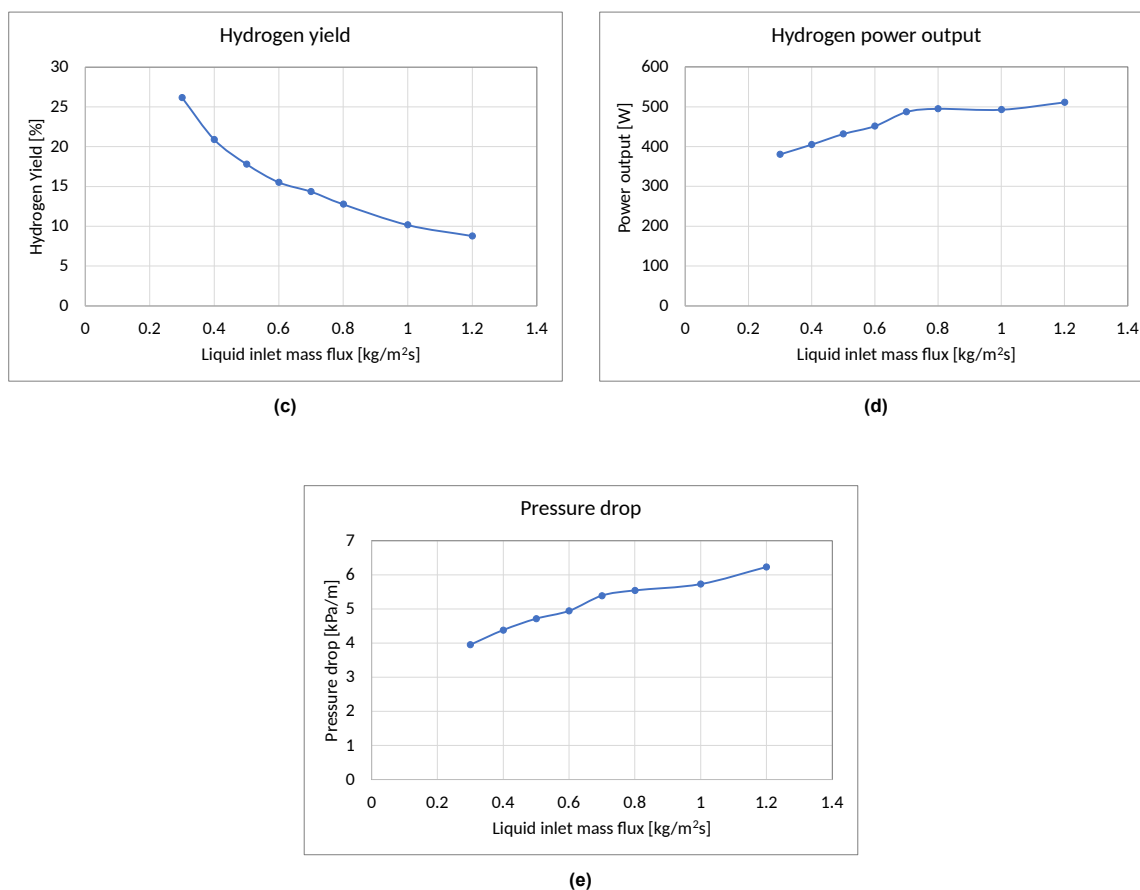
Figure 7.32: Output parameters as a function of inlet liquid mass flux for CFD simulations with input parameters given in Table 7.10 (cont.).

An increase in liquid mass flux leads to a corresponding increase in liquid interstitial velocity, as observed in the input parameter section of Table 7.11. Moreover, as depicted in Figure 7.32a, the average liquid interstitial velocity across the entire reactor also shows an increase with increasing inlet liquid mass flux. This translates to a lower residence time, as observed in Figure 7.32b, which then results in a lower hydrogen yield as seen in Figure 7.32c. Interestingly, the decreased hydrogen yield does not lead to a corresponding decrease in hydrogen power output due to the counteracting effect of the higher liquid mass flux. An increased liquid mass flux means that a greater mass of LOHC can be converted, even if it is to a lower extent, ultimately leading to greater hydrogen production.

It is important to highlight that a reduction in inlet mass flux does not result in a proportional reduction in average liquid velocity within the packed bed. To illustrate this, Figure 7.33 replicates Figure 7.32a but converting the inlet mass flux to inlet interstitial velocities. This graph reveals that halving the inlet velocity, for example, from 3 to 1.5 mm/s, results in only a 20% reduction in the overall liquid bed average velocity (from 36.4 to 29.8 mm/s). This non-proportional decrease is due to the high acceleration experienced by the liquid due to the substantial gas volumes produced in both scenarios which displace the liquid upstream.

The liquid acceleration is a limit of the current packed-bed reactor design that makes reaching increased residence times difficult even if the inlet velocity is reduced. To overcome this limitation, the reactor requires a way to remove gas and prevent the reduction of liquid volume fraction which triggers liquid acceleration. Potential solutions may include intermediate taps for gas removal, implementing shorter reactors in series with intermediate gas-liquid separation, or employing a solid membrane embedded in the wall to enable gas removal along the reactor.
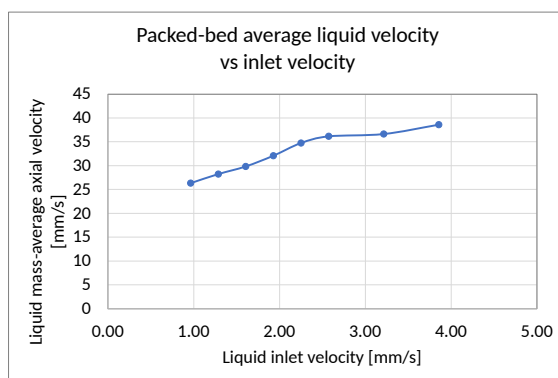
Figure 7.33: Packed bed mass-average liquid axial velocity plotted against inlet liquid velocity for input parameters detailed in Table 7.10. Note both velocities are interstitial velocities.

7.3.4. Pellet diameter study

A final sensitivity analysis will investigate the influence of pellet diameter on the reactor's behavior. Modifying the pellet diameter will alter the reaction kinetics as the catalyst surface area per unit volume will change. Smaller particle diameters are expected to increase the catalyst surface area, thereby offering more active sites for the LOHC to react. For this study, however, as information relating kinetics of NEC dehydrogenation and particle size is not available, the same reaction kinetics used up to this point will be maintained. Therefore, changing the particle diameter in the model will not reflect kinetics changes so any trend in conversion or hydrogen yield may not be accurate. Nevertheless, it remains possible to explore the impact of particle diameter on the reactor's hydrodynamics and heat transfer properties.

A change in particle diameter implies distinct hydrodynamics and varied flow resistance within the packed bed. To analyze these effects, the two-fluid momentum interaction model employed requires values of Ergun constants E_1 and E_2. Previous simulations used values of 215 and 1.8, respectively, based on Gunjal et al.'s research [42] studying a packed bed with 3 mm spherical particles. These values, however, are specific to the particle characteristics in that study, and should not be used for different particle sizes. As no information is at hand relating particular Ergun constants for various particle sizes, the recommended universal values proposed by Macdonald et al. [86] of $E_1 = 180$ and $E_2 = 1.8$ will be applied across all particle diameters. Table 7.12 summarizes the input parameters for this study.

Table 7.12: Input parameters for particle diameter sensitivity analysis.

Input parameter	Value
Flow configuration	Cocurrent upward flow
Fluid system	H2 - NEC
Reactor diameter [m]	0.0297
Reactor length [m]	2
Particle diameter [m]	**0.001−0.007**
Particle Shape	Spherical
Sphericity [-]	1
Mesh size	$0.7 \times d_p$
Ergun constant 1 [-]	180
Ergun constant 2 [-]	1.8
Inlet liquid mass flux [kg/m^{2}s]	0.6
Inlet temperature [K]	400
Inlet 12H-NEC mass fraction [-]	1
Wall temperature [K]	550
Reaction Kinetics	Dong et al. [32]
Operating pressure [bar]	5

The results of this study are summarized in Table 7.13 with some key parameters graphed as a function of particle diameter in Figures 7.34a through 7.34d for easier visualization.

Table 7.13: Main output parameters for particle diameter sensitivity analysis as described by Table 7.12

Input parameter	Units	Value	Value	Value	Value	Value	Value	Value
Particle diameter	[m]	0.001	0.002	0.003	0.004	0.005	0.006	0.007
Tube-to-particle diameter ratio	[-]	29.7	14.9	9.9	7.4	5.9	5.0	4.2
Output parameter	**Units**	**Value**	**Value**	**Value**	**Value**	**Value**	**Value**	**Value**
Pressure drop	[kPa/m]	18.46	7.27	4.96	3.43	2.65	2.41	2.17
Liquid holdup	[-]	0.089	0.084	0.098	0.099	0.098	0.104	0.105
Wetting efficiency	[%]	0.60	0.60	0.66	0.63	0.60	0.63	0.61
Outlet temperature	[K]	549.1	549.0	548.6	548.5	547.9	547.7	547.4
Hydrogen mass flow rate	[mg/s]	3.9	3.8	4.1	4.0	3.8	4.0	3.8
Hydrogen volumetric flow rate	[ml/s]	17.6	17.2	18.6	18.1	17.1	18.0	17.1
Hydrogen power output	[W]	471	458	493	480	454	477	454
Hydrogen yield	[%]	16.2	15.8	17.0	16.5	15.6	16.4	15.6
Outlet degree of hydrogenation	[%]	83.7	86.6	88.7	88.3	87.7	87.4	86.6
Heat of reaction	[W]	105	103	139	127	115	116	83
Wall heat transfer rate	[W]	268	265	299	289	276	283	265
Mass-average liquid axial velocity	[m/s]	0.020	0.029	0.033	0.036	0.036	0.036	0.035
Mass-average liquid residence time	[s]	100.3	68.8	60.6	55.1	55.9	55.3	57.8
Mass-average gas axial velocity	[m/s]	0.057	0.056	0.067	0.059	0.055	0.056	0.055
Gas mass flux	[kg/m^{2}s]	0.0057	0.0055	0.0059	0.0058	0.0055	0.0057	0.0055
Average wall heat transfer coefficient	[W/m^{2}K]	320.5	262.6	221.9	180.2	155.3	142.6	122.2
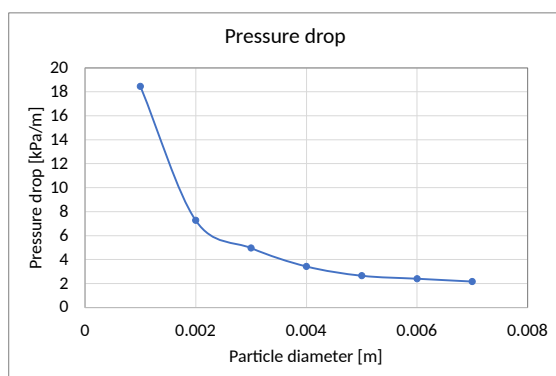
(a)
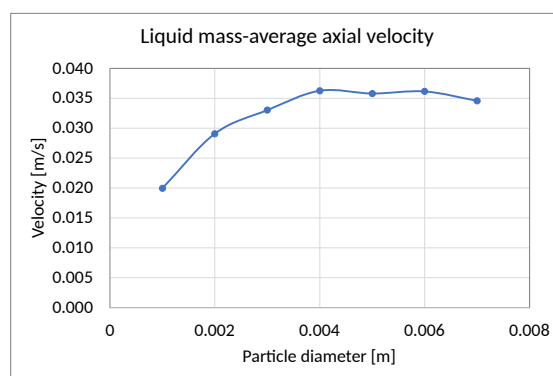
(b)

Figure 7.34: Output parameters as a function of particle diameter for CFD simulations with input parameters given in Table 7.12.
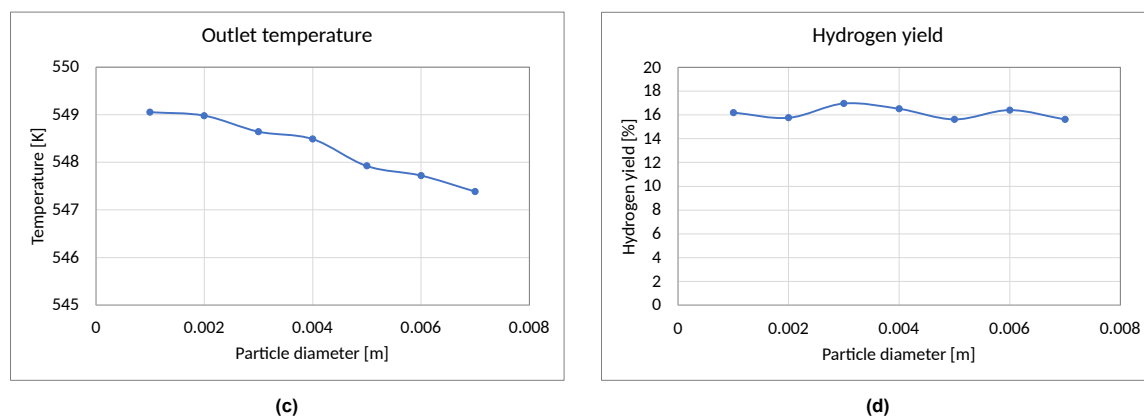
Figure 7.34: Output parameters as a function of particle diameter for CFD simulations with input parameters given in Table 7.12.

The most evident effect of particle diameter is the change in pressure drop observed in Figure 7.34a. As expected, smaller particle diameters result in greater flow resistance, leading to an increase in pressure drop across the bed. Additionally, smaller particle diameters lead to higher tube-to-particle diameter ratios, which, as observed in the reactor diameter sensitivity analysis, diminish the influence of the high porosity region near the wall. The higher tube-to-particle diameter ratio allows less fluid to bypass the bulk of the reactor, resulting in lower average fluid velocities. Figure 7.34b plots the packed bed's average liquid velocity, illustrating the decreasing velocity at lower particle diameters.

In this thin 0.0297 m diameter reactor, it is difficult to observe the impact of pellet diameter on heat transfer due to the small temperature differences within the reactor. However, it is possible to discern a trend in the output temperature, as shown in Figure 7.34c, where the output temperature is higher with smaller particle diameters. This improved heat transfer for smaller particle diameters may be attributed to the higher values of the wall heat transfer coefficient, which, as indicated in Table 7.13, rises as particle diameters decrease.

Finally, Figure 7.34d presents the hydrogen yield against particle diameter. The results show no definitive trend, as the hydrogen yield remains consistent across different particle diameters. It is important to note that since the same reaction kinetics were applied to all particle diameter simulations, no conclusions should be made from the results concerning hydrogen yield or production.

7.4. Improved reactor design

Based on what has been understood from the preceding sensitivity analyses, a final simulation will be run using improved design values. Each of the input parameters will be briefly discussed with the summary of input values detailed in Table 7.14.

Reactor diameter   The reactor diameter choice is primarily guided by the desired hydrogen production rate because a larger diameter generally corresponds to a higher hydrogen power output. Beyond this consideration, the reactor diameter should balance the hydrodynamic and heat transfer properties. A thicker reactor contributes to a higher tube-to-particle diameter ratio, effectively minimizing high porosity wall effects. On the other hand, a thinner reactor facilitates heat transfer to the bulk of the reactor. From the preceding reactor diameter study, a diameter of 0.15 m balances these factors by minimizing wall effects and maintaining efficient bulk heating.

Particle diameter   A particle diameter of 0.003 m is selected as particle diameters below 0.002 m were found to produce significant pressure drops.

Particle shape   While the CFD model was developed to consider the particle shape through a sphericity factor, all simulations were conducted with a sphericity value of 1, representing spherical particles. Further investigation is needed to fully comprehend the impact of particle shape on reactor performance.

Ergun constants Ideally, Ergun constants should be determined for each specific bed. In the absence of such measurements, a value of $E_1 = 180$ and $E_2 = 1.80$ are considered appropriate.

Inlet liquid mass flux An inlet liquid mass flux of 0.3 kg/m^{2}s is chosen as it promotes longer residence times without causing numerical instabilities observed in lower mass fluxes.

Wall temperature A wall temperature of 550 K is selected to enhance reaction rates while avoiding byproducts or NEC degradation.

Inlet temperature To maintain temperatures above 510 K throughout the reactor and avoid low reaction rates, an inlet temperature of 530 K is chosen.

Reactor length The preceding simulations demonstrated how increasing gas volume forces liquid downstream, resulting in higher liquid velocities and lower volume fractions of liquid. This leads to reduced reaction rates downstream. In the baseline case, for instance, 50% of the total hydrogen production occurred within a short span between 0.15 m and 0.65 m of the reactor's length, meaning that the remaining reactor length was less productive. For this final simulation, the reactor length will be split into two 1 m segments with intermediate gas-liquid separation, aiming to improve the productivity of the second reactor. These two segments are named Reactors 1.1 and Reactor 1.2 in Table 7.14 where the output temperature and LOHC mass fractions of Reactor 1.1 will be input to Reactor 1.2. An additional 2 m long reactor, named Reactor 2 in Table 7.14, will also be evaluated for comparison.

Table 7.14: Input parameters for improved reactor design. Reactors 1.1 and 1.2 are considered a system of two reactors in series with intermediate gas-liquid separation.

	Reactor 1.1	Reactor 1.2	Reactor 2
Input parameter	**Value**	**Value**	**Value**
Flow configuration	Coccurrent upward flow	Coccurrent upward flow	Coccurrent upward flow
Fluid system	H2 - NEC	H2 - NEC	H2 - NEC
Reactor diameter [m]	0.15	0.15	0.15
Reactor length [m]	1	1	2
Particle diameter [m]	0.003	0.003	0.003
Particle Shape	Spherical	Spherical	Spherical
Sphericity [-]	1	1	1
Mesh size	$0.7 \times d_p$	$0.7 \times d_p$	$0.7 \times d_p$
Ergun constant 1 [-]	180	180	180
Ergun constant 2 [-]	1.8	1.8	1.8
Inlet liquid mass flux [kg/m^{2}s]	0.3	0.3	0.3
Inlet temperature [K]	530	From Reactor 1 outlet	530
Inlet 12H-NEC mass fraction [-]	1	From Reactor 1 outlet	1
Wall temperature [K]	550	550	550
Reaction Kinetics	Dong et al. [32]	Dong et al. [32]	Dong et al. [32]
Operating pressure [bar]	5	5	5

The results of the above simulations for each of the three reactors is summarized in Table 7.15. Additionally, Table 7.16 adds the output parameters of Reactors 1.1 and 1.2 to compare the overall output of the system of these two reactors with Reactor 2.

Table 7.15: Main output parameters for the inlet liquid mass flux sensitivity analysis as described by Table 7.10

Output parameter	Units	Reactor 1.1 Value	Reactor 1.2 Value	Reactor 2 Value
Pressure drop	[kPa/m]	4.30	4.06	4.58
Liquid holdup	[-]	0.120	0.119	0.078
Wetting efficiency	[%]	0.62	0.62	0.60
Outlet temperature	[K]	526.0	526.6	539.6
Hydrogen mass flow rate	[mg/s]	52.5	45.0	72.6
Hydrogen volumetric flow rate	[ml/s]	228.2	195.6	323.3
Hydrogen power output	[W]	6302	5393	8714
Hydrogen yield	[%]	12.7	12.4	17.6
Outlet degree of hydrogenation	[%]	87.0	76.7	86.2
Heat of reaction	[W]	1414	1284	2019
Wall heat transfer rate	[W]	1569	1466	2514
Mass-average liquid axial velocity	[m/s]	0.0173	0.0157	0.0238
Mass-average liquid residence time	[s]	57.9	63.7	83.9
Mass-average gas axial velocity	[m/s]	0.030	0.035	0.045
Gas mass flux	[kg/m^{2}s]	0.0030	0.0025	0.0041
Outlet 12H-NEC mass fraction	[-]	0.70	0.50	0.66
Outlet 8-NEC mass fraction	[-]	0.23	0.31	0.27
Outlet 4H-NEC mass fraction	[-]	0.07	0.17	0.06
Outlet 0H-NEC mass fraction	[-]	0.004	0.017	0.002
Minimum bed temperature	[K]	507.5	507.9	505.6

Table 7.16: Output parameters for the system of Reactors 1.1 and 1.2, compared with the output parameters of Reactor 2.

Output parameter	Units	Reactor 1.1+1.2 Value	Reactor 2 Value
Hydrogen mass flow rate	[mg/s]	97.5	72.6
Hydrogen volumetric flow rate	[ml/s]	423.8	323.3
Hydrogen power output	[W]	11694	8714
Hydrogen yield	[%]	23.64	17.62
Outlet degree of hydrogenation	[%]	76.7	86.2
Heat of reaction	[W]	2697	2019
Wall heat transfer rate	[W]	3035	2514
Mass-average liquid residence time	[s]	121.7	83.9
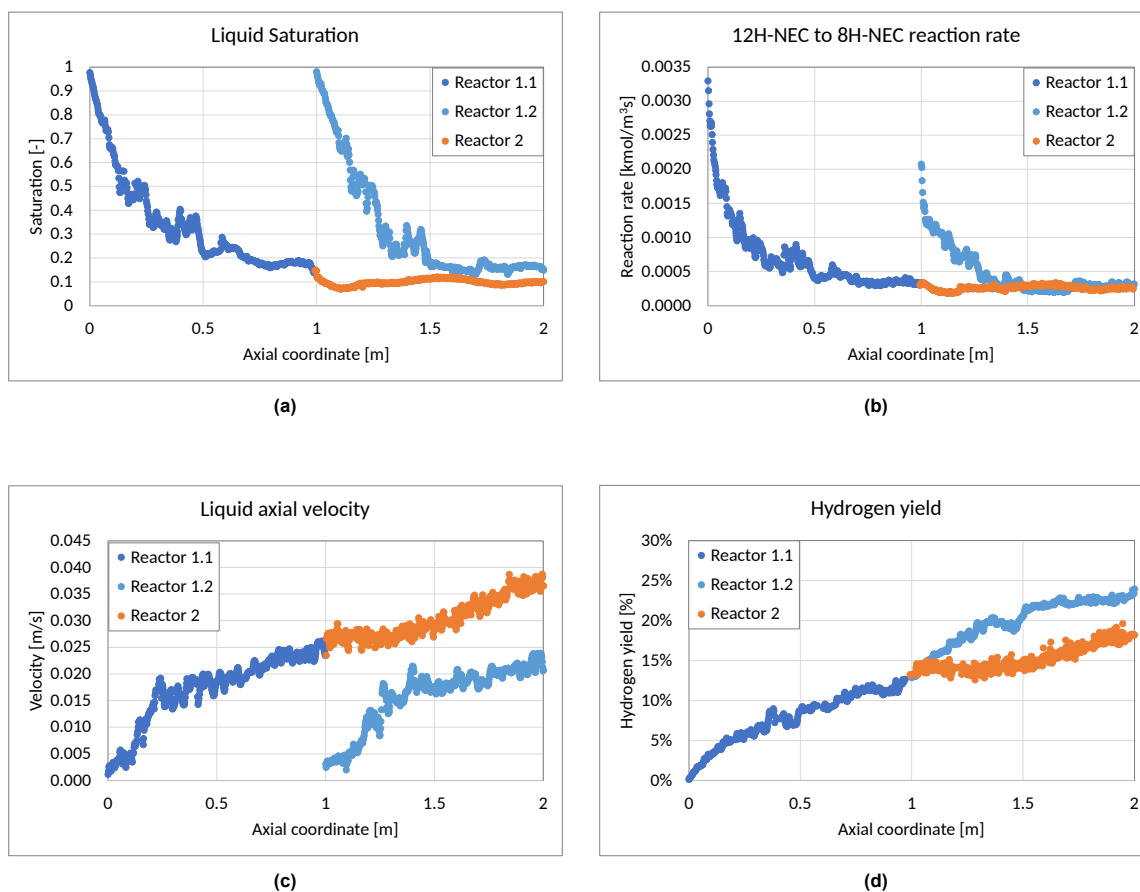
Figure 7.35: Plane average output parameters along axial coordinate for Reactors 1.1, 1.2, and 2 (as per Table 7.14). Note that Reactors 1.1 and 1.2 are configured in series, meaning that Reactor 1.1 encompasses axial coordinates from 0 to 1 m, while Reactor 1.2 spans from 1 to 2 m in these graphs. Reactor 2, spans from 0 to 2 m and shares identical data with Reactor 1.1 within the axial range of 0 to 1 m, leading to overlapping data points between these two reactors.

The motivation to partition the 2 m long reactor into two 1 m long reactors with intermediate gas-liquid separation is to increase liquid saturation and reduce its velocity to improve LOHC conversion. Figure 7.35a illustrates the liquid saturation drop from 1.00 to 0.15 due to increasing gas production within the first meter of the reactor. Then, after 1 m axial coordinate in Reactor 2, the liquid saturation continues to drop steadily to 0.09 by the end of the reactor. However, in Reactor 1.2 where all of the gas has been removed at the 1 m mark, liquid saturation is brought back to 1.00 followed by a similar decrease to around 0.20. This means that the concentration of liquid per unit volume in Reactor 1.2 is much greater than the second half of Reactor 2, thus increasing the contact between LOHC and catalyst particles promoting increased reaction rates. As an example, Figure 7.35b plots the reaction rate for the first reaction from 12H-NEC to 8H-NEC within the reactors, reflecting the liquid saturation curve as reaction rate is directly proportional to reactant concentration.

Furthermore, Figure 7.35c affirms the steady increase of liquid axial velocity in Reactor 2 throughout the entire length. Conversely, in Reactors 1.1 and 1.2, the axial velocity is brought back to a low value at the 1 m mark. This causes a reduction in the overall average liquid axial velocity in the system which results in a 45 % higher residence time compared to Reactor 2.

These combined effects have a positive impact on LOHC conversion, leading to increased hydrogen release. Figure 7.35d helps visualize this effect by graphing the hydrogen yield along the reactors' length. Beyond the 1 m axial coordinate, the increase in hydrogen yield in Reactor 2 slows down, whereas Reactor 1.2 experiences a faster increase in hydrogen yield.

One of the design criteria proposed was to avoid temperatures falling below 510 K within the bed to prevent the negative effect of lower temperature on reaction rates. Figure 7.36 and Figure 7.37 present the temperature contour plots for the three reactors under examination. The resulting minimum temperatures of 507.5, 507.9, and 505.6 K for each reactor, are all within the acceptable range. For

larger diameter reactors alternative heating methods such as internal resistance coils or heating tubes may be considered to improve heat transfer throughout the bed.
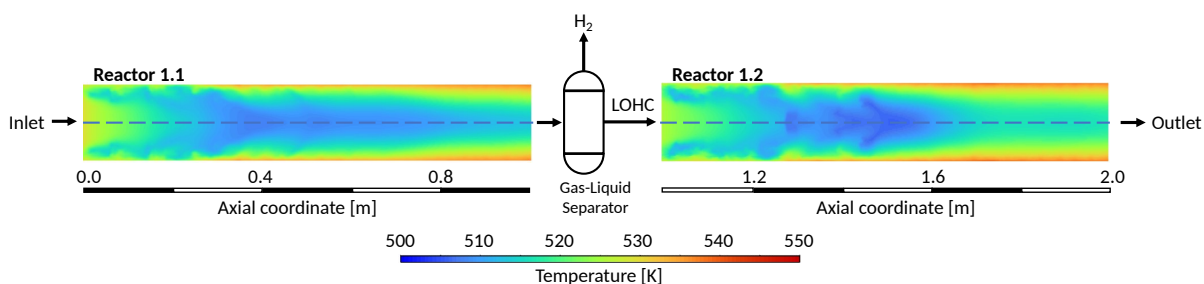
Figure 7.36: Temperature contour plot for Reactors 1.1 and 1.2 in series with intermediate gas-liquid separation. Simulation conducted per input parameters detailed in Table 7.14.
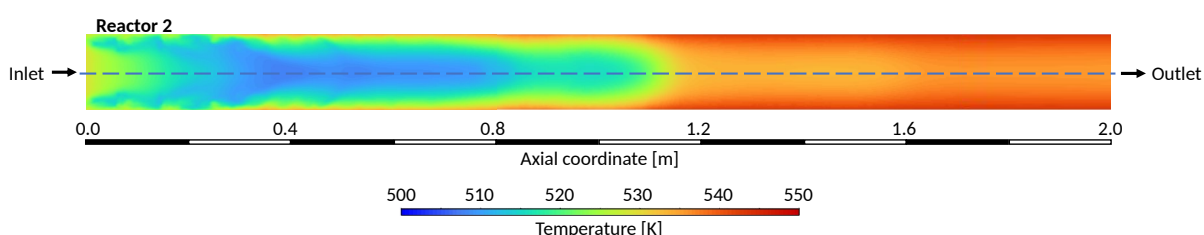
Figure 7.37: Temperature contour plot Reactor 2 for input parameters detailed in Table 7.14.

The design proposed for Reactor 2 exhibited improved performance in terms of LOHC conversion and hydrogen production compared to the previous 2 m long reactor designs examined designs during the sensitivity analyses. For instance, in comparison to the 0.15 m diameter reactor that was simulated in the reactor diameter sensitivity analysis, Reactor 2 resulted in a 19% higher hydrogen power output. Furthermore, dividing the reactor into two shorter units with intermediate gas-liquid separation yielded an additional 34% hydrogen power output as presented in Table 7.16. These findings highlight the significance of exploring reactor designs that facilitate gas removal, offering potential for enhancing reactor performance.

The idea of having intermediate gas-liquid removal could be potentially extended to incorporate more gas removal stages to maximize liquid saturation and hydrogen release from the LOHC. This, however, becomes less practical and implies additional equipment. For a final design, additional considerations such as target output and economic factors would need to be integrated. While the present research has contributed to a better understanding of the impact of various parameters on reactor performance, a cost estimation is necessary to evaluate the economic implications of altering each design parameter and find a balance between cost and reactor performance.

8
Conclusions

8.1. Final observations and conclusions

The present work has diligently aimed to construct a comprehensive CFD framework to model and understand the intricate dynamics of LOHC dehydrogenation within fixed-bed reactors. This began with a literature review to understand every aspect inherent to an LOHC dehydrogenation reactor and lay out the methodology necessary for simulating the distinct physical phenomenon in a cohesive model. The outcome is a computationally inexpensive design tool based on the Eulerian multiphase approach, which enables a deeper understanding of the previously obscured internal workings of these reactors. Moreover, the model was able to look into the complexities of LOHC dehydrogenation through a series of sensitivity analyses which provided insights into the general trends and reactor behaviors under different input conditions. The developed methodology can be easily adapted to model other reactor setups and multiphase chemical applications in packed beds. The framework hence opens doors for further research, and innovation in the field of reactive multiphase flows and reactor design.

From the hydrodynamic perspective, several conclusions can be made. First is the significance of an appropriate momentum interaction model for closing the momentum conservation equations. This thesis explored available models developed for multiphase flow through packed-beds and selected the two-fluid interaction model based on sound hydrodynamic principles. There were, however, difficulties in applying the model thanks to the highly changing values of fluid volume fraction within the reactor. It may be appropriate to look further into other phase interaction models that could be more precise for the current application.

Furthermore, the way in which the solid volume fraction is specified was also found to have a strong impact in overall flow characteristics and numerical stability of the CFD simulation. Parameters such as pressure drop, liquid holdup, and fluid velocities were found to be highly sensitive to the modeling of the high porosity region in the vicinity of the wall. In response, this work proposes combining an oscillating radial porosity function with an axial Fourier function to effectively represent the porosity distribution across the reactor. This representation has the advantage of being mesh size independent and promotes a stable numerical solution by avoiding abrupt changes between adjacent cells.

The simulations consistently resulted in low values of liquid holdup, wetting efficiency, and signs of liquid flow bypassing the bulk of the reactor, especially for low tube-to-particle diameter ratio reactors. These effects are detrimental to reactor performance as they imply lower concentrations of LOHC which subsequently lead to reduced reaction rates and low hydrogen yields. These effects stem from the high volumes of gas produced and while reactors with higher tube-to-particle diameter ratios can reduce these issues to some extent, the main cause, a high volume of gas, remains. The overall effect observed is a diminishing reactor efficiency along the reactor as gas is produced.

From the heat transfer standpoint, implementing the two-parameter pseudo-homogeneous heat transfer model proved straightforward as a single temperature field is shared among the three phases. This assumption is supported by evaluating Mear's [94] three heat transfer resistance criteria which confirmed that in a NEC dehydrogenation packed-bed reactor, the heat transfer resistance between the three phases is minimal. For distinct LOHCs or vastly different operating conditions or packing characteristics than those considered herein, it would be important to verify this assumption.

In simulations with a low inlet temperature and larger reactor diameters, instances of pronounced temperature gradients were found to cause buoyancy effects leading to zones of flow circulation. Notably, at the start of the reactor where fluid velocity is particularly slow, thermal effects were observed to cause zones of flow circulation. Furthermore, as reaction rates are exponentially influenced by temperature, the simulations observed that below 510 K reaction rate is too low reducing reactor efficiency.

It is therefore proposed to preheat the NEC to temperatures above 510 K before entering the reactor, or have a preliminary zone with inert packing at the beginning of a heated reactor to ensure sufficient heating before encountering the catalyst particles.

The most notable source of uncertainty in the CFD simulations stems from the constant reaction kinetics that were employed. The simulations used reaction kinetics measured by Dong et al. [32] in a temperature range between 410 and 440 K under atmospheric pressure, for a catalyst of unknown shape and dimensions. Extrapolating these kinetics to higher temperatures, different pressures, and distinct catalyst characteristics is likely to cause significant errors. Lacking additional information, this uncertainty was acknowledged but ideally the kinetics should be measured with a fully characterized catalyst under the operating temperatures and pressures to be used within the reactor.

Reactor design improvement

The series of simulations has led to a several ideas for improving reactor design, including raising the inlet temperature, employing a low inlet LOHC mass flux, and utilizing shorter reactors with intermediate gas-liquid separation, as tested in chapter 7. Additional possibilities to improve reactor efficiency by reducing the gas volume fraction include implementing a selectively permeable membrane around the packed bed, allowing hydrogen gas to escape along the entire reaction length while retaining the LOHC. Another possibility may be incorporating taps at various heights along the reactor wall as represented by Figure 8.1. The CFD simulations demonstrated that gas saturation is highest near the reactor wall due to the high porosity in this region. Consequently, positioning taps at these locations would facilitate the extraction of gas from the reactor. As some liquid may accompany the gas through these streams, they could be directed to a gas-liquid separator and the liquid recycled back into the reactor.

In reactors with tube-to-particle ratios less than 20, the effect of bypassing flow along the near-wall region was found to be significant. To reduce this effect, it may be beneficial to include internal baffles near the wall at several heights to disturb the bypassing flow and increase the LOHC residence time as represented by Figure 8.2. In addition to the increased residence time, baffles may also have the effect of enhancing heat transfer as heated fluid from the near wall region would be directed towards the bulk region of the reactor.
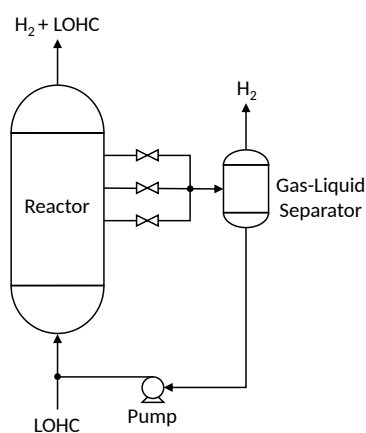
Figure 8.1: Reactor design with intermediate taps for gas removal.
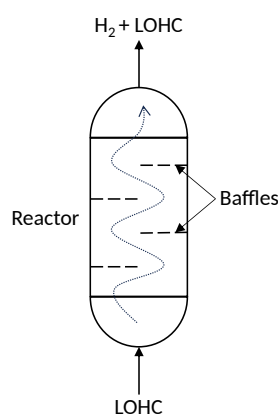
Figure 8.2: Reactor design with internal baffles for flow disruption.

Considering that the liquid exiting the reactor outlet will still be partially hydrogenated, adding a recycling stream for partially hydrogenated LOHC from the outlet will be required. After the reactor, first a gas-liquid separator would be required followed by a liquid-liquid separation step such as distillation to remove fully dehydrogenated LOHC. The hydrogenated LOHC species can then be recycled to the reactor inlet along with new hydrogenated LOHC. Further studies are required to determine the appropriate flow rate of the recycle stream and detail each separation step.

Lastly, in large diameter reactors, evenly heating the fluids becomes increasingly difficult. In this simulation, large temperature differences between the wall and the centerline were found for reactor diameters above 0.15 m. In these cases, other heating mechanisms may need to be considered such as internal heating coils or internal tubes with heating oil crossing the reactor. The current CFD model

was built assuming a jacked heated reactor, but the geometry may be modified to investigate other configurations while maintaining the same framework built for this model.

8.2. Scope for future research

8.2.1. Model refinement

The core of this thesis focused on comprehending the phenomena within an LOHC dehydrogenation reactor and devising strategies to integrate them into a CFD model. This involved relying on numerous models and correlations, both phenomenological and empirical, to estimate key parameters such as the momentum interphase coefficients, packed-bed properties, and heat transfer parameters. While the utilization of these correlations simplified the CFD model within an Eulerian framework, they each induce a certain level of uncertainty into the results. This leaves an opportunity to improve the accuracy of the CFD model by studying models that better represent the ongoing phenomena. For example, it is suggested to revisit the momentum interaction models to ensure that the interaction between phases across the span of conditions present within the reactor are accurately considered.

An additional domain for future research is related to the reaction kinetics which remained constant throughout this work. As explained, the catalyst is a key factor within LOHC dehydrogenation, and many catalyst characteristics contribute to define the overall reaction kinetics. An exhaustive investigation is required to select an appropriate catalyst for LOHC dehydrogenation and subsequently characterize the reacting kinetics as a function of temperature, and ideally, pressure. The resulting reaction kinetics model can then easily replace the existing kinetics model utilized by the CFD simulations.

As for the heat transfer aspect, it may be beneficial to research distinct wall temperature conditions that may be more realistic instead of the constant wall temperature assumed in the current model. An understanding of the jacketed heating system along with heating oil and reactor wall properties can allow a more realistic estimate of the wall temperature to be made. For example, if the heating oil is flowing counter-current to the fluids within the reactor, a linear temperature profile can be applied for the wall temperature with the highest temperature at the reactor outlet and the lowest at the reactor inlet. Other heating methods such as internal resistance coils or internal heating tubes could also be studied by building on CFD framework developed in this thesis.

Lastly, the model's flexibility can be leveraged to research alternate reactor configurations or facilitate the scaling up of existing reactor designs. Moreover, the model's boundary conditions and reaction kinetics can be adjusted to represent and study an LOHC hydrogenation reactor, necessary for a complete LOHC hydrogenation/dehydrogenation system. It will also be important for future research to include the economic implications of the design choices and constraint design parameters to reach a reactor design that balances performance with economic feasibility.

8.2.2. Experimental validation

The scope of this thesis has remained in developing and testing an LOHC dehydrogenation reactor CFD model without conducting experimental validation tests. While individual aspects of the model such as the hydrodynamics and heat transfer were validated independently against existing data, the combined effect of the LOHC dehydrogenation reactor was not compared to experimental results due to limited available data with insufficient details to identically replicate in the CFD model. Although the CFD model produced meaningful results and insights, it remains important that experimental data is collected with which the CFD model can be validated, and if required, tuned to better represent the real data.

Experimental tests can be conducted using a lab-scale setup similar to those developed by Voyex, shown in Figure 1.1. In these setups, the reactors are insulated stainless steel jacketed reactors capable of operating at the high temperatures. While observing inner flow patterns might be difficult, by measuring inlet and outlet flow conditions a good understanding of overall performance can be obtained. For example, pressure drop across the reactor can be measured by a differential pressure transmitter connected to the inlet and outlet of the reactor and compared to the pressure drop predicted by the CFD model. Furthermore, the hydrogen yield and level of dehydrogenation may be measured directly by measuring the outlet hydrogen flow rate with a volumetric flow transmitter, or by measuring the degree of hydrogenation of the exiting LOHC through a gas chromatography analysis. Finally, the heat requirements can be determined by measuring flow rates and temperature at the inlet and outlet of the reactor, along with similar measurements of the heating oil passing through the reactor jacket.

Additional measurements within the reactor may be made but are of increasing complexity and cost. For example, introducing a temperature sensor at the reactor's centerline and moving it along the axis can allow visualization of the axial temperature profile. A temperature rake may also be installed radially within the reactor, with multiple temperature sensing elements at distinct radial lengths, to construct a radial temperature profile. These techniques could help visualize the temperature profiles and validate them against the CFD simulations. Furthermore, by using the analytical solution to the pseudo-homogeneous heat transfer model along with experimental radial temperature profiles, the effective radial thermal conductivity and wall heat transfer coefficient can be calculated and compared with the values employed in the current CFD model.

It will be important that in an experimental setup, all instruments have the accuracy and sensitivity required for this application. For example, the pressure drop was found to be in the range of 2-20 kPa/m. Therefore, either a differential pressure transmitter or two gauge pressure transmitters with a scale and accuracy in this range are required.

In addition to overall input/output measurements and radial temperature assessments, non-invasive visualization techniques can be employed to gain insights into the inner flow characteristics of fixed-bed reactors. Such methods include:

- Particle image velocimetry (PIV)
- Particle tracking velocimetry (PTV)
- Laser Doppler anemometry (LDA)
- Laser Doppler velocimetry (LDV)
- Magnetic resonance imaging (MRI)
- Wire mesh sensors (WMS)

Some of these techniques including PIV, PTV, LDA and LDV require having transparent setups and an often complex refractive index matching processes to visualize the flow. These techniques could be used to study the hydrodynamics of a gas-liquid flow through a packed bed by matching the refractive index of the reactor, packing, and one of the phases, thus enabling visibility of the second phase. This, however, would require a non-reactive, isothermal flow, and would thus not be applicable for studying a full LOHC dehydrogenation reactor. In contrast, wire mesh sensors may be installed in an LOHC dehydrogenation reactor.

Wire-mesh sensors have extensive applications in studying multiphase flows due to their ability to provide cross-sectional images of conductivity or permittivity distribution in flow systems. Their design, as shown in Figure 8.3, consists of a plane of a matrix-like arrangement of wire electrodes placed in the fluid's cross-section [63]. This design creates a grid of crossing points where the fluid's conductivity or permittivity is measured. The spatial resolution of these sensors is determined by the number of wires, and the resulting conductance profile provides flow information. In LOHC dehydrogenation, the hydrogen gas and LOHC liquid have different conductance values, allowing the extraction of cross-sectional profiles of gas and liquid volume fractions. Additionally, using two sensors like those in Figure 8.3 with a small axial distance between them, enables the measurement of spatially resolved fluid velocity profiles by tracking the time for flow features to move from one sensor to another [123]. While installing such a sensor on a high temperature LOHC dehydrogenation reactor may be complex, they could provide valuable information on inner gas and liquid distributions and velocity fields, facilitating qualitative and quantitative validations against the CFD model.
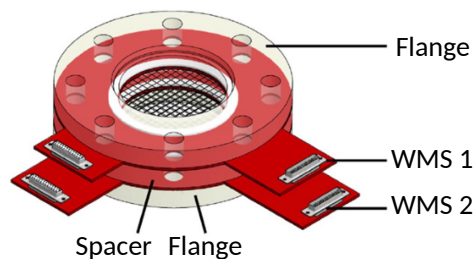
Figure 8.3: Wire-mesh twin sensor [123].

References

[1] Z. Abdin, C. Tang, Y. Liu, and K. Catchpole, "Large-scale stationary hydrogen storage via liquid organic hydrogen carriers," *iScience*, vol. 24, no. 9, p. 102 966, Jul. 2021, ISSN: 2589-0042. DOI: `10.1016/j.isci.2021.102966`.

[2] D. Alique, D. Martinez-Diaz, R. Sanz, and J. A. Calles, "Review of supported pd-based membranes preparation by electroless plating for ultra-pure hydrogen production," *Membranes*, vol. 8, no. 11, p. 5, Mar. 2018, ISSN: 2077-0375. DOI: `10.3390/membranes8010005`.

[3] J. R. Andrews and O. Biblarz, *Temperature Dependence of Gas Properties in Polynomial Form*. Monterey, California, Jan. 1981.

[4] I. ANSYS, *Fluent Customization Manual*, Release 2021 R2.

[5] R. Aslam, M. H. Khan, M. Ishaq, and K. Müller, "Thermophysical studies of dibenzyltoluene and its partially and fully hydrogenated derivatives," *Journal of Chemical & Engineering Data*, vol. 63, no. 12, pp. 4580–4587, Dec. 2018, ISSN: 0021-9568. DOI: `10.1021/acs.jced.8b00652`.

[6] M. J. Assael, J.-a. M. Assael, M. L. Huber, R. A. Perkins, and Y. Takata, "Correlation of the thermal conductivity of normal and parahydrogen from the triple point to 1000 k and up to 100 mpa," *Journal of Physical and Chemical Reference Data*, vol. 40, no. 3, Sep. 2011, ISSN: 0047-2689. DOI: `10.1063/1.3606499`. [Online]. Available: `https://pubs.aip.org/aip/jpr/article/40/3/033101/242016/Correlation-of-the-Thermal-Conductivity-of-Normal`.

[7] A. Atta, M. Hamidipour, S. Roy, K. D. P. Nigam, and F. Larachi, "Propagation of slow/fast-mode solitary liquid waves in trickle beds via electrical capacitance tomography and computational fluid dynamics," *Chemical Engineering Science*, vol. 65, no. 3, pp. 1144–1150, Feb. 2010, ISSN: 0009-2509. DOI: `10.1016/j.ces.2009.09.069`.

[8] A. Atta, S. Roy, and K. D. P. Nigam, "Prediction of pressure drop and liquid holdup in trickle bed reactor using relative permeability concept in cfd," *Chemical Engineering Science*, vol. 62, no. 21, pp. 5870–5879, Nov. 2007, ISSN: 0009-2509. DOI: `10.1016/j.ces.2007.06.008`.

[9] A. Atta, S. Roy, and K. D. P. Nigam, "A two-phase eulerian approach using relative permeability concept for modeling of hydrodynamics in trickle-bed reactors at elevated pressure," *Chemical Engineering Research and Design*, Special Issue – in Honour of Professor Klaas Roelof Westerterp on the occasion of his 80th birthday, vol. 88, no. 3, pp. 369–378, Mar. 2010, ISSN: 0263-8762. DOI: `10.1016/j.cherd.2009.06.011`.

[10] A. Attou, C. Boyer, and G. Ferschneider, "Modelling of the hydrodynamics of the cocurrent gas–liquid trickle flow through a trickle-bed reactor," *Chemical Engineering Science*, vol. 54, no. 6, pp. 785–802, Mar. 1999, ISSN: 0009-2509. DOI: `10.1016/S0009-2509(98)00285-1`.

[11] A. Attou and G. Ferschneider, "A simple model for pressure drop and liquid hold-up in packed-bed bubble reactors," vol. 54, pp. 5139–5144, Nov. 1999, ISSN: 0009-2509. DOI: `10.1016/S0009-2509(99)00267-5`.

[12] A. Attou and G. Ferschneider, "A two-fluid hydrodynamic model for the transition between trickle and pulse flow in a cocurrent gas–liquid packed-bed reactor," *Chemical Engineering Science*, vol. 55, no. 3, pp. 491–511, Feb. 2000, ISSN: 0009-2509. DOI: `10.1016/S0009-2509(99)00344-9`.

[13] M. Baniasadi and B. Peters, "Resolving multiphase flow through packed bed of solid particles using extended discrete element method with porosity calculation," *Industrial & Engineering Chemistry Research*, vol. 56, no. 41, pp. 11 996–12 008, Oct. 2017, ISSN: 0888-5885. DOI: `10.1021/acs.iecr.7b02903`.

[14] R. Bauer and E. U. Schlünder, "Effective radial thermal conductivity of packings in gas flow. part i. convective transport coefficient," *International Chemical Engineering*, vol. 18, no. 2, pp. 182–188, Apr. 1978.

[15] R. Bauer and E. U. Schlünder, "Effective radial thermal conductivity of packings in gas flow. part ii. thermal conductivity of the packing fraction without gas flow," *International Chemical Engineering*, vol. 18, no. 2, pp. 189–204, Apr. 1978.

[16] M. Bazmi, S. H. Hashemabadi, and M. Bayat, "Cfd simulation and experimental study for two-phase flow through the trickle bed reactors, sock and dense loaded by trilobe catalysts," *International Communications in Heat and Mass Transfer*, vol. 38, no. 3, pp. 391–397, Mar. 2011, ISSN: 0735-1933. DOI: 10.1016/j.icheatmasstransfer.2010.11.003.

[17] Z. Bensetiti, F. Larachi, B. P. A. Grandjean, and G. Wild, "Liquid saturation in cocurrent upflow fixed-bed reactors: A state-of-the-art correlation," *Chemical Engineering Science*, vol. 52, no. 21, pp. 4239–4247, Nov. 1997, ISSN: 0009-2509. DOI: 10.1016/S0009-2509(97)00267-4.

[18] F. Benyahia and K. E. O'Neill, "Enhanced voidage correlations for packed beds of various particle shapes and sizes," *Particulate Science and Technology*, vol. 23, no. 2, pp. 169–177, Apr. 2005, ISSN: 0272-6351. DOI: 10.1080/02726350590922242.

[19] F. E. Berger Bioucas, M. Piszko, M. Kerscher, *et al.*, "Thermal conductivity of hydrocarbon liquid organic hydrogen carrier systems: Measurement and prediction," *Journal of Chemical & Engineering Data*, vol. 65, no. 10, pp. 5003–5017, Oct. 2020, ISSN: 0021-9568. DOI: 10.1021/acs.jced.0c00613.

[20] B. Blais, M. Lassaigne, C. Goniva, L. Fradette, and F. Bertrand, "Development of an unresolved cfd–dem model for the flow of viscous suspensions and its application to solid–liquid mixing," *Journal of Computational Physics*, vol. 318, pp. 201–221, Aug. 2016, ISSN: 0021-9991. DOI: 10.1016/j.jcp.2016.05.008.

[21] A. Bourane, M. Elanany, T. V. Pham, and S. P. Katikaneni, "An overview of organic liquid phase hydrogen carriers," *International Journal of Hydrogen Energy*, vol. 41, no. 48, pp. 23 075–23 091, Dec. 2016, ISSN: 0360-3199. DOI: 10.1016/j.ijhydene.2016.07.167.

[22] M. Byun, H. Kim, C. Choe, and H. Lim, "Conceptual feasibility studies for cost-efficient and bi-functional methylcyclohexane dehydrogenation in a membrane reactor for h2 storage and production," *Energy Conversion and Management*, vol. 227, p. 113 576, Jan. 2021, ISSN: 0196-8904. DOI: 10.1016/j.enconman.2020.113576.

[23] C. S. Caldwell and A. L. Babb, "Diffusion in ideal binary liquid mixtures.," *The Journal of Physical Chemistry*, vol. 60, no. 1, pp. 51–56, Jan. 1956, ISSN: 0022-3654. DOI: 10.1021/j150535a014.

[24] G. A. Capelle, J. G. Mance, E. D. Larson, *et al.*, "Simultaneous raman and pyrometric temperature measurements in shock-wave-compressed toluene," *Journal of Applied Physics*, vol. 125, no. 22, p. 225 106, Jun. 2019, ISSN: 0021-8979. DOI: 10.1063/1.5096265.

[25] R. G. Carbonell, "Multiphase flow models in packed beds," *Oil & Gas Science and Technology*, vol. 55, no. 44, pp. 417–425, Jul. 2000, ISSN: 1294-4475, 1953-8189. DOI: 10.2516/ogst:2000030.

[26] J. Chase M.W., *NIST-JANAF Thermochemical Tables*, 4th Edition. Journal of Physical and Chemical Reference Data, 1998, vol. Monograph 9.

[27] Y.-R. Chen, T. Tsuru, and D.-Y. Kang, "Simulation and design of catalytic membrane reactor for hydrogen production via methylcyclohexane dehydrogenation," *International Journal of Hydrogen Energy*, vol. 42, no. 42, pp. 26 296–26 307, Oct. 2017, ISSN: 0360-3199. DOI: 10.1016/j.ijhydene.2017.08.174.

[28] A. Cybulski, R. E. Edvinsson, and J. A. Moulijn, "Monolithic catalysts for three-phase processes," in *Structured Catalysts and Reactors*, 2nd ed. Boca Raton, Florida, USA: CRC Press, 2005, pp. 355–392, ISBN: 978-1-4200-2800-3. [Online]. Available: https://doi-org.tudelft.idm.oclc.org/10.1201/9781420028003.

[29] M. H. Al-Dahhan, M. R. Khadilkar, Y. Wu, and M. P. Duduković, "Prediction of pressure drop and liquid holdup in high-pressure trickle-bed reactors," *Industrial & Engineering Chemistry Research*, vol. 37, no. 3, pp. 793–798, Mar. 1998, ISSN: 0888-5885. DOI: 10.1021/ie970460+.

[30] M. H. Al-Dahhan and M. P. Duduković, "Catalyst wetting efficiency in trickle-bed reactors at high pressure," *Chemical Engineering Science*, vol. 50, no. 15, pp. 2377–2389, Aug. 1995, ISSN: 0009-2509. DOI: 10.1016/0009-2509(95)00092-J.

[31] J. M. P. Q. Delgado, "A critical review of dispersion in packed beds," *Heat and Mass Transfer*, vol. 42, no. 4, pp. 279–310, Feb. 2006, ISSN: 1432-1181. DOI: 10.1007/s00231-005-0019-0.

[32] Y. Dong, M. Yang, P. Mei, C. Li, and L. Li, "Dehydrogenation kinetics study of perhydro-n-ethylcarbazole over a supported pd catalyst for hydrogen storage application," *International Journal of Hydrogen Energy*, vol. 41, no. 20, pp. 8498–8505, Jun. 2016, ISSN: 0360-3199. DOI: 10.1016/j.ijhydene.2016.03.157.

[33] M. P. Duduković, F. Larachi, and P. L. Mills, "Multiphase reactors – revisited," *Chemical Engineering Science*, vol. 54, no. 13, pp. 1975–1995, Jul. 1999, ISSN: 0009-2509. DOI: 10.1016/S0009-2509(98)00367-4.

[34] M. P. Duduković, F. Larachi, and P. L. Mills, "Multiphase catalytic reactors: A perspective on current knowledge and future trends," *Catalysis Reviews*, vol. 44, no. 1, pp. 123–246, Aug. 2002, ISSN: 0161-4940. DOI: 10.1081/CR-120001460.

[35] A. Dybbs and R. V. Edwards, "A new look at porous media fluid mechanics — darcy to turbulent," in *Fundamentals of Transport Phenomena in Porous Media*. Springer, Dordrecht, 1984, pp. 199–256. DOI: 10.1007/978-94-009-6175-3_4. [Online]. Available: https://link.springer.com/chapter/10.1007/978-94-009-6175-3_4.

[36] J. Escobedo and G. A. Mansoori, "Surface-tension prediction for liquid mixtures," *AIChE Journal*, vol. 44, no. 10, pp. 2324–2332, 1998, ISSN: 1547-5905. DOI: 10.1002/aic.690441021.

[37] A. Fikrt, R. Brehmer, V.-O. Milella, *et al.*, "Dynamic power supply by hydrogen bound to a liquid organic hydrogen carrier," *Applied Energy*, vol. 194, pp. 1–8, May 2017, ISSN: 0306-2619. DOI: 10.1016/j.apenergy.2017.02.070.

[38] M. Flávio Pinto Moreira, M. do Carmo Ferreira, and J. T. Freire, "Evaluation of pseudohomogeneous models for heat transfer in packed beds with gas flow and gas–liquid cocurrent downflow and upflow," *Chemical Engineering Science*, vol. 61, no. 6, pp. 2056–2068, Mar. 2006, ISSN: 0009-2509. DOI: 10.1016/j.ces.2005.11.003.

[39] D. Gidaspow, R. Bezburuah, and J. Ding, *Hydrodynamics of circulating fluidized beds: Kinetic theory approach*. May 1992. [Online]. Available: https://www.osti.gov/biblio/5896246.

[40] K. Grosser, R. G. Carbonell, and S. Sundaresan, "Onset of pulsing in two-phase cocurrent downflow through a packed bed," *AIChE Journal*, vol. 34, no. 11, pp. 1850–1860, 1988, ISSN: 1547-5905. DOI: 10.1002/aic.690341111.

[41] L. Grunberg and A. H. Nissan, "Mixture law for viscosity," *Nature*, vol. 164, no. 41754175, pp. 799–800, Nov. 1949, ISSN: 1476-4687. DOI: 10.1038/164799b0.

[42] P. R. Gunjal, M. N. Kashid, V. V. Ranade, and R. V. Chaudhari, "Hydrodynamics of trickle-bed reactors: Experiments and cfd modeling," *Industrial & Engineering Chemistry Research*, vol. 44, no. 16, pp. 6278–6294, Aug. 2005, ISSN: 0888-5885. DOI: 10.1021/ie0491037.

[43] P. R. Gunjal, V. V. Ranade, and R. V. Chaudhari, "Liquid distribution and rtd in trickle bed reactors: Experiments and cfd simulations," *The Canadian Journal of Chemical Engineering*, vol. 81, no. 3–4, pp. 821–830, 2003, ISSN: 1939-019X. DOI: 10.1002/cjce.5450810365.

[44] S. Gutsche, "Transfert de chaleur dans un réacteur à lit fixe à cocourant ascendant de gaz et de liquide," Texte intégral accessible uniquement aux membres de l'Université de Lorraine, Theses, Institut National Polytechnique de Lorraine, Apr. 1990. [Online]. Available: https://hal.univ-lorraine.fr/tel-01751268.

[45] S. Gutsche, G. Wild, N. Midoux, and H. Martin, "Hydrodynamik und wärmeübergang in zweiphasig im aufstrom durchströmten festbettreaktoren," German, *Chemie Ingenieur Technik*, vol. 61, no. 9, pp. 733–736, 1989, ISSN: 1522-2640. DOI: 10.1002/cite.330610914.

[46] A. Heidari and S. H. Hashemabadi, "Numerical evaluation of the gas–liquid interfacial heat transfer in the trickle flow regime of packed beds at the micro and meso-scale," *Chemical Engineering Science*, vol. 104, pp. 674–689, Dec. 2013, ISSN: 0009-2509. DOI: 10.1016/j.ces.2013.09.048.

[47] A. Heller, M. H. Rausch, P. S. Schulz, P. Wasserscheid, and A. P. Fröba, "Binary diffusion coefficients of the liquid organic hydrogen carrier system dibenzyltoluene/perhydrodibenzyltoluene," *Journal of Chemical & Engineering Data*, vol. 61, no. 1, pp. 504–511, Jan. 2016, ISSN: 0021-9568. DOI: `10.1021/acs.jced.5b00671`.

[48] N. Heublein, M. Stelzner, and T. Sattelmayer, "Hydrogen storage using liquid organic carriers: Equilibrium simulation and dehydrogenation reactor design," *International Journal of Hydrogen Energy*, vol. 45, no. 46, pp. 24 902–24 916, Sep. 2020, ISSN: 0360-3199. DOI: `10.1016/j.ijhydene.2020.04.274`.

[49] R. A. Holub, M. P. Duduković, and P. A. Ramachandran, "A phenomenological model for pressure drop, liquid holdup, and flow regime transition in gas-liquid trickle flow," *Chemical Engineering Science*, Twelfth International Symposium on Chemical Reaction Engineering Today, vol. 47, no. 9, pp. 2343–2348, Jun. 1992, ISSN: 0009-2509. DOI: `10.1016/0009-2509(92)87058-X`.

[50] R. A. Holub, M. P. Duduković, and P. A. Ramachandran, "Pressure drop, liquid holdup, and flow regime transition in trickle flow," *AIChE Journal*, vol. 39, no. 2, pp. 302–321, 1993, ISSN: 1547-5905. DOI: `10.1002/aic.690390211`.

[51] IEA, *World Energy Outlook 2022*. Paris, Nov. 2022. [Online]. Available: `https://www.iea.org/reports/world-energy-outlook-2022`.

[52] I. Iliuta, F. Larachi, and M. H. Al-Dahhan, "Double-slit model for partially wetted trickle flow hydrodynamics," *AIChE Journal*, vol. 46, no. 3, pp. 597–609, 2000, ISSN: 1547-5905. DOI: `10.1002/aic.690460318`.

[53] I. Iliuta and F. Larachi, "Three-phase fixed-bed reactors," in *Multiphase Catalytic Reactors*. John Wiley & Sons, Ltd, 2016, pp. 95–131, ISBN: 978-1-119-24849-1. DOI: `10.1002/9781119248491.ch5`. [Online]. Available: `https://onlinelibrary.wiley.com/doi/abs/10.1002/9781119248491.ch5`.

[54] I. Iliuta, F. Larachi, and B. P. A. Grandjean, "Pressure drop and liquid holdup in trickle flow reactors: Improved ergun constants and slip correlations for the slit model," *Industrial & Engineering Chemistry Research*, vol. 37, no. 12, pp. 4542–4550, Dec. 1998, ISSN: 0888-5885. DOI: `10.1021/ie980394r`.

[55] I. Iliuta and F. Larachi, "The generalized slit model: Pressure gradient, liquid holdup & wetting efficiency in gas–liquid trickle flow," *Chemical Engineering Science*, vol. 54, no. 21, pp. 5039–5045, Nov. 1999, ISSN: 0009-2509. DOI: `10.1016/S0009-2509(99)00228-6`.

[56] I. Iliuta, A. Ortiz-Arroyo, F. Larachi, B. P. A. Grandjean, and G. Wild, "Hydrodynamics and mass transfer in trickle-bed reactors: An overview," *Chemical Engineering Science*, vol. 54, no. 21, pp. 5329–5337, Nov. 1999, ISSN: 0009-2509. DOI: `10.1016/S0009-2509(99)00259-6`.

[57] A. Inc., "14.5.18. turbulence models," in *ANSYS Fluent Theory Guide*, Release 2023 R1.

[58] A. Inc., "14.5.7. interphase exchange coefficients," in *ANSYS Fluent User's Guide*, Release 2021 R2.

[59] T. F. S. Inc. "Palladium on 1/8-inch alumina pellets, 0.5% pd, thermo scientific chemicals." Accessed: 2023-18-05. (2023), [Online]. Available: `https://www.thermofisher.com/order/catalog/product/195082500`.

[60] D. Janecki, A. Burghardt, and G. Bartelmus, "Computational simulations of the hydrodynamic parameters of a trickle-bed reactor operating at periodically changing feeding the bed with liquid," *Chemical and Process Engineering*, vol. Vol. 29, z. 3, pp. 583–596, 2008, ISSN: 0208-6425.

[61] Y. Jiang, M. R. Khadilkar, M. H. Al-Dahhan, and M. P. Dudukovic, "Cfd of multiphase flow in packed-bed reactors: I. k-fluid modeling issues," *AIChE Journal*, vol. 48, no. 4, pp. 701–715, 2002, ISSN: 1547-5905. DOI: `10.1002/aic.690480406`.

[62] Y. Jiang, M. R. Khadilkar, M. H. Al-Dahhan, and M. P. Dudukovic, "Cfd of multiphase flow in packed-bed reactors: Ii. results and applications," *AIChE Journal*, vol. 48, no. 4, pp. 716–730, 2002, ISSN: 1547-5905. DOI: `10.1002/aic.690480407`.

[63] R. Kipping, H. Kryk, E. Schleicher, M. Gustke, and U. Hampel, "Application of a wire-mesh sensor for the study of chemical species conversion in a bubble column," *Chemical Engineering & Technology*, vol. 40, no. 8, pp. 1425–1433, 2017, ISSN: 1521-4125. DOI: `10.1002/ceat.201700005`.

[64] R. Krishna and S. T. Sie, "Strategies for multiphase reactor selection," *Chemical Engineering Science*, Chemical Reaction Engineering: Science & Technology, vol. 49, no. 24, Part A, pp. 4029–4065, Jan. 1994, ISSN: 0009-2509. DOI: `10.1016/S0009-2509(05)80005-3`.

[65] Z. V. Kuzeljevic and M. P. Dudukovic, "Computational modeling of trickle bed reactors," *Industrial & Engineering Chemistry Research*, vol. 51, no. 4, pp. 1663–1671, Feb. 2012, ISSN: 0888-5885. DOI: `10.1021/ie2007449`.

[66] A. S. Lamine, M. T. Colli Serrano, and G. Wild, "Hydrodynamics and heat transfer in packed bed with cocurrent upflow," *Chemical Engineering Science*, vol. 47, no. 13, pp. 3493–3500, Sep. 1992, ISSN: 0009-2509. DOI: `10.1016/0009-2509(92)85062-G`.

[67] A. S. Lamine, L. Gerth, H. Le Gall, and G. Wild, "Heat transfer in a packed bed reactor with cocurrent downflow of a gas and a liquid," *Chemical Engineering Science*, vol. 51, no. 15, pp. 3813–3827, Aug. 1996, ISSN: 0009-2509. DOI: `10.1016/0009-2509(96)00228-X`.

[68] A. Lara Márquez, F. Larachi, G. Wild, and A. Laurent, "Mass transfer characteristics of fixed beds with cocurrent upflow and downflow. a special refence to the effect of pressure.," *Chemical Engineering Science*, vol. 47, no. 13, pp. 3485–3492, Sep. 1992, ISSN: 0009-2509. DOI: `10.1016/0009-2509(92)85061-F`.

[69] A. Lara Márquez, G. Wild, and N. Midoux, "A review of recent chemical techniques for the determination of the volumetric mass-transfer coefficient kla in gas—liquid reactors," *Chemical Engineering and Processing: Process Intensification*, vol. 33, no. 4, pp. 247–260, Sep. 1994, ISSN: 0255-2701. DOI: `10.1016/0255-2701(94)01006-4`.

[70] F. Larachi, C. Alix, B. P. A. Grandjean, and A. Bernis, "Nu/sh correlation for particle-liquid heat and mass transfer coefficients in trickle beds based on péclet similarity," *Chemical Engineering Research and Design*, vol. 81, no. 6, pp. 689–694, Jul. 2003, ISSN: 0263-8762. DOI: `10.1205/026387603322150534`.

[71] F. Larachi, I. Iliuta, M. A. Al-Dahhan, and M. P. Dudukovic, "Discriminating trickle-flow hydrodynamic models: Some recommendations," *Industrial & Engineering Chemistry Research*, vol. 39, no. 2, pp. 554–556, Feb. 2000, ISSN: 0888-5885. DOI: `10.1021/ie990632y`.

[72] F. Larachi, L. Belfares, I. Iliuta, and B. P. A. Grandjean, "Heat and mass transfer in cocurrent gas−liquid packed beds. analysis, recommendations, and new correlations," *Industrial & Engineering Chemistry Research*, vol. 42, no. 1, pp. 222–242, Jan. 2003, ISSN: 0888-5885. DOI: `10.1021/ie020416g`.

[73] F. Larachi, Z. Bensetiti, B. P. A. Grandjean, and G. Wild, "Two-phase frictional pressure drop in flooded-bed reactors: A state-of-the-art correlation," *Chemical Engineering & Technology*, vol. 21, no. 11, pp. 887–893, 1998, ISSN: 1521-4125. DOI: `10.1002/(SICI)1521-4125(199811)21:11<887::AID-CEAT887>3.0.CO;2-B`.

[74] F. Larachi, S. Lévesque, and B. P. A. Grandjean, "Seamless mass transfer correlations for packed beds bridging random and structured packings," *Industrial & Engineering Chemistry Research*, vol. 47, no. 9, pp. 3274–3284, May 2008, ISSN: 0888-5885. DOI: `10.1021/ie070718o`.

[75] F. Larachi, G. Wild, A. Laurent, and N. Midoux, "Influence of gas density on the hydrodynamics of cocurrent gas-liquid upflow fixed bed reactors," *Industrial & Engineering Chemistry Research*, vol. 33, no. 3, pp. 519–525, Mar. 1994, ISSN: 0888-5885. DOI: `10.1021/ie00027a008`.

[76] F. Larachi, M. Cassanello, A. Laurent, N. Midoux, and G. Wild, "Gas–liquid interfacial areas in three-phase fixed bed reactors," *Chemical Engineering and Processing: Process Intensification*, vol. 36, no. 6, pp. 497–504, Dec. 1997, ISSN: 0255-2701. DOI: `10.1016/S0255-2701(97)00028-7`.

[77] J. W. Leachman, R. T. Jacobsen, S. G. Penoncello, and E. W. Lemmon, "Fundamental equations of state for parahydrogen, normal hydrogen, and orthohydrogen," *Journal of Physical and Chemical Reference Data*, vol. 38, no. 3, pp. 721–748, Sep. 2009, ISSN: 0047-2689. DOI: `10.1063/1.3160306`.

[78] E. W. Lemmon, I. H. Bell, M. L. Huber, and M. O. McLinden, *"thermophysical properties of fluid systems" in nist chemistry webbook*, Gaithersburg MD, 20899, 2023. DOI: `https://doi.org/10.18434/T4D303`. [Online]. Available: `http://webbook.nist.gov/chemistry/`.

[79] M. Leverett, "Capillary behavior in porous solids," *Transactions of the AIME*, vol. 142, no. 01, pp. 152–169, Dec. 1941, ISSN: 0081-1696. DOI: `10.2118/941152-G`.

[80] S. Li, J. Zhao, P. Lu, and Y. Xie, "Maximum packing densities of basic 3d objects," vol. 55, pp. 114–119, Jan. 2010, ISSN: 1861-9541. DOI: `10.1007/s11434-009-0650-0`.

[81] R. J. G. Lopes and R. M. Quinta-Ferreira, "Trickle-bed cfd studies in the catalytic wet oxidation of phenolic acids," *Chemical Engineering Science*, 8th International Conference on Gas-Liquid and Gas-Liquid-Solid Reactor Engineering, vol. 62, no. 24, pp. 7045–7052, Dec. 2007, ISSN: 0009-2509. DOI: `10.1016/j.ces.2007.08.085`.

[82] R. J. G. Lopes and R. M. Quinta-Ferreira, "Turbulence modelling of multiphase flow in high-pressure trickle-bed reactors," *Chemical Engineering Science*, vol. 64, no. 8, pp. 1806–1819, Apr. 2009, ISSN: 0009-2509. DOI: `10.1016/j.ces.2008.12.026`.

[83] R. J. G. Lopes and R. M. Quinta-Ferreira, "Volume-of-fluid-based model for multiphase flow in high-pressure trickle-bed reactor: Optimization of numerical parameters," *AIChE Journal*, vol. 55, no. 11, pp. 2920–2933, 2009, ISSN: 1547-5905. DOI: `10.1002/aic.11862`.

[84] R. J. G. Lopes and R. M. Quinta-Ferreira, "Evaluation of multiphase cfd models in gas–liquid packed-bed reactors for water pollution abatement," *Chemical Engineering Science*, 20th International Symposium in Chemical Reaction Engineering—Green Chemical Reaction Engineering for a Sustainable Future, vol. 65, no. 1, pp. 291–297, Jan. 2010, ISSN: 0009-2509. DOI: `10.1016/j.ces.2009.06.039`.

[85] P. Lovreglio, "Flow and dispersion in packed beds," Phd Thesis, Technische Universiteit Eindhoven, Eindhoven, Netherlands, Jun. 2020, ISBN: 9789038650487.

[86] I. F. Macdonald, M. S. El-Sayed, K. Mow, and F. A. L. Dullien, "Flow through porous media-the ergun equation revisited," *Industrial & Engineering Chemistry Fundamentals*, vol. 18, no. 3, pp. 199–208, Aug. 1979, ISSN: 0196-4313. DOI: `10.1021/i160071a001`.

[87] I. A. Makaryan and I. V. Sedov, "Catalytic reactors for dehydrogenation of liquid organic hydrogen carriers," *Russian Journal of Applied Chemistry*, vol. 94, no. 8, pp. 1011–1021, Aug. 2021, ISSN: 1608-3296. DOI: `10.1134/S1070427221080012`.

[88] I. E. Maloka, "Thermal conductivities of liquid mixtures," *Petroleum Science and Technology*, vol. 25, no. 8, pp. 1065–1072, Aug. 2007, ISSN: 1091-6466. DOI: `10.1081/LFT-200041074`.

[89] R. E. Maples, *Petroleum refinery process economics*, 2nd ed. Tulsa, Okla: PennWell Corp, 2000, ISBN: 978-0-87814-779-3.

[90] C. Marcandelli, G. Wild, A. S. Lamine, and J. R. Bernard, "Measurement of local particle–fluid heat transfer coefficient in trickle-bed reactors," *Chemical Engineering Science*, vol. 54, no. 21, pp. 4997–5002, Nov. 1999, ISSN: 0009-2509. DOI: `10.1016/S0009-2509(99)00223-7`.

[91] N. J. Mariani, O. M. Martínez, and G. F. Barreto, "Evaluation of heat transfer parameters in packed beds with cocurrent downflow of liquid and gas," *Chemical Engineering Science*, Proceedings of the 5th International Conference on Gas-Liquid and Gas-Liquid-Solid Reactor Engineering, vol. 56, no. 21, pp. 5995–6001, Nov. 2001, ISSN: 0009-2509. DOI: `10.1016/S0009-2509(01)00225-1`.

[92] N. J. Mariani, "Transferencia de calor en sistemas multifásicos," Spanish, Ph.D. dissertation, Universidad Nacional de La Plata, Mar. 2000. DOI: `10.35537/10915/1450`. [Online]. Available: `http://sedici.unlp.edu.ar/handle/10915/1450`.

[93] H. Matsuda, K. Tochigi, K. Kurihara, and T. Funazukuri, "Estimation of thermal conductivities for binary and ternary liquid mixtures using excess thermal conductivity model," *Journal of Solution Chemistry*, vol. 52, no. 1, pp. 105–133, Jan. 2023, ISSN: 1572-8927. DOI: `10.1007/s10953-022-01220-9`.

[94] D. E. Mears, "Diagnostic criteria for heat transport limitations in fixed bed reactors," *Journal of Catalysis*, vol. 20, no. 2, pp. 127–131, Feb. 1971, ISSN: 0021-9517. DOI: `10.1016/0021-9517(71)90073-X`.

[95]   R. A. Mischke and J. M. Smith, "Thermal conductivity of alumina catalyst pellets," *Industrial & Engineering Chemistry Fundamentals*, vol. 1, no. 4, pp. 288–292, Nov. 1962, ISSN: 0196-4313. DOI: `10.1021/i160004a011`.

[96]   K. Miyabe and R. Isogai, "Estimation of molecular diffusivity in liquid phase systems by the wilke–chang equation," *Journal of Chromatography A*, vol. 1218, no. 38, pp. 6639–6645, Jul. 2011, ISSN: 0021-9673. DOI: `10.1016/j.chroma.2011.07.018`.

[97]   S. Mochizuki, "Empirical expressions of liquid-solid mass transfer in concurrent gas-liquid upflow fixed beds," *Chemical Engineering Science*, vol. 37, no. 9, pp. 1422–1424, Jan. 1982, ISSN: 0009-2509. DOI: `10.1016/0009-2509(82)85015-X`.

[98]   P. M. Modisha, C. N. M. Ouma, R. Garidzirai, P. Wasserscheid, and D. Bessarabov, "The prospect of hydrogen storage using liquid organic hydrogen carriers," *Energy & Fuels*, vol. 33, no. 4, pp. 2778–2796, Apr. 2019, ISSN: 0887-0624. DOI: `10.1021/acs.energyfuels.9b00296`.

[99]   E. M. Moghaddam, E. A. Foumeny, A. I. Stankiewicz, and J. T. Padding, "Fixed bed reactors of non-spherical pellets: Importance of heterogeneities and inadequacy of azimuthal averaging," *Chemical Engineering Science: X*, vol. 1, p. 100 006, Feb. 2019, ISSN: 2590-1400. DOI: `10.1016/j.cesx.2019.100006`.

[100] E. M. Moghaddam, E. A. Foumeny, A. I. Stankiewicz, and J. T. Padding, "Hydrodynamics of narrow-tube fixed bed reactors filled with raschig rings," *Chemical Engineering Science: X*, vol. 5, p. 100 057, Jan. 2020, ISSN: 2590-1400. DOI: `10.1016/j.cesx.2020.100057`.

[101] E. M. Moghaddam, E. A. Foumeny, A. I. Stankiewicz, and J. T. Padding, "Heat transfer from wall to dense packing structures of spheres, cylinders and raschig rings," *Chemical Engineering Journal*, vol. 407, p. 127 994, Mar. 2021, ISSN: 1385-8947. DOI: `10.1016/j.cej.2020.127994`.

[102] E. M. Moghaddam, E. A. Foumeny, A. I. Stankiewicz, and J. T. Padding, "Rigid body dynamics algorithm for modeling random packing structures of nonspherical and nonconvex pellets," *Industrial & Engineering Chemistry Research*, vol. 57, no. 44, pp. 14 988–15 007, Nov. 2018, ISSN: 0888-5885. DOI: `10.1021/acs.iecr.8b03915`.

[103] E. J. Molga and K. R. Westerterp, *Gas−liquid interfacial area and holdup in a cocurrent upflow packed bed bubble column reactor at elevated pressures*, research-article, Mar. 1997. DOI: `10.1021/ie960188o`. [Online]. Available: `https://pubs.acs.org/doi/full/10.1021/ie960188o`.

[104] G. E. Mueller, "Prediction of radial porosity distributions in randomly packed fixed beds of uniformly sized spheres in cylindrical containers," *Chemical Engineering Science*, vol. 46, no. 2, pp. 706–708, Jan. 1991, ISSN: 0009-2509. DOI: `10.1016/0009-2509(91)80032-T`.

[105] K. Müller, K. Stark, V. N. Emel'yanenko, *et al.*, "Liquid organic hydrogen carriers: Thermophysical and thermochemical studies of benzyl- and dibenzyl-toluene derivatives," *Industrial & Engineering Chemistry Research*, vol. 54, no. 32, pp. 7967–7976, Aug. 2015, ISSN: 0888-5885. DOI: `10.1021/acs.iecr.5b01840`.

[106] T. Murugesan and V. Sivakumar, "Pressure drop and flow regimes in cocurrent gas–liquid upflow through packed beds," *Chemical Engineering Journal*, vol. 88, no. 1, pp. 233–243, Sep. 2002, ISSN: 1385-8947. DOI: `10.1016/S1385-8947(02)00039-6`.

[107] C. D. Muzny, M. L. Huber, and A. F. Kazakov, "Correlation for the viscosity of normal hydrogen obtained from symbolic regression," *Journal of Chemical & Engineering Data*, vol. 58, no. 4, pp. 969–979, Apr. 2013, ISSN: 0021-9568. DOI: `10.1021/je301273j`.

[108] H. Nadeem, I. Ben Salem, and M. Sassi, "Experimental visualization and investigation of multiphase flow regime transitions in two-dimensional trickle bed reactors," *Chemical Engineering Communications*, vol. 204, no. 3, pp. 388–397, Mar. 2017, ISSN: 0098-6445. DOI: `10.1080/00986445.2016.1205982`.

[109] D. Nemec and J. Levec, "Flow through packed bed reactors: 1. single-phase flow," *Chemical Engineering Science*, vol. 60, no. 24, pp. 6947–6957, Dec. 2005, ISSN: 0009-2509. DOI: `10.1016/j.ces.2005.05.068`.

[110] M. Niermann, A. Beckendorff, M. Kaltschmitt, and K. Bonhoff, "Liquid organic hydrogen carrier (lohc) – assessment based on chemical and economic properties," *International Journal of Hydrogen Energy*, vol. 44, no. 13, pp. 6631–6654, Mar. 2019, ISSN: 0360-3199. DOI: 10.1016/j.ijhydene.2019.01.199.

[111] S. Pachpute, *Basics of multi-phase flow and its cfd modeling*, Mar. 2020. [Online]. Available: https://cfdflowengineering.com/basics-of-multi-phase-flow-and-its-cfd-modeling/.

[112] S. Park, M. Naseem, and S. Lee, "Experimental assessment of perhydro-dibenzyltoluene dehydrogenation reaction kinetics in a continuous flow system for stable hydrogen supply," *Materials*, vol. 14, no. 2424, p. 7613, Jan. 2021, ISSN: 1996-1944. DOI: 10.3390/ma14247613.

[113] D.-Y. Peng and D. B. Robinson, "A new two-constant equation of state," *Industrial & Engineering Chemistry Fundamentals*, vol. 15, no. 1, pp. 59–64, Feb. 1976, ISSN: 0196-4313. DOI: 10.1021/i160057a011.

[114] R. Peters, R. Deja, Q. Fang, *et al.*, "A solid oxide fuel cell operating on liquid organic hydrogen carrier-based hydrogen – a kinetic model of the hydrogen release unit and system performance," *International Journal of Hydrogen Energy*, vol. 44, no. 26, pp. 13 794–13 806, May 2019, ISSN: 0360-3199. DOI: 10.1016/j.ijhydene.2019.03.220.

[115] W. Peters, M. Eypasch, T. Frank, *et al.*, "Efficient hydrogen release from perhydro-n-ethylcarbazole using catalyst-coated metallic structures produced by selective electron beam melting," vol. 8, pp. 641–649, Feb. 2015, ISSN: 1754-5706. DOI: 10.1039/C4EE03461A.

[116] W. Peters, A. Seidel, S. Herzog, A. Bösmann, W. Schwieger, and P. Wasserscheid, "Macrokinetic effects in perhydro-n-ethylcarbazole dehydrogenation and h2 productivity optimization by using egg-shell catalysts," *Energy & Environmental Science*, vol. 8, no. 10, pp. 3013–3021, Oct. 2015, ISSN: 1754-5706. DOI: 10.1039/C5EE02024G.

[117] B. E. Poling, J. M. Prausnitz, and J. P. O'Connell, *The properties of gases and liquids*, 5th ed. New York: McGraw-Hill, 2001, ISBN: 978-0-07-149999-6.

[118] A. V. Raghavendra Rao, R. Kishore Kumar, T. Sankarshana, and A. Khan, "Identification of flow regimes in a concurrent gas liquid upflow through packed beds," *Chemical Engineering & Technology*, vol. 34, no. 11, pp. 1909–1917, 2011, ISSN: 1521-4125. DOI: 10.1002/ceat.201100070.

[119] V. V. Ranade, "Multiphase flow processes," in *Computational Flow Modeling for Chemical Reactor Engineering*. Elsevier, 2002, pp. 85–122, ISBN: 978-0-12-576960-0. [Online]. Available: https://app.knovel.com/hotlink/pdf/id:kt00B5BNK2/computational-flow-modeling/multiphase-flow-processes.

[120] A. E. Sáez and R. G. Carbonell, "Hydrodynamic parameters for gas-liquid cocurrent flow in packed beds," *AIChE Journal*, vol. 31, no. 1, pp. 52–62, Jan. 1985, ISSN: 1547-5905. DOI: 10.1002/aic.690310105.

[121] Y. Saito and Y. Okada, "Topic: Organic hydride for hydrogen energy carrier," in *Energy Technology Roadmaps of Japan: Future Energy Systems Based on Feasible Technologies Beyond 2030*, Y. Kato, M. Koyama, Y. Fukushima, and T. Nakagaki, Eds. Tokyo: Springer Japan, 2016, pp. 459–462, ISBN: 978-4-431-55951-1. DOI: 10.1007/978-4-431-55951-1_34. [Online]. Available: https://doi.org/10.1007/978-4-431-55951-1_34.

[122] C. N. Satterfield, "Trickle-bed reactors," *AIChE Journal*, vol. 21, no. 2, pp. 209–228, 1975, ISSN: 1547-5905. DOI: 10.1002/aic.690210202.

[123] M. Schubert, A. Khetan, M. J. da Silva, and H. Kryk, "Spatially resolved inline measurement of liquid velocity in trickle bed reactors," *Chemical Engineering Journal*, vol. 158, no. 3, pp. 623–632, Apr. 2010, ISSN: 1385-8947. DOI: 10.1016/j.cej.2010.02.009.

[124] C. Sinn, J. Wentrup, G. R. Pesch, and J. Thöming, "Heat transport in open-cell foams: Cfd analysis of artificial heat sources vs fully resolved exothermal reactions," *Industrial & Engineering Chemistry Research*, vol. 60, no. 12, pp. 4542–4551, Mar. 2021, ISSN: 0888-5885. DOI: 10.1021/acs.iecr.0c05982.

[125] V. Sokolov and M. Yablokova, "Thermal conductivity of a stationary granular bed with upward gas-liquid flow," *Journal of Applied Chemistry of the USSR*, vol. 56, no. 3, pp. 551–553, 1983, ISSN: 0021-888X.

[126] F. Sotoodeh, B. J. M. Huber, and K. J. Smith, "Dehydrogenation kinetics and catalysis of organic heteroaromatics for hydrogen storage," *International Journal of Hydrogen Energy*, 2010 AIChE Annual Meeting Topical Conference on Hydrogen Production and Storage Special Issue, vol. 37, no. 3, pp. 2715–2722, Feb. 2012, ISSN: 0360-3199. DOI: 10.1016/j.ijhydene.2011.03.055.

[127] A. Souadnia and M. A. Latifi, "Analysis of two-phase flow distribution in trickle-bed reactors," *Chemical Engineering Science*, Proceedings of the 5th International Conference on Gas-Liquid and Gas-Liquid-Solid Reactor Engineering, vol. 56, no. 21, pp. 5977–5985, Nov. 2001, ISSN: 0009-2509. DOI: 10.1016/S0009-2509(01)00224-X.

[128] K. Stark, V. N. Emel'yanenko, A. A. Zhabina, *et al.*, "Liquid organic hydrogen carriers: Thermophysical and thermochemical studies of carbazole partly and fully hydrogenated derivatives," *Industrial & Engineering Chemistry Research*, vol. 54, no. 32, pp. 7953–7966, Aug. 2015, ISSN: 0888-5885. DOI: 10.1021/acs.iecr.5b01841.

[129] K. Stark, P. Keil, S. Schug, K. Müller, P. Wasserscheid, and W. Arlt, "Melting points of potential liquid organic hydrogen carrier systems consisting of n-alkylcarbazoles," *Journal of Chemical & Engineering Data*, vol. 61, no. 4, pp. 1441–1448, Apr. 2016, ISSN: 0021-9568. DOI: 10.1021/acs.jced.5b00679.

[130] C. G. Sun, F. H. Yin, A. Afacan, K. Nandakumar, and K. T. Chuang, "Modelling and simulation of flow maldistribution in random packed columns with gas-liquid countercurrent flow," *Chemical Engineering Research and Design*, Fluid Mixing, vol. 78, no. 3, pp. 378–388, Apr. 2000, ISSN: 0263-8762. DOI: 10.1205/026387600527275.

[131] M. Syamlal and T. O'Brien, "Computer simulation of bubbles in a fluidized bed," *AIChE Symposium Series*, vol. 85, no. 270, pp. 22–31, 1989.

[132] M. J. Szady and S. Sundaresan, "Effect of boundaries on trickle-bed hydrodynamics," *AIChE Journal*, vol. 37, no. 8, pp. 1237–1241, 1991, ISSN: 1547-5905. DOI: 10.1002/aic.690370813.

[133] M. J. Taulamet, N. J. Mariani, G. F. Barreto, and O. M. Martínez, "A critical review on heat transfer in trickle bed reactors," *Reviews in Chemical Engineering*, vol. 31, no. 2, pp. 97–118, Apr. 2015, ISSN: 2191-0235. DOI: 10.1515/revce-2014-0050.

[134] A. S. Teja, "Simple method for the calculation of heat capacities of liquid mixtures," *Journal of Chemical & Engineering Data*, vol. 28, no. 1, pp. 83–85, Jan. 1983, ISSN: 0021-9568. DOI: 10.1021/je00031a025.

[135] M. Tjahjono and M. Garland, "A new modified parachor model for predicting surface compositions of binary liquid mixtures. on the importance of surface volume representation," *Journal of Colloid and Interface Science*, vol. 345, no. 2, pp. 528–537, May 2010, ISSN: 0021-9797. DOI: 10.1016/j.jcis.2010.01.067.

[136] E. Tsotsas, "D6.3 thermal conductivity of packed beds," in *VDI Heat Atlas*, 2nd ed. Springer-Verlag, 2010, pp. 570–580. DOI: 10.1007/978-3-540-77877-6_26.

[137] M. Vångö, S. Pirker, and T. Lichtenegger, "Unresolved cfd–dem modeling of multiphase flow in densely packed particle beds," *Applied Mathematical Modelling*, vol. 56, pp. 501–516, Apr. 2018, ISSN: 0307-904X. DOI: 10.1016/j.apm.2017.12.008.

[138] D. Vortmeyer and J. Schuster, "Evaluation of steady flow profiles in rectangular and circular packed beds by a variational method," *Chemical Engineering Science*, vol. 38, no. 10, pp. 1691–1699, Jan. 1983, ISSN: 0009-2509. DOI: 10.1016/0009-2509(83)85026-X.

[139] B. Wang, T. Yan, T. Chang, *et al.*, "Palladium supported on reduced graphene oxide as a high-performance catalyst for the dehydrogenation of dodecahydro-n-ethylcarbazole," *Carbon*, vol. 122, pp. 9–18, Oct. 2017, ISSN: 0008-6223. DOI: 10.1016/j.carbon.2017.06.021.

[140] Y. Wang, J. Chen, and F. Larachi, "Modelling and simulation of trickle-bed reactors using computational fluid dynamics: A state-of-the-art review," *The Canadian Journal of Chemical Engineering*, vol. 91, no. 1, pp. 136–180, 2013, ISSN: 1939-019X. DOI: 10.1002/cjce.20702.

[141] M. Weber, M. Drobek, B. Rebière, *et al.*, "Hydrogen selective palladium-alumina composite membranes prepared by atomic layer deposition," *Journal of Membrane Science*, vol. 596, p. 117 701, Feb. 2020, ISSN: 0376-7388. DOI: 10.1016/j.memsci.2019.117701.

[142] V. W. Weekman Jr. and J. E. Myers, "Heat transfer characteristics of concurrent gas-liquid flow in packed beds," *AIChE Journal*, vol. 11, no. 1, pp. 13–17, 1965, ISSN: 1547-5905. DOI: 10.1002/aic.690110107.

[143] C. R. Wilke and P. Chang, "Correlation of diffusion coefficients in dilute solutions," *AIChE Journal*, vol. 1, no. 2, pp. 264–270, 1955, ISSN: 1547-5905. DOI: 10.1002/aic.690010222.

[144] Y. Yang, J. Yao, H. Wang, F. Yang, Z. Wu, and Z. Zhang, "Study on high hydrogen yield for large-scale hydrogen fuel storage and transportation based on liquid organic hydrogen carrier reactor," *Fuel*, vol. 321, p. 124 095, Aug. 2022, ISSN: 0016-2361. DOI: 10.1016/j.fuel.2022.124095.

[145] C. L. Yaws, X. Lin, L. Bu, and S. Nijhawan, "Appendix a: Coefficients for liquid thermal conductivity equation," in *Handbook of Thermal Conductivity*. Elsevier, 1995, vol. 3, pp. 366–371, ISBN: 978-0-88415-384-9. DOI: 10.1016/S1874-8783(06)80046-2. [Online]. Available: https://linkinghub.elsevier.com/retrieve/pii/S1874878306800462.

[146] B. Zdravkov, J. Čermák, M. Šefara, and J. Janků, "Pore classification in the characterization of porous materials: A perspective," *Open Chemistry*, vol. 5, no. 2, pp. 385–395, Jun. 2007, ISSN: 2391-5420. DOI: 10.2478/s11532-007-0017-9.

[147] L. Zhou, L. Sun, L. Xu, C. Wan, Y. An, and M. Ye, "Recent developments of effective catalysts for hydrogen storage technology using n-ethylcarbazole," *Catalysts*, vol. 10, no. 66, p. 648, Jun. 2020, ISSN: 2073-4344. DOI: 10.3390/catal10060648.

[148] H. P. Zhu, Z. Y. Zhou, R. Y. Yang, and A. B. Yu, "Discrete particle simulation of particulate systems: Theoretical developments," *Chemical Engineering Science*, Frontier of Chemical Engineering - Multi-scale Bridge between Reductionism and Holism, vol. 62, no. 13, pp. 3378–3396, Jul. 2007, ISSN: 0009-2509. DOI: 10.1016/j.ces.2006.12.089.

<div align="right">

A

</div>

User Defined Functions

A series of user-defined functions (UDFs) were written to incorporate sections of the model that are not directly available through the Ansys Fluent user interface. These are each referenced in the main body of the thesis indicating what each UDF is for. These UDFs were written in C programming language using macros developed by Fluent defined in the Fluent Customization Manual [4].

Many of the following UDFs employ user-defined memory slots (UDMs) which are memory slots throughout the reactor domain for custom parameters. These are used in the UDFs to store calculated values and make them accessible from the user interface. Table A.1 lists the main UDMs calculated from the UDFs throughout the entire bed domain.

The UDFs referenced in section A.16 and section A.17 calculate average values of distinct parameters at each plane as was described by Figure 7.2a and Figure 7.2b. This results in a single value at each axial height which is stored at every cell face along the reactor wall. These parameters are stored through additional UDMs that can be visualized by plotting their values along the reactor wall. Table A.2 lists these additional UDMs.

Table A.1: UDM parameters calculated by the UDFs.

UDM slot number	Parameter	Units
0	Liquid-gas interphase momentum exchange coefficient	[kg/(m^{3}s)]
1	Gas-solid interphase momentum exchange coefficient	[kg/(m^{3}s)]
2	Liquid-solid interphase momentum exchange coefficient	[kg/(m^{3}s)]
3	Solid volume fraction	[-]
4	Catalyst wetting efficiency	[-]
5	Mixture surface tension	[N/m]
6	Capillary pressure	[Pa]
7	Axial capillary pressure source term	[N/m^3]
8	Radial capillary pressure source term	[N/m^3]
9	Liquid thermal conductivity	[W/(m·K)]
10	Hydrogen thermal conductivity	[W/(m·K)]
11	Effective thermal conductivity	[W/(m·K)]
12	Wall heat transfer coefficient	[W/m^{2}K]
13	Dispersion Coefficient	[m^2/s]
14	Reaction rate 1 (12H-NEC to 8H-NEC)	[kmol/(m^{3}s)]
15	Reaction rate 2 (8H-NEC to 4H-NEC)	[kmol/(m^{3}s)]
16	Reaction rate 3 (4H-NEC to 0H-NEC)	[kmol/(m^{3}s)]
17	Outlet backflow temperature	[K]
18	Outlet backflow H8-NEC mass fraction	[-]
19	Outlet backflow H4-NEC mass fraction	[-]
20	Outlet backflow H0-NEC mass fraction	[-]
21	Initial gas volume fraction profile	[-]

Table A.2: UDM parameters used for visualizing plane average properties along the axial length of the reactor.

UDM slot number	Parameter	Units
22	Temperature	[K]
23	Liquid volume faction	[-]
24	Solid volume fraction	[-]
25	Solid volume fraction	[-]
26	Liquid axial velocity	[m/s]
27	Gas axial velocity	[m/s]
28	Liquid velocity magnitude	[m/s]
29	Gas velocity magnitude	[m/s]
30	Liquid density	[kg/m^3]
31	Liquid viscosity	[Pa·s)]
32	Liquid specific heat capacity	[J/(kg·K)]
33	Liquid thermal conductivity	[W/(m·K)]
34	Gas density	[kg/m^3]
35	Gas viscosity	[Pa·s)]
36	Gas specific heat capacity	[J/(kg·K)]
37	Gas thermal conductivity	[W/(m·K)]
38	Effective thermal conductivity	[W/(m·K)]
39	H0-NEC mass fraction	[-]
40	H4-NEC mass fraction	[-]
41	H8-NEC mass fraction	[-]
42	H12-NEC mass fraction	[-]
43	Reaction rate 1 (12H-NEC to 8H-NEC)	[kmol/(m^{3}s)]
44	Reaction rate 2 (8H-NEC to 4H-NEC)	[kmol/(m^{3}s)]
45	Reaction rate 3 (4H-NEC to 0H-NEC)	[kmol/(m^{3}s)]
46	Degree of hydrogenation	[-]
47	Liquid saturation	[-]
48	Gas saturation	[-]
49	H2 mass fraction	[-]
50	Gas mass flow	[kg/s]
51	Liquid mass flow	[kg/s]
52	H0-NEC mass flow	[kg/s]
53	H4-NEC mass flow	[kg/s]
54	H8-NEC mass flow	[kg/s]
55	H12-NEC mass flow	[kg/s]
56	Gas volumetric flow	[m^3/s]

A.1. Interface momentum exchange coefficients

A.1.1. Liquid-gas momentum exchange coefficient

```
/*****************************************************************************
UDF for calculating the liquid-gas interphase momentum exchange coefficient using
the two-fluid momentum interaction model (Attou et al. 1999)
*****************************************************************************/
#include "udf.h"

DEFINE_EXCHANGE_PROPERTY(liquid_gas_exchange_coefficient, cell, mix_thread, phase_1, phase_2)
{
    Thread *thread_g, *thread_l;
    real d_p, E1, E2, x_vel_g, x_vel_l, y_vel_g, y_vel_l, abs_v, slip_x, slip_y,
        rho_g, mu_g, void_g, void_l, void_s, k_g_l, term_1, term_2, limit;

    thread_l = THREAD_SUB_THREAD(mix_thread, phase_1);  /* Liquid phase thread */
    thread_g = THREAD_SUB_THREAD(mix_thread, phase_2);  /* Gas phase thread */

    /* Cell properties */
    x_vel_g = C_U(cell, thread_g);
```

```
18      y_vel_g = C_V(cell, thread_g);
19      x_vel_l = C_U(cell, thread_l);
20      y_vel_l = C_V(cell, thread_l);
21      slip_x = x_vel_g - x_vel_l;
22      slip_y = y_vel_g - y_vel_l;
23      abs_v = sqrt(slip_x * slip_x + slip_y * slip_y);  /* Calculate slip velocity */
24      void_g = C_VOF(cell, thread_g);  /* Gas volume fraction */
25      void_l = C_VOF(cell, thread_l);  /* Liquid volume fraction */
26      void_s = 1 - void_l - void_g;  /* Solid volume fraction */
27      rho_g = C_R(cell, thread_g);
28      mu_g = C_MU_L(cell, thread_g);
29
30      E1 = RP_Get_Input_Parameter("real-1");
31      E2 = RP_Get_Input_Parameter("real-2");
32      d_p = RP_Get_Input_Parameter("real-9");
33
34      limit = 0.10;  /* Gas volume fraction limit */
35      if (void_g < limit)
36      {
37          void_g = limit;
38      }
39      /* Calculate terms for the momentum exchange coefficient */
40      term_1 = ((E1 * mu_g * pow((1 - void_g), 2)) / (void_g * void_g * d_p * d_p)) * pow((
            void_s) / (1 - void_g), (2.0 / 3.0));
41      term_2 = ((E2 * rho_g * abs_v * (1 - void_g)) / (void_g * d_p)) * pow((void_s) / (1 -
            void_g), (1.0 / 3.0));
42      k_g_l = void_g * (term_1 + term_2);
43
44      if (k_g_l < 1)  /* Ensure the coefficient is not too small to avoid crashes */
45      {
46          C_UDMI(cell, mix_thread, 0) = 1;
47          return 1;
48      }
49      else
50      {
51          C_UDMI(cell, mix_thread, 0) = k_g_l;
52          return k_g_l;
53      }
54 }
```

A.1.2. Gas-solid momentum exchange coefficient

```
1  /********************************************************************************
2  UDF for calculating the gas-solid interphase momentum exchange coefficient using
3  the two-fluid momentum interaction model (Attou et al. 1999)
4  ********************************************************************************/
5  #include "udf.h"
6
7  DEFINE_EXCHANGE_PROPERTY(gas_solid_exchange_coefficient, cell, mix_thread, phase_1, phase_2)
8  {
9      Thread *thread_g, *thread_s;
10     real d_p, E1, E2, x_vel_g, x_vel_s, y_vel_g, y_vel_s, abs_v, slip_x, slip_y,
11         rho_g, mu_g, void_g, void_s, k_g_s, term_1, term_2, limit;
12
13     thread_g = THREAD_SUB_THREAD(mix_thread, phase_1);  /* Gas phase thread */
14     thread_s = THREAD_SUB_THREAD(mix_thread, phase_2);  /* Solid phase thread */
15
16     /* Cell properties */
17     x_vel_g = C_U(cell, thread_g);
18     y_vel_g = C_V(cell, thread_g);
19     x_vel_s = 0;
20     y_vel_s = 0;
21     slip_x = x_vel_g - x_vel_s;
22     slip_y = y_vel_g - y_vel_s;
23     abs_v = sqrt(slip_x * slip_x + slip_y * slip_y);  /* Calculate slip velocity */
24     void_g = C_VOF(cell, thread_g);  /* Gas volume fraction */
25     void_s = C_VOF(cell, thread_s);  /* Solid volume fraction */
26     rho_g = C_R(cell, thread_g);
27     mu_g = C_MU_L(cell, thread_g);
28
```

```
29      E1 = RP_Get_Input_Parameter("real-1");    /* Ergun constant 1 */
30      E2 = RP_Get_Input_Parameter("real-2");    /* Ergun constant 2 */
31      d_p = RP_Get_Input_Parameter("real-9");   /* Particle Diameter */
32
33      limit = 0.10;   /* Gas volume fraction limit */
34      if (void_g < limit)
35      {
36          void_g = limit;
37      }
38
39      /* Calculate terms for the momentum exchange coefficient */
40      term_1 = ((E1 * mu_g * pow((1 - void_g), 2)) / (void_g * void_g * d_p * d_p)) * pow((
            void_s) / (1 - void_g), (2.0 / 3.0));
41      term_2 = ((E2 * rho_g * abs_v * (1 - void_g)) / (void_g * d_p)) * pow((void_s) / (1 -
            void_g), (1.0 / 3.0));
42      k_g_s = void_g * (term_1 + term_2);
43
44      if (k_g_s < 1)   /* Ensure the coefficient is not too small to avoid crashes */
45      {
46          C_UDMI(cell, mix_thread, 1) = 1;
47          return 1;
48      }
49      else
50      {
51          C_UDMI(cell, mix_thread, 1) = k_g_s;
52          return k_g_s;
53      }
54  }
```

A.1.3. Liquid-solid momentum exchange coefficient

```
1   /*********************************************************************
2   UDF for calculating the liquid-solid interphase momentum exchange coefficient using
3   the two-fluid momentum interaction model (Attou et al. 1999)
4   *********************************************************************/
5   #include "udf.h"
6
7   DEFINE_EXCHANGE_PROPERTY(liquid_solid_exchange_coefficient, cell, mix_thread, phase_1,
        phase_2)
8   {
9       Thread *thread_l, *thread_s;
10      real d_p, E1, E2, x_vel_l, x_vel_s, y_vel_l, y_vel_s, abs_v, slip_x, slip_y,
11          rho_l, mu_l, void_l, void_s, k_l_s, term_1, term_2, limit;
12
13      thread_l = THREAD_SUB_THREAD(mix_thread, phase_1);   /* Liquid phase thread */
14      thread_s = THREAD_SUB_THREAD(mix_thread, phase_2);   /* Solid phase thread */
15
16      /* Cell properties */
17      x_vel_l = C_U(cell, thread_l);
18      y_vel_l = C_V(cell, thread_l);
19      x_vel_s = 0;
20      y_vel_s = 0;
21      slip_x = x_vel_l - x_vel_s;
22      slip_y = y_vel_l - y_vel_s;
23      abs_v = sqrt(slip_x * slip_x + slip_y * slip_y);   /* Calculate slip velocity */
24      void_l = C_VOF(cell, thread_l);   /* Liquid volume fraction */
25      void_s = C_VOF(cell, thread_s);   /* Solid volume fraction */
26      rho_l = C_R(cell, thread_l);
27      mu_l = C_MU_L(cell, thread_l);
28
29      E1 = RP_Get_Input_Parameter("real-1");    /* Ergun constant 1 */
30      E2 = RP_Get_Input_Parameter("real-2");    /* Ergun constant 2 */
31      d_p = RP_Get_Input_Parameter("real-9");   /* Particle Diameter */
32
33      limit = 0.10;   /* Liquid volume fraction limit */
34      if (void_l < limit)
35      {
36          void_l = limit;
37      }
38
```

```
39      /* Calculate terms for the momentum exchange coefficient */
40      term_1 = (E1 * mu_l * void_s * void_s) / (void_l * void_l * d_p * d_p);
41      term_2 = (E2 * rho_l * abs_v * void_s) / (void_l * d_p);
42      k_l_s = void_l * (term_1 + term_2);
43
44      if (k_l_s < 1)   /* Ensure the coefficient is not too small to avoid crashes */
45      {
46          C_UDMI(cell, mix_thread, 2) = 1;
47          return 1;
48      }
49      else
50      {
51          C_UDMI(cell, mix_thread, 2) = k_l_s;
52          return k_l_s;
53      }
54  }
```

A.2. Solid volume fraction profile

```
1  /*******************************************************************
2     UDF for generating solid and gas volume fraction profiles
3  *******************************************************************/
4  #include "udf.h"
5
6  DEFINE_INIT(solid_VOF_profile, mixture_domain)
7  {
8      real d_p,D,Sphericity,MeanBedPorosity,a,b,c,mu,sigma_percent,vof_s,L,f,
9          Estimated_Liquid_Holdup,vel_g,vof_g,sigma_wall,sigma_i;
10     int ID,N_max,N_min,n,i;
11     Thread *cell_threads_inlet, *cell_threads_outlet, *cell_threads;
12     /* Read input parameters */
13     d_p = RP_Get_Input_Parameter("real-9"); /* Particle diameter */
14     D = RP_Get_Input_Parameter("real-10"); /* Reactor diameter */
15     L = RP_Get_Input_Parameter("real-7"); /* Reactor length */
16     Sphericity = RP_Get_Input_Parameter("real-3"); /* Particle sphericity */
17     sigma_percent = RP_Get_Input_Parameter("real-6"); /* Standard deviation for axial
               porosity in bulk */
18     Estimated_Liquid_Holdup = RP_Get_Input_Parameter("real-11");/* Estimated liquid holdup*/
19     vel_g = RP_Get_Input_Parameter("real-5"); /* Gas inlet superficial velocity [m/s]*/
20     sigma_wall = sigma_percent; /* Standard deviation for axial porosity for cells near wall.
               In this case it is taken as the same standard deviation as the bulk*/
21
22
23     /* Mean bed porosity from Benyahia and O'Neill (2005) model */
24     MeanBedPorosity=(0.1504+(0.2024/Sphericity))+(1.0814/(pow(((D/d_p)+0.1226),2.)));
25     /* a parameter for Muller (1991) model */
26     if (D/d_p<13.0)
27      {
28     a = 8.243-(12.98/((D/d_p)+3.156));
29     }
30     else
31     {
32     a = 7.383-(2.932/((D/d_p)-9.864));
33     }
34     /* b parameter for Muller (1991) model */
35     b = 0.304-(0.724/(D/d_p));
36
37     N_max=floor(L/(d_p*5)); /* Number of harmonics */
38     N_min=10;
39     int array_size = N_max-N_min;
40     real An, Bn;
41     real An_store [array_size];
42     real Bn_store [array_size];
43
44     /*Fourier Transfer coefficients for cells in bulk*/
45     sigma_i=sigma_percent/sqrt(N_max-N_min+1);
46     i=0;
47     for (n = N_min; n <= N_max; ++n)
48   {
49     An = gauss_random()*sigma_i;
```

```
50      An_store[i] = An;
51      Bn = gauss_random()*sigma_i;
52      Bn_store[i] = Bn;
53      i=i+1;
54    }
55
56   /*Fourier Transfer coefficients for cells near wall in case a different standard deviation
          for these cells should be used */
57      real An_wall, Bn_wall,sigma_i_wall;
58      real An_store_wall [array_size];
59      real Bn_store_wall [array_size];
60      sigma_i_wall=sigma_wall/sqrt(N_max-N_min+1);
61      i=0;
62      for (n = N_min; n <= N_max; ++n)
63    {
64      An_wall = gauss_random()*sigma_i_wall;
65      An_store_wall[i] = An_wall;
66      Bn_wall = gauss_random()*sigma_i_wall;
67      Bn_store_wall[i] = Bn_wall;
68      i=i+1;
69    }
70      cell_t cell;
71      real xc[ND_ND];   /* ND_ND constant is defined as 2 for Fluent 2D and as 3 for Fluent 3D*/
72
73      for (ID = 12; ID<=16; ++ID) /* All domain zones ID 12 through 16 */
74  {
75       /*  Lookup threads in zone ID  */
76       cell_threads = Lookup_Thread(mixture_domain, ID);
77
78       /* loop over all cells in cell thread */
79          begin_c_loop(cell,cell_threads)
80      {
81          C_CENTROID(xc,cell,cell_threads);
82          /* Solid volume fraction from Muller (1991) model */
83          mu = 1-(MeanBedPorosity+(1-MeanBedPorosity)*j0(a*(((D/2)-xc[1])/d_p))
84                  *exp(-b*(((D/2)-xc[1])/d_p)));
85          f=0; /* Initialize expansion */
86          i=0;
87
88          if (xc[1]>((D/2)-2*d_p)) /* Cells near wall */
89          {
90              for (n = N_min; n <= N_max; ++n)
91              {
92              f =f+An_store_wall[i]*cos(2*n*xc[0]*M_PI)+Bn_store_wall[i]*sin(2*n*xc[0]*M_PI);
93              i=i+1;
94              }
95              f = f+1; /* Center f around 1 */
96
97              if (mu<=0.35) /* Minimum solid volume fraction*/
98               {
99                 mu= 0.35;
100               }
101             vof_s = f*mu;
102          }
103          else /* Cells in bulk */
104          {
105              for (n = N_min; n <= N_max; ++n)
106              {
107              f = f + An_store[i]*cos(2*n*xc[0]*M_PI) + Bn_store[i]*sin(2*n*xc[0]*M_PI);
108              i=i+1;
109              }
110              f = f+1; /* Center f around 1 */
111              vof_s = f*mu;
112          }
113
114          if (vof_s>=0.7) /* Maximum solid volume fraction related to packing limit */
115          {
116           C_UDMI(cell,cell_threads,3) = 0.7;
117          }
118          else if (vof_s<=0.3)
119          {
```

```
120        C_UDMI(cell,cell_threads,3) = 0.3;
121        }
122        else
123        {
124        C_UDMI(cell,cell_threads,3) = vof_s;
125        }
126        vof_s = C_UDMI(cell,cell_threads,3); /* Solid volume fraction */
127          /* Estimated gas volume fraction for case initialization*/
128        vof_g = (1-vof_s)*((MeanBedPorosity-Estimated_Liquid_Holdup)/MeanBedPorosity);
129        C_UDMI(cell,cell_threads,21) = vof_g;
130    }
131        end_c_loop(cell,cell_threads)
132 }
133  }
```

A.3. External particle wetting efficiency

```
1  /*****************************************************************************
2     UDF for calculating cell external particle wetting efficiency using
3     correlation by Al-Dahhan and Dudukovic (1995)
4  *****************************************************************************/
5  # include "udf.h"
6
7  DEFINE_ADJUST(Wetting_Efficiency, domain)
8  {
9     real d_p, g, rho_l, mu_l, Porosity, Pressure_Gradient, x_vel_l, y_vel_l,
10        abs_v_l, Re_l, Ga_l, Wetting_efficiency, vof_l, superficial_vel_l;
11    Thread *t, *thread_s, *thread_l;
12    cell_t c;
13    Domain *mixture_domain;
14    d_p = RP_Get_Input_Parameter("real-9"); /* Particle diameter */
15    g = 9.81; /* Acceleration due to gravity */
16    mixture_domain=Get_Domain(1);
17      /* loop over all threads in domain */
18      thread_loop_c (t,mixture_domain)
19     {
20      thread_s = THREAD_SUB_THREAD(t, 2);/* get solid phase cell thread*/
21      thread_l = THREAD_SUB_THREAD(t, 0);/* get liquid phase cell thread */
22      /* loop over all cells in cell thread */
23     begin_c_loop (c,t)
24      {
25       rho_l = C_R(c, thread_l); /* Liquid density [kg/m3]*/
26       mu_l = C_MU_L(c, thread_l); /* Liquid viscosity [kg/m.s]*/
27       Porosity = 1-C_VOF(c,thread_s); /* Cell porosity [-]*/
28       Pressure_Gradient = NV_MAG(C_P_G(c,t));
29       x_vel_l = C_U(c, thread_l);
30       y_vel_l = C_V(c, thread_l);
31       abs_v_l = sqrt(x_vel_l*x_vel_l + y_vel_l*y_vel_l); /*Interstitialvelocity [m/s]*/
32       vof_l = C_VOF(c, thread_l); /* Liquid volume fraction [-]*/
33       superficial_vel_l = abs_v_l*vof_l; /*Superficial liquid velocity [m/s]*/
34       Re_l = (superficial_vel_l*rho_l*d_p)/(mu_l*(1.0-Porosity));
35       Ga_l = (pow(d_p,3.0)*pow(rho_l,2.0)*g*pow(Porosity,3.0))/
36           (pow(mu_l,2.0)*pow((1.0-Porosity),3.0));
37       Wetting_efficiency = 1.104*pow(Re_l,(1.0/3.0))*
38           pow(((1.0+(Pressure_Gradient/(g*rho_l)))/Ga_l),(1.0/9.0));
39       if (Wetting_efficiency>1)
40       {
41           C_UDMI(c,t,4) = 1;
42       }
43       else
44       {
45           C_UDMI(c,t,4) = Wetting_efficiency;
46       }
47      }
48      end_c_loop (c,t)
49      }
50  }
```

A.4. Capillary pressure

The capillary pressure calculation requires calculating gas and solid volume fraction gradients. As this is not readily provided by Fluent, the gas and solid volume fractions are first stored in a user-defined scalar (UDS) by the UDF in section A.5, and then its gradient is calculated with a macro in the UDF below. Table A.3 lists the UDS slot numbers used.

Table A.3: User defined scalar numbering

UDS slot number	Parameter	Units
0	Gas volume faction	[-]
1	Solid volume fraction	[-]

```c
1  /***********************************************************************
2  UDF for calculating capillary pressure per Attou and Ferschneider (2000)
3  ***********************************************************************/
4  #include "udf.h"
5
6  DEFINE_ADJUST(Capillary_Pressure_Attou, domain)
7  {
8     real d_p, sigma, rho_l, rho_g, vof_s, vof_g, F, P_c;
9     Thread *t, *thread_s, *thread_l, *thread_g;
10    cell_t c;
11    Domain *mixture_domain;
12    d_p = RP_Get_Input_Parameter("real-9"); /* Particle diameter */
13
14
15    mixture_domain=Get_Domain(1);
16       /* loop over all threads in domain */
17       thread_loop_c (t,mixture_domain)
18     {
19      thread_l = THREAD_SUB_THREAD(t, 0);/* get liquid phase cell thread */
20      thread_g = THREAD_SUB_THREAD(t, 1);/* get gas phase cell thread */
21      thread_s = THREAD_SUB_THREAD(t, 2);/* get solid phase cell thread*/
22
23       /* loop over all cells in cell thread */
24     begin_c_loop (c,t)
25      {
26       sigma = C_UDMI(c,t,5); /*Surface Tension [N/m]*/
27       rho_l = C_R(c, thread_l);
28       rho_g = C_R(c, thread_g);
29       vof_s = C_VOF(c, thread_s);
30       vof_g = C_VOF(c, thread_g);
31
32       F = 1.0+88.1*(rho_g/rho_l);
33       /*Capillary pressure [Pa]*/
34       P_c=2.0*sigma*pow((vof_s/(1- vof_g)),(1.0/3.0))*(5.416/d_p)*F;
35
36       C_UDMI(c,t,6) = P_c;
37      }
38     end_c_loop (c,t)
39     }
40  }
41
42  /***********************************************************************
43  UDF for specifying an axial momentum source term in liquid phase to
44  account for capillary pressure
45  ***********************************************************************/
46
47   DEFINE_SOURCE(Capillary_Pressure_Axial_Source,cell,t,dS,eqn)
48  {
49     real d_p, sigma, source, void_s, void_g, rho_g, rho_l, DVOFNX_g, DVOFNX_s,
50         wetting_eff, term_1, term_2, F;
51
52     Thread *thread_s, *thread_l, *thread_g ;
53     d_p = RP_Get_Input_Parameter("real-9");
54
```

```
55      Thread *mixture_thread = THREAD_SUPER_THREAD(t);
56
57      thread_l = THREAD_SUB_THREAD(mixture_thread, 0);/* get liquid phase cell thread */
58      thread_g = THREAD_SUB_THREAD(mixture_thread, 1);/* get gas phase cell thread */
59      thread_s = THREAD_SUB_THREAD(mixture_thread, 2);/* get solid phase cell thread*/
60
61       /* find properties*/
62      sigma = C_UDMI(cell,mixture_thread,5); /*Surface Tension [N/m] */
63      void_s = C_VOF(cell, thread_s);/* solid vol frac*/
64      void_g = C_VOF(cell, thread_g);/* gas vol frac*/
65      rho_g = C_R(cell, thread_g); /* gas density*/
66      rho_l = C_R(cell, thread_l); /* liquid density*/
67
68      DVOFNX_g = C_UDSI_G(cell,t,0)[0]; /* Axial gas volume fraction gradient*/
69      DVOFNX_s = C_UDSI_G(cell,t,1)[0]; /* Axial solid volume fraction gradient*/
70
71      wetting_eff = C_UDMI(cell,mixture_thread,4); /*Wetting efficiency [%]*/
72
73      F = 1.0+88.1*(rho_g/rho_l);
74
75      term_1 = (2.0/3.0)*sigma*(5.416/d_p)*pow((void_s)/(1.0-void_g),(-2.0/3.0));
76      term_2 = (1.0/(1.0-void_g))*DVOFNX_s+(void_s/pow((1.0-void_g),2.0))*DVOFNX_g;
77
78      source = (1.0-wetting_eff)*term_1*term_2*F; /*Axial source term [N/m3]*/
79      C_UDMI(cell,mixture_thread,7)=source;
80      dS[eqn] = 0;
81      return source;
82  }
83
84  /****************************************************************************
85  UDF for specifying a radial momentum source term in liquid phase to
86  account for capillary pressure
87  ****************************************************************************/
88
89   DEFINE_SOURCE(Capillary_Pressure_Radial_Source,cell,t,dS,eqn)
90  {
91      real d_p, sigma, source, void_s, void_g, rho_g, rho_l, DVOFNY_g, DVOFNY_s,
92       wetting_eff, term_1, term_2, F;
93
94      Thread  *thread_s, *thread_l, *thread_g ;
95      d_p = RP_Get_Input_Parameter("real-9");
96
97      Thread *mixture_thread = THREAD_SUPER_THREAD(t);
98
99      thread_l = THREAD_SUB_THREAD(mixture_thread, 0);/* get liquid phase cell thread */
100     thread_g = THREAD_SUB_THREAD(mixture_thread, 1);/* get gas phase cell thread */
101     thread_s = THREAD_SUB_THREAD(mixture_thread, 2);/* get solid phase cell thread*/
102
103      /* find properties*/
104     sigma = C_UDMI(cell,mixture_thread,5); /*Surface Tension [N/m] */
105     void_s = C_VOF(cell, thread_s);/* solid vol frac*/
106     void_g = C_VOF(cell, thread_g);/* gas vol frac*/
107     rho_g = C_R(cell, thread_g); /* gas density*/
108     rho_l = C_R(cell, thread_l); /* liquid density*/
109
110     DVOFNY_g = C_UDSI_G(cell,t,0)[1]; /* Radial gas volume fraction gradient*/
111     DVOFNY_s = C_UDSI_G(cell,t,1)[1]; /* Radial solid volume fraction gradient*/
112
113     wetting_eff = C_UDMI(cell,mixture_thread,4); /*Wetting efficiency [%]*/
114
115     F = 1.0+88.1*(rho_g/rho_l);
116
117     term_1 = (2.0/3.0)*sigma*(5.416/d_p)*pow((void_s)/(1.0- void_g),(-2.0/3.0));
118     term_2 = (1.0/(1.0-void_g))*DVOFNY_s+(void_s/pow((1.0-void_g),2.0))*DVOFNY_g;
119
120     source = (1.0-wetting_eff)*term_1*term_2*F; /*Radial source term [N/m3]*/
121     C_UDMI(cell,mixture_thread,8)=source;
122     dS[eqn] = 0;
123     return source;
124  }
```

A.5. Volume fractions

```c
/*************************************************************************
UDF to store values of gas and solid volume fraction in user defined scalars (UDS).
This is further used by the capillary pressure UDF to calculate volume fraction
gradients and to then evaluate the momentum source terms due to capillary effect.
*************************************************************************/
# include "udf.h"

DEFINE_ADJUST(VOF_Gradient, domain)
{
    Thread *t;
    cell_t c;
    face_t f;
    int domain_ID_gas=3; /* Gas phase ID */
    int domain_ID_solid=4; /* Solid phase ID*/
    Domain *mixture_domain, *gas_domain, *solid_domain;
    mixture_domain=Get_Domain(1);
    gas_domain = Get_Domain(domain_ID_gas);
    solid_domain = Get_Domain(domain_ID_solid);

    /* Fill UDS with the variable. */
    thread_loop_c (t,gas_domain)
      {
      begin_c_loop (c,t)
         {
         C_UDSI(c,t,0) = C_VOF(c,t);
         }
      end_c_loop (c,t)
      }
    thread_loop_f (t,gas_domain)
      {
      if (THREAD_STORAGE(t,SV_UDS_I(0))!=NULL)
        begin_f_loop (f,t)
         {
         F_UDSI(f,t,0) = F_VOF(f,t);
         }
      end_f_loop (f,t)
      }
       /* Fill UDS with the variable. */
    thread_loop_c (t,solid_domain)
      {
      begin_c_loop (c,t)
         {
         C_UDSI(c,t,1) = C_VOF(c,t);
         }
      end_c_loop (c,t)
      }
    thread_loop_f (t,solid_domain)
      {
      if (THREAD_STORAGE(t,SV_UDS_I(1))!=NULL)
        begin_f_loop (f,t)
         {
         F_UDSI(f,t,1) = F_VOF(f,t);
         }
      end_f_loop (f,t)
      }
}
```

A.6. Mass flow rates

```c
/*************************************************************************
   UDF to plot plane-averaged mass flows. UDF executed at every iteration to visualize
   the mass flow imbalance, hydrogen yield, and degree of hydrogenation monitors
   throughout the solution process.
*************************************************************************/
#include "udf.h"

DEFINE_ADJUST(Mass_Flow_Rates, domain)
```

```
9   {
10      Domain *mixture_domain;
11      mixture_domain=Get_Domain(1);
12      real Cell_axial_length;
13      Cell_axial_length = RP_Get_Input_Parameter("real-12"); /* Cell size axial length */
14      Thread *t, *Wall_Thread, *thread_l, *thread_g;
15      int i,ID;
16      cell_t cell, c0;
17      Thread *t0, *t_cell;
18      face_t f, f_wall;
19
20      /*   Intermediate calculation variables   */
21      real DoH_cell, L_mass_flow_cell, G_mass_flow_cell, G_volumetric_flow_cell,
22          L_mass_flow_cell_abs, L_mass_flow_abs, H0NEC_mass_flow_cell,
23          H4NEC_mass_flow_cell, H8NEC_mass_flow_cell, H12NEC_mass_flow_cell,
24          DoH_int, Area_Weight;
25
26      /* Parameters */
27      real DoH, L_mass_flow, G_mass_flow, G_volumetric_flow, H0NEC_mass_flow,
28          H4NEC_mass_flow, H8NEC_mass_flow, H12NEC_mass_flow, Y_0, Y_1, Y_2, Y_3,
29          x_vel_l, rho_l, x_vel_g, rho_g, VOF_l, VOF_g;
30
31      /* Coordinate parameters */
32      real xa[ND_ND];  /* Coordinates of wall faces*/
33      real xb[ND_ND];  /* Coordinates of domain faces*/
34      real x_a, x_b, y_b, A_x;
35      real A[ND_ND]; /*face area normal vector */
36
37      /* Variables for Mole fraction calculation */
38      real M_0,M_1,M_2,M_3,M_avg,X_0,X_1,X_2,X_3;
39      M_0 = 195.2597;   /*Molecular weight of H0-NEC [g/mol]*/
40      M_1 = 199.2915;   /*Molecular weight of H4-NEC [g/mol]*/
41      M_2 = 203.3232;   /*Molecular weight of H8-NEC [g/mol]*/
42      M_3 = 207.3550;   /*Molecular weight of H12-NEC [g/mol]*/
43
44  for (ID = 24; ID<=28; ++ID) /* Wall section zones ID 24, 25, 26, 27, and 28 */
45  {
46      Wall_Thread = Lookup_Thread(mixture_domain,ID); /* Wall thread */
47      begin_f_loop(f_wall,Wall_Thread)  /* Loop over faces on wall thread*/
48        {
49          /* Variable initialization */
50        G_mass_flow=0.0;
51        G_volumetric_flow=0.0;
52        L_mass_flow=0.0;
53        L_mass_flow_abs = 0.0;
54        H0NEC_mass_flow=0.0;
55        H4NEC_mass_flow=0.0;
56        H8NEC_mass_flow=0.0;
57        H12NEC_mass_flow=0.0;
58        DoH_int=0.0;
59
60        F_CENTROID(xa,f_wall,Wall_Thread);
61        x_a = xa[0]; /* wall face centroid axial coordinate */
62        i=0;
63        /* loops over all face threads in a domain*/
64         thread_loop_f (t,mixture_domain)
65        {
66        /* loop over all faces in face threads */
67        begin_f_loop (f,t)
68         {
69          F_CENTROID(xb,f,t);
70          x_b = xb[0]; /* face centroid axial coordinate */
71          y_b = xb[1]; /* face centroid radial coordinate*/
72
73          if  (x_b>(x_a+0.25*Cell_axial_length) && x_b<(x_a+0.75*Cell_axial_length))
74          {
75          F_AREA(A,f,t);
76          A_x = fabs(A[0]); /*Projected radial length of face*/
77          Area_Weight = A_x*2*M_PI; /*Equal to pi*(r_upper^2 - r_lower^2)*/
78          cell = F_C0(f,t);   /*Adjacent Cell Index*/
79          t_cell = THREAD_T0(t); /*Adjacent Cell Thread*/
```

```
80          thread_l = THREAD_SUB_THREAD(t_cell, 0);/* liquid phase cell thread */
81          thread_g = THREAD_SUB_THREAD(t_cell, 1);/* gas phase cell thread */
82
83          /* Cell Properties */
84          x_vel_l = C_U(cell, thread_l);
85          x_vel_g = C_U(cell, thread_g);
86          rho_l = C_R(cell, thread_l);
87          rho_g = C_R(cell, thread_g);
88          VOF_l = C_VOF(cell, thread_l);
89          VOF_g = C_VOF(cell, thread_g);
90          Y_0 = C_YI(cell,thread_l,0); /*Mass fraction of H0-NEC*/
91          Y_1 = C_YI(cell,thread_l,1); /*Mass fraction of H4-NEC*/
92          Y_2 = C_YI(cell,thread_l,2); /*Mass fraction of H8-NEC*/
93          Y_3 = C_YI(cell,thread_l,3); /*Mass fraction of H12-NEC*/
94          /*Average molecular weight of mixture [g/mol]*/
95          M_avg = 1/((Y_0/M_0)+(Y_1/M_1)+(Y_2/M_2)+(Y_3/M_3));
96          X_0 = (Y_0/M_0)*M_avg ; /*Mole fraction of H0-NEC*/
97          X_1 = (Y_1/M_1)*M_avg ; /*Mole fraction of H4-NEC*/
98          X_2 = (Y_2/M_2)*M_avg ; /*Mole fraction of H8-NEC*/
99          X_3 = (Y_3/M_3)*M_avg ; /*Mole fraction of H12-NEC*/
100         DoH_cell = (X_1 + 2*X_2 + 3*X_3)/3;
101
102         /* Cell flow rates */
103         L_mass_flow_cell=rho_l*VOF_l*x_vel_l*Area_Weight;
104         G_mass_flow_cell=rho_g*VOF_g*x_vel_g*Area_Weight;
105         G_volumetric_flow_cell=VOF_g*x_vel_g*Area_Weight;
106
107         H0NEC_mass_flow_cell = L_mass_flow_cell*Y_0;
108         H4NEC_mass_flow_cell = L_mass_flow_cell*Y_1;
109         H8NEC_mass_flow_cell= L_mass_flow_cell*Y_2;
110         H12NEC_mass_flow_cell = L_mass_flow_cell*Y_3;
111
112         /* Total flow rates */
113         L_mass_flow = L_mass_flow + L_mass_flow_cell;
114         G_mass_flow = G_mass_flow + G_mass_flow_cell;
115         G_volumetric_flow = G_volumetric_flow + G_volumetric_flow_cell;
116         H0NEC_mass_flow= H0NEC_mass_flow + H0NEC_mass_flow_cell;
117         H4NEC_mass_flow= H4NEC_mass_flow + H4NEC_mass_flow_cell;
118         H8NEC_mass_flow= H8NEC_mass_flow + H8NEC_mass_flow_cell;
119         H12NEC_mass_flow= H12NEC_mass_flow + H12NEC_mass_flow_cell;
120
121         /* Mass-Weighted Average Properties */
122          /* Cell properties times cell absolute mass flow rate */
123         L_mass_flow_cell_abs=rho_l*VOF_l*fabs(x_vel_l*Area_Weight);
124         L_mass_flow_abs = L_mass_flow_abs + L_mass_flow_cell_abs;
125
126         DoH_int = DoH_int + DoH_cell*L_mass_flow_cell_abs;
127         i=i+1;
128        }
129      }
130    end_f_loop (f,t)
131    }
132
133       /* Plane Mass-Weighted Average Properties */
134       DoH = DoH_int / L_mass_flow_abs ;
135
136       /* Record values in user defined memory slots */
137       F_UDMI(f_wall,Wall_Thread,46) = DoH;
138       c0 = F_C0(f_wall,Wall_Thread);
139       t0 = F_C0_THREAD(f_wall,Wall_Thread);
140       C_UDMI(c0,t0,46)=F_UDMI(f_wall,Wall_Thread,46);
141
142       F_UDMI(f_wall,Wall_Thread,50) = G_mass_flow;
143       c0 = F_C0(f_wall,Wall_Thread);
144       t0 = F_C0_THREAD(f_wall,Wall_Thread);
145       C_UDMI(c0,t0,50)=F_UDMI(f_wall,Wall_Thread,50);
146
147       F_UDMI(f_wall,Wall_Thread,51) = L_mass_flow;
148       c0 = F_C0(f_wall,Wall_Thread);
149       t0 = F_C0_THREAD(f_wall,Wall_Thread);
150       C_UDMI(c0,t0,51)=F_UDMI(f_wall,Wall_Thread,51);
```

```
151
152            F_UDMI(f_wall,Wall_Thread,52) = H0NEC_mass_flow;
153            c0 = F_C0(f_wall,Wall_Thread);
154            t0 = F_C0_THREAD(f_wall,Wall_Thread);
155            C_UDMI(c0,t0,52)=F_UDMI(f_wall,Wall_Thread,52);
156
157            F_UDMI(f_wall,Wall_Thread,53) = H4NEC_mass_flow;
158            c0 = F_C0(f_wall,Wall_Thread);
159            t0 = F_C0_THREAD(f_wall,Wall_Thread);
160            C_UDMI(c0,t0,53)=F_UDMI(f_wall,Wall_Thread,53);
161
162            F_UDMI(f_wall,Wall_Thread,54) = H8NEC_mass_flow;
163            c0 = F_C0(f_wall,Wall_Thread);
164            t0 = F_C0_THREAD(f_wall,Wall_Thread);
165            C_UDMI(c0,t0,54)=F_UDMI(f_wall,Wall_Thread,54);
166
167            F_UDMI(f_wall,Wall_Thread,55) = H12NEC_mass_flow;
168            c0 = F_C0(f_wall,Wall_Thread);
169            t0 = F_C0_THREAD(f_wall,Wall_Thread);
170            C_UDMI(c0,t0,55)=F_UDMI(f_wall,Wall_Thread,55);
171
172            F_UDMI(f_wall,Wall_Thread,56) = G_volumetric_flow;
173            c0 = F_C0(f_wall,Wall_Thread);
174            t0 = F_C0_THREAD(f_wall,Wall_Thread);
175            C_UDMI(c0,t0,56)=F_UDMI(f_wall,Wall_Thread,56);
176
177        }
178     end_f_loop(f_wall,Wall_Thread)
179 }
180  }
```

A.7. Hydrogen thermal conductivity

```
1  /********************************************************************
2     UDF for calculating Hydrogen Thermal Conductivity
3  ********************************************************************/
4  # include "udf.h"
5
6  DEFINE_ADJUST(Hydrogen_Thermal_Conductivity, domain)
7  {
8     real T_g,k_h2;
9     Thread *t,  *thread_g;
10    cell_t c;
11    Domain *mixture_domain;
12    mixture_domain=Get_Domain(1);
13       /* loop over all threads in domain */
14       thread_loop_c (t,mixture_domain)
15      {
16      thread_g = THREAD_SUB_THREAD(t, 1);/* get gas phase cell thread */
17
18       /* loop over all cells in cell thread */
19      begin_c_loop (c,t)
20       {
21       T_g = C_T(c, thread_g); /*Gas (Mixture) Temperature*/
22
23       if (T_g>=100 && T_g<500)
24       {
25        k_h2 = 0.02009705 + 3.234622E-04*T_g + 2.1637249E-06*pow(T_g,2.0)
26             - 6.49151204E-09*pow(T_g,3.0) + 5.52407932E-12*pow(T_g,4.0);
27       }
28       else if (T_g>=500 && T_g<1500)
29       {
30        k_h2 = 0.1083105 + 2.21163789E-04*T_g + 2.26380948E-07*pow(T_g,2.0)
31             - 1.74258636E-10*pow(T_g,3.0) + 4.6468625E-14*pow(T_g,4.0);
32       }
33       else if (T_g>=1500 && T_g<=2000)
34       {
35        k_h2 = -0.28107269 + 1.09703479E-03*T_g - 5.27318283E-07*pow(T_g,2.0)
36             + 1.2403865E-10*pow(T_g,3.0);
```

```
37         }
38          else
39         {
40          k_h2 = 0.1672 ; /*Hydrogen thermal conductivity at ambient conditions*/
41         }
42         C_UDMI(c,t,10) = k_h2;
43        }
44       end_c_loop (c,t)
45       }
46  }
47
48  /********************************************************************
49     UDF for initializing values for Hydrogen Thermal Conductivity
50  ********************************************************************/
51  DEFINE_INIT(Initialize_Hydrogen_Thermal_Conductivity, domain)
52  {
53      real T_g,k_h2;
54      Thread *t,  *thread_g;
55      cell_t c;
56      Domain *mixture_domain;
57
58      mixture_domain=Get_Domain(1);
59          /* loop over all threads in domain */
60          thread_loop_c (t,mixture_domain)
61        {
62         thread_g = THREAD_SUB_THREAD(t, 1);/* get gas phase cell thread */
63
64          /* loop over all cells in cell thread */
65        begin_c_loop (c,t)
66          {
67          T_g = C_T(c, thread_g); /*Gas (Mixture) Temperature*/
68
69          if (T_g>=100 && T_g<500)
70          {
71           k_h2 = 0.02009705 + 3.234622E-04*T_g + 2.1637249E-06*pow(T_g,2.0)
72               - 6.49151204E-09*pow(T_g,3.0) + 5.52407932E-12*pow(T_g,4.0);
73          }
74          else if (T_g>=500 && T_g<1500)
75          {
76           k_h2 = 0.1083105 + 2.21163789E-04*T_g + 2.26380948E-07*pow(T_g,2.0)
77               - 1.74258636E-10*pow(T_g,3.0) + 4.6468625E-14*pow(T_g,4.0);
78          }
79          else if (T_g>=1500 && T_g<=2000)
80          {
81           k_h2 = -0.28107269 + 1.09703479E-03*T_g - 5.27318283E-07*pow(T_g,2.0)
82               + 1.2403865E-10*pow(T_g,3.0);
83          }
84           else
85          {
86           k_h2 = 0.1672 ; /*Hydrogen thermal conductivity at ambient conditions*/
87          }
88          C_UDMI(c,t,10) = k_h2;
89         }
90       end_c_loop (c,t)
91       }
92  }
```

A.8. Liquid mixture thermal conductivity

```
1  /*********************************************************************************
2     UDF for calculating liquid NEC mixture Thermal
3     Conductivity using model by Berger Bioucas (2020)
4  *********************************************************************************/
5  # include "udf.h"
6
7  DEFINE_ADJUST(NEC_Thermal_Conductivity, domain)
8  {
9      real T_cell,T_ref,A,B,C_0,C_1,C_2,C_3,M_0,M_1,M_2,M_3,M_avg,
10         rho_ref_0,rho_ref_1,rho_ref_2,rho_ref_3,rho_0,rho_1,
```

```
11          rho_2,rho_3,Y_0,Y_1,Y_2,Y_3,X_0,X_1,X_2,X_3, k_0,k_1,k_2,k_3,k_mix;
12     Thread *t, *thread_l;
13     cell_t c;
14     Domain *mixture_domain;
15
16     T_ref = 303.15; /*Reference Temperature for Berger Bioucas model [K]*/
17     A = 0.1083;
18     B = 4.823;
19     C_0 = 2.2;        /*C for dehydrogenated molecule*/
20     C_1 = 2.133;      /*Interpolated C for partially hydrogenated molecule*/
21     C_2 = 2.066;      /*Interpolated C for partially hydrogenated molecule*/
22     C_3 = 2.0;        /*C for hydrogenated molecule*/
23
24     M_0 = 195.2597;   /*Molecular weight of H0-NEC [g/mol]*/
25     M_1 = 199.2915;   /*Molecular weight of H4-NEC [g/mol]*/
26     M_2 = 203.3232;   /*Molecular weight of H8-NEC [g/mol]*/
27     M_3 = 207.3550;   /*Molecular weight of H12-NEC [g/mol]*/
28         /*Densities of NEC species at reference temperature [g/cm^3 [(Stark, 2015)*/
29     rho_ref_0 = 1.313467-0.0007238*T_ref;  /*H0-NEC*/
30     rho_ref_1 = 1.2553362-0.0006966*T_ref; /*H4-NEC*/
31     rho_ref_2 = 1.210127-0.0006907*T_ref;  /*H8-NEC*/
32     rho_ref_3 = 1.1482329-0.0007092*T_ref; /* H12-NEC */
33
34     mixture_domain=Get_Domain(1);
35         /* loop over all threads in domain */
36         thread_loop_c (t,mixture_domain)
37       {
38        thread_l = THREAD_SUB_THREAD(t, 0);/* get liquid phase cell thread */
39
40        /* loop over all cells in cell thread */
41       begin_c_loop (c,t)
42        {
43         T_cell = C_T(c, thread_l); /*Liquid Temperature*/
44        /*Densities of NEC species at operating temperature [g/cm^3 [(Stark, 2015)*/
45         rho_0 = 1.313467-0.0007238*T_cell;  /*H0-NEC*/
46         rho_1 = 1.2553362-0.0006966*T_cell; /*H4-NEC*/
47         rho_2 = 1.210127-0.0006907*T_cell;  /*H8-NEC*/
48         rho_3 = 1.1482329-0.0007092*T_cell; /*H12-NEC*/
49            /*Thermal conductivity of NEC species [W/m.K] (Berger Bioucas, 2020)*/
50         k_0 =(A*(rho_ref_0)+B*(pow(rho_ref_0,2)/M_0))
51              *pow((rho_0/rho_ref_0),(C_0*rho_0)); /*H0-NEC*/
52         k_1 =(A*(rho_ref_1)+B*(pow(rho_ref_1,2)/M_1))
53              *pow((rho_1/rho_ref_1),(C_1*rho_1)); /*H4-NEC*/
54         k_2 =(A*(rho_ref_2)+B*(pow(rho_ref_2,2)/M_2))
55              *pow((rho_2/rho_ref_2),(C_2*rho_2)); /*H8-NEC*/
56         k_3 =(A*(rho_ref_3)+B*(pow(rho_ref_3,2)/M_3))
57              *pow((rho_3/rho_ref_3),(C_3*rho_3)); /*H12-NEC*/
58        /*Mass fractions*/
59        Y_0 = C_YI(c,thread_l,0); /*H0-NEC*/
60        Y_1 = C_YI(c,thread_l,1); /*H4-NEC*/
61        Y_2 = C_YI(c,thread_l,2); /*H8-NEC*/
62        Y_3 = C_YI(c,thread_l,3); /*H12-NEC*/
63        /*Average molecular weight of mixture*/
64        M_avg = 1/(((Y_0/M_0)+(Y_1/M_1)+(Y_2/M_2)+(Y_3/M_3)));
65        /*Mole fractions*/
66        X_0 = (Y_0/M_0)*M_avg ; /*H0-NEC*/
67        X_1 = (Y_1/M_1)*M_avg ; /*H4-NEC*/
68        X_2 = (Y_2/M_2)*M_avg ; /*H8-NEC*/
69        X_3 = (Y_3/M_3)*M_avg ; /*H12-NEC*/
70            /*Mixture thermal conductivity [W/m.K] (Matsuda et al. 2023):*/
71        k_mix = (exp(X_0*log(k_0*M_0)+X_1*log(k_1*M_1)
72                    +X_2*log(k_2*M_2)+X_3*log(k_3*M_3)))/M_avg;
73        C_UDMI(c,t,9) = k_mix;
74        }
75       end_c_loop (c,t)
76       }
77 }
78
79 /************************************************************
80    UDF for initializing values for Hydrogen Thermal Conductivity
81 ************************************************************/
```

```
82  DEFINE_INIT(Initialize_NEC_Thermal_Conductivity, domain)
83   {
84      real T_cell,T_ref,A,B,C_0,C_1,C_2,C_3,M_0,M_1,M_2,M_3,M_avg,
85          rho_ref_0,rho_ref_1,rho_ref_2,rho_ref_3,rho_0,rho_1,rho_2,
86          rho_3,Y_0,Y_1,Y_2,Y_3,X_0,X_1,X_2,X_3,k_0,k_1,k_2,k_3,k_mix;
87      Thread *t,  *thread_l;
88      cell_t c;
89      Domain *mixture_domain;
90
91      T_ref = 303.15; /*Reference Temperature for Berger Bioucas model [K]*/
92      A = 0.1083;
93      B = 4.823;
94      C_0 = 2.2;        /*C for dehydrogenated molecule*/
95      C_1 = 2.133;      /*Interpolated C for partially hydrogenated molecule*/
96      C_2 = 2.066;      /*Interpolated C for partially hydrogenated molecule*/
97      C_3 = 2.0;        /*C for hydrogenated molecule*/
98
99      M_0 = 195.2597;   /*Molecular weight of H0-NEC [g/mol]*/
100     M_1 = 199.2915;   /*Molecular weight of H4-NEC [g/mol]*/
101     M_2 = 203.3232;   /*Molecular weight of H8-NEC [g/mol]*/
102     M_3 = 207.3550;   /*Molecular weight of H12-NEC [g/mol]*/
103         /*Densities of NEC species at reference temperature [g/cm^3 [(Stark, 2015)*/
104     rho_ref_0 = 1.313467-0.0007238*T_ref; /*H0-NEC*/
105     rho_ref_1 = 1.2553362-0.0006966*T_ref; /*H4-NEC*/
106     rho_ref_2 = 1.210127-0.0006907*T_ref; /*H8-NEC*/
107     rho_ref_3 = 1.1482329-0.0007092*T_ref; /* H12-NEC */
108
109     mixture_domain=Get_Domain(1);
110        /* loop over all threads in domain */
111        thread_loop_c (t,mixture_domain)
112      {
113        thread_l = THREAD_SUB_THREAD(t, 0);/* get liquid phase cell thread */
114
115        /* loop over all cells in cell thread */
116      begin_c_loop (c,t)
117       {
118        T_cell = C_T(c, thread_l); /*Liquid Temperature*/
119       /*Densities of NEC species at operating temperature [g/cm^3 [(Stark, 2015)*/
120        rho_0 = 1.313467-0.0007238*T_cell; /*H0-NEC*/
121        rho_1 = 1.2553362-0.0006966*T_cell; /*H4-NEC*/
122        rho_2 = 1.210127-0.0006907*T_cell; /*H8-NEC*/
123        rho_3 = 1.1482329-0.0007092*T_cell; /*H12-NEC*/
124            /*Thermal conductivity of NEC species [W/m.K] (Berger Bioucas, 2020)*/
125        k_0 =(A*(rho_ref_0)+B*(pow(rho_ref_0,2)/M_0))
126              *pow((rho_0/rho_ref_0),(C_0*rho_0)); /*H0-NEC*/
127        k_1 =(A*(rho_ref_1)+B*(pow(rho_ref_1,2)/M_1))
128              *pow((rho_1/rho_ref_1),(C_1*rho_1)); /*H4-NEC*/
129        k_2 =(A*(rho_ref_2)+B*(pow(rho_ref_2,2)/M_2))
130              *pow((rho_2/rho_ref_2),(C_2*rho_2)); /*H8-NEC*/
131        k_3 =(A*(rho_ref_3)+B*(pow(rho_ref_3,2)/M_3))
132              *pow((rho_3/rho_ref_3),(C_3*rho_3)); /*H12-NEC*/
133        /*Mass fractions*/
134        Y_0 = C_YI(c,thread_l,0); /*H0-NEC*/
135        Y_1 = C_YI(c,thread_l,1); /*H4-NEC*/
136        Y_2 = C_YI(c,thread_l,2); /*H8-NEC*/
137        Y_3 = C_YI(c,thread_l,3); /*H12-NEC*/
138        /*Average molecular weight of mixture*/
139        M_avg = 1/((Y_0/M_0)+(Y_1/M_1)+(Y_2/M_2)+(Y_3/M_3));
140        /*Mole fractions*/
141        X_0 = (Y_0/M_0)*M_avg ; /*H0-NEC*/
142        X_1 = (Y_1/M_1)*M_avg ; /*H4-NEC*/
143        X_2 = (Y_2/M_2)*M_avg ; /*H8-NEC*/
144        X_3 = (Y_3/M_3)*M_avg ; /*H12-NEC*/
145            /*Mixture thermal conductivity [W/m.K] (Matsuda et al. 2023):*/
146        k_mix = (exp(X_0*log(k_0*M_0)+X_1*log(k_1*M_1)
147                  +X_2*log(k_2*M_2)+X_3*log(k_3*M_3)))/M_avg;
148        C_UDMI(c,t,9) = k_mix;
149       }
150      end_c_loop (c,t)
151      }
152  }
```

A.9. Liquid mixture viscosity

```c
/************************************************************************
    UDF that specifies liquid viscosity mixing law (Grunberg-Nissan, 1949)
**************************************************************************/
#include "udf.h"

DEFINE_PROPERTY(Mixture_viscosity,c,t)
{
    real sum, M_sum, M_avg, mix_visc, MW, Y, X, viscosity;
    int i;              /* Species index */
    Material *sp;       /* Species Pointer */
    Property *prop;     /* Pointer to property array */
    sum = 0.0;
    M_sum = 0.0;

/* Loop through species to calculate average molecular weight of mixture [kg/kmol]*/
    mixture_species_loop(THREAD_MATERIAL(t),sp,i)
       {
        MW = MATERIAL_PROP(sp,PROP_mwi); /*Molecular weight of species i [kg/kmol]*/
        Y = C_YI(c,t,i); /*Mass fraction of species i*/
        M_sum += Y/MW; /*Sum for calculating average molecular weight of mixture*/
       }
    M_avg = 1/M_sum; /*Average molecular weight of mixture [kg/kmol]*/

    mixture_species_loop(THREAD_MATERIAL(t),sp,i)
       {
        MW = MATERIAL_PROP(sp,PROP_mwi); /*Molecular weight of species i [kg/kmol]*/
        Y = C_YI(c,t,i); /*Mass fraction of species i*/
        X = (Y/MW)*M_avg; /*Mole fraction of species i*/
        prop = (MATERIAL_PROPERTY(sp)); /* Returns a real pointer to the Property array */
        viscosity = generic_property(c,t,prop,PROP_mu,C_T(c,t)); /*Species viscosity[kg/m.s]
           */
        sum += X*log(viscosity);
       }
    mix_visc = exp(sum); /*Mixture viscosity [kg/m.s]*/
    return mix_visc;
}
```

A.10. Mixture surface tension

```c
/************************************************************************
   UDF for calculating NEC liquid mixture Surface Tension (Stark, 2015)
**************************************************************************/
# include "udf.h"

DEFINE_ADJUST(Surface_Tension, domain)
{
    real M_0,M_1,M_2,M_3,T,Y_0,Y_1,Y_2,Y_3,M_avg,X_0,X_1,X_2,X_3,
       sigma_0,sigma_1,sigma_2,sigma_3,sigma_mix;
    Thread *t, *thread_l;
    cell_t c;
    Domain *mixture_domain;

    M_0 = 195.2597;   /*Molecular weight of H0-NEC [g/mol]*/
    M_1 = 199.2915;   /*Molecular weight of H4-NEC [g/mol]*/
    M_2 = 203.3232;   /*Molecular weight of H8-NEC [g/mol]*/
    M_3 = 207.3550;   /*Molecular weight of H12-NEC [g/mol]*/

    mixture_domain=Get_Domain(1);
       /* loop over all threads in domain */
       thread_loop_c (t,mixture_domain)
       {
        thread_l = THREAD_SUB_THREAD(t, 0);/* get liquid phase cell thread */

         /* loop over all cells in cell thread */
       begin_c_loop (c,t)
       {
        T = C_T(c, thread_l); /*Liquid Temperature*/
```

```
29
30          Y_0 = C_YI(c,thread_l,0); /*Mass fraction of H0-NEC*/
31          Y_1 = C_YI(c,thread_l,1); /*Mass fraction of H4-NEC*/
32          Y_2 = C_YI(c,thread_l,2); /*Mass fraction of H8-NEC*/
33          Y_3 = C_YI(c,thread_l,3); /*Mass fraction of H12-NEC*/
34          /*Average molecular weight of mixture [g/mol]:*/
35          M_avg = 1/((Y_0/M_0)+(Y_1/M_1)+(Y_2/M_2)+(Y_3/M_3));
36
37          X_0 = (Y_0/M_0)*M_avg ; /*Mole fraction of H0-NEC*/
38          X_1 = (Y_1/M_1)*M_avg ; /*Mole fraction of H4-NEC*/
39          X_2 = (Y_2/M_2)*M_avg ; /*Mole fraction of H8-NEC*/
40          X_3 = (Y_3/M_3)*M_avg ; /*Mole fraction of H12-NEC*/
41
42          sigma_0 = 0.0711760 - 9.96E-05*T; /*Surface Tension of H0-NEC [N/m]*/
43          (No correlation available, equal to that of H4-NEC)*/
44          sigma_1 = 0.0711760 - 9.96E-05*T; /*Surface Tension of H4-NEC [N/m] */
45          sigma_2 = 0.063109 - 8.50E-05*T; /*Surface Tension of H8-NEC [N/m] */
46          sigma_3 = 0.0593586 - 8.81E-05*T; /*Surface Tension of H12-NEC [N/m] */
47          /*Mole fraction weighted mixture surface tension [N/m]:*/
48          sigma_mix = X_0*sigma_0+X_1*sigma_1+X_2*sigma_2+X_3*sigma_3;
49          C_UDMI(c,t,5) = sigma_mix;
50         }
51       end_c_loop (c,t)
52       }
53 }
54
55 /****************************************************************
56    UDF for initializing values of NEC Surface Tension
57 ****************************************************************/
58
59 DEFINE_INIT(Initialize_Surface_Tension, domain)
60 {
61      real M_0,M_1,M_2,M_3,T,Y_0,Y_1,Y_2,Y_3,M_avg,X_0,X_1,X_2,X_3,
62         sigma_0,sigma_1,sigma_2,sigma_3,sigma_mix;
63     Thread *t, *thread_l;
64     cell_t c;
65     Domain *mixture_domain;
66
67     M_0 = 195.2597;   /*Molecular weight of H0-NEC [g/mol]*/
68     M_1 = 199.2915;   /*Molecular weight of H4-NEC [g/mol]*/
69     M_2 = 203.3232;   /*Molecular weight of H8-NEC [g/mol]*/
70     M_3 = 207.3550;   /*Molecular weight of H12-NEC [g/mol]*/
71
72     mixture_domain=Get_Domain(1);
73        /* loop over all threads in domain */
74        thread_loop_c (t,mixture_domain)
75       {
76        thread_l = THREAD_SUB_THREAD(t, 0);/* get liquid phase cell thread */
77
78        /* loop over all cells in cell thread */
79       begin_c_loop (c,t)
80        {
81        T = C_T(c, thread_l); /*Liquid Temperature*/
82
83        Y_0 = C_YI(c,thread_l,0); /*Mass fraction of H0-NEC*/
84        Y_1 = C_YI(c,thread_l,1); /*Mass fraction of H4-NEC*/
85        Y_2 = C_YI(c,thread_l,2); /*Mass fraction of H8-NEC*/
86        Y_3 = C_YI(c,thread_l,3); /*Mass fraction of H12-NEC*/
87        /*Average molecular weight of mixture [g/mol]:*/
88        M_avg = 1/((Y_0/M_0)+(Y_1/M_1)+(Y_2/M_2)+(Y_3/M_3));
89
90        X_0 = (Y_0/M_0)*M_avg ; /*Mole fraction of H0-NEC*/
91        X_1 = (Y_1/M_1)*M_avg ; /*Mole fraction of H4-NEC*/
92        X_2 = (Y_2/M_2)*M_avg ; /*Mole fraction of H8-NEC*/
93        X_3 = (Y_3/M_3)*M_avg ; /*Mole fraction of H12-NEC*/
94
95        sigma_0 = 0.0711760 - 9.96E-05*T; /*Surface Tension of H0-NEC [N/m]
96        (No correlation available, equal to that of H4-NEC)*/
97        sigma_1 = 0.0711760 - 9.96E-05*T; /*Surface Tension of H4-NEC [N/m]*/
98        sigma_2 = 0.063109 - 8.50E-05*T; /*Surface Tension of H8-NEC [N/m] */
99        sigma_3 = 0.0593586 - 8.81E-05*T; /*Surface Tension of H12-NEC [N/m]*/
```

```
100          /*Mole fraction weighted mixture surface tension [N/m]:*/
101          sigma_mix = X_0*sigma_0+X_1*sigma_1+X_2*sigma_2+X_3*sigma_3;
102          C_UDMI(c,t,5) = sigma_mix;
103        }
104      end_c_loop (c,t)
105      }
106  }
```

A.11. Chemical Kinetics

```
1  /************************************************************************
2    UDF for computing NEC dehydrogenation reaction rates.
3   ************************************************************************/
4  #include "udf.h"
5
6  /* H12-NEC to H8-NEC */
7  DEFINE_HET_RXN_RATE(H12NEC_H8NEC, c, t, hr, mw, yi, rr, rr_t) {
8      Thread *thread_l;
9      real T_cell, M_0, M_1, M_2, M_3, Y_0, Y_1, Y_2, Y_3, rho_l, vof_l;
10     real A, Ea, R, k, Rate;
11
12     if (THREAD_ID(t) == 12) { /* Packed Bed zone ID */
13         thread_l = THREAD_SUB_THREAD(t, 0); /* Liquid phase cell thread */
14
15         Y_0 = C_YI(c, thread_l, 0); /* Mass fraction of H0-NEC */
16         Y_1 = C_YI(c, thread_l, 1); /* Mass fraction of H4-NEC */
17         Y_2 = C_YI(c, thread_l, 2); /* Mass fraction of H8-NEC */
18         Y_3 = C_YI(c, thread_l, 3); /* Mass fraction of H12-NEC */
19         M_0 = 195.2597; /* Molecular weight of H0-NEC [kg/kmol] */
20         M_1 = 199.2915; /* Molecular weight of H4-NEC [kg/kmol] */
21         M_2 = 203.3232; /* Molecular weight of H8-NEC [kg/kmol] */
22         M_3 = 207.3550; /* Molecular weight of H12-NEC [kg/kmol] */
23
24         T_cell = C_T(c, thread_l); /* Liquid temperature [K] */
25         rho_l = C_R(c, thread_l); /* Liquid density [kg/m3] */
26         vof_l = C_VOF(c, thread_l); /* Liquid volume fraction [K] */
27
28         A = 826; /* Pre-Exponential factor [s^-1] */
29         Ea = 56300; /* Activation Energy [J/mol] */
30         R = 8.31446261815324; /* Universal gas constant [J/mol.K] */
31         k = A * exp((-Ea) / (R * T_cell)); /* Rate constant [s^-1] */
32
33         Rate = k * ((Y_3 * rho_l * vof_l) / (M_3)); /* Reaction rate [kmol/m3.s] */
34         *rr = Rate;
35     } else {
36         /* No reaction outside of packed bed zone */
37         Rate = 0;
38         *rr = Rate;
39     }
40     C_UDMI(c, t, 14) = Rate;
41 }
42
43 /* H8-NEC to H4-NEC */
44 DEFINE_HET_RXN_RATE(H8NEC_H4NEC, c, t, hr, mw, yi, rr, rr_t) {
45     Thread *thread_l;
46     real T_cell, M_0, M_1, M_2, M_3, Y_0, Y_1, Y_2, Y_3, rho_l, vof_l;
47     real A, Ea, R, k, Rate;
48
49     if (THREAD_ID(t) == 12) { /* Packed Bed zone ID */
50         thread_l = THREAD_SUB_THREAD(t, 0); /* Liquid phase cell thread */
51
52         Y_0 = C_YI(c, thread_l, 0); /* Mass fraction of H0-NEC */
53         Y_1 = C_YI(c, thread_l, 1); /* Mass fraction of H4-NEC */
54         Y_2 = C_YI(c, thread_l, 2); /* Mass fraction of H8-NEC */
55         Y_3 = C_YI(c, thread_l, 3); /* Mass fraction of H12-NEC */
56         M_0 = 195.2597; /* Molecular weight of H0-NEC [kg/kmol] */
57         M_1 = 199.2915; /* Molecular weight of H4-NEC [kg/kmol] */
58         M_2 = 203.3232; /* Molecular weight of H8-NEC [kg/kmol] */
59         M_3 = 207.3550; /* Molecular weight of H12-NEC [kg/kmol] */
```

```
60
61          T_cell = C_T(c, thread_l); /* Liquid temperature [K] */
62          rho_l = C_R(c, thread_l); /* Liquid density [kg/m3] */
63          vof_l = C_VOF(c, thread_l); /* Liquid volume fraction [K] */
64
65          A = 1406; /* Pre-Exponential factor [s^-1] */
66          Ea = 59200; /* Activation Energy [J/mol] */
67          R = 8.31446261815324; /* Universal gas constant [J/mol.K] */
68          k = A * exp((-Ea) / (R * T_cell)); /* Rate constant [s^-1] */
69
70          Rate = k * ((Y_2 * rho_l * vof_l) / (M_2)); /* Reaction rate [kmol/m3.s] */
71          *rr = Rate;
72      } else {
73          /* No reaction outside of packed bed zone */
74          Rate = 0;
75          *rr = Rate;
76      }
77      C_UDMI(c, t, 15) = Rate;
78 }
79
80 /* H4-NEC to H0-NEC */
81 DEFINE_HET_RXN_RATE(H4NEC_H0NEC, c, t, hr, mw, yi, rr, rr_t) {
82      Thread *thread_l;
83      real T_cell, M_0, M_1, M_2, M_3, Y_0, Y_1, Y_2, Y_3, rho_l, vof_l;
84      real A, Ea, R, k, Rate;
85
86      if (THREAD_ID(t) == 12) { /* Packed Bed zone ID */
87          thread_l = THREAD_SUB_THREAD(t, 0); /* Liquid phase cell thread */
88
89          Y_0 = C_YI(c, thread_l, 0); /* Mass fraction of H0-NEC */
90          Y_1 = C_YI(c, thread_l, 1); /* Mass fraction of H4-NEC */
91          Y_2 = C_YI(c, thread_l, 2); /* Mass fraction of H8-NEC */
92          Y_3 = C_YI(c, thread_l, 3); /* Mass fraction of H12-NEC */
93          M_0 = 195.2597; /* Molecular weight of H0-NEC [kg/kmol] */
94          M_1 = 199.2915; /* Molecular weight of H4-NEC [kg/kmol] */
95          M_2 = 203.3232; /* Molecular weight of H8-NEC [kg/kmol] */
96          M_3 = 207.3550; /* Molecular weight of H12-NEC [kg/kmol] */
97
98          T_cell = C_T(c, thread_l); /* Liquid temperature [K] */
99          rho_l = C_R(c, thread_l); /* Liquid density [kg/m3] */
100         vof_l = C_VOF(c, thread_l); /* Liquid volume fraction [K] */
101
102         A = 6007; /* Pre-Exponential factor [s^-1] */
103         Ea = 73100; /* Activation Energy [J/mol] */
104         R = 8.31446261815324; /* Universal gas constant [J/mol.K] */
105         k = A * exp((-Ea) / (R * T_cell)); /* Rate constant [s^-1] */
106
107         Rate = k * ((Y_1 * rho_l * vof_l) / (M_1)); /* Reaction rate [kmol/m3.s] */
108         *rr = Rate;
109     } else {
110         /* No reaction outside of packed bed zone */
111         Rate = 0;
112         *rr = Rate;
113     }
114     C_UDMI(c, t, 16) = Rate;
115 }
```

A.12. Effective radial thermal conductivity

```
1  /**********************************************************************
2     UDF to set value of cell effective radial thermal conductivity
3  **********************************************************************/
4  #include "udf.h"
5
6  DEFINE_PROPERTY(cell_thermal_conductivity,cell,subthread)
7  {
8      Thread *thread_g, *thread_l, *thread_s;
9      real Sphericity, tc_s, tc_l, tc_g, cp_l, cp_g, d_p, D, vof_g, vof_l,
10          vof_s, porosity, T, rho_l, rho_g, x_vel_l, y_vel_l, abs_v_l,
```

```
11          x_vel_g, y_vel_g, abs_v_g, C_f, phi, sigma, emissivity, k_rad,
12          kappa, B, N, theta, tc_so, Pe_l, Pe_g, f, K, beta_l, term_1,
13          term_2, term_3, tc_eff;
14     Thread *mix_thread = THREAD_SUPER_THREAD(subthread);
15     thread_l = THREAD_SUB_THREAD(mix_thread, 0);/* get liquid phase cell thread */
16     thread_g = THREAD_SUB_THREAD(mix_thread, 1);/* get gas phase cell thread */
17     thread_s = THREAD_SUB_THREAD(mix_thread, 2);/* get solid phase cell thread*/
18
19     Sphericity = RP_Get_Input_Parameter("real-3"); /* Particle sphericity */
20     tc_s = RP_Get_Input_Parameter("real-8") ; /*Thermal conductivity of solid [W/m.K]
21     (Mischke and Smith 1962, Alumina, 38% void fraction) */
22     tc_l = C_UDMI(cell,mix_thread,9); /*Thermal conductivity of liquid mixture [W/m.K] */
23     tc_g = C_UDMI(cell,mix_thread,10); /*Thermal conductivity of gas (Hydrogen) [W/m.K] */
24     cp_l = C_CP(cell, thread_l); /*Specific heat of liquid [J/kg.K] */
25     cp_g = C_CP(cell, thread_g); /*Specific heat of gas [J/kg.K] */
26     d_p = RP_Get_Input_Parameter("real-9"); /* Particle diameter */
27     D = RP_Get_Input_Parameter("real-10"); /* Reactor diameter */
28     vof_s = C_VOF(cell, thread_s);/* solid volume fraction*/
29     vof_l = C_VOF(cell, thread_l);/* liquid volume fraction*/
30     vof_g = C_VOF(cell, thread_g);/* gas volume fraction*/
31     porosity = 1.0-vof_s;
32     T = C_T(cell, thread_g); /*Mixture Temperature*/
33     rho_l = C_R(cell, thread_l); /*liquid density*/
34     rho_g = C_R(cell, thread_g); /*gas density*/
35     x_vel_l = C_U(cell, thread_l);
36     y_vel_l = C_V(cell, thread_l);
37     abs_v_l = sqrt(x_vel_l*x_vel_l + y_vel_l*y_vel_l); /*Interstitial liquid velocity*/
38     x_vel_g = C_U(cell, thread_g);
39     y_vel_g = C_V(cell, thread_g);
40     abs_v_g = sqrt(x_vel_g*x_vel_g + y_vel_g*y_vel_g); /*Interstitial gas velocity*/
41
42     /*Conduction contribution tc_so, Bauer and Schlunder (1978)*/
43       /*Shape factor for stagnant bed thermal conductivity */
44      if (Sphericity<1.0)
45         {
46         C_f = 2.5; /*Shape factor for cylindrical particles*/
47         }
48     else
49         {
50         C_f = 1.25; /*Shape factor for spherical particles*/
51         }
52     phi = 0.0077;/*Flattening coefficient*/
53     sigma=5.670374419*pow(10.0,-8.0); /*Stefan-Boltzmann constant */
54     emissivity = 0.85; /*Emissivity of toluene, G. A. Capelle 2019*/
55
56     k_rad = ((4.0*sigma)/((2/emissivity)-1))*pow(T,3.0)*(d_p/tc_g) ;
57     kappa = tc_s/tc_l;
58     B = C_f*pow(((1-porosity)/porosity),(10.0/9.0));
59     N = 1.0+((k_rad-B)/kappa);
60     theta = (2.0/N)*(((B*(kappa+k_rad-1.0))/(pow(N,2.0)*kappa))*log((kappa+k_rad)/B)
61                 +(((B+1)/(2*B))*(k_rad-B))-((B-1)/N));
62     tc_so = (1-sqrt(1-porosity))*(1+k_rad*porosity)*tc_g+sqrt(1-porosity)
63                 *(phi*kappa+(1-phi)*theta)*tc_l;
64
65      /*Effective thermal conductivity tc_eff, Gutsche (1989)*/
66        /*Shape factor for effective thermal conductivity */
67      if (Sphericity<1.0)
68         {
69         f = 1.75; /*Shape factor for cylindrical particles*/
70         }
71     else
72         {
73         f = 1.15; /*Shape factor for spherical particles*/
74         }
75     Pe_l = rho_l*vof_l*abs_v_l*d_p*cp_l/tc_l; /*Liquid Peclet number*/
76     Pe_g = rho_g*vof_g*abs_v_g*d_p*cp_g/tc_g; /*Gas Peclet number*/
77     K = 8.0*(2.0-pow((1-2*(d_p/D)),2.0));
78     beta_l = vof_l/porosity; /*Liquid saturation*/
79     term_1 = tc_so/tc_l;
80     if (beta_l > 0.97) /* For pure liquid (Shlünder, 1966) */
81     {
```

```
82      term_2 = (Pe_l*f)/(K);
83      term_3 = 0.0;
84    }
85    else if (beta_l < 0.03) /* For pure gas (Shlünder, 1966) */
86    {
87      term_2 = 0.0;
88      term_3 = (Pe_g*f)/(K);
89    }
90    else /* For both liquid and gas  Gutsche (1989) */
91    {
92      term_2 = (Pe_l*f)/(beta_l*K);
93      term_3 = (Pe_g*f*tc_g)/((1-beta_l)*K*tc_l);
94    }
95    tc_eff = tc_l*(term_1+term_2+term_3);/*Effective thermal conductivity */
96    C_UDMI(cell,mix_thread,11) = tc_eff;
97    return tc_eff;
98  }
```

A.13. Wall heat transfer coefficient

```
1  /************************************************************************
2  UDF for specifying wall heat transfer coefficient
3  ************************************************************************/
4  #include "udf.h"
5
6  DEFINE_PROFILE(MP_wall_heat_transfer_coefficient,Wall_Thread,k)
7  {
8     Domain *mixture_domain;
9     mixture_domain=Get_Domain(1);
10    real d_p, Cell_axial_length;
11    Cell_axial_length = RP_Get_Input_Parameter("real-12"); /* Cell size axial length */
12    d_p = RP_Get_Input_Parameter("real-9"); /* Particle diameter */
13    Thread *t,*thread_s, *thread_l;
14    int i;
15    cell_t cell, c0;
16    Thread *t0, *t_cell;
17    face_t f, f_wall;
18
19     /*  Cell calculation variables  */
20    real L_mass_flow_cell_abs, VOF_l_cell, VOF_s_cell, x_vel_l_cell,
21    y_vel_l_cell, abs_u_l_cell,rho_l_cell, mu_l_cell, cp_l_cell, tc_l_cell, htc_cell;
22
23    /*  Intermediate calculation variables  */
24    real htc_int, L_mass_flow_abs, Area_Weight;
25
26    /* Parameters */
27    real Porosity, d_ec, liquid_saturation, Re_l, Pr_l, htc;
28
29    /* Coordinate parameters */
30    real xa[ND_ND];  /* Coordinates of wall faces*/
31    real xb[ND_ND];  /* Coordinates of domain faces*/
32    real x_a, x_b, y_b, A_x;
33    real A[ND_ND]; /*face area normal vector */
34
35    begin_f_loop(f_wall,Wall_Thread)  /* Loop over faces on wall*/
36      {
37        /* Variable initialization */
38        L_mass_flow_abs=0.0;
39        htc_int=0.0;
40
41        F_CENTROID(xa,f_wall,Wall_Thread);
42        x_a = xa[0]; /* wall face centroid axial coordinate */
43        i=0;
44
45     /* loops over all face threads in a domain*/
46        thread_loop_f (t,mixture_domain)
47        {
48        /* loop over all cells in cell thread */
49        begin_f_loop (f,t)
```

```
50          {
51          F_CENTROID(xb,f,t);
52          x_b = xb[0]; /* face centroid axial coordinate */
53          y_b = xb[1]; /* face centroid radial coordinate*/
54           if  (x_b>(x_a+0.25*Cell_axial_length) && x_b<(x_a+0.75*Cell_axial_length))
55          {
56          F_AREA(A,f,t);
57          A_x = fabs(A[0]); /*Projected radial length of face*/
58          Area_Weight = A_x*2*M_PI; /*Equal to pi*(r_upper^2 - r_lower^2)*/
59          cell = F_C0(f,t);   /*Adjacent Cell Index*/
60          t_cell = THREAD_T0(t); /*Adjacent Cell Thread*/
61          thread_l = THREAD_SUB_THREAD(t_cell, 0);/* liquid phase cell thread */
62          thread_s = THREAD_SUB_THREAD(t_cell, 2);/* solid phase cell thread */
63
64           /* Cell Properties */
65          rho_l_cell = C_R(cell, thread_l);
66          mu_l_cell = C_MU_L(cell, thread_l);
67          cp_l_cell = C_CP(cell, thread_l);
68          VOF_l_cell =  C_VOF(cell, thread_l);
69          VOF_s_cell =  C_VOF(cell, thread_s);
70          x_vel_l_cell = C_U(cell, thread_l);
71          y_vel_l_cell = C_V(cell, thread_l);
72          /*Interstitial liquid velocity*/
73          abs_u_l_cell = sqrt(x_vel_l_cell*x_vel_l_cell + y_vel_l_cell*y_vel_l_cell);
74          tc_l_cell = C_UDMI(cell,t_cell,9); /* Liquid thermal conductivity */
75
76          /* Cell Heat Transfer Coefficient Calculation */
77          Porosity = 1.0-VOF_s_cell;
78          d_ec = ((2.0*Porosity)/(3.0*(1.0-Porosity)))*d_p;
79          liquid_saturation = VOF_l_cell/Porosity;
80          Re_l = (VOF_l_cell*rho_l_cell*abs_u_l_cell*d_ec)/(Porosity*mu_l_cell*
                    liquid_saturation);
81          Pr_l = (cp_l_cell*mu_l_cell)/tc_l_cell;
82          htc_cell = ((0.26*pow(Re_l, 0.43)*pow(Pr_l, (1.0/3.0)))*tc_l_cell)/d_ec;
83
84          /* Cell flow rates */
85          L_mass_flow_cell_abs=rho_l_cell*VOF_l_cell*fabs(x_vel_l_cell*Area_Weight);
86
87          /* Total flow rates */
88          L_mass_flow_abs = L_mass_flow_abs + L_mass_flow_cell_abs;
89
90          /* Mass-Weighted Average Properties */
91          htc_int = htc_int + htc_cell*L_mass_flow_cell_abs;
92
93          i=i+1;
94          }
95          }
96      end_f_loop (f,t)
97      }
98          /* Plane Mass-Weighted Average Properties */
99      htc = htc_int/L_mass_flow_abs;
100     F_UDMI(f_wall,Wall_Thread,12) = htc;
101         /* Get the cell id of the cell adjacent to the face*/
102     c0 = F_C0(f_wall,Wall_Thread);
103         /* Get the Thread id of the cells adjacent to the face*/
104     t0 = F_C0_THREAD(f_wall,Wall_Thread);
105         /*Store the F_UDMI into cell UDMI for graphical visualization*/
106     C_UDMI(c0,t0,12)=F_UDMI(f_wall,Wall_Thread,12);
107     F_PROFILE(f_wall,Wall_Thread,k) = htc;
108     }
109   end_f_loop(f_wall,Wall_Thread)
110 }
```

A.14. Backflow temperature and species mass fractions boundary conditions

```c
/*******************************************************************
 UDFs for defining outlet backflow boundary conditions
 ******************************************************************/
#include "udf.h"

/* Temperature */
DEFINE_PROFILE(outlet_temperature,t,i)
{
real T;
cell_t c0;
face_t f;
Thread *t0, *thread_l;
int outlet_ID = 18; /* Outlet ID */
Domain *d = Get_Domain(2); /* Liquid domain */
Thread *t_outlet = Lookup_Thread(d,outlet_ID); /* Liquid outlet thread */
begin_f_loop(f,t)
 {
  c0 = F_C0(f,t); /* Get the cell id of the cell adjacent to the face*/
  t0 = F_C0_THREAD(f,t); /* Get the Thread id of the cell adjacent to the face*/

  T = C_T(c0,t0); /* Temperature of cell */
  C_UDMI(c0,t0,17)=T;
  F_PROFILE(f,t,i) = T;
 }
end_f_loop(f,t)
}

/* H8-NEC mass fraction */
DEFINE_PROFILE(outlet_H8_NEC,t,i)
{
real Y; /* Mass fraction */
cell_t c0;
face_t f;
Thread *t0, *thread_l;
int outlet_ID = 18; /* Outlet ID */
Domain *d = Get_Domain(2); /* Liquid domain */
Thread *t_outlet = Lookup_Thread(d,outlet_ID); /* Liquid outlet thread */
begin_f_loop(f,t)
 {
  c0 = F_C0(f,t); /* Get the cell id of the cell adjacent to the face*/
  t0 = F_C0_THREAD(f,t); /* Get the Thread id of the cell adjacent to the face*/

  Y = C_YI(c0,t0,2); /* Mass fraction H8_NEC at face */
  C_UDMI(c0,t0,18) = Y;
  F_PROFILE(f,t,i) = Y;
 }
end_f_loop(f,t)
}

/* H4-NEC mass fraction */
DEFINE_PROFILE(outlet_H4_NEC,t,i)
{
real Y; /* Mass fraction */
cell_t c0;
face_t f;
Thread *t0, *thread_l;
int outlet_ID = 18; /* Outlet ID */
Domain *d = Get_Domain(2); /* Liquid domain */
Thread *t_outlet = Lookup_Thread(d,outlet_ID); /* Liquid outlet thread */
begin_f_loop(f,t)
 {
  c0 = F_C0(f,t); /* Get the cell id of the cell adjacent to the face*/
  t0 = F_C0_THREAD(f,t); /* Get the Thread id of the cell adjacent to the face*/

  Y = C_YI(c0,t0,1); /* Mass fraction H4_NEC at face */
  C_UDMI(c0,t0,19) = Y;
  F_PROFILE(f,t,i) = Y;
```

```
68
69  }
70  end_f_loop(f,t)
71  }
72
73  /* H0-NEC mass fraction */
74  DEFINE_PROFILE(outlet_H0_NEC,t,i)
75  {
76  real Y; /* Mass fraction */
77  cell_t c0;
78  face_t f;
79  Thread *t0, *thread_l;
80  int outlet_ID = 18; /* Outlet ID */
81  Domain *d = Get_Domain(2); /* Liquid domain */
82  Thread *t_outlet = Lookup_Thread(d,outlet_ID); /* Liquid outlet thread */
83  begin_f_loop(f,t)
84    {
85     c0 = F_C0(f,t); /* Get the cell id of the cell adjacent to the face*/
86     t0 = F_C0_THREAD(f,t); /* Get the Thread id of the cell adjacent to the face*/
87
88     Y = C_YI(c0,t0,0); /* Mass fraction H4_NEC at face */
89     C_UDMI(c0,t0,20) = Y;
90     F_PROFILE(f,t,i) = Y;
91    }
92  end_f_loop(f,t)
93  }
```

A.15. Hydrodynamic dispersion coefficient

```
1   /***********************************************************************
2     UDF to compute hydrodynamic dispersion coefficient
3   ***********************************************************************/
4   #include "udf.h"
5
6   DEFINE_DIFFUSIVITY(Dispersion_Coefficient,c,t,i)
7   {
8       real T_cell,M_0,M_1,M_2,M_3,Y_0,Y_1,Y_2,Y_3,rho_0,rho_1,rho_2,rho_3,
9           visc_0_cP,visc_1_cP,visc_2_cP,visc_3_cP,visc_0,visc_1,visc_2,visc_3,
10          bp_0,bp_1,bp_2,bp_3,rho_bp_0,rho_bp_1,rho_bp_2,rho_bp_3,V_0,V_1,
11          V_2,V_3,phi_0,phi_1,phi_2,phi_3, D_dilute_01,D_dilute_02,D_dilute_03,
12          D_dilute_10,D_dilute_12,D_dilute_13,D_dilute_20,D_dilute_21,D_dilute_23,
13          D_dilute_30,D_dilute_31,D_dilute_32,D_01,D_02,D_03,D_12,D_13,D_23,D_0_m,
14          D_1_m,D_2_m,D_3_m,d_p,x_vel_l,y_vel_l,abs_v_l,Pe_m_0,Pe_m_1,Pe_m_2,Pe_m_3,
15          Sc_0,Sc_1,Sc_2,Sc_3,Pe_t_0,Pe_t_1,Pe_t_2,Pe_t_3,D_r_0,D_r_1,D_r_2,D_r_3,D_r_avg;
16
17      d_p = RP_Get_Input_Parameter("real-9"); /* Particle diameter [m] */
18      Thread *thread_l;
19      Thread *mix_thread = THREAD_SUPER_THREAD(t);
20      thread_l = THREAD_SUB_THREAD(mix_thread, 0);/* get liquid phase cell thread */
21
22      T_cell = C_T(c,thread_l); /*Cell temperature [K]*/
23
24      /* Molecular weights of NEC species [g/mol] */
25      M_0 = 195.2597; /* H0-NEC */
26      M_1 = 199.2915; /* H4-NEC */
27      M_2 = 203.3232; /* H8-NEC */
28      M_3 = 207.3550; /* H12-NEC */
29
30      /* Mass fractions of NEC species [-] */
31      Y_0 = C_YI(c,thread_l,0); /* H0-NEC */
32      Y_1 = C_YI(c,thread_l,1); /* H4-NEC */
33      Y_2 = C_YI(c,thread_l,2); /* H8-NEC */
34      Y_3 = C_YI(c,thread_l,3); /* H12-NEC */
35
36      /* Viscosity of NEC species [cP] (Stark, 2015)*/
37      visc_0_cP = exp(-198.5107397+(14092.471/T_cell)+27.4111475*log(T_cell)
38                  +0.000000000000694*pow(T_cell,2.0)); /* H0-NEC */
39      visc_1_cP = exp(-8.474341421+(5607.607/T_cell)-1.46520555*log(T_cell)
40                  +0.0000242*pow(T_cell,2.0)); /* H4-NEC */
```

```
41      visc_2_cP = exp(-51.67196212+(5951.08459/T_cell)+6.23125641*log(T_cell)
42                      -0.000000061*pow(T_cell,2.0)); /* H8-NEC */
43      visc_3_cP = exp(-121.3831627+(8035.86187/T_cell)+16.8924989*log(T_cell)
44                      -0.00000000365*pow(T_cell,2.0)); /* H12-NEC */
45
46      bp_0 = 621.45; /*Boiling point of H0-NEC [K]*/
47      bp_1 = 624.05; /*Boiling point of H4-NEC [K]*/
48      bp_2 = 588.525; /*Boiling point of H8-NEC [K]*/
49      bp_3 = 553.0; /*Boiling point of H12-NEC [K]*/
50
51      /* Boiling point density of NEC species [g/cm^3] (Stark, 2015)*/
52      rho_bp_0 = 1.313467-0.0007238*bp_0; /* H0-NEC */
53      rho_bp_1 = 1.2553362-0.0006966*bp_1; /* H4-NEC */
54      rho_bp_2 = 1.210127-0.0006907*bp_2; /* H8-NEC */
55      rho_bp_3 = 1.1482329-0.0007092*bp_3; /* H12-NEC */
56
57      /* Molar volume at boiling point of NEC species [cm^3/mol] */
58      V_0 = M_0/rho_bp_0; /* H0-NEC */
59      V_1 = M_1/rho_bp_1; /* H4-NEC */
60      V_2 = M_2/rho_bp_2; /* H8-NEC */
61      V_3 = M_3/rho_bp_3; /* H12-NEC */
62
63      /* Association factors for NEC species [-] */
64      phi_0 = 1; /* H0-NEC */
65      phi_1 = 1; /* H4-NEC */
66      phi_2 = 1; /* H8-NEC */
67      phi_3 = 1; /* H12-NEC */
68
69      /* Infinite dilution binary diffusion coefficients [m^2/s] */
70      /* H0-NEC = Species 0; H4-NEC = Species 1; H8-NEC = Species 2; H12-NEC = Species 3 */
71      D_dilute_01 = ((0.000000074*pow((phi_0*M_1),0.5)*T_cell)
72                      /(visc_1_cP*pow(V_0,0.6)))/10000; /* 0 in 1 */
73      D_dilute_02 = ((0.000000074*pow((phi_0*M_2),0.5)*T_cell)
74                      /(visc_2_cP*pow(V_0,0.6)))/10000; /* 0 in 2 */
75      D_dilute_03 = ((0.000000074*pow((phi_0*M_3),0.5)*T_cell)
76                      /(visc_3_cP*pow(V_0,0.6)))/10000; /* 0 in 3 */
77      D_dilute_10 = ((0.000000074*pow((phi_1*M_0),0.5)*T_cell)
78                      /(visc_0_cP*pow(V_1,0.6)))/10000; /* 1 in 0 */
79      D_dilute_12 = ((0.000000074*pow((phi_1*M_2),0.5)*T_cell)
80                      /(visc_2_cP*pow(V_1,0.6)))/10000; /* 1 in 2 */
81      D_dilute_13 = ((0.000000074*pow((phi_1*M_3),0.5)*T_cell)
82                      /(visc_3_cP*pow(V_1,0.6)))/10000; /* 1 in 3 */
83      D_dilute_20 = ((0.000000074*pow((phi_2*M_0),0.5)*T_cell)
84                      /(visc_0_cP*pow(V_2,0.6)))/10000; /* 2 in 0 */
85      D_dilute_21 = ((0.000000074*pow((phi_2*M_1),0.5)*T_cell)
86                      /(visc_1_cP*pow(V_2,0.6)))/10000; /* 2 in 1 */
87      D_dilute_23 = ((0.000000074*pow((phi_2*M_3),0.5)*T_cell)
88                      /(visc_3_cP*pow(V_2,0.6)))/10000; /* 2 in 3 */
89      D_dilute_30 = ((0.000000074*pow((phi_3*M_0),0.5)*T_cell)
90                      /(visc_0_cP*pow(V_3,0.6)))/10000; /* 3 in 0 */
91      D_dilute_31 = ((0.000000074*pow((phi_3*M_1),0.5)*T_cell)
92                      /(visc_1_cP*pow(V_3,0.6)))/10000; /* 3 in 1 */
93      D_dilute_32 = ((0.000000074*pow((phi_3*M_2),0.5)*T_cell)
94                      /(visc_2_cP*pow(V_3,0.6)))/10000; /* 3 in 2 */
95
96      if(Y_0+Y_1 <= 0)
97      {
98          D_01 = D_dilute_01;
99      }
100     else
101     {
102         /* Binary  diffusion coefficient of 0 in 1 [m^2/s] */
103         D_01 = D_dilute_01 + (Y_0/(Y_0+Y_1))*(D_dilute_10-D_dilute_01);
104     }
105     if(Y_0+Y_2 <= 0)
106     {
107         D_02 = D_dilute_02;
108     }
109     else
110     {
111         /* Binary  diffusion coefficient of 0 in 2 [m^2/s] */
```

```
112        D_02 = D_dilute_02 + (Y_0/(Y_0+Y_2))*(D_dilute_20-D_dilute_02);
113    }
114    if(Y_0+Y_3 <= 0)
115    {
116        D_03 = D_dilute_03;
117    }
118    else
119    {
120        /* Binary  diffusion coefficient of 0 in 3 [m^2/s] */
121        D_03 = D_dilute_03 + (Y_0/(Y_0+Y_3))*(D_dilute_30-D_dilute_03);
122    }
123    if(Y_1+Y_2 <= 0)
124    {
125        D_12 = D_dilute_12;
126    }
127    else
128    {
129        /* Binary  diffusion coefficient of 1 in 2 [m^2/s] */
130        D_12 = D_dilute_12 + (Y_1/(Y_1+Y_2))*(D_dilute_21-D_dilute_12);
131    }
132    if(Y_1+Y_3 <= 0)
133    {
134        D_13 = D_dilute_13;
135    }
136    else
137    {
138        /* Binary  diffusion coefficient of 1 in 3 [m^2/s] */
139        D_13 = D_dilute_13 + (Y_1/(Y_1+Y_3))*(D_dilute_31-D_dilute_13);
140    }
141    if(Y_2+Y_3 <= 0)
142    {
143        D_23 = D_dilute_23;
144    }
145    else
146    {
147        /* Binary  diffusion coefficient of 2 in 3 [m^2/s] */
148        D_23 = D_dilute_23 + (Y_2/(Y_2+Y_3))*(D_dilute_32-D_dilute_23);
149    }
150
151    if(Y_0 < 1.0)
152    {
153     /* Mixture diffusion coefficient of 0 [m^2/s] */
154     D_0_m = (1.0-Y_0)/((Y_1/D_01)+(Y_2/D_02)+(Y_3/D_03));
155    }
156    else
157    {
158     D_0_m = 10E-10; /* Case where Y_0 = 1 [m^2/s] */
159    }
160    if(Y_1 < 1.0)
161    {
162     /* Mixture diffusion coefficient of 1 [m^2/s] */
163     D_1_m = (1.0-Y_1)/((Y_0/D_01)+(Y_2/D_12)+(Y_3/D_13));
164    }
165    else
166    {
167     D_1_m = 10E-10; /* Case where Y_1 = 1 [m^2/s] */
168    }
169     if(Y_2 < 1.0)
170    {
171     /* Mixture diffusion coefficient of 2 [m^2/s] */
172     D_2_m = (1.0-Y_2)/((Y_0/D_02)+(Y_1/D_12)+(Y_3/D_23));
173    }
174    else
175    {
176     D_2_m = 10E-10; /* Case where Y_2 = 1 [m^2/s] */
177    }
178     if(Y_3 < 1.0)
179    {
180     /* Mixture diffusion coefficient of 3 [m^2/s] */
181     D_3_m = (1.0-Y_3)/((Y_0/D_03)+(Y_1/D_13)+(Y_2/D_23));
182    }
```

```
183      else
184      {
185       D_3_m = 10E-10; /* Case where Y_3 = 1 [m^2/s] */
186      }
187      x_vel_l = C_U(c, thread_l);
188      y_vel_l = C_V(c, thread_l);
189      abs_v_l = sqrt(x_vel_l*x_vel_l + y_vel_l*y_vel_l);/*Interstitial liquid velocity [m/s]*/
190
191      /* Density of species at cell temperature [kg/m^3] (Stark, 2015) */
192      rho_0 = (1.313467-0.0007238*T_cell)*1000; /* H0-NEC */
193      rho_1 = (1.2553362-0.0006966*T_cell)*1000; /* H4-NEC */
194      rho_2 = (1.210127-0.0006907*T_cell)*1000; /* H8-NEC */
195      rho_3 = (1.1482329-0.0007092*T_cell)*1000; /* H12-NEC */
196
197      /* Viscosity of species at cell temperature [kg/m.s] (Stark, 2015) */
198      visc_0 = visc_0_cP*0.001; /* H0-NEC */
199      visc_1 = visc_1_cP*0.001; /* H4-NEC */
200      visc_2 = visc_2_cP*0.001; /* H8-NEC */
201      visc_3 = visc_3_cP*0.001; /* H12-NEC */
202
203      /*Peclet numbers [-] */
204      Pe_m_0 = (abs_v_l*d_p)/D_0_m; /* 0 */
205      Pe_m_1 = (abs_v_l*d_p)/D_1_m; /* 1 */
206      Pe_m_2 = (abs_v_l*d_p)/D_2_m; /* 2 */
207      Pe_m_3 = (abs_v_l*d_p)/D_3_m; /* 3 */
208
209      /*Schmidt numbers [-] */
210      Sc_0 = visc_0/(rho_0*D_0_m); /* 0 */
211      Sc_1 = visc_1/(rho_1*D_1_m); /* 1 */
212      Sc_2 = visc_2/(rho_2*D_2_m); /* 2 */
213      Sc_3 = visc_3/(rho_3*D_3_m); /* 3 */
214
215      if (Sc_0<550.0)
216      {
217          /*Peclet number based on radial dispersion for 0 [-] */
218          Pe_t_0 = (0.058*Sc_0+14.0)-(0.058*Sc_0+2.0)*(exp((-352*pow(Sc_0,0.5))/Pe_m_0));
219      }
220      else
221      {
222          /*Peclet number based on radial dispersion for 0 [-] */
223          Pe_t_0 = 45.9-33.9*(exp((-15.0*Sc_0)/Pe_m_0));
224      }
225      if (Sc_1<550.0)
226      {
227          /*Peclet number based on radial dispersion for 1 [-] */
228          Pe_t_1 = (0.058*Sc_1+14.0)-(0.058*Sc_1+2.0)*(exp((-352*pow(Sc_1,0.5))/Pe_m_1));
229      }
230      else
231      {
232          /*Peclet number based on radial dispersion for 1 [-] */
233          Pe_t_1 = 45.9-33.9*(exp((-15.0*Sc_1)/Pe_m_1));
234      }
235      if (Sc_2<550.0)
236      {
237          /*Peclet number based on radial dispersion for 2 [-] */
238          Pe_t_2 = (0.058*Sc_2+14.0)-(0.058*Sc_2+2.0)*(exp((-352*pow(Sc_2,0.5))/Pe_m_2));
239      }
240      else
241      {
242          /*Peclet number based on radial dispersion for 2 [-] */
243          Pe_t_2 = 45.9-33.9*(exp((-15.0*Sc_2)/Pe_m_2));
244      }
245      if (Sc_3<550.0)
246      {
247          /*Peclet number based on radial dispersion for 3 [-] */
248          Pe_t_3 = (0.058*Sc_3+14.0)-(0.058*Sc_3+2.0)*(exp((-352*pow(Sc_3,0.5))/Pe_m_3));
249      }
250      else
251      {
252          /*Peclet number based on radial dispersion for 3 [-] */
253          Pe_t_3 = 45.9-33.9*(exp((-15.0*Sc_3)/Pe_m_3));
```

```
254        }
255        /*Radial dispersion coefficients [m^2/s] */
256        D_r_0 = (abs_v_l*d_p)/Pe_t_0; /* 0 */
257        D_r_1 = (abs_v_l*d_p)/Pe_t_1; /* 1 */
258        D_r_2 = (abs_v_l*d_p)/Pe_t_2; /* 2 */
259        D_r_3 = (abs_v_l*d_p)/Pe_t_3; /* 3 */
260
261        /*Mass average radial dispersion coefficient [m^2/s] */
262        D_r_avg = Y_0*D_r_0+Y_1*D_r_1+Y_2*D_r_2+Y_3*D_r_3;
263        C_UDMI(c,mix_thread,13) = D_r_avg;
264        return D_r_avg;
265    }
```

A.16. Volume average properties

```
1    **********************************************************************
2       UDF to plot plane volume-averaged properties.
3       UDF executed upon command after solution process has ended.
4    **********************************************************************/
5    #include "udf.h"
6
7    DEFINE_ON_DEMAND(Plane_Volume_Averaged_Properties)
8    {
9        Domain *mixture_domain;
10       mixture_domain=Get_Domain(1);
11       real Cell_axial_length;
12       Cell_axial_length = RP_Get_Input_Parameter("real-12"); /* Cell size axial length */
13       Thread *t, *Wall_Thread, *thread_l, *thread_g, *thread_s;
14       int i,ID;
15       cell_t cell, c0;
16       Thread *t0, *t_cell;
17       face_t f, f_wall;
18
19       /*  Cell calculation variables  */
20       real V_total, T_cell, VOF_l_cell, VOF_g_cell, VOF_s_cell, x_vel_l_cell, x_vel_g_cell,
21           y_vel_l_cell, y_vel_g_cell, abs_u_l_cell, abs_u_g_cell, rho_l_cell, mu_l_cell,
22           cp_l_cell, tc_l_cell, rho_g_cell, mu_g_cell, cp_g_cell, tc_g_cell, tc_eff_cell,
23           Y0_cell, Y1_cell, Y2_cell, Y3_cell, R1_cell, R2_cell, R3_cell, DoH_cell,
24           L_sat_cell, G_sat_cell, H2_mass_cell;
25
26       /*  Intermediate calculation variables  */
27       real T_int, VOF_l_int, VOF_g_int, VOF_s_int, x_vel_l_int, x_vel_g_int, abs_u_l_int,
28           abs_u_g_int, rho_l_int, mu_l_int, cp_l_int, tc_l_int, rho_g_int, mu_g_int,
29           cp_g_int, tc_g_int, tc_eff_int, Y0_int, Y1_int, Y2_int, Y3_int, R1_int, R2_int,
30           R3_int, DoH_int, L_sat_int, G_sat_int, H2_mass_int, Area_Weight;
31
32       /* Parameters */
33       real T, VOF_l, VOF_g, VOF_s, x_vel_l, x_vel_g, abs_u_l, abs_u_g, rho_l, mu_l, cp_l,
34           tc_l, rho_g, mu_g, cp_g, tc_g, tc_eff, Y0, Y1, Y2, Y3, R1, R2, R3, DoH, L_sat,
35           G_sat, H2_mass, Volume;
36
37       /* Coordinate parameters */
38       real xa[ND_ND];  /* Coordinates of wall cells*/
39       real xb[ND_ND];  /* Coordinates of domain cells*/
40       real x_a, x_b, y_b, A_x;
41       real A[ND_ND]; /*face area normal vector */
42
43       /* Variables for Mole fraction calculation */
44       real M_0,M_1,M_2,M_3,M_avg,X_0,X_1,X_2,X_3;
45       M_0 = 195.2597;   /*Molecular weight of H0-NEC [g/mol]*/
46       M_1 = 199.2915;   /*Molecular weight of H4-NEC [g/mol]*/
47       M_2 = 203.3232;   /*Molecular weight of H8-NEC [g/mol]*/
48       M_3 = 207.3550;   /*Molecular weight of H12-NEC [g/mol]*/
49
50  for (ID = 24; ID<=28; ++ID) /* Wall section zones ID 24, 25, 26, 27, and 28 */
51  {
52       Wall_Thread = Lookup_Thread(mixture_domain,ID); /* Wall thread */
53
54       begin_f_loop(f_wall,Wall_Thread)  /* Loop over cells on wall*/
```

```
55        {
56          /* Variable initialization */
57          V_total = 0.0;
58          DoH_int=0.0;
59          T_int=0.0;
60          VOF_l_int=0.0;
61          VOF_g_int=0.0;
62          VOF_s_int=0.0;
63          x_vel_l_int=0.0;
64          x_vel_g_int=0.0;
65          abs_u_l_int=0.0;
66          abs_u_g_int=0.0;
67          rho_l_int=0.0;
68          mu_l_int=0.0;
69          cp_l_int=0.0;
70          tc_l_int=0.0;
71          rho_g_int=0.0;
72          mu_g_int=0.0;
73          cp_g_int=0.0;
74          tc_g_int=0.0;
75          tc_eff_int=0.0;
76          Y0_int=0.0;
77          Y1_int=0.0;
78          Y2_int=0.0;
79          Y3_int=0.0;
80          R1_int=0.0;
81          R2_int=0.0;
82          R3_int=0.0;
83          L_sat_int=0.0;
84          G_sat_int=0.0;
85          H2_mass_int=0.0;
86
87          F_CENTROID(xa,f_wall,Wall_Thread);
88          x_a = xa[0]; /* wall face centroid axial coordinate */
89          i=0;
90          /* loops over all face threads in a domain*/
91          thread_loop_f (t,mixture_domain)
92        {
93          /* loop over all faces in face threads */
94        begin_f_loop (f,t)
95          {
96           F_CENTROID(xb,f,t);
97           x_b = xb[0]; /* face centroid axial coordinate */
98           y_b = xb[1]; /* face centroid radial coordinate*/
99
100           if  (x_b>(x_a+0.25*Cell_axial_length) && x_b<(x_a+0.75*Cell_axial_length))
101           {
102            F_AREA(A,f,t);
103            A_x = fabs(A[0]); /*Projected radial length of face*/
104            Area_Weight = A_x*2*M_PI; /*Equal to pi*(r_upper^2 - r_lower^2)*/
105            cell = F_C0(f,t);   /*Adjacent Cell Index*/
106            t_cell = THREAD_T0(t); /*Adjacent Cell Thread*/
107            thread_l = THREAD_SUB_THREAD(t_cell, 0);/* liquid phase cell thread */
108            thread_g = THREAD_SUB_THREAD(t_cell, 1);/* gas phase cell thread */
109            thread_s = THREAD_SUB_THREAD(t_cell, 2);/* solid phase cell thread */
110
111            /* Cell Properties */
112            Volume = C_VOLUME(cell,t_cell)*2*M_PI; /*cell volume */
113            T_cell = C_T(cell, thread_l);
114            VOF_l_cell =  C_VOF(cell, thread_l);
115            VOF_g_cell =  C_VOF(cell, thread_g);
116            VOF_s_cell =  C_VOF(cell, thread_s);
117            x_vel_l_cell = C_U(cell, thread_l);
118            y_vel_l_cell = C_V(cell, thread_l);
119            /*Interstitial liquid velocity*/
120            abs_u_l_cell = sqrt(x_vel_l_cell*x_vel_l_cell + y_vel_l_cell*y_vel_l_cell);
121            x_vel_g_cell = C_U(cell, thread_g);
122            y_vel_g_cell = C_V(cell, thread_g);
123            /*Interstitial gas velocity*/
124            abs_u_g_cell = sqrt(x_vel_g_cell*x_vel_g_cell + y_vel_g_cell*y_vel_g_cell);
125            rho_l_cell = C_R(cell, thread_l);
```

```
126            mu_l_cell = C_MU_L(cell, thread_l);
127            cp_l_cell = C_CP(cell, thread_l);
128            tc_l_cell = C_UDMI(cell,t_cell,9); /* Liquid thermal conductivity */
129            rho_g_cell = C_R(cell, thread_g);
130            mu_g_cell = C_MU_L(cell, thread_g);
131            cp_g_cell = C_CP(cell, thread_g);
132            tc_g_cell =  C_UDMI(cell,t_cell,10); /* Gas thermal conductivity */
133            tc_eff_cell = C_UDMI(cell,t_cell,11); /* Effective thermal conductivity */
134            Y0_cell = C_YI(cell,thread_l,0); /* Mass fraction of H0-NEC */
135            Y1_cell = C_YI(cell,thread_l,1); /* Mass fraction of H4-NEC */
136            Y2_cell = C_YI(cell,thread_l,2); /* Mass fraction of H8-NEC */
137            Y3_cell = C_YI(cell,thread_l,3); /* Mass fraction of H12-NEC */
138            /*Average molecular weight of mixture [g/mol]*/
139            M_avg = 1/((Y0_cell/M_0)+(Y1_cell/M_1)+(Y2_cell/M_2)+(Y3_cell/M_3));
140            X_0 = (Y0_cell/M_0)*M_avg ; /* Mole fraction of H0-NEC */
141            X_1 = (Y1_cell/M_1)*M_avg ; /* Mole fraction of H4-NEC */
142            X_2 = (Y2_cell/M_2)*M_avg ; /* Mole fraction of H8-NEC */
143            X_3 = (Y3_cell/M_3)*M_avg ; /* Mole fraction of H12-NEC */
144            DoH_cell = (X_1 + 2*X_2 + 3*X_3)/3;
145
146            R1_cell = C_UDMI(cell,t_cell,14); /* Reaction rate 1 */
147            R2_cell = C_UDMI(cell,t_cell,15); /* Reaction rate 2 */
148            R3_cell = C_UDMI(cell,t_cell,16); /* Reaction rate 3 */
149            L_sat_cell = VOF_l_cell/(1-VOF_s_cell);
150            G_sat_cell = VOF_g_cell/(1-VOF_s_cell);
151            H2_mass_cell = (rho_g_cell*G_sat_cell)/(rho_g_cell*G_sat_cell+rho_l_cell*L_sat_cell)
                   ;
152
153            /* Total Volume */
154            V_total = V_total + Volume;
155
156            /* Volume-Weighted Average Properties */
157               /* Cell properties times cell volume*/
158            T_int = T_int + T_cell*Volume;
159            VOF_l_int = VOF_l_int + VOF_l_cell*Volume;
160            VOF_g_int = VOF_g_int + VOF_g_cell*Volume;
161            VOF_s_int = VOF_s_int + VOF_s_cell*Volume;
162            x_vel_l_int = x_vel_l_int + x_vel_l_cell*Volume;
163            x_vel_g_int = x_vel_g_int + x_vel_g_cell*Volume;
164            abs_u_l_int = abs_u_l_int + abs_u_l_cell*Volume;
165            abs_u_g_int = abs_u_g_int + abs_u_g_cell*Volume;
166            rho_l_int = rho_l_int + rho_l_cell*Volume;
167            mu_l_int = mu_l_int + mu_l_cell*Volume;
168            cp_l_int = cp_l_int + cp_l_cell*Volume;
169            tc_l_int = tc_l_int + tc_l_cell*Volume;
170            rho_g_int = rho_g_int + rho_g_cell*Volume;
171            mu_g_int = mu_g_int + mu_g_cell*Volume;
172            cp_g_int = cp_g_int + cp_g_cell*Volume;
173            tc_g_int = tc_g_int + tc_g_cell*Volume;
174            tc_eff_int = tc_eff_int + tc_eff_cell*Volume;
175            Y0_int = Y0_int + Y0_cell*Volume;
176            Y1_int = Y1_int + Y1_cell*Volume;
177            Y2_int = Y2_int + Y2_cell*Volume;
178            Y3_int = Y3_int + Y3_cell*Volume;
179            DoH_int = DoH_int + DoH_cell*Volume;
180            R1_int = R1_int + R1_cell*Volume;
181            R2_int = R2_int + R2_cell*Volume;
182            R3_int = R3_int + R3_cell*Volume;
183            L_sat_int = L_sat_int + L_sat_cell*Volume;
184            G_sat_int = G_sat_int + G_sat_cell*Volume;
185            H2_mass_int = H2_mass_int + H2_mass_cell*Volume;
186
187            i=i+1;
188          }
189        }
190      end_f_loop (f,t)
191      }
192        /* Plane Volume-Weighted Average Properties */
193        T = T_int/V_total;
194        VOF_l = VOF_l_int/V_total;
195        VOF_g = VOF_g_int/V_total;
```

```
196          VOF_s = VOF_s_int/V_total;
197          x_vel_l = x_vel_l_int/V_total;
198          x_vel_g = x_vel_g_int/V_total;
199          abs_u_l = abs_u_l_int/V_total;
200          abs_u_g = abs_u_g_int/V_total;
201          rho_l = rho_l_int/V_total;
202          mu_l = mu_l_int/V_total;
203          cp_l = cp_l_int/V_total;
204          tc_l = tc_l_int/V_total;
205          rho_g = rho_g_int/V_total;
206          mu_g = mu_g_int/V_total;
207          cp_g = cp_g_int/V_total;
208          tc_g = tc_g_int/V_total;
209          tc_eff = tc_eff_int/V_total;
210          Y0 = Y0_int/V_total;
211          Y1 = Y1_int/V_total;
212          Y2 = Y2_int/V_total;
213          Y3 = Y3_int/V_total;
214          DoH = DoH_int/V_total;
215          R1 = R1_int/V_total;
216          R2 = R2_int/V_total;
217          R3 = R3_int/V_total;
218          L_sat = L_sat_int/V_total;
219          G_sat = G_sat_int/V_total;
220          H2_mass = H2_mass_int/V_total;
221
222          /* Record values in user defined memory slots */
223          F_UDMI(f_wall,Wall_Thread,22) = T;
224          c0 = F_C0(f_wall,Wall_Thread);
225          t0 = F_C0_THREAD(f_wall,Wall_Thread);
226          C_UDMI(c0,t0,22)=F_UDMI(f_wall,Wall_Thread,22);
227
228          F_UDMI(f_wall,Wall_Thread,23) = VOF_l;
229          c0 = F_C0(f_wall,Wall_Thread);
230          t0 = F_C0_THREAD(f_wall,Wall_Thread);
231          C_UDMI(c0,t0,23)=F_UDMI(f_wall,Wall_Thread,23);
232
233          F_UDMI(f_wall,Wall_Thread,24) = VOF_g;
234          c0 = F_C0(f_wall,Wall_Thread);
235          t0 = F_C0_THREAD(f_wall,Wall_Thread);
236          C_UDMI(c0,t0,24)=F_UDMI(f_wall,Wall_Thread,24);
237
238          F_UDMI(f_wall,Wall_Thread,25) = VOF_s;
239          c0 = F_C0(f_wall,Wall_Thread);
240          t0 = F_C0_THREAD(f_wall,Wall_Thread);
241          C_UDMI(c0,t0,25)=F_UDMI(f_wall,Wall_Thread,25);
242
243          F_UDMI(f_wall,Wall_Thread,26) = x_vel_l;
244          c0 = F_C0(f_wall,Wall_Thread);
245          t0 = F_C0_THREAD(f_wall,Wall_Thread);
246          C_UDMI(c0,t0,26)=F_UDMI(f_wall,Wall_Thread,26);
247
248          F_UDMI(f_wall,Wall_Thread,27) = x_vel_g;
249          c0 = F_C0(f_wall,Wall_Thread);
250          t0 = F_C0_THREAD(f_wall,Wall_Thread);
251          C_UDMI(c0,t0,27)=F_UDMI(f_wall,Wall_Thread,27);
252
253          F_UDMI(f_wall,Wall_Thread,28) = abs_u_l;
254          c0 = F_C0(f_wall,Wall_Thread);
255          t0 = F_C0_THREAD(f_wall,Wall_Thread);
256          C_UDMI(c0,t0,28)=F_UDMI(f_wall,Wall_Thread,28);
257
258          F_UDMI(f_wall,Wall_Thread,29) = abs_u_g;
259          c0 = F_C0(f_wall,Wall_Thread);
260          t0 = F_C0_THREAD(f_wall,Wall_Thread);
261          C_UDMI(c0,t0,29)=F_UDMI(f_wall,Wall_Thread,29);
262
263          F_UDMI(f_wall,Wall_Thread,30) = rho_l;
264          c0 = F_C0(f_wall,Wall_Thread);
265          t0 = F_C0_THREAD(f_wall,Wall_Thread);
266          C_UDMI(c0,t0,30)=F_UDMI(f_wall,Wall_Thread,30);
```

```
267
268          F_UDMI(f_wall,Wall_Thread,31) = mu_l;
269          c0 = F_C0(f_wall,Wall_Thread);
270          t0 = F_C0_THREAD(f_wall,Wall_Thread);
271          C_UDMI(c0,t0,31)=F_UDMI(f_wall,Wall_Thread,31);
272
273          F_UDMI(f_wall,Wall_Thread,32) = cp_l;
274          c0 = F_C0(f_wall,Wall_Thread);
275          t0 = F_C0_THREAD(f_wall,Wall_Thread);
276          C_UDMI(c0,t0,32)=F_UDMI(f_wall,Wall_Thread,32);
277
278          F_UDMI(f_wall,Wall_Thread,33) = tc_l;
279          c0 = F_C0(f_wall,Wall_Thread);
280          t0 = F_C0_THREAD(f_wall,Wall_Thread);
281          C_UDMI(c0,t0,33)=F_UDMI(f_wall,Wall_Thread,33);
282
283          F_UDMI(f_wall,Wall_Thread,34) = rho_g;
284          c0 = F_C0(f_wall,Wall_Thread);
285          t0 = F_C0_THREAD(f_wall,Wall_Thread);
286          C_UDMI(c0,t0,34)=F_UDMI(f_wall,Wall_Thread,34);
287
288          F_UDMI(f_wall,Wall_Thread,35) = mu_g;
289          c0 = F_C0(f_wall,Wall_Thread);
290          t0 = F_C0_THREAD(f_wall,Wall_Thread);
291          C_UDMI(c0,t0,35)=F_UDMI(f_wall,Wall_Thread,35);
292
293          F_UDMI(f_wall,Wall_Thread,36) = cp_g;
294          c0 = F_C0(f_wall,Wall_Thread);
295          t0 = F_C0_THREAD(f_wall,Wall_Thread);
296          C_UDMI(c0,t0,36)=F_UDMI(f_wall,Wall_Thread,36);
297
298          F_UDMI(f_wall,Wall_Thread,37) = tc_g;
299          c0 = F_C0(f_wall,Wall_Thread);
300          t0 = F_C0_THREAD(f_wall,Wall_Thread);
301          C_UDMI(c0,t0,37)=F_UDMI(f_wall,Wall_Thread,37);
302
303          F_UDMI(f_wall,Wall_Thread,38) = tc_eff;
304          c0 = F_C0(f_wall,Wall_Thread);
305          t0 = F_C0_THREAD(f_wall,Wall_Thread);
306          C_UDMI(c0,t0,38)=F_UDMI(f_wall,Wall_Thread,38);
307
308          F_UDMI(f_wall,Wall_Thread,39) = Y0;
309          c0 = F_C0(f_wall,Wall_Thread);
310          t0 = F_C0_THREAD(f_wall,Wall_Thread);
311          C_UDMI(c0,t0,39)=F_UDMI(f_wall,Wall_Thread,39);
312
313          F_UDMI(f_wall,Wall_Thread,40) = Y1;
314          c0 = F_C0(f_wall,Wall_Thread);
315          t0 = F_C0_THREAD(f_wall,Wall_Thread);
316          C_UDMI(c0,t0,40)=F_UDMI(f_wall,Wall_Thread,40);
317
318          F_UDMI(f_wall,Wall_Thread,41) = Y2;
319          c0 = F_C0(f_wall,Wall_Thread);
320          t0 = F_C0_THREAD(f_wall,Wall_Thread);
321          C_UDMI(c0,t0,41)=F_UDMI(f_wall,Wall_Thread,41);
322
323          F_UDMI(f_wall,Wall_Thread,42) = Y3;
324          c0 = F_C0(f_wall,Wall_Thread);
325          t0 = F_C0_THREAD(f_wall,Wall_Thread);
326          C_UDMI(c0,t0,42)=F_UDMI(f_wall,Wall_Thread,42);
327
328          F_UDMI(f_wall,Wall_Thread,43) = R1;
329          c0 = F_C0(f_wall,Wall_Thread);
330          t0 = F_C0_THREAD(f_wall,Wall_Thread);
331          C_UDMI(c0,t0,43)=F_UDMI(f_wall,Wall_Thread,43);
332
333          F_UDMI(f_wall,Wall_Thread,44) = R2;
334          c0 = F_C0(f_wall,Wall_Thread);
335          t0 = F_C0_THREAD(f_wall,Wall_Thread);
336          C_UDMI(c0,t0,44)=F_UDMI(f_wall,Wall_Thread,44);
337
```

```
338         F_UDMI(f_wall,Wall_Thread,45) = R3;
339         c0 = F_C0(f_wall,Wall_Thread);
340         t0 = F_C0_THREAD(f_wall,Wall_Thread);
341         C_UDMI(c0,t0,45)=F_UDMI(f_wall,Wall_Thread,45);
342
343         F_UDMI(f_wall,Wall_Thread,46) = DoH;
344         c0 = F_C0(f_wall,Wall_Thread);
345         t0 = F_C0_THREAD(f_wall,Wall_Thread);
346         C_UDMI(c0,t0,46)=F_UDMI(f_wall,Wall_Thread,46);
347
348         F_UDMI(f_wall,Wall_Thread,47) = L_sat;
349         c0 = F_C0(f_wall,Wall_Thread);
350         t0 = F_C0_THREAD(f_wall,Wall_Thread);
351         C_UDMI(c0,t0,47)=F_UDF(f_wall,Wall_Thread,47);
352
353         F_UDMI(f_wall,Wall_Thread,48) = G_sat;
354         c0 = F_C0(f_wall,Wall_Thread);
355         t0 = F_C0_THREAD(f_wall,Wall_Thread);
356         C_UDMI(c0,t0,48)=F_UDMI(f_wall,Wall_Thread,48);
357
358         F_UDMI(f_wall,Wall_Thread,49) = H2_mass;
359         c0 = F_C0(f_wall,Wall_Thread);
360         t0 = F_C0_THREAD(f_wall,Wall_Thread);
361         C_UDMI(c0,t0,49)=F_UDMI(f_wall,Wall_Thread,49);
362       }
363     end_f_loop(f_wall,Wall_Thread)
364 }
365  }
```

A.17. Mass average properties

```
1  /************************************************************************
2     UDF to plot plane mass-averaged properties.
3     UDF executed upon command after solution process has ended.
4     ************************************************************************/
5  #include "udf.h"
6
7  DEFINE_ON_DEMAND(Plane_Mass_Averaged_Properties)
8  {
9     Domain *mixture_domain;
10    mixture_domain=Get_Domain(1);
11    real Cell_axial_length;
12    Cell_axial_length = RP_Get_Input_Parameter("real-12"); /* Cell size axial length */
13    Thread *t, *Wall_Thread, *thread_l, *thread_g, *thread_s;
14    int i,ID;
15    cell_t cell, c0;
16    Thread *t0, *t_cell;
17    face_t f, f_wall;
18
19    /*  Cell calculation variables  */
20    real L_mass_flow_cell_abs, G_mass_flow_cell_abs, T_cell, VOF_l_cell, VOF_g_cell,
21         VOF_s_cell, x_vel_l_cell, x_vel_g_cell, y_vel_l_cell, y_vel_g_cell, abs_u_l_cell,
22         abs_u_g_cell, rho_l_cell, mu_l_cell, cp_l_cell, tc_l_cell, rho_g_cell, mu_g_cell,
23         cp_g_cell, tc_g_cell, tc_eff_cell, Y0_cell, Y1_cell, Y2_cell, Y3_cell, R1_cell,
24         R2_cell, R3_cell, DoH_cell, L_sat_cell, G_sat_cell, H2_mass_cell;
25
26    /*  Intermediate calculation variables  */
27    real T_int, VOF_l_int, VOF_g_int, VOF_s_int, x_vel_l_int, x_vel_g_int, abs_u_l_int,
28         abs_u_g_int, rho_l_int, mu_l_int, cp_l_int, tc_l_int, rho_g_int, mu_g_int,
29         cp_g_int, tc_g_int, tc_eff_int, Y0_int, Y1_int, Y2_int, Y3_int, R1_int, R2_int,
30         R3_int, DoH_int, L_sat_int, G_sat_int, H2_mass_int, Area_Weight;
31
32    /* Parameters */
33    real L_mass_flow_abs, G_mass_flow_abs, T, VOF_l, VOF_g, VOF_s, x_vel_l, x_vel_g,
34         abs_u_l, abs_u_g, rho_l, mu_l, cp_l, tc_l, rho_g, mu_g, cp_g, tc_g, tc_eff,
35         Y0, Y1, Y2, Y3, R1, R2, R3, DoH, L_sat, G_sat, H2_mass;
36
37    /* Coordinate parameters */
38    real xa[ND_ND];  /* Coordinates of wall cells*/
```

```c
39      real xb[ND_ND];   /* Coordinates of domain cells*/
40      real x_a, x_b, y_b, A_x;
41      real A[ND_ND]; /*face area normal vector */
42
43      /* Variables for Mole fraction calculation */
44      real M_0,M_1,M_2,M_3,M_avg,X_0,X_1,X_2,X_3;
45      M_0 = 195.2597;   /*Molecular weight of H0-NEC [g/mol]*/
46      M_1 = 199.2915;   /*Molecular weight of H4-NEC [g/mol]*/
47      M_2 = 203.3232;   /*Molecular weight of H8-NEC [g/mol]*/
48      M_3 = 207.3550;   /*Molecular weight of H12-NEC [g/mol]*/
49
50
51  for (ID = 24; ID<=28; ++ID) /* Wall section zones ID 24, 25, 26, 27, and 28 */
52  {
53      Wall_Thread = Lookup_Thread(mixture_domain,ID); /* Wall thread */
54
55      begin_f_loop(f_wall,Wall_Thread)  /* Loop over cells on wall*/
56        {
57          /* Variable initialization */
58          L_mass_flow_abs = 0.0;
59          G_mass_flow_abs = 0.0;
60          DoH_int=0.0;
61          T_int=0.0;
62          VOF_l_int=0.0;
63          VOF_g_int=0.0;
64          VOF_s_int=0.0;
65          x_vel_l_int=0.0;
66          x_vel_g_int=0.0;
67          abs_u_l_int=0.0;
68          abs_u_g_int=0.0;
69          rho_l_int=0.0;
70          mu_l_int=0.0;
71          cp_l_int=0.0;
72          tc_l_int=0.0;
73          rho_g_int=0.0;
74          mu_g_int=0.0;
75          cp_g_int=0.0;
76          tc_g_int=0.0;
77          tc_eff_int=0.0;
78          Y0_int=0.0;
79          Y1_int=0.0;
80          Y2_int=0.0;
81          Y3_int=0.0;
82          R1_int=0.0;
83          R2_int=0.0;
84          R3_int=0.0;
85          L_sat_int=0.0;
86          G_sat_int=0.0;
87          H2_mass_int=0.0;
88
89          F_CENTROID(xa,f_wall,Wall_Thread);
90          x_a = xa[0]; /* wall face centroid axial coordinate */
91          i=0;
92          /* loops over all face threads in a domain*/
93          thread_loop_f (t,mixture_domain)
94          {
95          /* loop over all faces in face threads */
96          begin_f_loop (f,t)
97            {
98            F_CENTROID(xb,f,t);
99            x_b = xb[0]; /* face centroid axial coordinate */
100           y_b = xb[1]; /* face centroid radial coordinate*/
101
102            if  (x_b>(x_a+0.25*Cell_axial_length) && x_b<(x_a+0.75*Cell_axial_length))
103            {
104            F_AREA(A,f,t);
105            A_x = fabs(A[0]); /*Projected radial length of face*/
106            Area_Weight = A_x*2*M_PI; /*Equal to pi*(r_upper^2 - r_lower^2)*/
107            cell = F_C0(f,t);  /*Adjacent Cell Index*/
108            t_cell = THREAD_T0(t); /*Adjacent Cell Thread*/
109            thread_l = THREAD_SUB_THREAD(t_cell, 0);/* liquid phase cell thread */
```

```c
110        thread_g = THREAD_SUB_THREAD(t_cell, 1);/* gas phase cell thread */
111        thread_s = THREAD_SUB_THREAD(t_cell, 2);/* solid phase cell thread */
112
113        /* Cell Properties */
114        T_cell = C_T(cell, thread_l);
115        VOF_l_cell =  C_VOF(cell, thread_l);
116        VOF_g_cell =  C_VOF(cell, thread_g);
117        VOF_s_cell =  C_VOF(cell, thread_s);
118        x_vel_l_cell = C_U(cell, thread_l);
119        y_vel_l_cell = C_V(cell, thread_l);
120        /*Interstitial liquid velocity*/
121        abs_u_l_cell = sqrt(x_vel_l_cell*x_vel_l_cell + y_vel_l_cell*y_vel_l_cell);
122        x_vel_g_cell = C_U(cell, thread_g);
123        y_vel_g_cell = C_V(cell, thread_g);
124        /*Interstitial gas velocity*/
125        abs_u_g_cell = sqrt(x_vel_g_cell*x_vel_g_cell + y_vel_g_cell*y_vel_g_cell);
126        rho_l_cell = C_R(cell, thread_l);
127        mu_l_cell = C_MU_L(cell, thread_l);
128        cp_l_cell = C_CP(cell, thread_l);
129        tc_l_cell = C_UDMI(cell,t_cell,9); /* Liquid thermal conductivity */
130        rho_g_cell = C_R(cell, thread_g);
131        mu_g_cell = C_MU_L(cell, thread_g);
132        cp_g_cell = C_CP(cell, thread_g);
133        tc_g_cell =  C_UDMI(cell,t_cell,10); /* Gas thermal conductivity */
134        tc_eff_cell = C_UDMI(cell,t_cell,11); /* Effective thermal conductivity */
135        Y0_cell = C_YI(cell,thread_l,0); /*Mass fraction of H0-NEC*/
136        Y1_cell = C_YI(cell,thread_l,1); /*Mass fraction of H4-NEC*/
137        Y2_cell = C_YI(cell,thread_l,2); /*Mass fraction of H8-NEC*/
138        Y3_cell = C_YI(cell,thread_l,3); /*Mass fraction of H12-NEC*/
139        /*Average molecular weight of mixture [g/mol]*/
140        M_avg = 1/((Y0_cell/M_0)+(Y1_cell/M_1)+(Y2_cell/M_2)+(Y3_cell/M_3));
141        X_0 = (Y0_cell/M_0)*M_avg ; /*Mole fraction of H0-NEC*/
142        X_1 = (Y1_cell/M_1)*M_avg ; /*Mole fraction of H4-NEC*/
143        X_2 = (Y2_cell/M_2)*M_avg ; /*Mole fraction of H8-NEC*/
144        X_3 = (Y3_cell/M_3)*M_avg ; /*Mole fraction of H12-NEC*/
145        DoH_cell = (X_1 + 2*X_2 + 3*X_3)/3;
146
147        R1_cell = C_UDMI(cell,t_cell,14); /* Reaction rate 1*/
148        R2_cell = C_UDMI(cell,t_cell,15); /* Reaction rate 2*/
149        R3_cell = C_UDMI(cell,t_cell,16); /* Reaction rate 3*/
150        L_sat_cell = VOF_l_cell/(1-VOF_s_cell);
151        G_sat_cell = VOF_g_cell/(1-VOF_s_cell);
152        H2_mass_cell = (rho_g_cell*G_sat_cell)/(rho_g_cell*G_sat_cell+rho_l_cell*L_sat_cell)
                    ;
153
154          /* Cell absolute flow rates */
155        L_mass_flow_cell_abs=rho_l_cell*VOF_l_cell*fabs(x_vel_l_cell*Area_Weight);
156        G_mass_flow_cell_abs=rho_g_cell*VOF_g_cell*fabs(x_vel_g_cell*Area_Weight);
157
158        /* Total flow rates */
159        L_mass_flow_abs = L_mass_flow_abs + L_mass_flow_cell_abs;
160        G_mass_flow_abs = G_mass_flow_abs + G_mass_flow_cell_abs;
161
162        /* Mass-Weighted Average Properties */
163          /* Cell properties times cell mass flow rate */
164        T_int = T_int + T_cell*L_mass_flow_cell_abs;
165        VOF_l_int = VOF_l_int + VOF_l_cell*L_mass_flow_cell_abs;
166        VOF_g_int = VOF_g_int + VOF_g_cell*G_mass_flow_cell_abs;
167        VOF_s_int = VOF_s_int + VOF_s_cell*L_mass_flow_cell_abs;
168        x_vel_l_int = x_vel_l_int + x_vel_l_cell*L_mass_flow_cell_abs;
169        x_vel_g_int = x_vel_g_int + x_vel_g_cell*G_mass_flow_cell_abs;
170        abs_u_l_int = abs_u_l_int + abs_u_l_cell*L_mass_flow_cell_abs;
171        abs_u_g_int = abs_u_g_int + abs_u_g_cell*G_mass_flow_cell_abs;
172        rho_l_int = rho_l_int + rho_l_cell*L_mass_flow_cell_abs;
173        mu_l_int = mu_l_int + mu_l_cell*L_mass_flow_cell_abs;
174        cp_l_int = cp_l_int + cp_l_cell*L_mass_flow_cell_abs;
175        tc_l_int = tc_l_int + tc_l_cell*L_mass_flow_cell_abs;
176        rho_g_int = rho_g_int + rho_g_cell*G_mass_flow_cell_abs;
177        mu_g_int = mu_g_int + mu_g_cell*G_mass_flow_cell_abs;
178        cp_g_int = cp_g_int + cp_g_cell*G_mass_flow_cell_abs;
179        tc_g_int = tc_g_int + tc_g_cell*G_mass_flow_cell_abs;
```

```
180            tc_eff_int = tc_eff_int + tc_eff_cell*L_mass_flow_cell_abs;
181            Y0_int = Y0_int + Y0_cell*L_mass_flow_cell_abs;
182            Y1_int = Y1_int + Y1_cell*L_mass_flow_cell_abs;
183            Y2_int = Y2_int + Y2_cell*L_mass_flow_cell_abs;
184            Y3_int = Y3_int + Y3_cell*L_mass_flow_cell_abs;
185            DoH_int = DoH_int + DoH_cell*L_mass_flow_cell_abs;
186            R1_int = R1_int + R1_cell*L_mass_flow_cell_abs;
187            R2_int = R2_int + R2_cell*L_mass_flow_cell_abs;
188            R3_int = R3_int + R3_cell*L_mass_flow_cell_abs;
189            L_sat_int = L_sat_int + L_sat_cell*L_mass_flow_cell_abs;
190            G_sat_int = G_sat_int + G_sat_cell*L_mass_flow_cell_abs;
191            H2_mass_int = H2_mass_int + H2_mass_cell*L_mass_flow_cell_abs;
192
193          i=i+1;
194        }
195      }
196    end_f_loop (f,t)
197      }
198        /* Plane Mass-Weighted Average Properties */
199        T = T_int/L_mass_flow_abs;
200        VOF_l = VOF_l_int/L_mass_flow_abs;
201        VOF_g = VOF_g_int/L_mass_flow_abs;
202        VOF_s = VOF_s_int/L_mass_flow_abs;
203        x_vel_l = x_vel_l_int/L_mass_flow_abs;
204        x_vel_g = x_vel_g_int/G_mass_flow_abs;
205        abs_u_l = abs_u_l_int/L_mass_flow_abs;
206        abs_u_g = abs_u_g_int/G_mass_flow_abs;
207        rho_l = rho_l_int/L_mass_flow_abs;
208        mu_l = mu_l_int/L_mass_flow_abs;
209        cp_l = cp_l_int/L_mass_flow_abs;
210        tc_l = tc_l_int/L_mass_flow_abs;
211        rho_g = rho_g_int/G_mass_flow_abs;
212        mu_g = mu_g_int/G_mass_flow_abs;
213        cp_g = cp_g_int/G_mass_flow_abs;
214        tc_g = tc_g_int/G_mass_flow_abs;
215        tc_eff = tc_eff_int/L_mass_flow_abs;
216        Y0 = Y0_int/L_mass_flow_abs;
217        Y1 = Y1_int/L_mass_flow_abs;
218        Y2 = Y2_int/L_mass_flow_abs;
219        Y3 = Y3_int/L_mass_flow_abs;
220        DoH = DoH_int/L_mass_flow_abs;
221        R1 = R1_int/L_mass_flow_abs;
222        R2 = R2_int/L_mass_flow_abs;
223        R3 = R3_int/L_mass_flow_abs;
224        L_sat = L_sat_int/L_mass_flow_abs;
225        G_sat = G_sat_int/L_mass_flow_abs;
226        H2_mass = H2_mass_int/L_mass_flow_abs;
227
228        /* Record values in user defined memory slots */
229        F_UDMI(f_wall,Wall_Thread,22) = T;
230        c0 = F_C0(f_wall,Wall_Thread);
231        t0 = F_C0_THREAD(f_wall,Wall_Thread);
232        C_UDMI(c0,t0,22)=F_UDMI(f_wall,Wall_Thread,22);
233
234        F_UDMI(f_wall,Wall_Thread,23) = VOF_l;
235        c0 = F_C0(f_wall,Wall_Thread);
236        t0 = F_C0_THREAD(f_wall,Wall_Thread);
237        C_UDMI(c0,t0,23)=F_UDMI(f_wall,Wall_Thread,23);
238
239        F_UDMI(f_wall,Wall_Thread,24) = VOF_g;
240        c0 = F_C0(f_wall,Wall_Thread);
241        t0 = F_C0_THREAD(f_wall,Wall_Thread);
242        C_UDMI(c0,t0,24)=F_UDMI(f_wall,Wall_Thread,24);
243
244        F_UDMI(f_wall,Wall_Thread,25) = VOF_s;
245        c0 = F_C0(f_wall,Wall_Thread);
246        t0 = F_C0_THREAD(f_wall,Wall_Thread);
247        C_UDMI(c0,t0,25)=F_UDMI(f_wall,Wall_Thread,25);
248
249        F_UDMI(f_wall,Wall_Thread,26) = x_vel_l;
250        c0 = F_C0(f_wall,Wall_Thread);
```

```
251        t0 = F_C0_THREAD(f_wall,Wall_Thread);
252        C_UDMI(c0,t0,26)=F_UDMI(f_wall,Wall_Thread,26);
253
254        F_UDMI(f_wall,Wall_Thread,27) = x_vel_g;
255        c0 = F_C0(f_wall,Wall_Thread);
256        t0 = F_C0_THREAD(f_wall,Wall_Thread);
257        C_UDMI(c0,t0,27)=F_UDMI(f_wall,Wall_Thread,27);
258
259        F_UDMI(f_wall,Wall_Thread,28) = abs_u_l;
260        c0 = F_C0(f_wall,Wall_Thread);
261        t0 = F_C0_THREAD(f_wall,Wall_Thread);
262        C_UDMI(c0,t0,28)=F_UDMI(f_wall,Wall_Thread,28);
263
264        F_UDMI(f_wall,Wall_Thread,29) = abs_u_g;
265        c0 = F_C0(f_wall,Wall_Thread);
266        t0 = F_C0_THREAD(f_wall,Wall_Thread);
267        C_UDMI(c0,t0,29)=F_UDMI(f_wall,Wall_Thread,29);
268
269        F_UDMI(f_wall,Wall_Thread,30) = rho_l;
270        c0 = F_C0(f_wall,Wall_Thread);
271        t0 = F_C0_THREAD(f_wall,Wall_Thread);
272        C_UDMI(c0,t0,30)=F_UDMI(f_wall,Wall_Thread,30);
273
274        F_UDMI(f_wall,Wall_Thread,31) = mu_l;
275        c0 = F_C0(f_wall,Wall_Thread);
276        t0 = F_C0_THREAD(f_wall,Wall_Thread);
277        C_UDMI(c0,t0,31)=F_UDMI(f_wall,Wall_Thread,31);
278
279        F_UDMI(f_wall,Wall_Thread,32) = cp_l;
280        c0 = F_C0(f_wall,Wall_Thread);
281        t0 = F_C0_THREAD(f_wall,Wall_Thread);
282        C_UDMI(c0,t0,32)=F_UDMI(f_wall,Wall_Thread,32);
283
284        F_UDMI(f_wall,Wall_Thread,33) = tc_l;
285        c0 = F_C0(f_wall,Wall_Thread);
286        t0 = F_C0_THREAD(f_wall,Wall_Thread);
287        C_UDMI(c0,t0,33)=F_UDMI(f_wall,Wall_Thread,33);
288
289        F_UDMI(f_wall,Wall_Thread,34) = rho_g;
290        c0 = F_C0(f_wall,Wall_Thread);
291        t0 = F_C0_THREAD(f_wall,Wall_Thread);
292        C_UDMI(c0,t0,34)=F_UDMI(f_wall,Wall_Thread,34);
293
294        F_UDMI(f_wall,Wall_Thread,35) = mu_g;
295        c0 = F_C0(f_wall,Wall_Thread);
296        t0 = F_C0_THREAD(f_wall,Wall_Thread);
297        C_UDMI(c0,t0,35)=F_UDMI(f_wall,Wall_Thread,35);
298
299        F_UDMI(f_wall,Wall_Thread,36) = cp_g;
300        c0 = F_C0(f_wall,Wall_Thread);
301        t0 = F_C0_THREAD(f_wall,Wall_Thread);
302        C_UDMI(c0,t0,36)=F_UDMI(f_wall,Wall_Thread,36);
303
304        F_UDMI(f_wall,Wall_Thread,37) = tc_g;
305        c0 = F_C0(f_wall,Wall_Thread);
306        t0 = F_C0_THREAD(f_wall,Wall_Thread);
307        C_UDMI(c0,t0,37)=F_UDMI(f_wall,Wall_Thread,37);
308
309        F_UDMI(f_wall,Wall_Thread,38) = tc_eff;
310        c0 = F_C0(f_wall,Wall_Thread);
311        t0 = F_C0_THREAD(f_wall,Wall_Thread);
312        C_UDMI(c0,t0,38)=F_UDMI(f_wall,Wall_Thread,38);
313
314        F_UDMI(f_wall,Wall_Thread,39) = Y0;
315        c0 = F_C0(f_wall,Wall_Thread);
316        t0 = F_C0_THREAD(f_wall,Wall_Thread);
317        C_UDMI(c0,t0,39)=F_UDMI(f_wall,Wall_Thread,39);
318
319        F_UDMI(f_wall,Wall_Thread,40) = Y1;
320        c0 = F_C0(f_wall,Wall_Thread);
321        t0 = F_C0_THREAD(f_wall,Wall_Thread);
```

```
322            C_UDMI(c0,t0,40)=F_UDMI(f_wall,Wall_Thread,40);
323
324            F_UDMI(f_wall,Wall_Thread,41) = Y2;
325            c0 = F_C0(f_wall,Wall_Thread);
326            t0 = F_C0_THREAD(f_wall,Wall_Thread);
327            C_UDMI(c0,t0,41)=F_UDMI(f_wall,Wall_Thread,41);
328
329            F_UDMI(f_wall,Wall_Thread,42) = Y3;
330            c0 = F_C0(f_wall,Wall_Thread);
331            t0 = F_C0_THREAD(f_wall,Wall_Thread);
332            C_UDMI(c0,t0,42)=F_UDMI(f_wall,Wall_Thread,42);
333
334            F_UDMI(f_wall,Wall_Thread,43) = R1;
335            c0 = F_C0(f_wall,Wall_Thread);
336            t0 = F_C0_THREAD(f_wall,Wall_Thread);
337            C_UDMI(c0,t0,43)=F_UDMI(f_wall,Wall_Thread,43);
338
339            F_UDMI(f_wall,Wall_Thread,44) = R2;
340            c0 = F_C0(f_wall,Wall_Thread);
341            t0 = F_C0_THREAD(f_wall,Wall_Thread);
342            C_UDMI(c0,t0,44)=F_UDMI(f_wall,Wall_Thread,44);
343
344            F_UDMI(f_wall,Wall_Thread,45) = R3;
345            c0 = F_C0(f_wall,Wall_Thread);
346            t0 = F_C0_THREAD(f_wall,Wall_Thread);
347            C_UDMI(c0,t0,45)=F_UDMI(f_wall,Wall_Thread,45);
348
349            F_UDMI(f_wall,Wall_Thread,46) = DoH;
350            c0 = F_C0(f_wall,Wall_Thread);
351            t0 = F_C0_THREAD(f_wall,Wall_Thread);
352            C_UDMI(c0,t0,46)=F_UDMI(f_wall,Wall_Thread,46);
353
354            F_UDMI(f_wall,Wall_Thread,47) = L_sat;
355            c0 = F_C0(f_wall,Wall_Thread);
356            t0 = F_C0_THREAD(f_wall,Wall_Thread);
357            C_UDMI(c0,t0,47)=F_UDMI(f_wall,Wall_Thread,47);
358
359            F_UDMI(f_wall,Wall_Thread,48) = G_sat;
360            c0 = F_C0(f_wall,Wall_Thread);
361            t0 = F_C0_THREAD(f_wall,Wall_Thread);
362            C_UDMI(c0,t0,48)=F_UDMI(f_wall,Wall_Thread,48);
363
364            F_UDMI(f_wall,Wall_Thread,49) = H2_mass;
365            c0 = F_C0(f_wall,Wall_Thread);
366            t0 = F_C0_THREAD(f_wall,Wall_Thread);
367            C_UDMI(c0,t0,49)=F_UDMI(f_wall,Wall_Thread,49);
368          }
369      end_f_loop(f_wall,Wall_Thread)
370 }
371  }
```